Cyclic Plasticity and Creep of Power Plant Materials

Abdullah Aziz Saad, MSc

Thesis submitted to the University of Nottingham

for the degree of Doctor of Philosophy

MARCH 2012

Abstract

The thermo-mechanical fatigue (TMF) of power plant components is caused by the cyclic operation of power plant due to startup and shutdown processes and due to the fluctuation of demand in daily operation. Thus, a time-dependent plasticity model is required in order to simulate the component response under cyclic thermo-mechanical loading. The overall aim behind this study is to develop a material constitutive model, which can predict the creep and cyclic loading behaviour at high temperature environment, based on the cyclic loading test data of the P91 and the P92 steels.

The tests on all specimens in the study were performed using the Instron 8862 TMF machine system with a temperature uniformity of less than ±10°C within the gauge section of the specimen. For the isothermal tests on the P91 steel, fully-reversed, strain-controlled tests were conducted on a parent material of the steel at 400, 500 and 600°C. For the P92 steel, the same loading parameters in the isothermal tests were performed on a parent material and a weld metal of the steels at 500, 600 and 675°C. Strain-controlled thermo-mechanical fatigue tests were conducted on the parent materials of the P91 and the P92 steels under temperature ranges of 400-600°C and 500-675°C, respectively, with in-phase (IP) and out-of-phase (OP) loading. In general, the steels exhibit cyclic softening behaviour throughout the cyclic test duration under both isothermal and anisothermal conditions.

The cyclic softening behaviour of the P91 steel was further studied by analyzing stress-strain data at 600°C and by performing microstructural investigations. Scanning electron microscope (SEM) and transmission electron microscope (TEM) images were used to investigate microstructural evolution and the crack initiation of

the steel at different life fractions of the tests. The TEM images of the interrupted test specimens revealed subgrain coarsening during the cyclic tests. On the other hand, the SEM images showed the initiation of microcracks at the end of the stabilisation period and the cracks were propagated in the third stage of cyclic softening.

A unified, Chaboche, viscoplasticity model, which includes combined isotropic softening and kinematic hardening with a viscoplastic flow rule for time-dependent effects, was used to model the TMF behaviour of the steels The constants in the viscoplasticity model were initially determined from the first cycle stress-strain data, the maximum stress evolution during tests and the stress relaxation data. Then, the initial constants were optimized using a least-squares optimization algorithm in order to improve the general fit of the model to experimental data. The prediction of the model was further improved by including the linear nonlinear isotropic hardening in order to obtain better stress-strain behaviour in the stabilisation period.

The developed viscoplasticity model was subsequently used in the finite element simulations using the ABAQUS software. The focus of the simulation is to validate the performance of the model under various types of loading. Simulation results have been compared with the isothermal test data with different strain ranges and also the anisothermal cyclic testing data, for both in-phase and out-of-phase loadings. The model's performance under 3-dimensional stress conditions was investigated by testing and simulating the P91 steel using a notched specimen under stress-controlled conditions. The simulation results show a good comparison to the experimental data.

List of publications

1. Saad A. A., Hyde C. J., Sun W. and Hyde T. H. Thermal-mechanical fatigue simulation of a P91 steel in a temperature range of 400-600˚C. Materials at High Temperature 28 (3), 212-218, 2011.
2. Saad A. A., Sun W., Hyde T. H., and Tanner D. W. J. Cyclic softening behaviour of a P91 steel under low cycle fatigue at high temperature. Procedia Engineering 10, 1103-1108, 2011.
3. Saad A. A., Hyde T. H., Sun W. and Hyde C. J. Constitutive model development of P91 steel and its simulation in TMF conditions. ESIA11 Conf. on Engineering Structural Integrity Assessment. 25-24 May 2011, Manchester, UK.
4. Hyde C. J., Sun W., Hyde T. H., Saad A. A. Thermo-mechanical fatigue testing and simulation using a viscoplasticty model. 21st Int. Workshop on Computational Mechanics of Materials, 22-24 August 2011, Limerick, Ireland.
5. Saad A. A., Hyde C. J., Sun W. and Hyde T. H. Thermal-mechanical fatigue simulation of a P91 steel in a temperature range of 400-600°C. HIDA-5 Int. Conf., 23-25 June 2010, Guildford, UK.
6. Hyde C. J., Sun W., Hyde T. H., Saad A. A. Thermo-mechanical fatigue testing and simulation using a viscoplasticity model. (Accepted for Journal of Computational Materials Science).

Acknowledgements

I would like to take this opportunity to express my gratitude to my supervisors, Professor Thomas Hyde and Dr Wei Sun, for their expertise, continued support and valuable advice during my PhD study. Also, I would like to thank Professor Sean Leen for his supervision during the first year of my research.

I wish to thank the technical staffs from the Department of Mechanical, Materials and Manufacturing Engineering of the University of Nottingham, particularly Mr Thomas Buss and Mr Brian Webster for their help with the experimental aspects of this work. Thank you to Dr Nigel Neate, Mr Keith Dinsdale and Mr Martin Roe, for the training in handling the SEM and TEM equipments. Also, I thank my fellow researchers in the University Technology Centre and the Structural Integrity and Dynamics group for their friendship and knowledge sharing.

I must thank Universiti Sains Malaysia and Ministry of Higher Education Malaysia for financial support through academic staff training program, which enable me to further my study in the University of Nottingham. Also, I would like to acknowledge the support of EPSRC through the Supergen 2 programme and its industrial partners for their valuable contributions to my project.

Finally, I would like to express my special thanks to my wife, Zuraihana Bachok, and my kids for their love and support during my study in Nottingham. Also, I thank my family members and friends for their support and encouragement.

Nomenclature

D	Damage
EBSD	Electron backscatter diffraction
FE	Finite element
IP	In-phase
LB	Lower bound
N_{sta}	Number of cycles to reach the beginning of linear softening stage
N_{tan}	Number of cycles to reach the final softening stage
N_f	Number of cycles to failure
N_{fin}	Final number of cycles applied in the cyclic test
OP	Out-of-phase
PID	Proportional, integral and derivative
SEM	Scanning electron microscopy
TC	Thermocouple
TEM	Transmission electron microscopy
TMF	Thermo-mechanical fatigue
UB	Upper bound

List of contents

Chapter 1 - Introduction

1.1 Background

The need for the power generation industry to improve the thermal efficiency of power plant has led to the development of 9-12%Cr martensitic steels (Ennis et al., 2003). The research on these materials has focussed on its creep strength, due to its intended application at high temperature. However, understanding the thermo-mechanical behaviour of power plant materials has become more important as the current operation involves more cyclic operation, which has introduced the possibility of thermo-mechanical fatigue (TMF) problems.

The required cyclic operation of power plant due to market forces and competition has increased the concern of researchers on creep-fatigue interaction behaviour. During start up, shut down or load changes of power plant operation, severe thermal gradients between the inside and outside of components due to rapid rates of change of steam temperatures may cause high stress levels to develop (Shibli and Starr, 2007). For instance, bore cracking was found in power plant components and it has been associated with thermal fatigue loading (Brett, 2003). To avoid thermal fatigue, caused by frequent cycling, one solution is to utilise higher creep strength alloy steels for pressure vessel construction (Shibli, 2008) so that the thickness of the power plant components can be reduced. However, the stress-strain behaviour of new power plant components needs to be understood first. This can be predicted by finite element simulation as previously modelled by Hyde et al. (2003) for pipe weldments under creep conditions at high temperature. The simulation of the components requires a suitable constitutive material model which can accurately predict the stress-strain behaviour and the failure life.

The majority of previous studies on power plant materials have been related to the creep behaviour under constant load operation. For example, creep constitutive equations have been developed for the parent, heat-affected zone (HAZ) and weld materials of Cr-Mo-V steel welds in the range 565-640˚C (Hayhurst et al., 2005). Similar studies have been carried out, for a P91 steel, in order to develop a creep constitutive model with a damage capability (Hyde et al, 2006). The development of these creep constitutive models have contributed to the gaining of a better understanding of the material behaviour in such applications as welding process modelling (Yaghi et al., 2008) and failure prediction in multiaxial components (Hayhurst et al., 2008).

In contrast to the above applications, the constitutive models which deal with creep and cyclic loading conditions of power plant materials have had relatively little attention. Thus, a model which can include both cyclic and viscous effects is required. A commonly used model is the unified viscoplasticity model originally developed by Chaboche (Chaboche and Rousselier, 1983). This viscoplasticity model has been used in many researches, including the studies on aeroengine materials such as nickel-base alloys (Yaguchi et al., 2002). However, the viscoplasticity model is rarely used to represent the behaviour of power plant materials.

1.2 Objectives

The objectives of the research are:

- To obtain quality stress-strain data from the P91 and the P92 steels under cyclic plasticity and creep conditions in isothermal and anisothermal tests using an available testing machine systems in the University of Nottingham;

- To develop material constitutive models for P91 and P92 steels which can accurately predict their creep and cyclic plasticity behaviour in a high temperature environments;
- To investigate the cyclic softening behaviour of the steels by analyzing the stress-strain behaviour and observing the microstructural evolutions throughout the lifetime of the steels;
- To implement the viscoplasticity model in a commercial finite element software and simulate the stress-strain behaviour of the steels under thermo-mechanical fatigue loading conditions.

1.3 Thesis Outline

Chapter 2 presents the literature review on the material constitutive model which includes typical cyclic plasticity components, such as kinematic and isotropic hardening, and also a viscoplasticity model. Examples of previous work on material behaviour modelling under cyclic thermo-mechanical conditions are also presented. The developments of the P91 and the P92 steels used in the study are briefly introduced.

The experimental equipment and procedures used for the isothermal and anisothermal tests are described in Chapter 3. The details of the materials used, the geometries of the specimens and the implemented loading in the testing programmes are presented. Typical results of the tests are reported at the end of this chapter.

In Chapter 4, the experimental stress-strain data, particularly for the P91 steel at 600°C, are further analyzed in order to understand the steel's evolution under cyclic loading. The results of microstructure investigation of the steel at different life

fractions of the tests using scanning and transmission electron microscopes are also presented.

Chapter 5 presents the development of the unified viscoplasticity model for the P91 and the P92 steels using the isothermal strain-controlled test data. The procedures for determining the initial material constants are described. Then, the optimisation programme, used to improve the stress-strain prediction of the model, is described and the predicted results are compared to the experimental data. A modification to the isotropic hardening model is also presented in order to improve the cyclic softening prediction of the steels.

In Chapter 6, finite element simulations of the steels' behaviour using the viscoplasticity model using a commercial finite element software, ABAQUS, are described. Simulation results of an axisymmetric model under isothermal conditions at various strain ranges, a notched specimen model under isothermal stress-controlled condition and an axisymmetric model under cyclic thermo-mechanical conditions are compared to experimental data to validate the prediction capability of the developed model.

Finally, Chapter 7 presents the overall research conclusions and suggests the possible future work.

Chapter 2 – Literature review

2.1 Overview

This literature review chapter is mainly concerned with material constitutive models in relation to the steels used in this study, namely P91 and P92 steels. As the material deforms cyclically under thermomechanical fatigue loading conditions, plastic behaviour becomes important and the strain hardening behaviours such as isotropic and kinematic hardening are reviewed in this Chapter. This chapter also includes information on the development of the P91 and P92 steels, which have been specifically developed for power plant applications and designed to have a specific microstructure, in order to produce steels with good high temperature mechanical behaviour.

2.2 Introduction to material behaviour modelling

In general, a material behaviour model is used to describe the stress-strain behaviour of a material. It can be divided into two classes (Charkaluk et al., 2002). The first model class is a physically-based model type representing a mechanical behaviour by considering microstructure evolutions of materials. This kind of model is used to represent both microscopic phenomena, such as microstructure evolution, and macroscopic mechanical behaviour, such as creep and relaxation, on a material scale. For example, cyclic softening behaviour of the martensitic 9Cr1Mo steel has been modelled by analyzing and measuring the dislocation density using transmission electron microscopy; the microstructure size and the macroscopic stresses of cyclic softening phenomenon can then be predicted (Sauzay et al., 2005, Sauzay et al., 2008). The second model class is a phenomenological-based model type based on the results of mechanical tests on a material. This material model is used to predict the stress-strain behaviour of a material and the model can

be further used to predict the stress-strain behaviour of a mechanical structure using, typically, a finite element simulation. The second model will be the focus of this study.

2.3 Elastic and plastic deformation

When a load is applied to a body, a deformation will occur in either elastic or elastic-plastic conditions, which depends on the magnitude of the applied load. In the elastic deformation range, the body is returned to its original shape when the load is removed. On the other hand, plastic deformation is irreversible and occurrs when the load is such that some position within the component exceeds the elastic limit. In terms of the physics of the phenomena, the elastic deformation involves a variation in the interatomic distances without changes of place while plastic deformation modifies interatomic bonds caused by slip movement in the microstructure of the material (Lemaitre and Chaboche, 1994).

As reported by Timoshenko (1953), Robert Hooke studied the elasticity phenomenon by measuring how far a wire string, of around 30 feet in length deformed under an applied load. In the test, the magnitude of the extension was found to be proportional to the applied weight. Thus, the deformation of an elastic spring is generally described mathematically by the following equation:

$$F = kx \tag{2.1}$$

where F is applied force, x is associated displacement and k is the proportionality factor, which is often referred to as the spring constant.

Based on equation 2.1, the force and the displacement characteristics depend on the size of the measured body. Thus, stress, σ, which refers to the ratio of the applied force to the cross sectional area, and strain, ε, which refers to the ratio of

the extension to the initial length, are introduced to eliminate the geometrical factors (Callister, 2000). Equation 2.1 can be rewritten as:

$$\sigma = E\varepsilon \tag{2.2}$$

where E is proportionality constant which is often referred to as the Young's modulus or the modulus of elasticity (Hertzberg, 1996) for the material. Equation 2.2 is also known as Hooke's law, which describes the linear stress-strain response of a material.

Plastic deformation occurs when the applied load (or stress) exceeds a certain level of stress called the elastic limit. Above this limit, the stress is no longer proportional to strain. However, the exact stress at which this limit occurs is difficult to determine experimentally as it depends on the accuracy of the strain measurement device used. Thus, a conventional elastic limit or a yield stress value is determined by constructing a straight line parallel to the linear elastic stress-strain curve at a specified strain offset, commonly 0.2%. The intersection point between the parallel line and the experimental curve is taken as the yield stress (0.2% proof stress) value. For example, the yield stress value of P91 steel at room temperature with a 0.2% criterion is 415 MPa (Vaillant et al., 2008). In some cases, a lower strain offset of 0.02% is used when the permanent strain obtained with the former criterion is high when compared to the elastic strain (Lemaitre and Chaboche, 1994).

Irreversible deformation may also happen at stresses below the conventional elastic limit if the load is maintained for a long time. This type of deformation is referred to as creep, the magnitude of which is a function of stress, time and temperature. The creep effect is significant at high temperatures and is generally significant when the temperature of the material is greater than approximately 0.4 of the absolute melting temperature, T_m. A creep test is conducted by applying a constant load to a

specimen, which results in three stages of creep deformation. In the primary stage, the strain rate decreases with time as the material approaches a steady-state stage. The creep strain increases steadily in the secondary stage with a constant, minimum, strain rate. Finally, the strain rate accelerates during tertiary creep until final failure occurs (Bhadeshia, 2003; Evans and Wilshire, 1985). The secondary stage of creep usually occupies the longest period of time in a creep test and the steady-state creep rate behaviour is usually expressed by a power law, also referred to as Norton's law, which is given by the following equation:

$$\dot{\varepsilon} = A\sigma^n \tag{2.3}$$

where A and n are material constants which can be determined from data obtained in the secondary stage.

2.4 Cyclic plasticity

When subjected to cyclic loading condition, the plastic deformations which occur in materials exhibit several phenomena such as the Bauschinger effect, cyclic hardening/softening and material ratchetting. The cyclic loading of a material, under tension-compression conditions, produces a hysteresis loop. The stress-strain behaviour which occurs under cyclic loading, with time independent effects are normally represented by isotropic hardening, kinematic hardening or some combination of both the isotropic and kinematic hardening models.

2.4.1 Isotropic hardening model

Isotropic hardening describes the change which occurs in the equivalent stress, defining the size of the yield surface, as a function of accumulated plastic strain. A schematic description of the isotropic hardening model is shown in Figure 2.1.

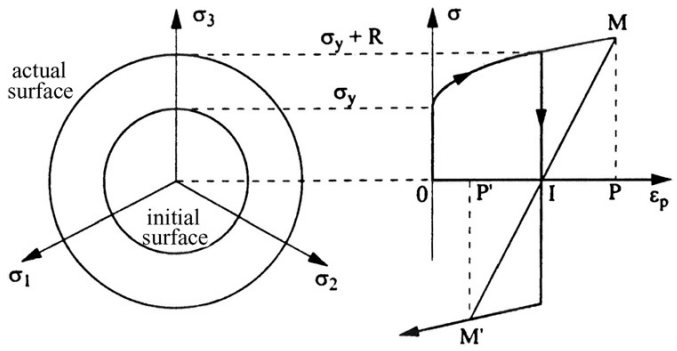

Figure 2.1: Schematic representation of isotropic hardening on the deviatoric plane and in tension-compression test conditions (Chaboche, 2008)

Isotropic hardening, or alternatively, the change in the size of the yield surface is represented by a scalar variable, R, and also known as a drag stress (Chaboche and Rousselier, 1983). The rate of evolution of isotropic hardening is represented by the following equation:-

$$\dot{R} = b(Q - R)\dot{p} \tag{2.4}$$

where p is the accumulated plastic strain, Q is the asymptotic value of R and b define the speed at which the saturation value, when variable R is constant, is approached. Equation 2.4 can be integrated with respect to time to give the following equation:-

$$R = Q(1 - e^{-bp}) \tag{2.5}$$

By using the von Mises loading function, the yield criterion for the isotropic hardening model, in the uniaxial form, is given in the following equation:-

$$f = |\sigma| - R - \sigma_Y = 0 \tag{2.6}$$

where σ_Y is the initial uniaxial yield stress in tension, or the initial elastic limit, as shown in Figure 2.1.

Under cyclic loading conditions, an undamaged material (in which cracks do not generally influence the mechanical behaviour) exhibits an evolution of the plastic strain range as the number of cycles increases which is referred to as cyclic

hardening or cyclic softening behaviour. The cyclic hardening of a material refers to the decrease of the plastic strain range, associated with an increase of the stress amplitude with increasing number of cycles in a cyclic test. This is observed under strain-controlled test conditions. This behaviour has been observed in many materials such as 316 stainless steel (Hyde et al., 2010; Kim et al., 2008; Mannan and Valsan, 2006), high nickel-chromium materials (Leen et al., 2010) and nickel-based superalloys (Zhan et al, 2008; Kim et al., 2007; Yaguchi et al., 2002). On the other hand, the plastic strain range increases as cyclic loading continues in a material, exhibiting cyclic softening behaviour such as is found to occur in a 55NiCrMoV8 (Bernhart et al., 1999) and 9Cr-1Mo steel (Nagesha et al., 2002; Shankar et al., 2006; Fournier et al., 2006; Fournier et al., 2009a). The cyclic hardening phenomenon indicates an increase of material's strength (Chaboche, 2008) in which the elastic strain range increases for a constant strain range. In the isotropic hardening model, this phenomenon is represented by an increase of the elastic limit ($\sigma_Y + R$). For a material exhibiting cyclic softening behaviour, the constant Q is negative so that a stabilized yield surface becomes smaller than the initial one (Chaboche, 2008).

The presence of isotropic hardening can be demonstrated by conducting biaxial tension tests such as tension-torsion tests (Lemaitre and Chaboche, 1994). For example, Murakami et al. (1989) conducted tension-torsion tests for a type 316 stainless steel and showed the evolution of cyclic hardening at different temperatures. Murakami et al. (1989) also found that the temperature of the test affected the ratio of the stress amplitudes at the saturated state to that in the initial cycle; it also affected the accumulated inelastic strain required to reach cyclic stabilization.

Regarding the effect of temperature, it also affects the cyclic evolution of certain materials. For example, cast iron has been shown to exhibit cyclic hardening behaviour at temperatures below 500°C, while the material has evolved in a cyclic softening condition when the test temperature is above 600°C (Constantinescu et al., 2004)

Generally, a material under cyclic loading shows a stabilized stage, in the middle of its lifetime. However, some materials, such as a martensitic type steels, exhibit an initially rapid load decrease followed by linear cyclic softening behaviour without the stabilization of the stress amplitude for a strain-controlled test. In dealing with this behaviour, Bernhart et al. (1999) employed a two-stage isotropic hardening model, as given by the following equation:-

$$R(p) = Q_1.p + Q_2(q).(1 - \exp(-b.p)) \qquad (2.7)$$

From the stress amplitude evolution data, the Q_2 constant is determined from the difference between the stress at first cycle and the stress approximately at the end of the primary load decrease while the Q_1 constant is identified from the slope of the secondary stage, as shown in Figure 2.2. This type of isotropic hardening model has been used for anisothermal loading conditions (Zhang et al, 2002).

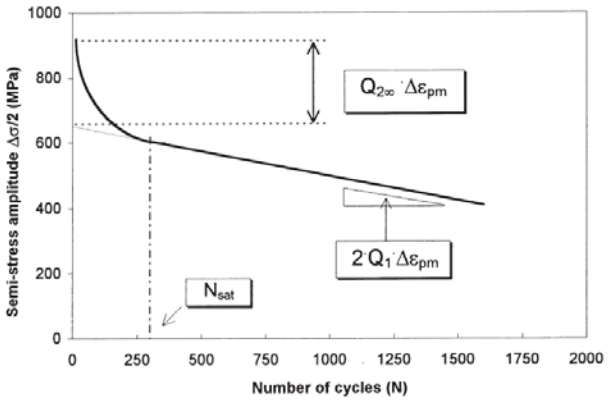

Figure 2.2: Schematical representation of the two-stage cyclic softening model (Bernhart et al., 1999)

2.4.2 Kinematic hardening model

The hardening of a material, which occurs due to plastic deformation, can also be represented by use of a kinematic hardening model. The model uses a different theoretical approach to that of the isotropic hardening model, in that the yield surface translates in stress space, rather than expand (Dunne and Petrinic, 2005). The kinematic hardening parameter χ is a tensor, also called the backstress or rest stress tensor (Chaboche and Rousselier, 1983), which defines the instantaneous position of the loading surface (Lemaitre and Chaboche, 1994). Figure 2.3 is a schematic description of the kinematic hardening model in stress space and the corresponding model in a tension-compression test, in which k represents elastic limit value.

In a tension-compression test, it is typically found that the yield stress in compression is lower than that if the test was carried out in tension first. This behaviour is known as the Bauschinger effect in which plastic deformation increases the yield strength in the direction of plastic flow and decreases it in the reverse direction (Zhang and Jiang, 2008). The kinematic hardening model is more appropriate for representing this phenomenon where the model assumes that the elastic region remains constant, both initially and during cyclic loading (Dunne and Petrinic, 2005), as illustrated, schematically, in Figure 2.4. The use of the kinematic hardening model, in predicting the Bauschinger effect, can be found in Chun et al. (2002).

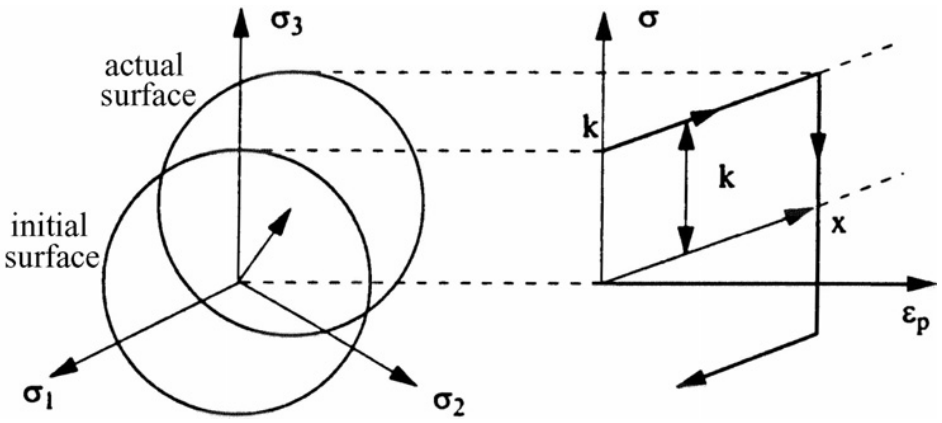

Figure 2.3: Schematic representation of kinematic hardening in deviatoric plane and in tension-compression test (Chaboche, 2008)

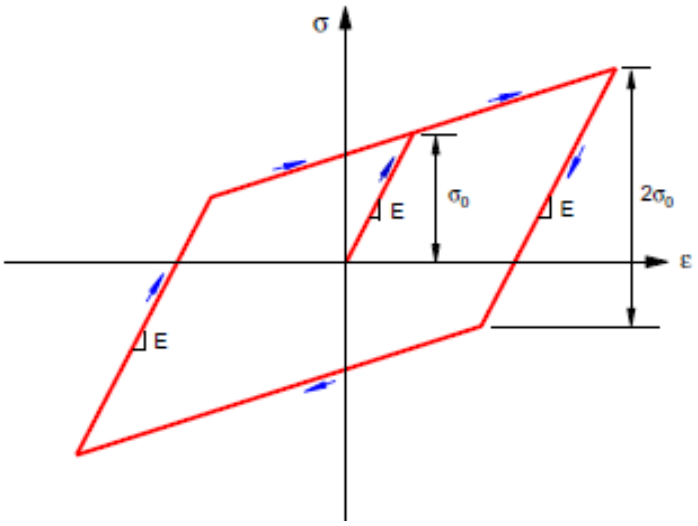

Figure 2.4: Schematic illustration of the Bauschinger effect in which the elastic limit is represented by σ_0 in this figure (Jiang and Zhang, 2008)

The yield criterion for the kinematic hardening model, in the uniaxial form, is given by the following equation:-

$$f = |\sigma - \chi| - k \tag{2.8}$$

where k is the initial yield stress value. In the kinematic hardening model, the initial yield stress is also described as the initial elastic limit or the initial size of the yield surface (Chaboche, 1989; Lemaitre and Chaboche, 1994).

The simplest model used to describe kinematic hardening uses a linear relationship between the change in kinematic hardening and the change in plastic strain. The linear kinematic hardening model, originally developed by Prager (1949), is given by the following equation:-

$$\dot{\boldsymbol{\chi}} = \frac{2}{3} c \dot{\boldsymbol{\varepsilon}}_p \tag{2.9}$$

where c is the material constant, which represent the gradient of the linear relationship (Avanzini, 2008). For the uniaxial loading case, Equation 2.9 is given by the following:-

$$\dot{\chi} = c \dot{\varepsilon}_p \tag{2.10}$$

where χ represents a scalar variable; the magnitude of χ is 3/2 times the kinematic hardening tensor parameter (Dunne and Petrinic, 2005). Mroz (1967) proposed an improvement to the linear kinematic hardening model by introducing a multilinear model which consists of a multisurface model representing a constant work hardening modulus in stress space.

Linear strain hardening is rarely observed in the actual cyclic loading tests. Generally, the stress-strain behaviour obtained from cyclic loading tests is a nonlinear relationship. The Amstrong-Frederick type kinematic hardening model, originally developed in 1966, has been used widely to represent this nonlinear stress-strain relationship. The model introduces a recall term, called dynamic recovery, into the linear model (Frederick and Armstrong, 2007) which is given by the following equation:-

$$\dot{\boldsymbol{\chi}} = \frac{2}{3} c \dot{\boldsymbol{\varepsilon}}_p - \gamma \boldsymbol{\chi} \dot{p} \tag{2.11}$$

where γ is a material constant. The recall term incorporates a fading memory effect of the strain path and causes a nonlinear response for the stress-strain behaviour

(Bari and Hassan, 2000). For the nonlinear kinematic hardening model of the time-independent plasticity behaviour, the value of c/γ determines the saturation of stress value in the plastic region and its combination with the k value represents the maximum stress for the plasticity test (Dunne and Petrinic, 2005). The saturated stress is described, schematically, in Figure 2.5.

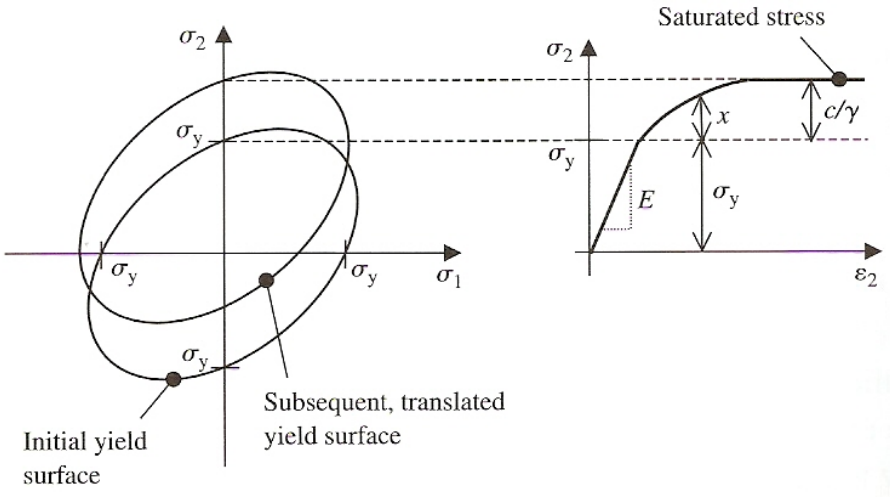

Figure 2.5: Schematic representation of saturated stress represented by the nonlinear kinematic hardening model (Dunne and Petrinic, 2005)

The constants in the nonlinear kinematic hardening model are represented by different equation than that in equation 2.11, as found in Chaboche and Rousselier (1983), Zhan and Tong (2007) and Gong et al. (2010), for example. The equation is given as follows:-

$$\dot{\boldsymbol{\chi}} = C\left(\frac{2}{3}a\dot{\boldsymbol{\varepsilon}}_p - \boldsymbol{\chi}\dot{p}\right) \tag{2.12}$$

where a is the saturation of the stress value in the plastic region, which is identical to the value of c/γ, and C represents the speed to reach the saturation value, which is equal to γ. In general, both of the nonlinear kinematic hardening equations (2.11 and 2.12) are the same, except for the fact that the constants are different in definition.

The Amstrong-Frederick hardening relation has been modified by decomposing the total backstress into a number of additive parts (Jiang and Kurath, 1996). The reason for the superposition of the kinematic hardening model is to extend the validity of the kinematic hardening model to a larger domain in stress and strain (Chaboche and Rousselier, 1983). The model is also intended to describe the ratchetting behaviour better (Lemaitre and Chaboche, 1994). Thus, the total backstress χ is given by the following equation:

$$\chi = \sum_{i=1}^{M} \chi_i \tag{2.13}$$

where χ_i is a part of the total backstress, i=1,2,…, M and M is the number of the additive components of the kinematic hardening. The model is usually decomposed into two or three kinematic variables. However, more variables are sometimes employed in certain cases, for example, in the study of the ratchetting effect (Bari and Hassan, 2000), in order to get a better agreement with experimental data. It is suggested by Chaboche (1986) that the first rule (χ_1) should start hardening with a very large modulus and that it stabilizes quickly. For example, the superposition of three kinematic hardening variables is shown in Figure 2.6.

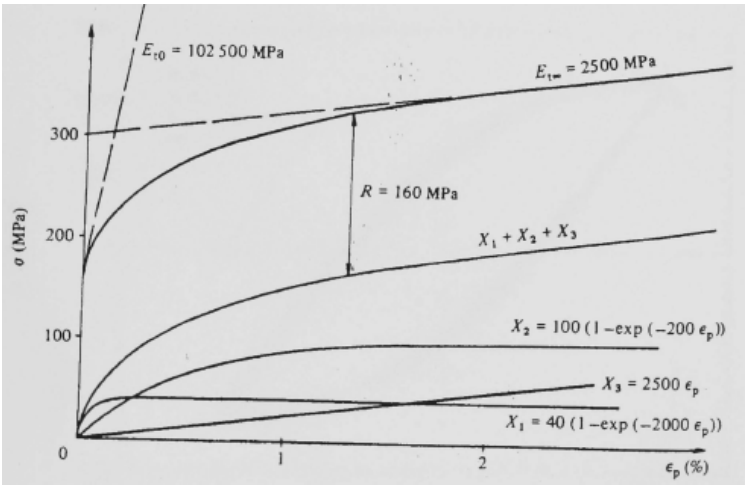

Figure 2.6: The stress-strain curve obtained from the superposition of three kinematic hardening variables (Lemaitre and Chaboche, 1994)

2.4.3 Combined isotropic-kinematic hardening model

Both the cyclic hardening/softening and Bauschinger phenomena are normally observed in tests of the real material. This observation indicates the requirement to combine both isotropic and kinematic hardening rules in order to predict the strain hardening and the cyclic hardening/softening of engineering materials. The yield criterion of the combined isotropic and kinematic hardening models, in the uniaxial form, is given by the following equation:-

$$f = |\sigma - \chi| - k - R \tag{2.14}$$

Theoretically, the behaviour of the material with a combined isotropic and kinematic hardening model will include both the translation and the expansion/contraction of the yield surface in stress space. An example of the implementation of this combined model can be found in Zhao et al. (2001). In this paper, the author used a time independent cyclic plasticity model combined with isotropic hardening and two nonlinear kinematic hardening rules, to predict the behaviour of a nickel base superalloy, at 300°C.

2.5 Time-dependent cyclic plasticity

The repeated loading of engineering components at high temperature may involve both plasticity and creep behaviour. The constitutive model for this condition is known as a time-dependent or a rate-dependent plasticity in which the plastic strain and the creep strain contribute to the total strain value.

2.5.1 Uncoupled elastoplasticity-creep

Conventionally, the creep (time-dependent) and the plasticity (time-independent) behaviour are modelled by an uncoupled elastic-plasticity-creep model. In the model, the stress-strain behaviour is represented by a creep model such as the

Norton's law and by a typical plasticity model such as the isotropic and kinematic hardening models. For example, Shang et al. (2006) used the model to represent the behaviour of superplastic forming dies. The constants for the selected creep and plasticity models are determined separately in a constant loading test and in cyclic loading tests, respectively, and there is no interaction assumed to occur between those constants in the creep and plasticity equations. In certain conditions, particularly for cyclic creep (ratchetting effect) and creep-plasticity interaction, the combination of the plasticity and creep equations give unsatisfactory results when compared to experimental data (Krempl, 2000). Thus, a viscoplasticity model has been used more frequently than the uncoupled elastic-plasticity-creep model to describe time-dependent plasticity behaviour at high temperature.

2.5.2 Unified viscoplasticity model

According to Lemaitre (2001), the viscoplasticity model refers to the mechanical response of materials in plastic condition which exhibits time dependent effect represented by a viscosity function. A well known viscoplasticity model is the unified viscoplasticity model proposed by Chaboche (Chaboche and Rousselier, 1983). The model is known as the "unified" viscoplasticity model for two reasons (Chaboche, 1989). Firstly, the plastic and the creep strains are represented simultaneously by one parameter and these strains are called the viscoplastic strain. Consequently, the strain does not exhibit a discontinuity under different types of loading. Secondly, the same hardening rules as the time independent plasticity rule are employed in the viscoplasticity model.

The viscoplastic strain rate of the model, in the uniaxial form, is given by the following equations:-

$$\dot{\varepsilon}_p = \left\langle \frac{f}{Z} \right\rangle^n \operatorname{sgn}(\sigma - \chi) \tag{2.15}$$

where:

$$\operatorname{sgn}(x) = \begin{cases} 1, x > 0 \\ 0, x = 0 \\ -1, x < 0 \end{cases} \quad \text{and} \quad \langle x \rangle = \begin{cases} x, x \geq 0 \\ 0, x < 0 \end{cases} \tag{2.16}$$

$$f = |\sigma - \chi| - k - R \tag{2.17}$$

In the unified viscoplasticity model, the total stress can be decomposed into four parts, namely initial yield stress k, drag stress R, backstress χ and viscous stress, σ_v as given by the following equation:-

$$\sigma = \chi + (R + k + \sigma_v) \operatorname{sgn}(\sigma - \chi) \tag{2.18}$$

The viscous stress which represents the rate dependency of the stress is a power function of the accumulated plastic strain rate as follows:-

$$\sigma_v = Z\dot{p}^{1/n} \tag{2.19}$$

The viscous stress is also known as the overstress due to the fact that the viscoplastic formulation allows the stress state to overpass the purely elastic domain (Chaboche, 2001). A schematic representation of the total stress decomposition in the unified viscoplasticity model is shown in Figure 2.7.

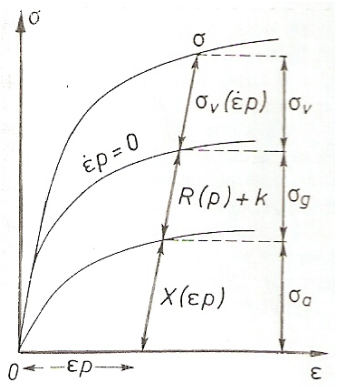

Figure 2.7: The decompositions of stress in the tensile test according the unified viscoplasticity model (Chaboche and Rousselier, 1983)

The unified viscoplasticity model has been used by Tong and his co-workers to predict the stress-strain behaviour of a nickel-based superalloy. For example, Zhao et al. (2001) developed the unified model to predict the stabilized cyclic loops of a nickel base superalloy at various strain ranges and at high temperatures. At the beginning of the work, only one strain rate was used in the study. An optimisation method was used to improve the initially determined parameters by minimizing the difference between the predicted and the experimental stress values. The optimisation method was further improved by considering several types of test data in the optimisation process such as monotonic, cyclic, relaxation and creep test data (Tong and Vermeulen, 2003; and Tong et al., 2004) and this process resulted in better predictions for the cyclic and creep tests by using only a single inelastic strain variable within the model. Additional terms can be included in the model such as a static recovery term (Zhan and Tong, 2007) and a plastic strain memory term (Zhan et al., 2008) in order to improve the model's prediction for more complex stress-strain behaviour. It can be seen from the works of Tong and his co-workers that the viscoplasticity model for the nickel-based superalloy has been developed in several stages, starting from a simple model, and the optimisation program has been used to determine the material constants.

Yaguchi and Takahashi (2000) used a unified viscoplastic model to represent the cyclic behaviour of modified 9Cr-1Mo steel under temperatures between 200 and 600°C. In the proposed model, the applied stress has been divided into three components; a back stress, an effective stress and an aging stress. The aging stress in the model is similar to the isotropic hardening variable, but is represented by different equations. The cyclic softening behaviour of the modified 9Cr-1Mo steel is represented by a modified kinematic hardening equation. The constants of the

model were determined by a step-by-step procedure and it involves a trial-and-error method. The model shows a good capability to describe the inelastic behaviour of modified 9Cr-1Mo steel under monotonic tension, stress relaxation, creep and anisothermal cyclic deformation. In order to improve the ratchetting behaviour prediction, Yaguchi and Takahashi (2005) modified their model by using the Ohno-Wang kinematic hardening rules. Koo and Lee (2007) also investigated the ratchetting behaviour of the modified 9Cr-1Mo steel at 600°C; however, a rate-independent model incorporating a kinematic hardening rule with three-decomposed rules and an isotropic hardening rule was used in their work.

In general, the phenomenologically based model is capable of predicting the behaviour of undamaged material for which the stress-strain prediction of the model is true up to a certain number of cycles and normally covers the majority of life cycles. In order to simulate the behaviour of a material for the whole of fatigue process, the material constitutive model could be combined with continuum damage mechanics theory. The damage mechanics theory enables the modelling of the material's strength degradation and the often rapid collapse of the specimen (Oller et al., 2005). The fatigue damage evolution is described in terms of the number of cycles and it may depend on several variables such as stress, plastic strain, damage variable, D, temperature or hardening variables (Shang and Yao, 1999)

For higher temperature applications, the creep-fatigue damage may be combined to provide a unified viscoplasticity model which can predict the failure of the specimen. The evolution of the combined damage approach is described by the following equation (Chaboche and Gallerneau, 2001):-

$$dD = f_C(\sigma, D, T)dt + f_F(\sigma_{\max}, \sigma, D, T)dN \qquad (2.20)$$

where the evolution of creep damage is based on the time evolution while the fatigue damage evolution is based on the evolution of the number of cycles. The model has been successfully applied to a nickel based superalloy (Yeom et al., 2007, El Gharad et al., 2006) and a single crystal (Dunne and Hayhurst, 1992a; Dunne and Hayhurst, 1992b). However, the inclusion of a creep-damage model into the constitutive equation requires many types of test loading configurations to be implemented and thus many specimens are required in the testing program (Dunne et al., 1992).

2.5 3 Two-layer viscoplasticity model

The two layer viscoplasticity material model is another type of viscoplasticity model which is available in commercial finite element software such as Abaqus. The model can be used to simulate the effect of time dependent behaviour as well as time independent behaviour. This model was developed by Kichenin et al. (1996). The model divides the viscous (time dependent effect) and time independent plasticity components into two independent parallel layers or networks which are known as the elastic-plastic network and the elastic-viscous network, as shown in Figure 2.8.

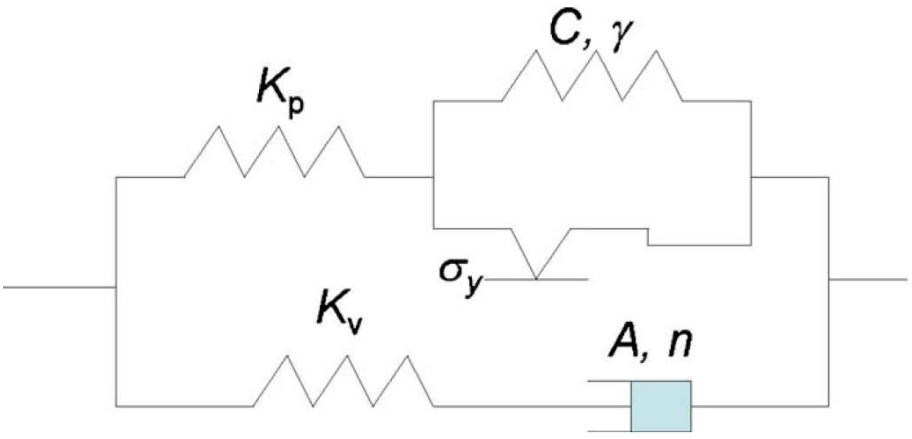

Figure 2.8: One-dimensional rheological representation of the two-layer viscoplasticity model (Leen et al., 2010)

The interactions of elastic-plastic and elastic-viscous networks are controlled by the user-specified ratio, f . The parameter is defined by the following equation:-

$$f = \frac{K_v}{K_p + K_v} \tag{2.21}$$

where K_v and K_p are the elastic modulus in the viscous and the plastic networks, respectively. The f value lies in the range 0 and 1 in which a value close to 1 indicates a high contribution of elastic viscous network. In isothermal conditions, the total strain is decomposed into elastic, ε_e , plastic, ε_p and viscous, ε_v , strain components, as follows:-

$$\varepsilon = \varepsilon_e + (1 - f)\varepsilon_p + f\varepsilon_v \tag{2.22}$$

The total stress of the model is divided into two different stresses, i.e., σ_p and σ_v , which control the evolution of plasticity and viscous effects in each network, respectively.

General plasticity and creep models can be implemented in the two-layer viscoplasticity model. For example, Figiel and Gunther (2008) used the nonlinear isotropic and the kinematic hardening model in the elastic-plastic network while the Norton power law model was selected for the elastic-viscous network. The model constants in the study were obtained by fitting the results of finite element simulations to quasi-static tensile and relaxation experimental tests carried out at various temperatures. Similar plasticity and creep models were chosen by Leen et al. (2010) which include combined isotropic-kinematic hardening plasticity and power law creep model to be used in the two-layer viscoplasticity model. Leen et al. (2010) determined the material constants for the combined isotropic-kinematic hardening by conducting isothermal cyclic tests while the creep model constants were identified from isothermal stress relaxation tests carried out at various

temperatures. Finally, the user-specified ratio, f, is identified by a fitting process which compares finite element predictions with experimental stress relaxation results.

The two-layer viscoplasticity model has been derived for several materials in order to represent the stress-strain behaviour, particularly for high temperature application. Charkaluk et al. (2002) used the two-layer viscoplasticity model to represent the cyclic behaviour of a cast iron, which is used in exhaust manifold structures. Leen et al. (2010) characterized the cyclic elastic-plastic-creep behaviour of a high nickel-chromium material (XN40F) which is used in superplastic forming tools at temperatures in the range 20°C to 900°C. The model has also been used to analyse polyelectrolyte membranes in fuel cells (Solasi et al. (2008). In earlier work on this model carried out by Kichenin et al. (1996), the nonlinear visco-elasticity behaviour of polyethylene was represented.

2.6 Material behaviour under TMF conditions

A great deal of research has been carried out in order to characterize the thermomechanical behaviour of engineering materials, using types of material models. For example, the two-layer model and the unified viscoplasticity model have been used to predict the behaviour of an exhaust manifold under thermomechanical fatigue conditions; both models exhibited similar mechanical responses (Charkaluk et al., 2002). Yaguchi et al. (2002) applied the unified viscoplasticity model to predict the anisothermal behaviour of a nickel-based superalloy between 450 and 950°C. The two-layer viscoplasticity model has also been successfully used to predict the behaviour of a high nickel-chromium material used in a superplastic forming process (Leen et al., 2010). Minichmayr et al. (2008) used the nonlinear kinematic hardening model and the Norton creep model to

describe the behaviour of aluminium-silicon cast alloy, machined from cylinder heads of combustion engines.

The constants for the material behaviour model in anisothermal conditions are commonly developed by determining material model constants under isothermal conditions for several temperatures in a specified temperature range. For example, Hyde et al. (2010) developed a unified Chaboche viscoplasticity model for a 316 stainless steel using isothermal strain-controlled test data with ±0.3% strain amplitude for temperatures in the range 300 and 600°C. The model gives good predictions when compared with experimental in-phase and out-of-phase thermomechanical fatigue test results even though the TMF tests were subjected to a higher mechanical strain range. The same approach was used by Leen et al. (2010) and Yaguchi et al. (2002) to characterize the thermomechanical fatigue behaviour of materials with a two-layer viscoplasticity and a unified viscoplasticity model, respectively.

The behaviour of P91 steel under thermomechanical fatigue loading conditions was studied by Okrajni et al. (2008). In the study, out-of-phase TMF loading was applied to a hollow specimen subjected to temperatures with the range 200 and 450°C. A mathematical model was developed, based on a low-cycle isothermal fatigue tests, and the top and bottom values of stress and strain were used in the model. The model gives good predictions when compared with the experimental results, as shown in Figure 2.9(a). However, only the behaviour of the steel at the sample size, was included in this study. The thermomechanical behaviour of another power plant material, ie, a P23 steel, was modelled by Hartrott et al. (2009) using a unified viscoplasticity model, which is a phenomenological-based model, and the model's

prediction results show a good comparison to experimental test data, as shown in Figure 2.9(b).

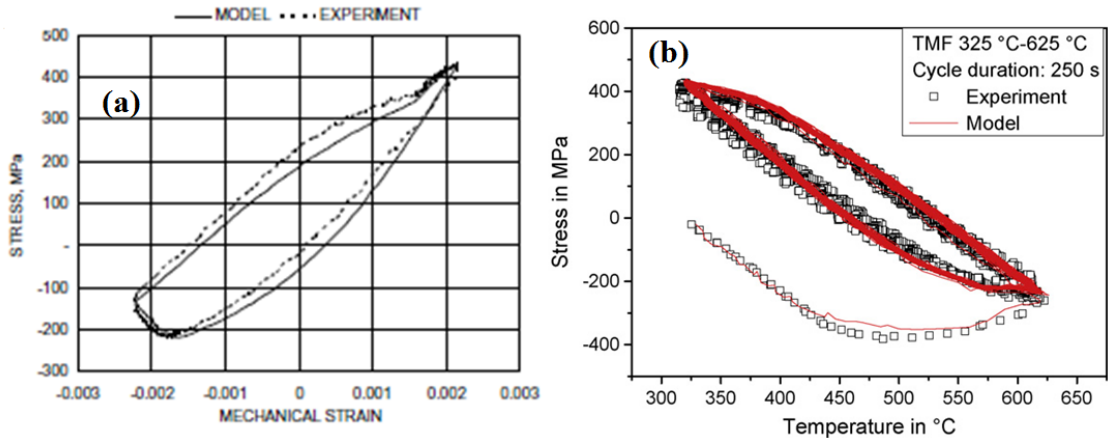

Figure 2.9: The comparison between the model prediction and the experimental results of TMF test for power plant materials for (a) P91 steel (Okrajni et al., 2008) and (b) P23 steel (Hartrott et al., 2009)

Finite element simulation can be used to predict a structure's behaviour under thermo-mechanical fatigue conditions. For example, Constantinescu et al. (2004) used FE simulations to predict the behaviour of an exhaust manifold under thermomechanical loading cycles. The analysis helped them to identify the possible location of a crack initiation site under thermomechanical fatigue loading conditions. FE analysis of structures, under TMF conditions, helps to design complex structures with more accurate lifetime predictions (Charkaluk et al., 2002). The simulation results for cast iron exhaust manifolds under the thermomechanical fatigue conditions shows very promising results when compared with tests on the actual structures, as shown in Figure 2.10.

The behaviour of large structures such as superplastic forming (SPF) tools, used in the aerospace industry, can also be predicted by use of finite element simulation, as shown by Deshpande and his co-workers (Deshpande et al., 2010a; Deshpande et

al., 2010b; Deshpande et al., 2008). In their work, complex, cyclic, thermal and mechanical loading, due to the heating and cooling of tools which occurs during the handling of the SPF press, were used in the FE simulations. The results of this work has contributed to a better operation of superplastic forming process in order to increase the lifetime of the SPF tool.

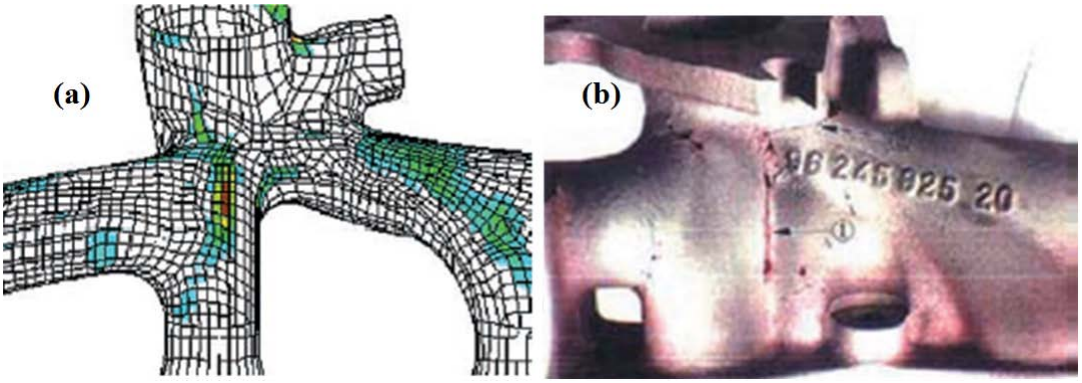

Figure 2.10: The cast iron exhaust manifolds condition as the result of thermomechanical fatigue loading in which (a) the predicted cracked area is shown by red contour and (b) the cracked area on the test structure is observed at similar location (Charkaluk et al., 2002)

2.7 P91 and P92 steel

2.7.1 Introduction to P91 and P92 steel

In the power generating industry, the economic efficiency of power plant operation has been improved by designing better power plant structures and by developing new steels with better properties. The creep properties of power plant materials have been of major concern to material scientists due to the need to operate the power plants at high temperatures over long periods of time. The steels used in conditions are known as creep-resistant steels (Abe et al., 2008).

Examples of creep resistant steels are P91 and P92 steels. In power plant application, the steels have been used in superheater and reheater tubes and also in the headers and in the steam piping at high temperatures, as shown in Figure

2.11. In general, P91 steel consists of 9% chromium and 1% molybdenum while P92 steel consists of 9% chromium, 1.75% tungsten and 0.5% molybdenum (Haarmann et al., 2002; Richardot et al., 2000). The steels are ferritic/martensitic type steels which are commonly grouped as 9-12%Cr steels. The ferritic type of steel has a lower thermal expansion coefficient value, as compared to an austenitic type steel (Ennis and Czyrska-Filemonowicz, 2003), which is an advantage for the ferritic type steel when dealing with thermal fatigue problems.

The demand for ferritic steels with higher creep strength has contributed to the development of 9Cr martensitic steel (Shibli and Starr, 2007). P91, or Grade 91 steel, was originally developed by Oak Ridge National Laboratory (ORNL) in the late 1970s as a modification to 9Cr-1Mo steel (Bendick et al., 2010). The modification consisted of the addition of vanadium, niobium and nitrogen and also the reduction of carbon, chromium, silicon, molybdenum, phosphorus and sulphur content (Swindeman et al., 2004). Thus, the steel is also known as a modified 9Cr-1Mo steel. P91 steel has been used in the UK power industry, either in retrofit or new build applications (Brett, 2007). P92 steel was originally developed under Nippon Steel's program in 1990s (Ennis and Czyrska-Filemonowicz, 2003). The steel was developed in order to improve the P91 steel behaviour by adding tungsten (W) and boron (B) content and reducing the molybdenum content (Richardot et al., 2000). The P92 steel has better creep strength by approximately 10-20% compared with P91 steel; thus, P92 pipe wall thicknesses can be reduced, resulting in improved behaviour of the steel under thermal fatigue situations (Vaillant et al., 2008). The chemical compositions in accordance with ASTM standard, for P91 and P92 steels are given in Table 2.1.

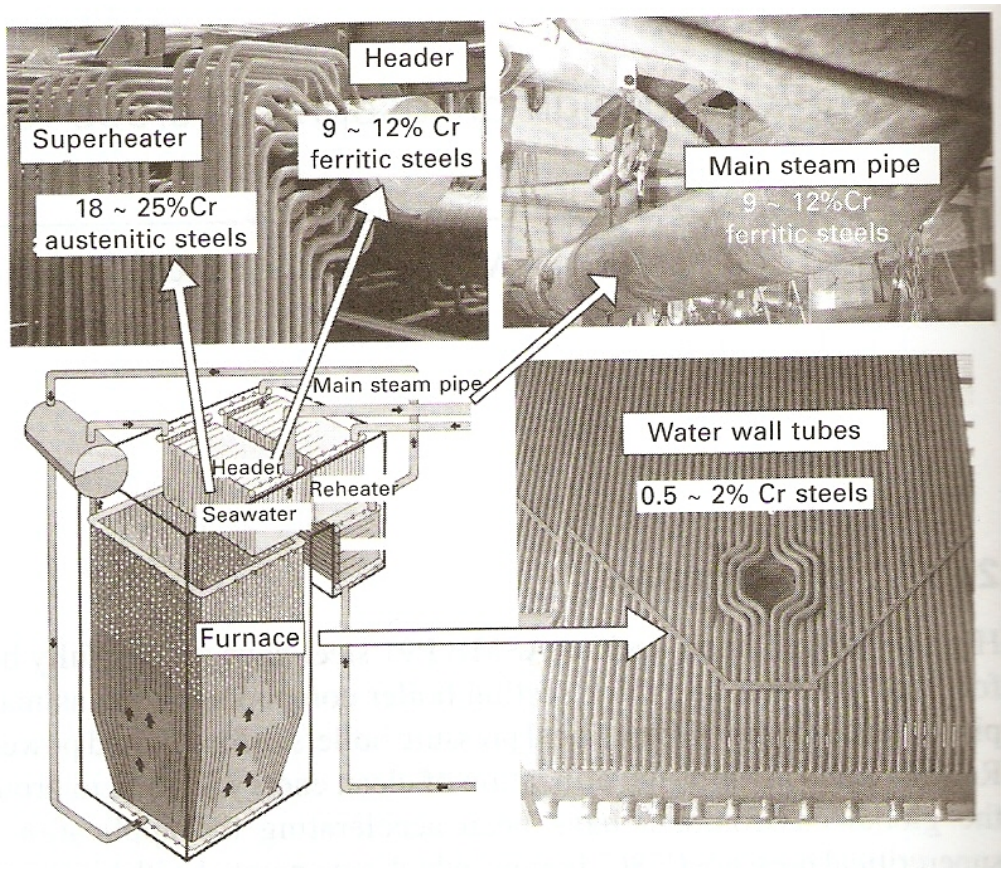

Figure 2.11: Schematic illustration and photographs of a fossil fired boiler and typical materials (Igarashi, 2008)

Table 2.1: Chemical compositions (weight percent) in accordance with ASTM standard (Vaillant et al., 2008)

Grades	Cr	Mo	C	Si	S	P	Al	V	Nb	N	W	B
P91	8.00	0.85	0.08	0.20	-	-	-	0.18	0.06	0.03	-	-
	9.50	1.05	0.12	0.50	0.01	0.02	0.04	0.25	0.10	0.07	-	-
P92	8.50	0.30	0.07	-	-	-	-	0.15	0.04	0.03	1.5	0.001
	9.50	0.60	0.13	0.50	0.01	0.02	0.04	0.25	0.09	0.07	2.0	0.006

In general, 9-12%Cr steels are heat treated, which consists of an austenitizing and tempering procedure, during their manufacturing, in order to meet the requirements of the steel's specifications. The steel is austenised at a temperature around 1100°C. The cooling process, from austenizing temperature to room temperature, produces a martensitic structure with a high dislocation density. Then, the steel is tempered at temperature at around 750°C in order to improve the ductility and

impact strength. Subgrains and dislocation networks are formed during tempering (Maruyama et al., 2001; Ennis and Czyrska-Filemonowicz, 2003). Different temperatures and periods of heat treatments are reported in the literature for 9-12%Cr steels, as listed in Fournier et al. (2009b). The different parameters used for the austenitizing and tempering processes can affect the microstructure of the steels. For example, selecting a high austenitising temperature results in an increase in the lath width and an increase in the prior austenite grain size (Ennis and Czyrska-Filemonowicz, 2003). The variation in heat treatment can also result in slight differences in mechanical properties.

2.7.2 The microstructure

Two major morphologies are observed in ferritic/martensitic steels, namely plate and lath martensite, as shown in Figure 2.12. Plate martensite consists of lenticular (lens-shaped) crystals and a zigzag pattern of smaller plates. On the other hand, lath martensite consists of a fine structure of parallel lath-shaped crystals. The parallel groups with the same crystal orientations are referred to as blocks and the groups of blocks, which may have different orientations, are known as packets (Krauss, 1999). The crystal orientations can be investigated by using the scanning electron microscope (SEM) with electron backscattering diffraction (EBSD) capability (Kitahara et al., 2006). It has been observed that most heat-treatable commercial steels have the lath-type morphology including the 9-12%Cr steels (Morito et al., 2003).

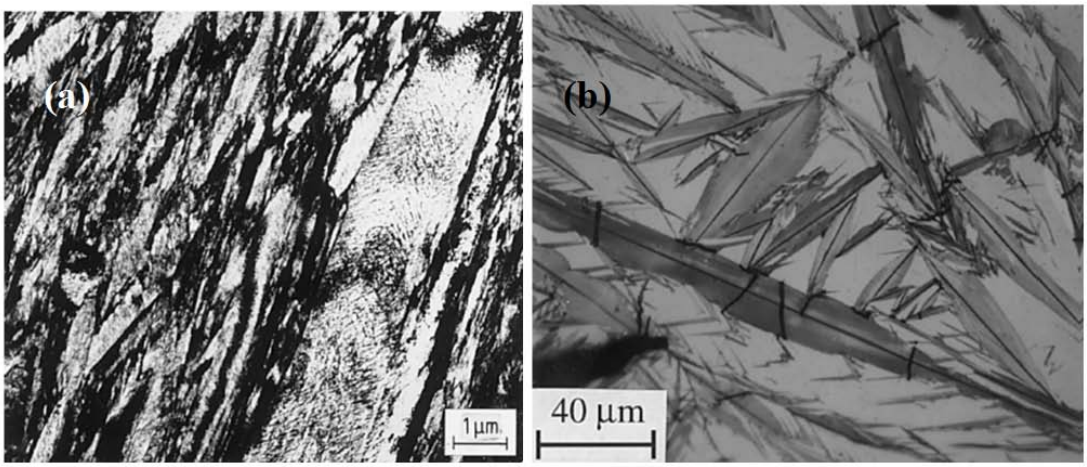

Figure 2.12: The example of microstructure of (a) lath martensite in a 4140 steel and (b) plate martensite in the Fe-1.86%Cr alloy (Krauss. 1999)

A schematic representation of a lath martensite microstructure of a 9-12%Cr steels is shown in Figure 2.13(a). The microstructure consists of prior austenite grain, packets, blocks, laths and subgrains. The prior austenite grain boundaries existed before the steel was quenched into the martensite regime (Faulkner, 2008). The size of the grains is around 10 to 30 μm (Fournier et al., 2011a). In the prior austenite grain structure, several packets can appear inside each grain and as many as six blocks can appear within a packet. The blocks are approximately 4 μm wide. Within a block, laths are elongated and divided into subgrains which contain a high density of dislocations. The widths of the lath are typically less than 1μm with low angle boundaries, which have misorientation angles of less than 5° (Kitahara et al., 2006; Sauzay et al., 2005). Two main types of precipitates are observed in the 9-12%Cr steels, namely $M_{23}C_6$ and MX precipitate. The $M_{23}C_6$ carbide particles are mainly located on grain boundaries and subgrain boundaries, while the MX carbonitrides particles are distributed homogeneously within subgrains, as shown in Figure 2.13(b) (Maruyama et al., 2001).

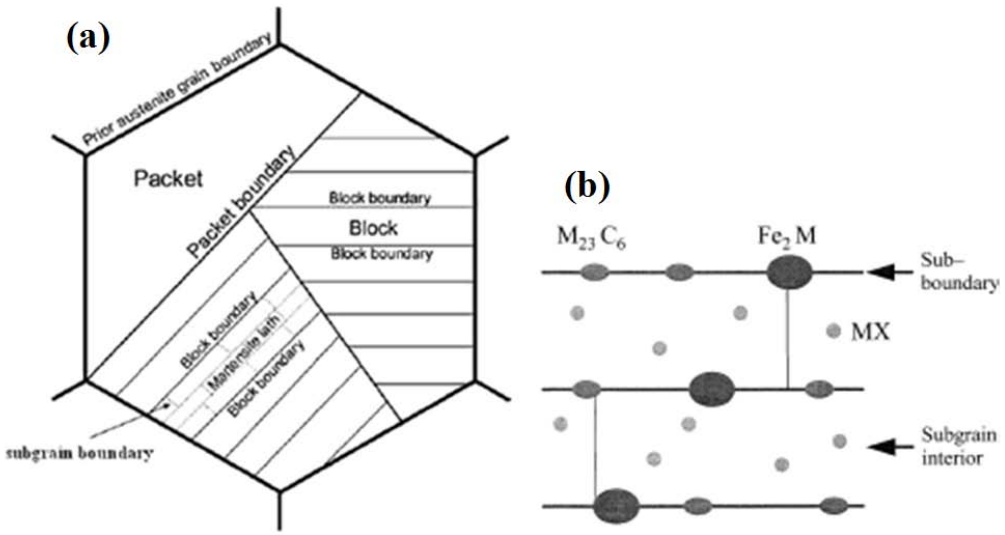

Figure 2.13: The schematic of (a) lath martensite microstructure (Fournier et al., 2009b) and (b) precipitates (Maruyama et al., 2001) of 9-12% Cr steels

The microstructure of martensitic steels contributes to the strength of the material. For example, the subgrain boundaries, the dislocations and the precipitates characteristics influence the deformation of the steel. The subgrain boundaries become obstacles to dislocation motion during inelastic deformation such as that which occurs in creep and fatigue conditions (Kostka et al., 2007). The precipitates contribute to the creep strength of the steel by pinning grain boundaries so that the grain size is stabilized during high temperature application (Faulkner, 2008). Smaller precipitates, distributed within subgrains, may act as obstacles to the mobility of the subgrain dislocations (Fournier et al., 2011a).

2.7.3 The microstructural evolution under cyclic loading test

Comparisons between as-received specimens and those that have failed under cyclic loading conditions for 9-12%Cr steels, reveals that an increase of subgrain size and a decrease of dislocation density has occurred (Armas et al., 2004; Dubey et al., 2005; Fournier et al., 2009b). The microstructural evolution in the steels have been investigated using transmission electron microscopy (TEM) and examples of the subgrain coarsening which occurs are shown in Figure 2.14. Cyclic inelastic

deformation leads to the coarsening of the subgrains where experimental results show that the subgrains sizes increase with an increase in the applied plastic strain. It has been found that microstructural coarsening, under cyclic loading, occurs on a subgrain scale without modifying the block of laths (Fournier et al., 2009b; Kimura et al., 2006). Also, the blocks are more homogeneous after cyclic loading which may indicate the disappearance of subgrain boundaries. This observation may be a result of the limitation of scanning electron microscopy (SEM) in observing the microstructural evolution of the steel, due to the fact that SEM can only observe high angle boundaries, which include prior austenite grains, packets and blocks (Kimura et al., 2006).

Scanning electron microscope and optical microscopy have been used to study crack initiation and propagation modes in 9-12%Cr steels under cyclic loading conditions. The microstructural observation of the fatigue specimen of the modified 9Cr-1Mo steel, such as a test with a strain rate of $3x10^{-3}$ s^{-1}, has revealed a transgranular crack type with crack branching, as shown in Figure 2.15. It has also been found that the oxidation may influence the crack initiation and propagation, particularly at low strain amplitudes (e.g. ±0.25%) and high temperatures (Nagesha et al., 2002; Shankar et al., 2006).

The interaction between creep and fatigue behaviours within cyclic loading tests produces greater microstructural evolutions than occur in pure fatigue tests. For example, from the Figure 2.14(d), the subgrain size of the creep-fatigue tests specimens are up to 3 times greater after the test while the coarsening of the subgrains in pure fatigue tests show lower increases of subgrains with them being up to 2 times greater than those in the as-received specimens (Fournier et al., 2009b). This observation indicates the test duration effect on the microstructural

evolution of the steel which the subgrain size increases with the increase of the holding period duration (Shankar et al., 2006). The precipitates structure may also be changed due to exposure to elevated temperature and stresses over a long period of time, particularly in long term creep tests. However, the coarsening of precipitates is hardly observed in creep-fatigue tests with short duration (Fournier et al., 2009b). Also, the interaction of creep and fatigue behaviour can be identified by the crack growth type in which creep damage becomes more influential as the hold period increases, as shown schematically in Figure 2.16.

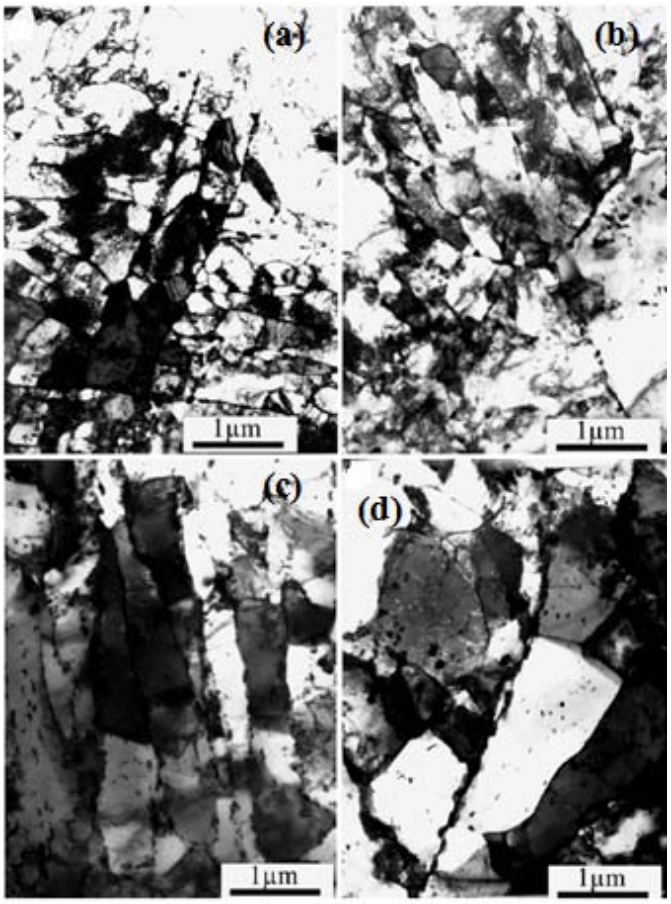

Figure 2.14: Bright-field TEM images of the P91 steel specimen for (a) as-received condition, (b) pure fatigue test with 0.3% strain range, (c) creep-fatigue test with 0.4% strain range and 0.1% creep strain and (d) creep-fatigue test with 0.7% strain range and 0.5% creep strain. (Fournier et al., 2009b)

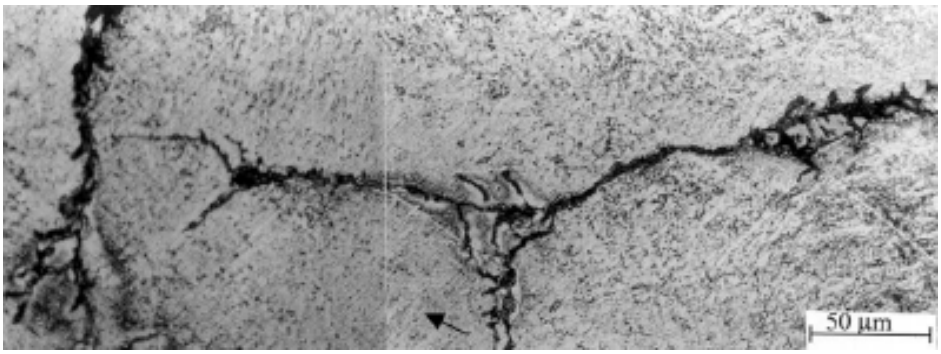

Figure 2.15: The transgranular crack with crack branching observed on the modified 9Cr-1Mo steel under fatigue loading at 600°C (Nagesha et al., 2002)

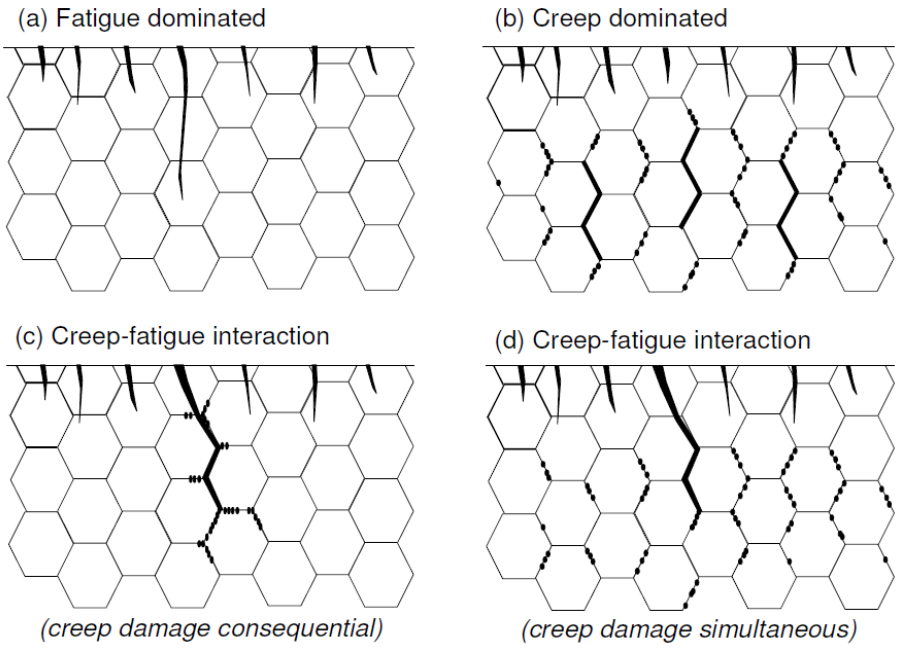

Figure 2.16: The schematic of crack propagation in a test with (a) fatigue dominated, (b) creep dominated, (c) creep-fatigue interaction (due to consequential creep damage accumulation) and (d) creep-fatigue interaction (due to simultaneous creep damage accumulation) (Holdsworth, 2010)

The 9-12%Cr steels exhibit softening behaviour under cyclic loading condition. The softening of the steel may be the result of several mechanisms, such as: annihilation of dislocations, change from the original lath structure to cells or equiaxed subgrains, degradation of strength due to coarsening of precipitates and stress reduction associated with the surface oxide film formation during deformation (Nagesha et al., 2002). In short term fatigue and creep-fatigue tests, the coarsening

of precipitates can be ignored (Fournier et al., 2009b). Based on TEM observations, it seems that the cyclic softening behaviour can be correlated with the coarsening of the initial martensite laths and subgrains and with the decrease of the dislocation density which contributes to the reduction of obstacles to dislocation motions. The changes of the obstacle density affect the stress required for the dislocation motions and thus contribute to the reduction of measured stress in the cyclic softened materials (Fournier et al., 2011a).

The subgrain coarsening of 9-12%Cr steels can be associated with the mechanism of dislocation annihilation. In the steel's microstructure, the subgrains are the small structures located along the martensite lath separated by the subgrain boundaries. The subgrain boundaries consist of dislocation networks, which, when compared with the subgrain interiors, are hard regions in the microstructure of the ferritic steels (Hald, 2008). During cyclic loading, mobile dislocations, which are located inside the subgrains, can move towards subgrain boundary dislocations of opposite sign (Sauzay et al., 2005) as shown in Figure 2.17. If the distance between the mobile and the subgrain dislocations is less than a critical annihilation distance, the dislocations involved may be annihilated (Essmann and Mughrabi, 1979). The repetition of cyclic loading contributes to the successive annihilation events which decrease the density of subgrains dislocations. Eventually, the subgrains boundaries disappear when no dislocation remains inside it (Fournier et al., 2011b).

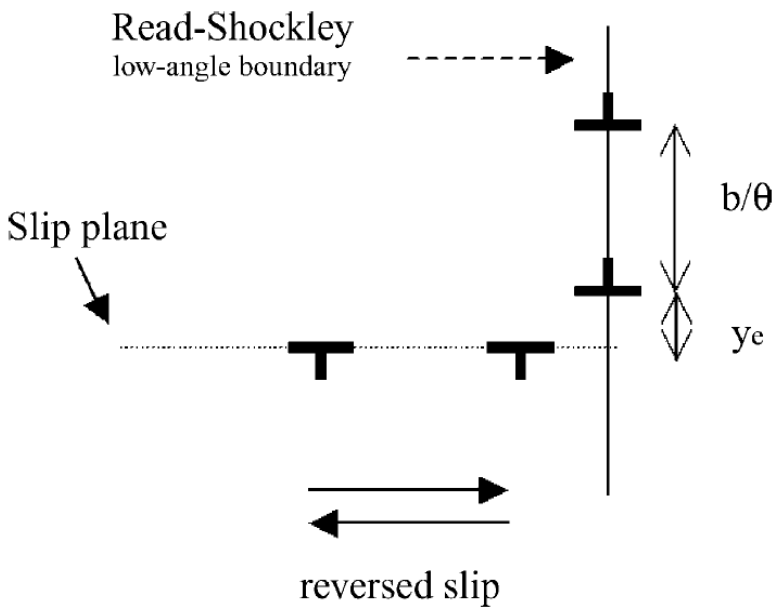

Figure 2.17: The schematic of the annihilation mechanism consist of the interactions between subgrain boundary dislocations and mobile dislocations (Sauzay et al., 2005)

Chapter 3 – Experimental work

3.1 Overview

This chapter presents the experimental work carried out on P91 and P92 materials at high temperatures. General information on the capability of the testing machines and the specimen preparation is described. Several types of test loading types were used in the tests, e.g., some tests were carried out with constant temperatures and some with variable temperatures (i.e. isothermal and anisothermal, respectively), various types of strain loading, strain amplitudes and designs of specimen were used. Results obtained from these tests are presented at the end of this Chapter.

3.2 Testing facilities

An Instron 8862 TMF testing system was used to perform the isothermal and anisothermal tests. The system consists of the load frame, servo electric actuator, power amplifier, load cell and control electronics. The TMF machine system is shown in Figure 3.1.

The machine is controlled by a servo electric screw driven actuator for forces up to 100kN. The maximum frequency is 1Hz and the minimum speed is 1 micrometer/hour in a displacement controlled test. Strain is measured by high temperature extensometer with ceramic rods and a gauge length of 12.5mm. This extensometer can be used at temperatures up to 1200˚C.

The heat is supplied by high frequency induction heating. The heat is produced by the interaction of a test specimen, which is a metal, with the magnetic field generated by the flow of alternating current in an induction coil. The coil is made of copper tubing designed to enable the temperature gradient along the gauge section

to be controlled to within ±10˚C of the target temperature. The induction heating enables a fast heating rate up to 50˚C per second to be achieved and a cooling rate up to 25˚C per second is achieved with forced air. These test control capabilities are important in thermo-mechanical fatigue tests in order to achieve the required temperature cycles. The temperature readings were obtained by the use of either thermocouples or pyrometry; the former device was used in the majority of the tests performed for this work.

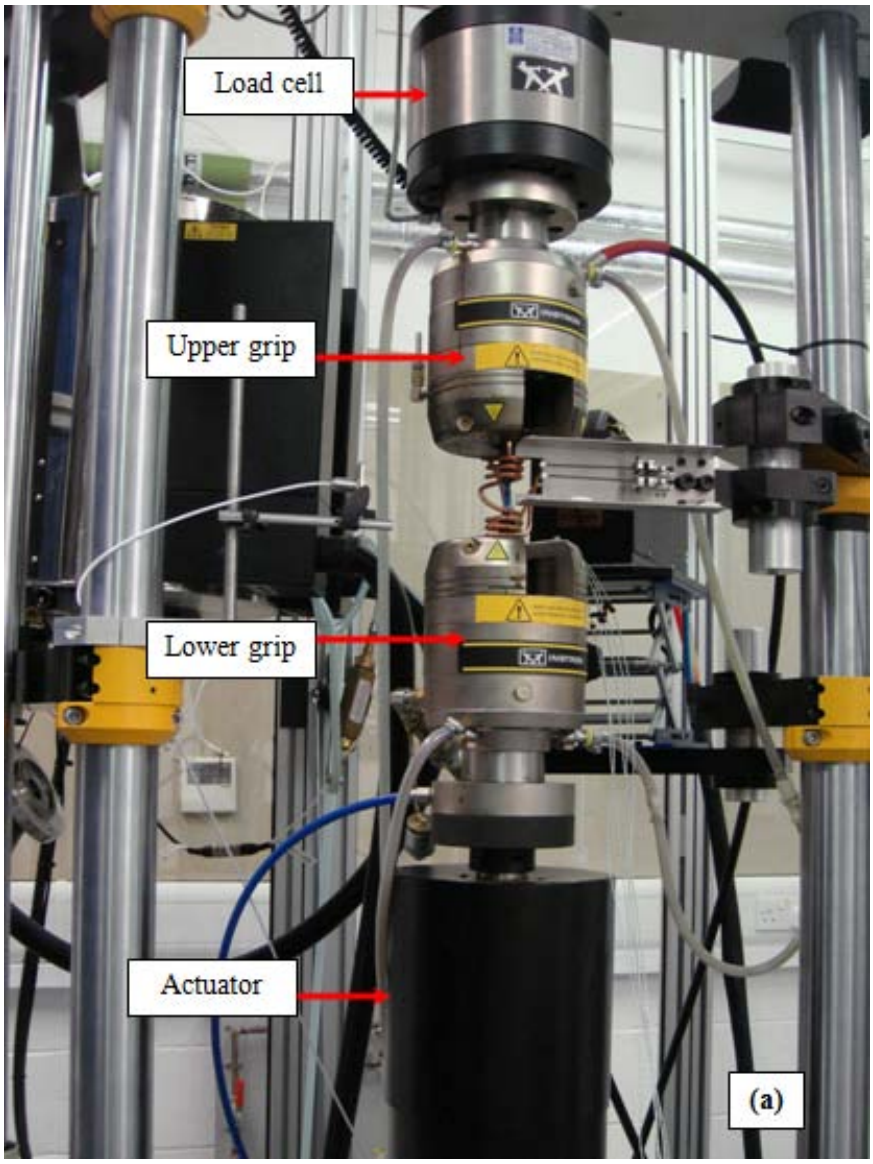

Figure 3.1: The Instron 8862 TMF machine system: (a) the TMF machine main structure, and (b) the controller of the system

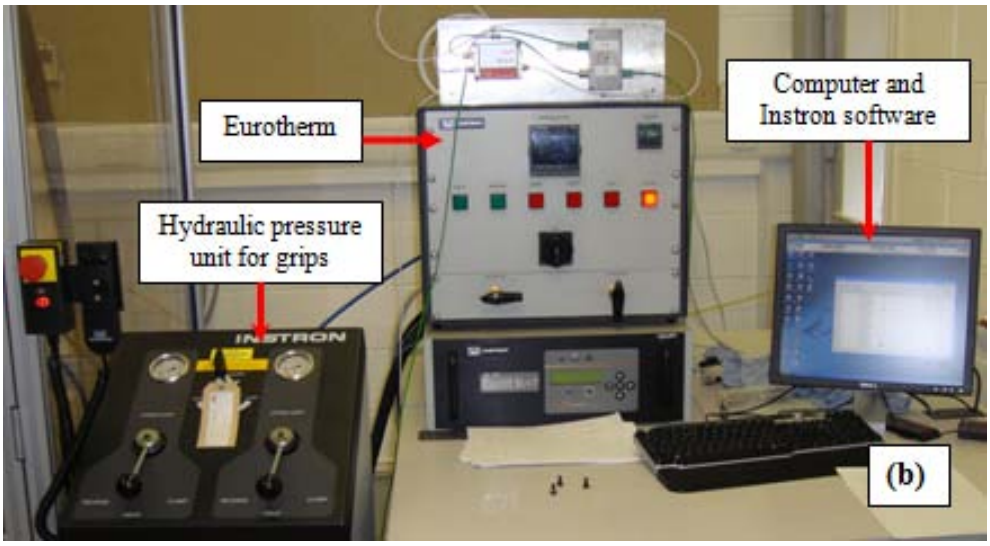

Figure 3.1: (contd.) The Instron 8862 TMF machine system: (a) the TMF machine main structure, and (b) the controller of the system

3.3 Material and specimen preparation

The materials used in this work were 9%Cr steel alloys, i.e., P91 and P92 steels. The materials provided were from steam pipe sections and multi-pass weld pads as part of the SUPERGEN project. The P91 and P92 pipe had outer diameter of 298.5mm and 355mm, respectively, and wall thickness of 55mm and 30mm, respectively. The P91 steel was austenized at 1060˚C for 45 minutes and tempered at 760˚C for 2 hours. On the other hand, the P92 steel was austenized at 1070˚C for 45 minutes and tempered at 780˚C for 108 minutes. The chemical compositions of the two materials are given in Table 3.1.

Table 3.1: Chemical compositions for the P91 and P92 steels (wt%)

	Cr	Mo	C	Si	S	P	Al	V	Nb	N	W	B
P91	8.60	1.02	0.12	0.34	<0.002	0.017	0.007	0.24	0.070	0.060	0.03	-
P92	8.62	0.33	0.10	0.45	0.002	0.015	0.019	0.21	0.076	0.047	1.86	0.0034

Cylindrical, button-end, specimens (e.g. Fig. 3.2) were machined from the P91 and P92 steels. For parent metals, the test specimens were cut from the steam pipe

sections; the P92 weld specimens were machined from the longitudinal direction of the supplied weld pad. All specimens had an overall length of 160mm, which is 10mm longer than that suggested by the TMF machine supplier; this was more convenient for the production of a coil which gave the required temperatures within the tolerance limits. The button-end design of the specimens, as shown in Figures 3.2, 3.3 and 3.4, enable the TMF machine system to be used within maximum load for the machine, i.e., 35kN during the test. The middle section of the specimen is called as the gauge section. The middle section was at least 15mm in order to allow the placement of the extensometer arms which have a length of 12.5mm. This section was finished by a fine machining and polishing to create an average roughness value of 0.8μm.

Three test specimen types were used. First, a solid TMF specimen, as shown in Figure 3.2, was used in the majority of the tests, particularly for the strain-controlled isothermal tests. For the anisothermal tests, a tubular specimen with a 4mm diameter hole, as shown in Figure 3.3, was used in order to have a thin wall along the gauge section so that radial temperature variations can be ignored during the anisothermal test. Finally, a notched TMF specimen, as shown in Figure 3.4, was machined with a notch radius of 2mm in the gauge section in order to create a multiaxial stress state in the specimen.

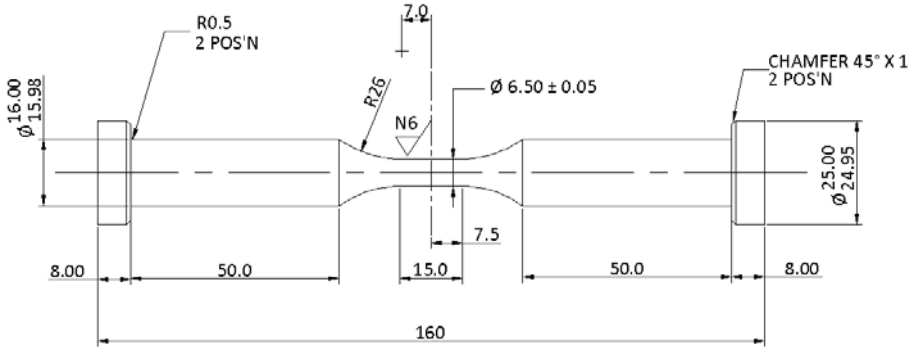

Figure 3.2: The solid TMF specimen used in isothermal test

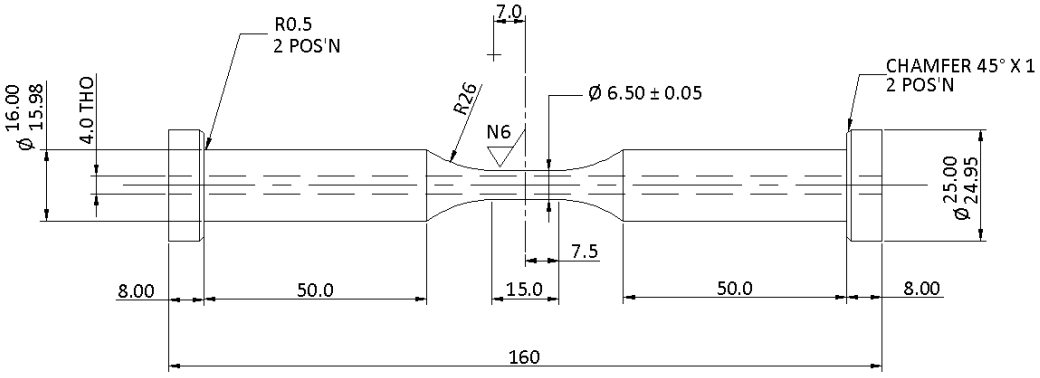

Figure 3.3: The tubular TMF specimen used in TMF test

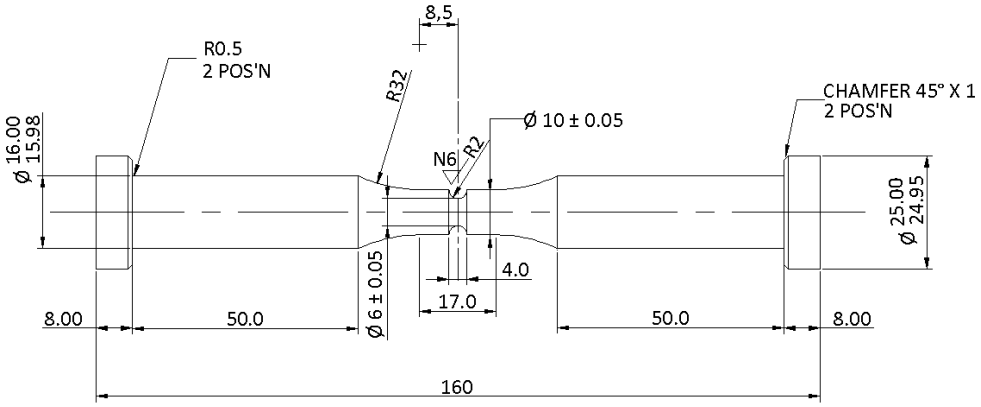

Figure 3.4: The notched TMF specimen used in load-controlled test

3.4 Testing procedures for the P91 steel

The work on the P91 steel can be divided into two stages. The first stage of the experimental work involved the investigation of the P91 parent metal. Most of the effort on this material was carried out in order to get a better understanding of the behaviour of this martensitic type material in cyclic loading conditions at high temperatures. Several types of tests were carried out on the P91 specimens, including isothermal cyclic plasticity, thermomechanical fatigue and notched-bar testing.

3.4.1 Isothermal cyclic plasticity test of P91 steel

Strain-controlled testing was used to investigate the behaviour of P91 under cyclic plasticity conditions in isothermal conditions. The aims of the tests are firstly, to obtain the stress-strain behaviour of the material so that a constitutive material behaviour model can be developed based on these data. Secondly, a fatigue life model, particularly under low cycle fatigue conditions, can be developed. The solid TMF specimens (i.e. Fig. 3.2) were used in these tests.

The test loading conditions were based on the high temperature requirement of power plant and to produce a deformation which will give plastic behaviour. The isothermal tests of P91 specimens were conducted at 400, 500 and 600°C. At each temperature, displacement controlled tests with a strain amplitude of ±0.5% and a strain rate of 0.1%/s were performed in fully reversed tension-compression conditions. The strain amplitude value was selected to ensure that significant plasticity would occur with this amplitude. Using the same strain amplitude at each temperature, tests with a hold period, in tension, for 2 minutes were performed in order to study the time-dependency effect. The duration of hold period was chosen so that constant rate of stress drop, in each cycle, was recorded in the test. In addition, several strain-controlled tests, with the same strain rate, were performed at 600°C with strain amplitudes of ±0.2%, 0.25% and 0.4%.

Actions performed prior to starting the test

Prior to starting up each test, temperature calibration of the TMF machine system was performed in order to obtain a temperature variation within the gauge length of ±10°C of the target temperature. This can be achieved by designing the copper coil for the P91 steel specimen by adjusting its shape particularly the number of coil turns and the pitch between each coil turn. The characterization of the copper coil

shape controls the density of magnetic flux, induced by the induction heating system, and thus determines the specimen's temperature. Five thermocouples were welded on the gauge section, as shown in Figure 3.5, to measure the temperature during thermal calibration. A coil from previous tests on a RR1000 specimen, as shown in Figure 3.6(a) which gave temperature gradient of within ±10°C for the RR1000, was used as a starting design shape. However, that coil design produced a temperature variation of more than ±15°C, even after adjusting the pitch of coil turn. Another shape of coil as shown in Figure 3.6(b) was used and there was an improvement for temperature reading. The final design of the coil shape for P91 specimen tests is shown in Figure 3.7; this gave the required temperature variation along the gauge section as plotted in Figure 3.8.

For the P91 steel isothermal strain-controlled tests, the temperatures during the tests were measured by using thermocouples (TC). Two K-type thermocouples were used in each test; one thermocouple acted as the main TC which controls the required temperature for a test and another thermocouple was used to check the reading of the main TC before starting the test. The thermocouple wires were attached to the specimen's surface by spot welding and the distance between the two thermocouple wires must be less than 1mm as suggested by Hahner et al. (2008). If the TC readings indicate an unacceptable variation of temperature, the qualities of the spot welds are checked and repetition of the spot welding process may be performed if necessary.

From previous tests on RR1000, using the TMF machine system (Hyde, 2010), cracks were found at the TC spot weld positions on the gauge section. In order to avoid that situation, temperature in the strain-controlled tests of P91 steel was measured by positioning thermocouples away from the gauge section, i.e., on the

shoulder of the specimen. Thus, the temperature ratio between the centre of the gauge section and the specimen's shoulder were recorded, at the position shown in Figure 3.9(a). Average temperature readings at the shoulder position for corresponding gauge section temperatures of 400, 500 and 600°C, obtained from the setup of this experiment, were 344, 429 and 516°C, respectively. For the actual tests, both thermocouples were placed on the specimen's shoulder, as shown in Figure 3.9(b), and the temperature ratios were used in the test.

In order to obtain a good response for a specified test loading, the PID (proportional, integral, derivative) values of the TMF machine system were tuned. The strain amplitudes and testing periods for the actual tests were applied on a specimen and the PID values were adjusted accordingly to get a good fit to controlled shape parameter (strain, load or temperature). The values of P 36, I 2 and D 0 were used for the P91 steel tests determined by trial-and-error process. This procedure was performed using the temperature calibration specimen.

Actual test

Once the temperature calibration and PID tuning procedures were completed, the actual tests were performed, using new P91 specimens. Thermocouples were instrumented on the specimen as shown in Figure 3.9(b) and then, the specimen was installed on the test rig, as shown in Figure 3.7. A verification of Young's modulus was performed at room temperature to ensure correct operation of the extensometer. The applied load in the Young's modulus verification was small, to ensure that it was within the elastic limit, in order to avoid an irreversible displacement in the specimen before starting the test. Correct operation of the extensometer resulted in a reasonable smooth plot of linear data and the measured Young's modulus values were comparable to reference values at the same

temperature. After verifying the extensometer set-up, the specimen was heated up to the required temperature.

The specimen was heated up to the required temperature within 30 seconds from room temperature. The specimen was continued to be heated without applying any load for up to 5 minutes in order to get stabilized temperatures throughout the solid specimen. During that time, the mechanical strain waveform was set as required and a failure criterion, which set the condition for the machine to stop, was defined as a given percent decrease of maximum stress from certain cycle. From the results of the first test on a P91 specimen at 600°C with ±0.5% strain amplitude, using a 50% stress decrease from the 50^{th} cycle as the failure criterion, the specimen were found to totally fracture and the extensometer fell down. This may cause damage of the extensometer if it occurs regularly. Thus, a lower percent of stress decrease, i.e., 30% stress drop from the 50^{th} cycle, was defined as the failure criterion for the remaining tests and the tests were found to stop without causing total fracture of the specimen. Visible cracks were observed on all specimens' surfaces. Test data were recorded automatically by the Instron TMF software.

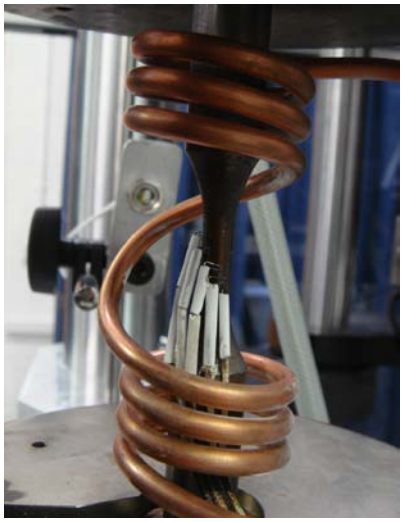

Figure 3.5: The positions of the 5 thermocouples along the gauge section during temperature calibration stage

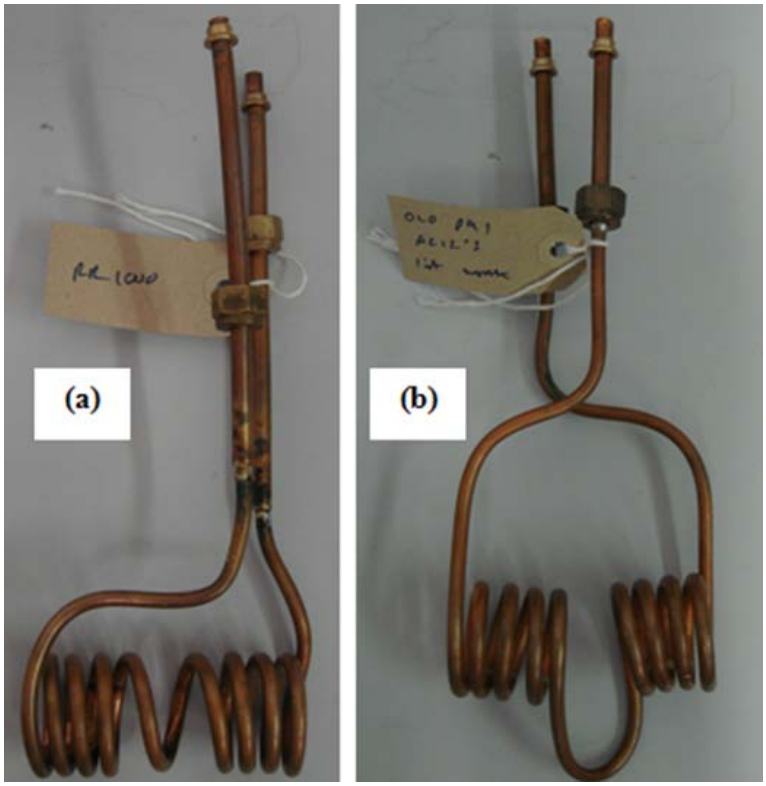

Figure 3.6: Different designs of coil which were used in the intial stage of temperature calibration, (a) a coil used in previous RR1000 tests and (b) a new coil made and tested for P91 test specimens140

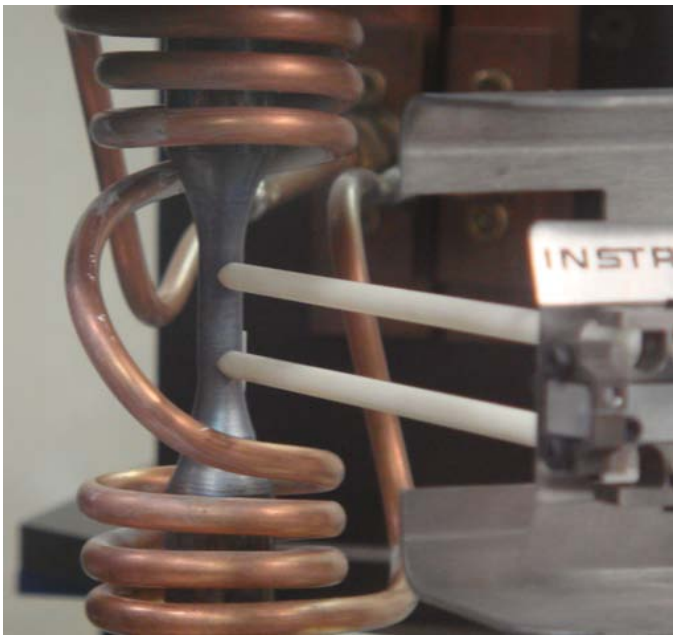

Figure 3.7: TMF test machine set-up used for P91 specimens with finalised design of the induction heating coil and the extensometry

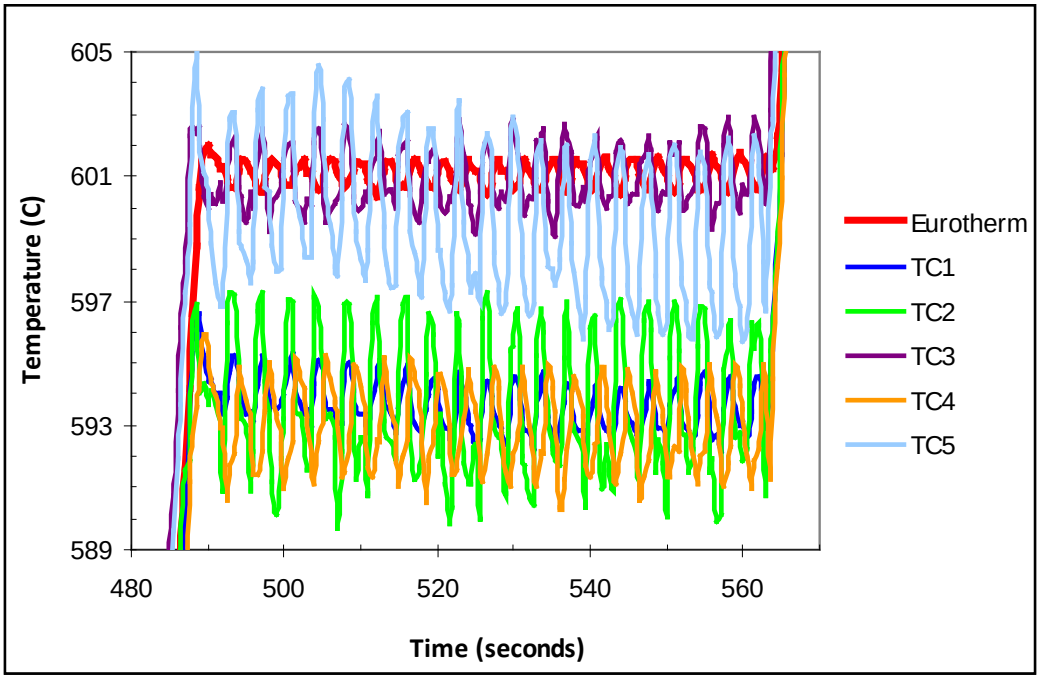

Figure 3.8: Temperature reading at 600°C (normal) during the temperature calibration stage from the 5 thermocouples on the gauge section where TC1 to TC5 represent the locations of the thermocouples from top to bottom

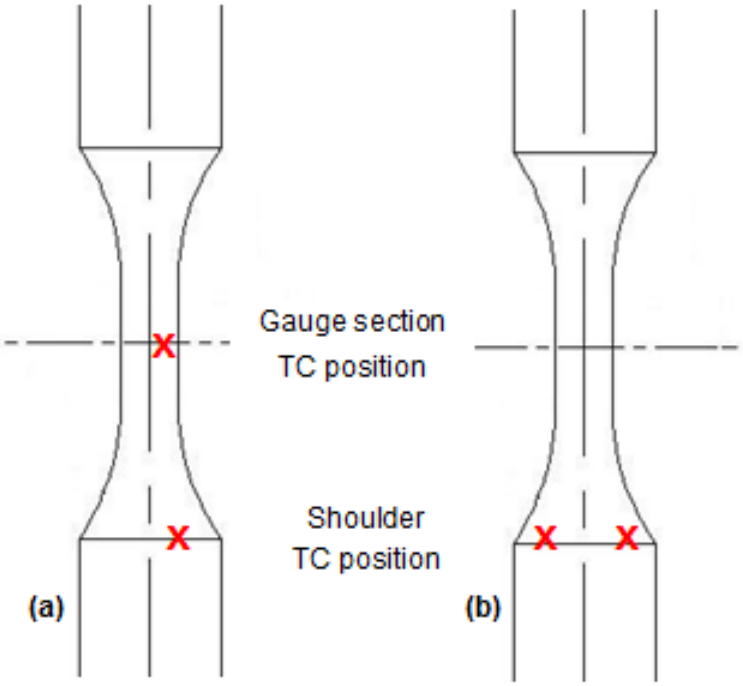

Figure 3.9: The positions of thermocouples on the gauge section and the shoulder of the specimen for (a) measuring the temperature ratio and (b) during the strain-controlled tests of the P91 steel

3.4.2 Thermo-mechanical fatigue testing of P91 steel

The aim of the thermomechanical fatigue (TMF) testing of the P91 steel specimens was to observe the effects of cyclic mechanical loading and temperature on the behaviour of the steel. The test data obtained from the TMF tests were also used to verify the viscoplasticity model developed in this study for predicting anisothermal behaviour. The tubular specimen, as shown in Figure 3.3, was used for the TMF tests. A mechanical strain range of ±0.5% was used for all of the TMF tests for two temperature ranges, i.e., of 400-500˚C and 400-600˚C. The TMF tests were carried out under in-phase loading conditions (maximum temperature at maximum strain) up to failure and out-of-phase loading conditions (minimum temperature at maximum strain), as shown schematically in Figure 3.10. All of the TMF tests were carried out with a period of 60s per cycle.

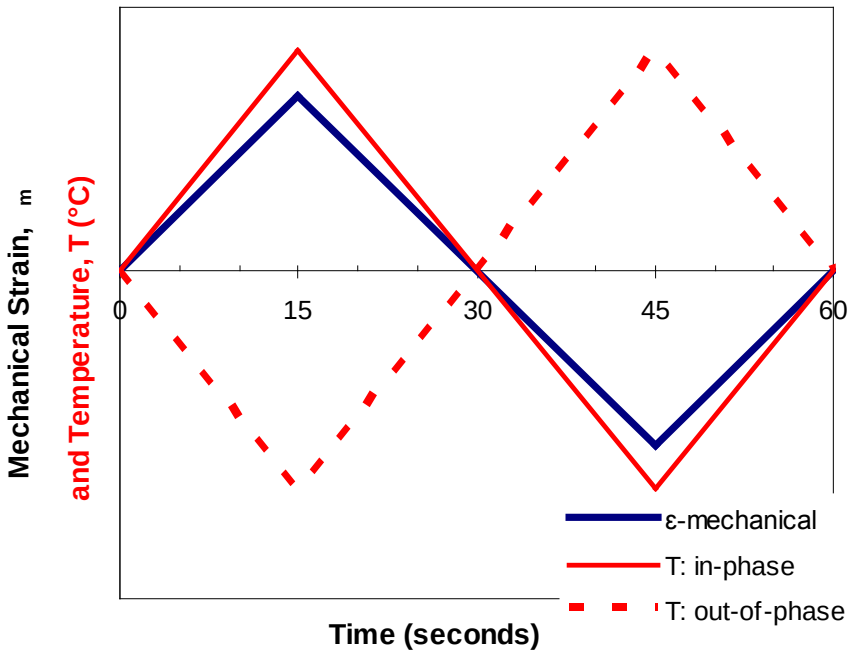

Figure 3.10: Schematic representation of anisothermal strain-controlled loading with in-phase and out-of-phase temperature cycles

An infra-red pyrometer was used instead of thermocouples at the specimen shoulders to measure temperatures in the TMF tests. The controlled temperature at the specimen's shoulder causes difficulty in determining the temperature along the gauge section when temperature is cycled. A pyrometer is a non-contacting device for measuring the temperature and hence surface crack due to spot-welding can be avoided. However, an oxide layer, which forms during testing, may affect the accuracy of temperature measurement (Beck and Rau, 2008). An initial study was implemented to assess the severity of the oxide layer formed during the test by preoxidising the specimen at 650°C for 24 hours. It was found that the P91 specimen surface was not significantly oxidised compared to other specimens used in previous tests in the lab such as stainless steel and RR1000 specimens. Thus, the effect of oxidation on pyrometer reading was neglected in this study.

In order to use the pyrometer in the test, the emissivity values for the required temperature between 400 and 600°C were determined prior to starting the TMF test. For this purpose, the initial thermal cycling study was performed by attaching 5 thermocouples on the gauge section's surface to measure the temperature variation, as shown in Figure 3.5. The temperatures of the specimens in the tests were controlled by the use of the middle thermocouple. The specimen was heated to a specified temperature and the temperature was kept constant for several minutes to stabilize the temperature of the specimen. The corresponding emissivity value was then recorded. This process was repeated at other temperatures within the required temperature range. The recorded emissivity values at 400, 500 and 600°C are 0.615, 0.625 and 0.635 respectively. Each emissivity value was then used in a temperature cycling test, controlled by pyrometer. This was done in order to get an emissivity value which can give a better temperature reading for the specified temperature range and to ensure that the maximum temperature

variations within gauge length of the specimen are within the required range, i.e., ±10°C (Hahner et al., 2008). The emissivity value of 0.625 was used in the TMF tests.

For the thermomechanical fatigue test, the TMF software divides the test into four stages, namely, stabilisation, measurement, verification and test stage. The first three stages were the preparatory stages in which only a temperature waveform was applied and resultant thermal strains were measured and verified. The thermal strain was measured by using the extensometers data and recorded at the base time interval. In the test stage, the mechanical strain cycle of ±0.5% was defined in the TMF software; the mechanical strain can only be realized by controlling the total strain applied to the specimen considering the thermal strain measured in the preparatory stages. For example, the total strain applied to a specimen in the tension direction, for TMF in-phase tests was higher than the defined mechanical strain due to the contribution of thermal strain (expansion of specimen due to increase of temperature). In contrast, the thermal and mechanical strains were opposite in direction for the TMF out-of-phase tests and hence resulted in shorter applied total strain in the test. The 30% stress drop from the 50^{th} cycle was also used as the failure criterion for the TMF test.

3.4.2 Cyclic notched bar test of P91 steel

The cyclic notched bar tests on P91 steel were performed using a fully reversed load-controlled condition in order to verify the capability of the material model under multiaxial conditions. The nominal stress amplitude was 300MPa on the minimum notch section and a constant temperature of 600°C was applied to the specimens throughout the test. The stress value was chosen in order to produce a similar strain range effect, on the notch section, as that in the isothermal strain-controlled tests on

a P91 solid specimen at 600°C. The TMF notched specimen, as shown in Figure 3.4, was used for the tests. Two types of loading were used for the tests: firstly, the load was continuously applied in triangular waveform with a cyclic period of 20 seconds; and secondly, a dwell period of 2 minutes, which is the same duration as the cyclic test on the P91 solid specimen, was introduced in the previous triangular waveform at peak loading. Each test was performed until failure occurred.

For the notched bar tests, thermocouples were used to measure the test specimen temperature. However, the position of the main TC was not on the shoulder of specimen. The main TC was attached on the gauge section which was 2 mm above the notch corner as shown in Figure 3.11. During thermal calibration, two additional thermocouples were attached on the centre of the notched surface. The ratio between the main TC and the thermocouples reading for notch section was recorded, making sure that the temperature was 600°C at the centre. In the actual tests, the main and guide TC were attached to new P91 notched specimens without any TC on notched radius.

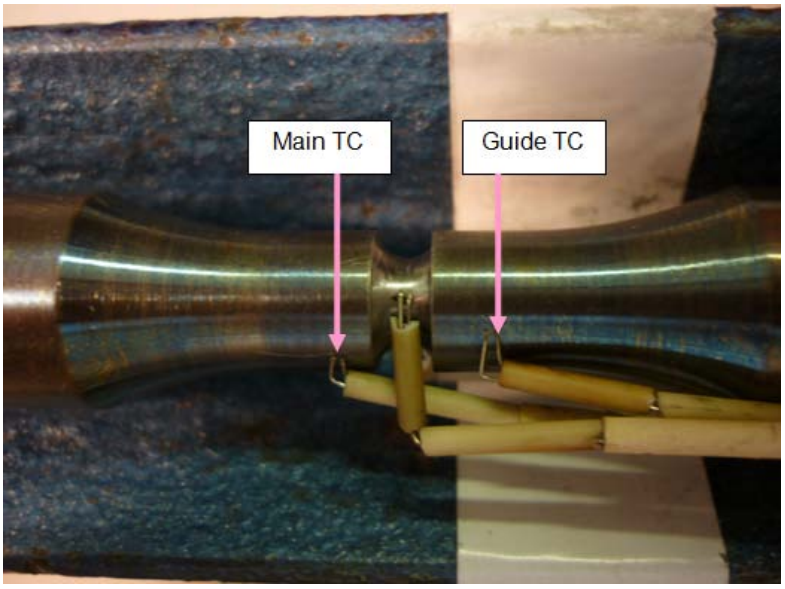

Figure 3.11: 4 thermocouples were attached to the gauge section during thermal calibration

3.5 Testing procedures for the P92 steel

The second stage of the experimental work was performed on P92 parent material and weld metal. Isothermal strain controlled and thermomechanical fatigue tests were carried out on P92 specimens using the same TMF machine system, in which the solid and tubular TMF specimens designs already described, were used, respectively. The difference was that the maximum test temperature was increased to 675°C, to reflect the higher temperature capability of P92 compared with P91 in real applications. The isothermal tests were performed at 500, 600 and 675°C with a strain amplitude of ±0.5% and a strain rate of 0.1%/s. Then, tests with dwell periods of 5 minutes at the peak tensile strain were also performed for each temperature. The thermomechanical fatigue tests were carried out in a temperature range of 500 to 675°C with in-phase and out-of-phase loading, with a 60 seconds cycle period.

The isothermal and TMF tests, of the P92 parent and weld specimens, were performed using the same procedures as have been described for the P91 parent metal specimens, except for the temperature measurement method. For this stage, the main thermocouples, which controlled the test temperature, were attached in the middle of gauge section for both the isothermal and the TMF tests, as shown in Figure 3.12(a). From trial tests on P91 specimen at the end of stage 1, it seems that cracks may not have initiated at welding point of the thermocouple wires, as found in the works of Hyde (2010) for RR1000 specimens, if care is taken during the spot welding, i.e., the lowest possible current is used which will ensure that the contact between thermocouple wires and specimen's surface is strong enough. In addition, a solid specimen was used in all of the strain-controlled tests for this study, rather than the tubular specimens used in the strain-controlled tests for the previous study.

The locations of major cracks were observed and recorded for the P92 tests in relation to the location of the main TC on gauge section. The first test on the P92 material was performed using a P92 parent material specimen under an isothermal, strain-controlled condition, at 600°C. Figure 3.12(b) shows the major cracks on the gauge section surface; these cracks were located 3 mm below the thermocouples. A crack investigation using an optical microscope shows a closer view of the major crack which can be seen to have a width of 90 micrometer, as shown in Figure 3.13(a). The crack width is approximately 30 percent of the TC wire width. There was no crack near the spot weld position, as shown in Figure 3.13(b). For other strain-controlled test specimens, the major cracks were also found to occur at positions away from the spot weld locations.

Prior to starting the TMF test on P92 specimen, an initial investigation, using scanning electron microscope on the previously tested tubular specimens used in the P91 TMF tests, was conducted. Many cracks were found to initiate and propagate from the inner and outer surface of the specimens, as shown in Figure 3.14. The quality of the inner surface finishing of the specimen, which was difficult to control, may also have contributed to the initiation of the cracks. From these observations, it was decided to control the temperature by attaching the main TC to the middle of the gauge section. Furthermore, the number of cycles to failure for the TMF tests, which might be affected by early crack formation, is not the concern of this test. The tests were performed to investigate the development of the cyclic, plastic, stress-strain loops.

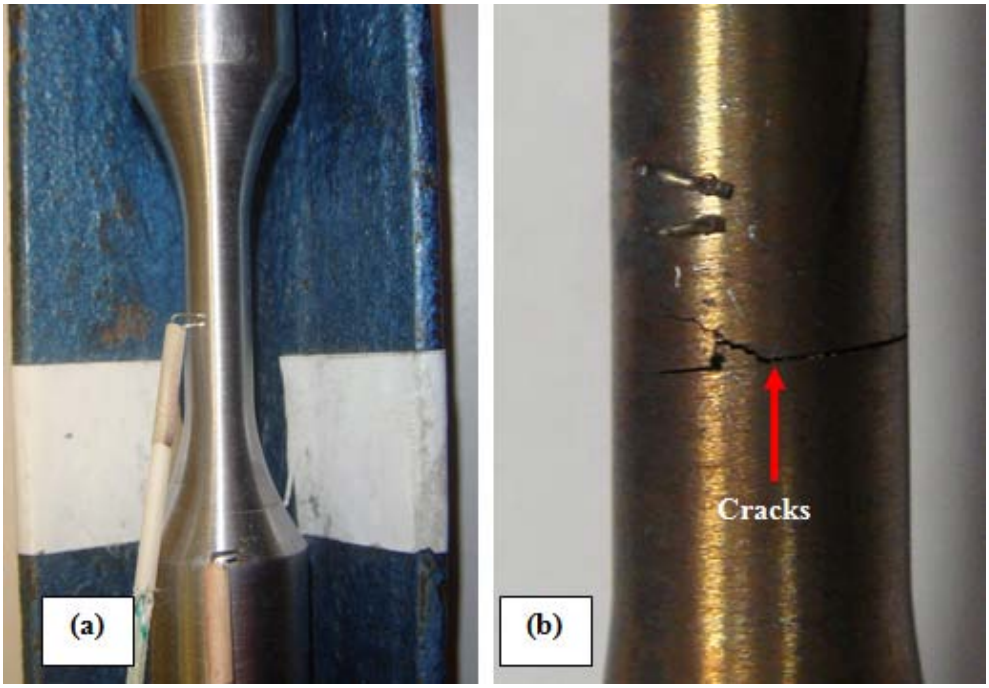

Figure 3.12: An image of the P92 parent metal surface with (a) the main and guide TC positions before test and (b) the image of a visible major crack, after test, with the thermocouple, located 3mm below

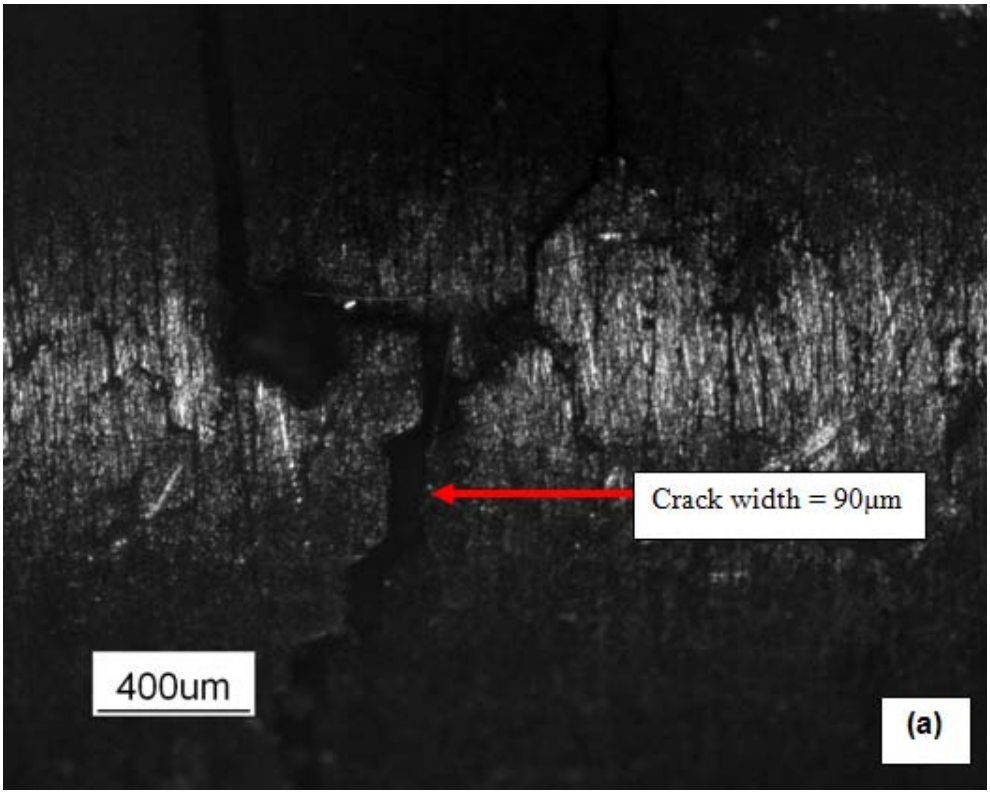

Figure 3.13: Images from optical microscope focussing on (a) the major crack on the specimen and (b) the TC wires positions

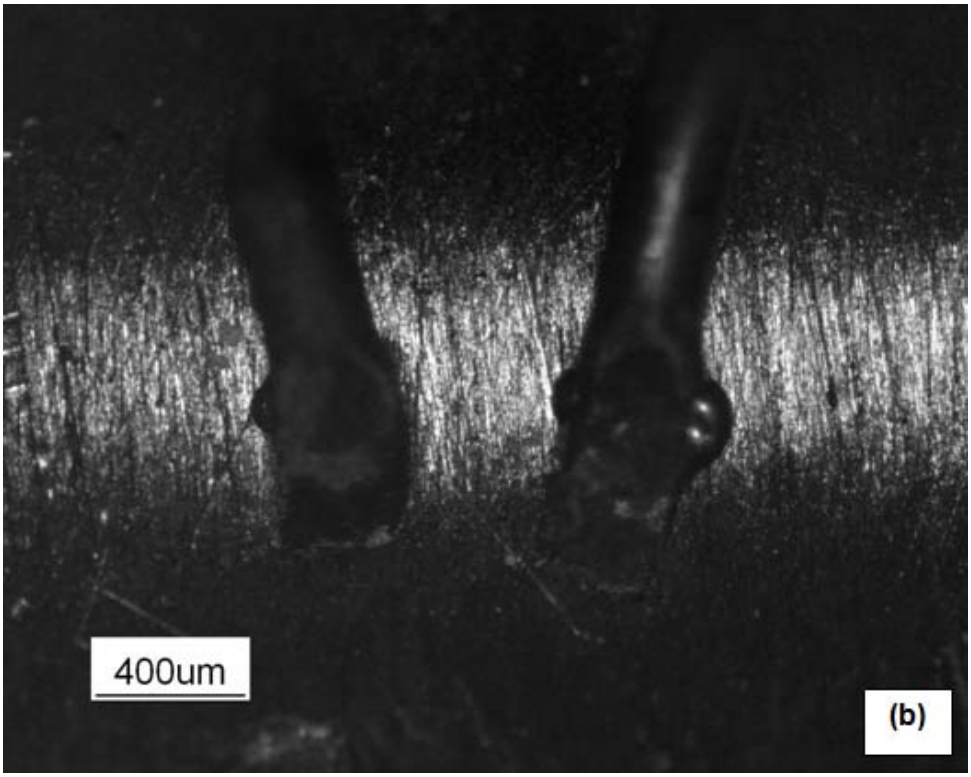

Figure 3.13: (contd.) Images from optical micrograph focussing on (a) the major crack on the specimen and (b) the TC wires positions

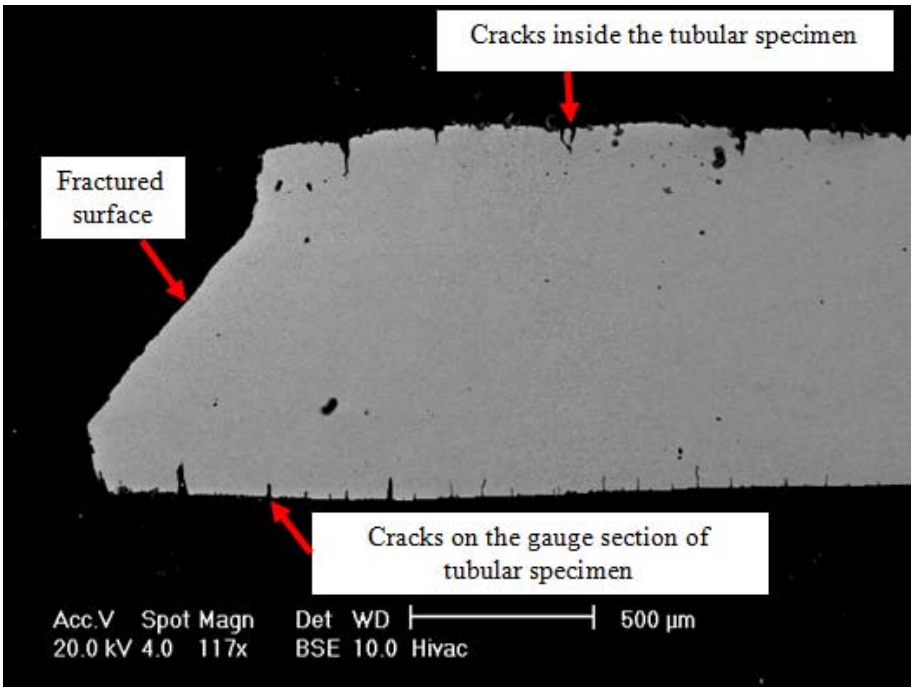

Figure 3.14: SEM images of a tested P91 tubular specimen showing many cracks on the inside and outside of TMF specimen in longitudinal direction

3.6 Experimental results

This section presents some typical results obtained from experimental works on the P91 and P92 materials. The effects of the strain-controlled cyclic loading and the holding period in the isothermal tests, on the material behaviour, are described. The data from these two tests were used in the constitutive model development; this will be explained further in Chapter 4. Results obtained from the thermomechanical fatigue tests and the load-controlled notched bar tests are also presented; these data will be used to verify the material model performance.

3.6.1 Strain-controlled cyclic loading tests

Figure 3.15 shows a typical stress-strain hysteresis loop for a strain-controlled fatigue test. Important parameters such as stress range, $\Delta\sigma$, plastic (or inelastic) strain range, $\Delta\varepsilon_p$, total strain range, $\Delta\varepsilon_t$, (which is the controlled parameter in the test) and elastic strain range, $\Delta\varepsilon_e$, can be identified from the stress-strain hysteresis loop as shown in Figure 3.15. In the case of the P91 specimens with ±0.5% strain amplitude, significant plasticity was observed from the hysteresis loop where the width of the loop at the mean stress (plastic strain range) represents approximately 60 percent of the total strain range.

The first cycle of the hysteresis loop, at different temperatures, shows the effect of the temperature on the resultant response. The slope of linear stress-strain data in tension and compression, as shown in Figure 3.16 for P91 material, depends on temperature, i.e., the slope decreases as temperature increases. The test at the higher temperature also produced a lower peak stress level as well as a higher plastic strain range compare with the others at the lower temperatures. Similar trends in the results were observed for the P92 parent and weld materials, as shown

in Figure 3.17. The figure compares the stress level at each test temperature for both P92 parent and weld materials. It can be seen that the stress-strain behaviours of both materials are practically the same during the first cycle. The P91 parent material data is compared with the P92 parent material data at 500 and 600°C, in Figure 3.18; this indicates a slight difference in the maximum and minimum stress levels attained in the tests with the same strain range and strain rate. The P92 material has slightly higher stress values, by about 30 MPa, than those of the P91 steel. Similar trends in stress level comparison for P91 and P92 materials have also been reported by Vaillant et al. (2008).

The P91 and P92 steels exhibit cyclic softening behaviour. Generally, the behaviour in fatigue loading tests is associated with the increase of plastic strain range in a material as a result of continuous cyclic loading. Figure 3.19 shows the evolution of plastic strain range observed in the tension-compression test of P91 and P92 materials. It can be seen from the graph that the plastic strain ranges increase rapidly during the initial stage and then become stable after approximately a quarter of the total number of cycles. In some P92 results, particularly at 600°C, the plastic strain range increases during the last stages of the test. The figure also shows that the plastic strain ranges recorded at higher temperature are always higher than the values at lower temperature, which may have a contribution due to the greater creep which occurs at higher temperature.

Figure 3.20 shows another aspect of cyclic softening behaviour. For a strain-controlled fatigue test, it can be seen that the stress range decreases as the cycles increase. There are similar trends for all tests performed at different temperatures, see Fig. 3.20, where the stress range evolves in three different stages. The stress range levels decrease rapidly in the initial stage before slowly decreasing in the

middle region of the test. In the latter stages, the stress levels continue to rapidly decrease until failure occurs. The second stage seems to have the largest portion of the cyclic period. From Figure 3.20, it is also clear that the number of cycles to failure decreases when temperature increases between 400 and 600°C for both P91 and P92 materials. However, the number of cycles to failure for P92 at 675°C was found to be higher than the failure cycles of the same material at 600°C. The recorded stress-strain loops at the end of the tests at different temperatures for P92 are shown in Figure 3.21. Interestingly, it can be seen at the bottom of compression data for the three loops that there is a "hysteresis loop tail", which indicates the occurrence of cracks (Dunne et al., 1992). For example, a visible crack was observed on the P92 parent material test at 1042 cycles and 600°C with a 90µm crack width as shown in Figure 3.13(a).

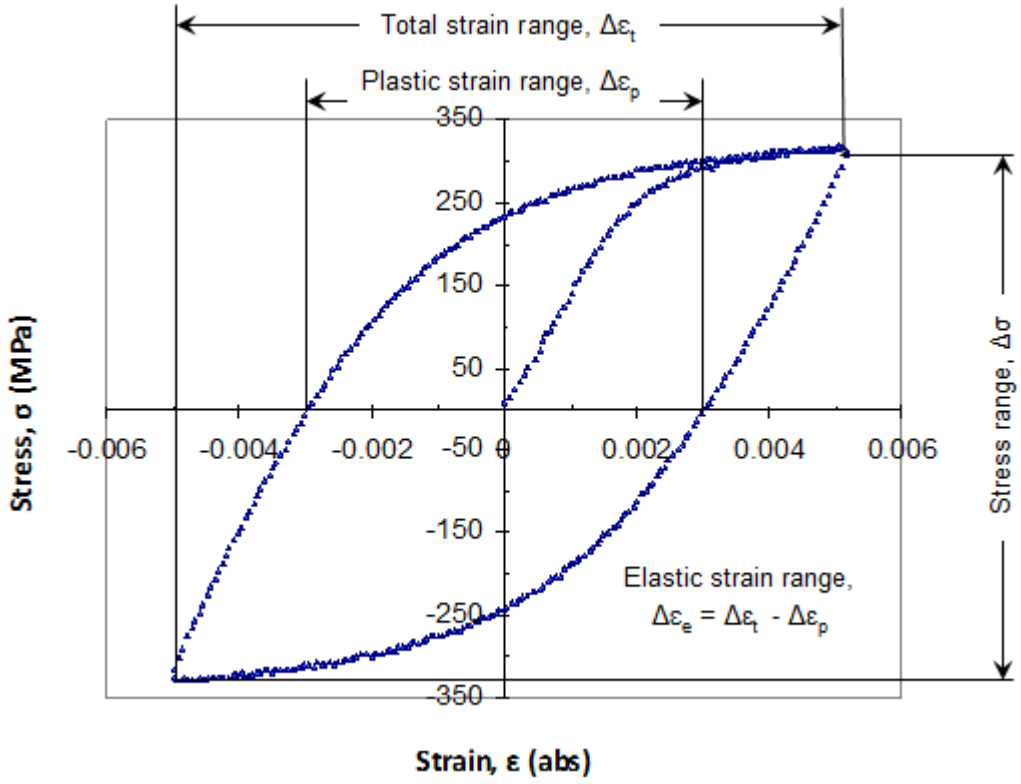

Figure 3.15: Example of typical stress-strain hysteresis loop and the parameters determined from the loop for an isothermal strain-controlled test

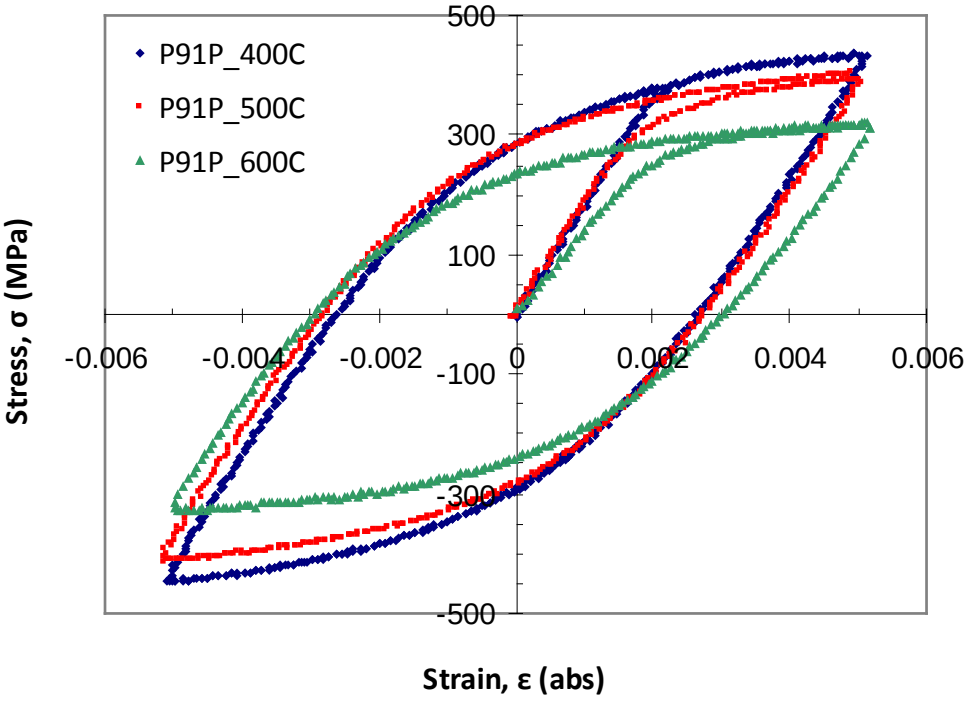

Figure 3.16: The stress-strain loop for the P91 parent (P91P) material during the first complete cycle of a tension-compression test at various temperatures

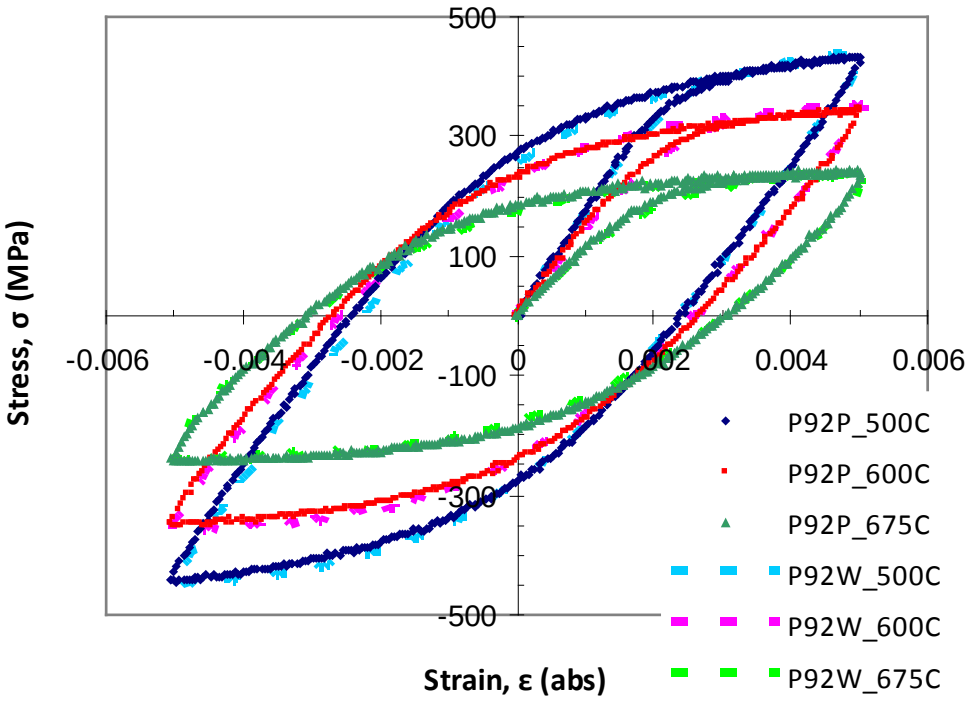

Figure 3.17: The stress-strain loop for the P92 parent (P92P) and the weld (P92W) during the first complete cycle of a tension-compression test at various temperatures

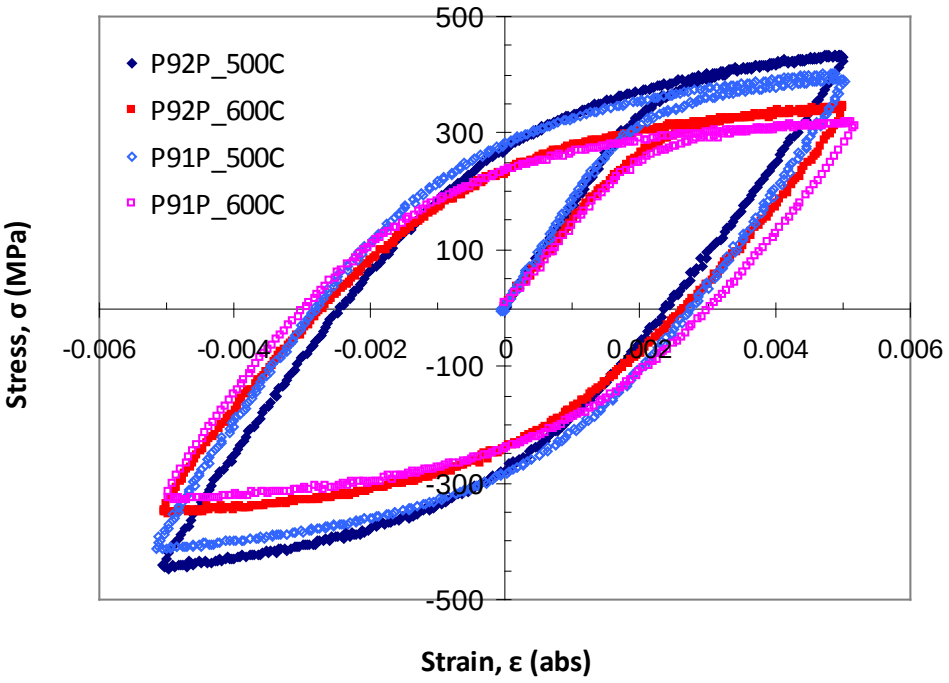

Figure 3.18: Comparison of the stress-strain behaviour of P91 and P92 parent materials for isothermal test at 500 and 600°C

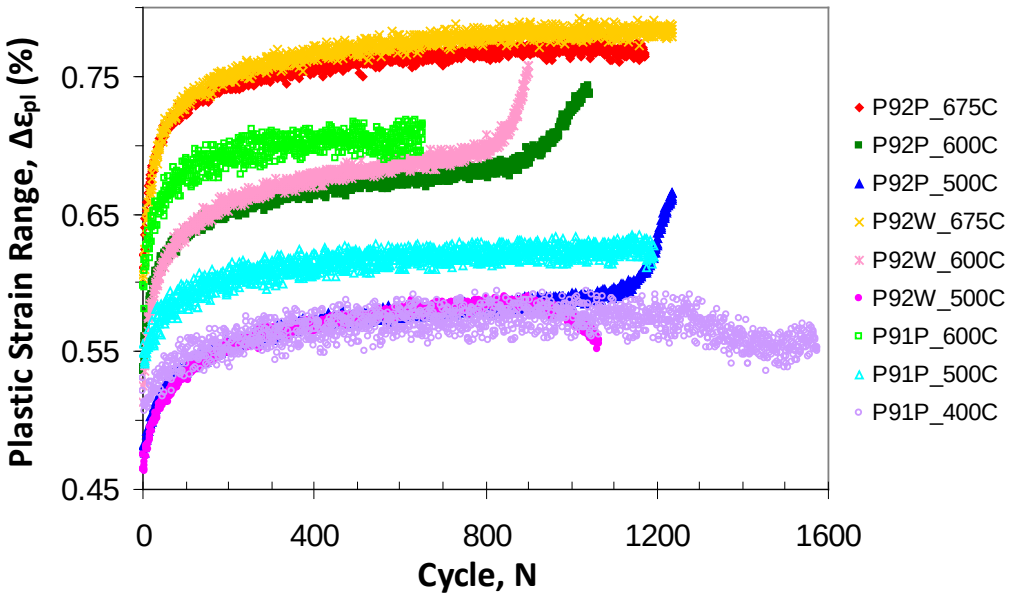

Figure 3.19: The evolution of plastic strain ranges in isothermal tension-compression tests indicating the cyclic softening behaviour

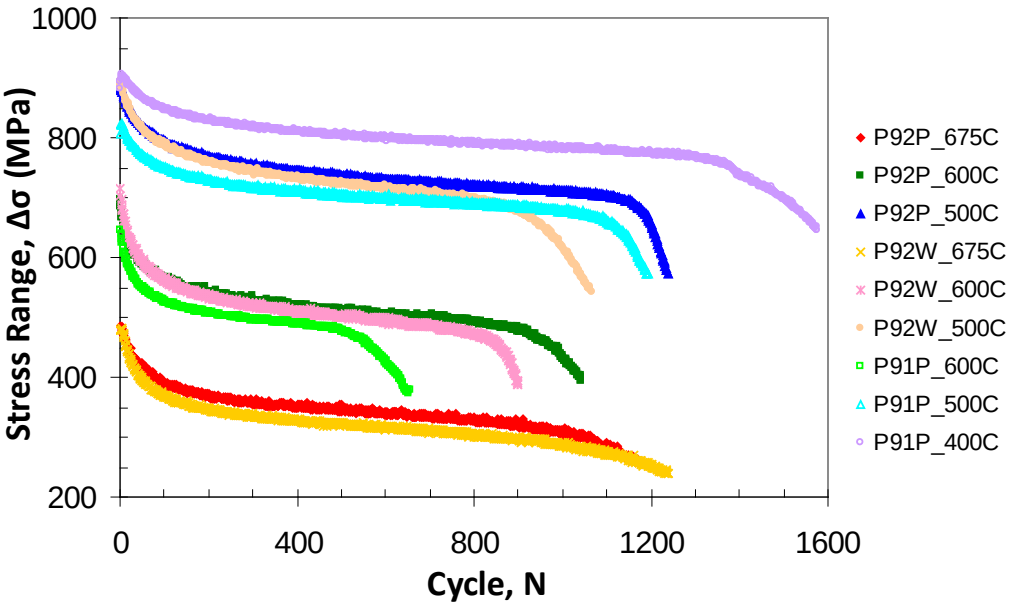

Figure 3.20: The evolution of stress ranges in isothermal tension-compression tests which can be divided into three stages for each test

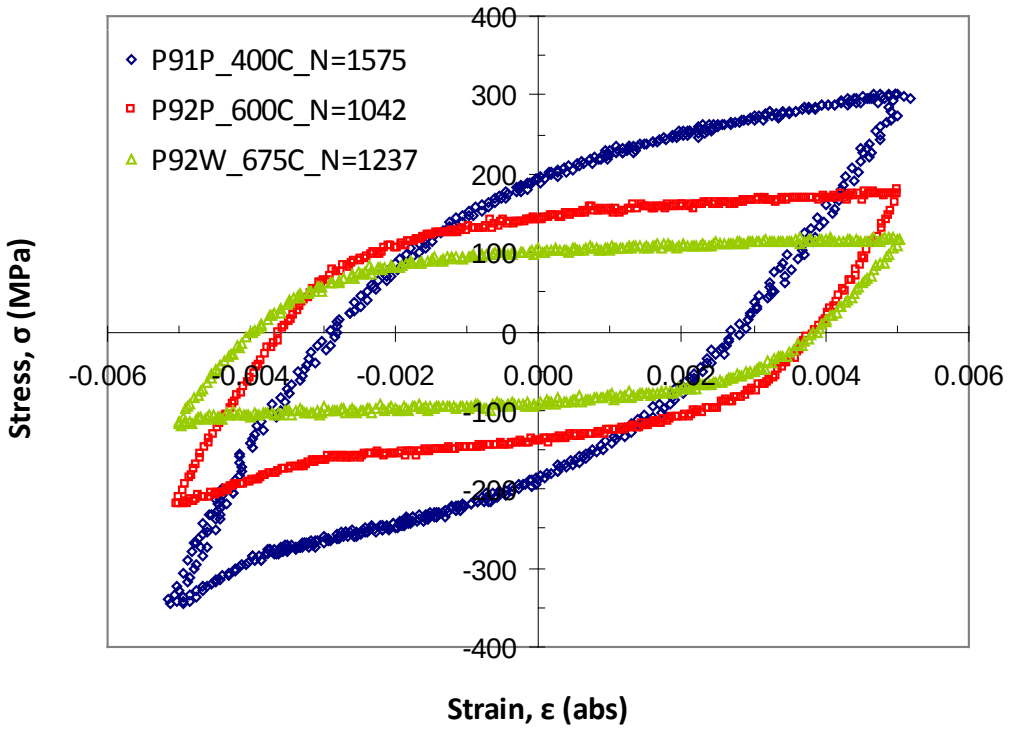

Figure 3.21: Example of the stress-strain loop of the last cycle recorded in isothermal tension-compression tests indicating the “hysteresis loop tail” at the base of compressive stress part of the loop

3.6.2 Hold period test

In the isothermal dwell period tests, the holding period for the tensile strain caused a stress relaxation behaviour, which indicates a time-dependency effect for P91 and P92 materials at high temperature. Figure 3.22 shows the stress relaxation behaviour for P91 parent material in which the stress difference between the starting and the last point of the holding period for 400, 500 and 600°C are 80, 110 and 179 MPa, respectively, showing an increasing value of stress relaxation as temperature increases. However, the results of the stress relaxation behaviour of the P92 materials, as shown in Figure 3.23, exhibit a different trend, i.e., the stress relaxation for the test at 675°C, with a value of 167 MPa, is lower than the relaxation stress at 600°C, in which the value is 197 MPa. Both P92 parent and weld materials show similar stress relaxation behaviour in the first cycle.

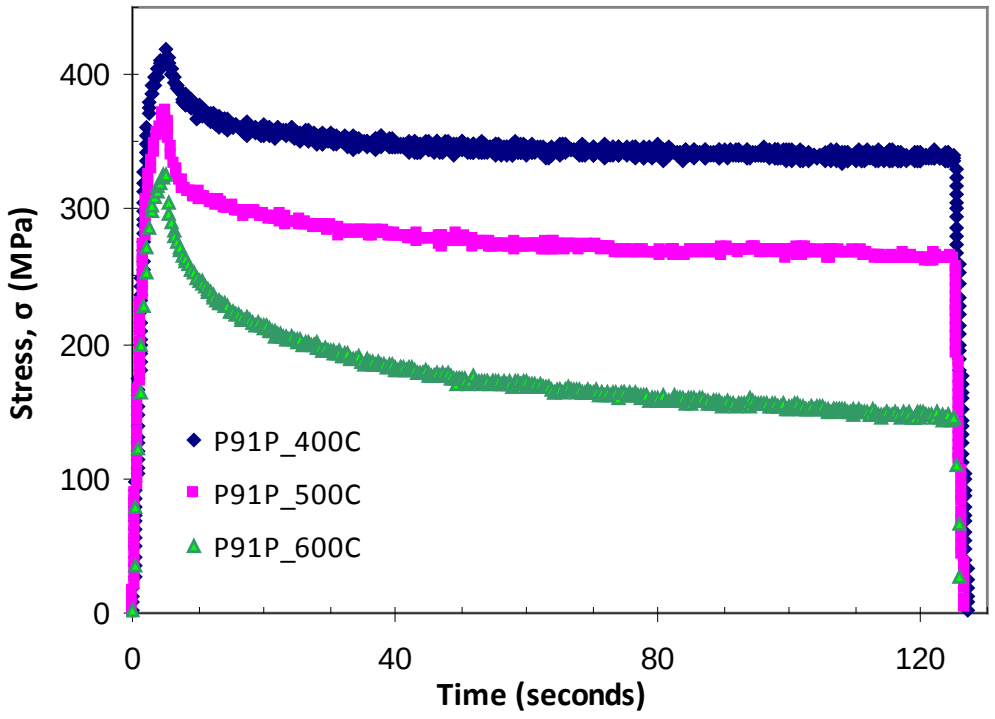

Figure 3.22: Stress relaxation data for the P91 parent material in the first cycle of isothermal tests with a 2 minute dwell period

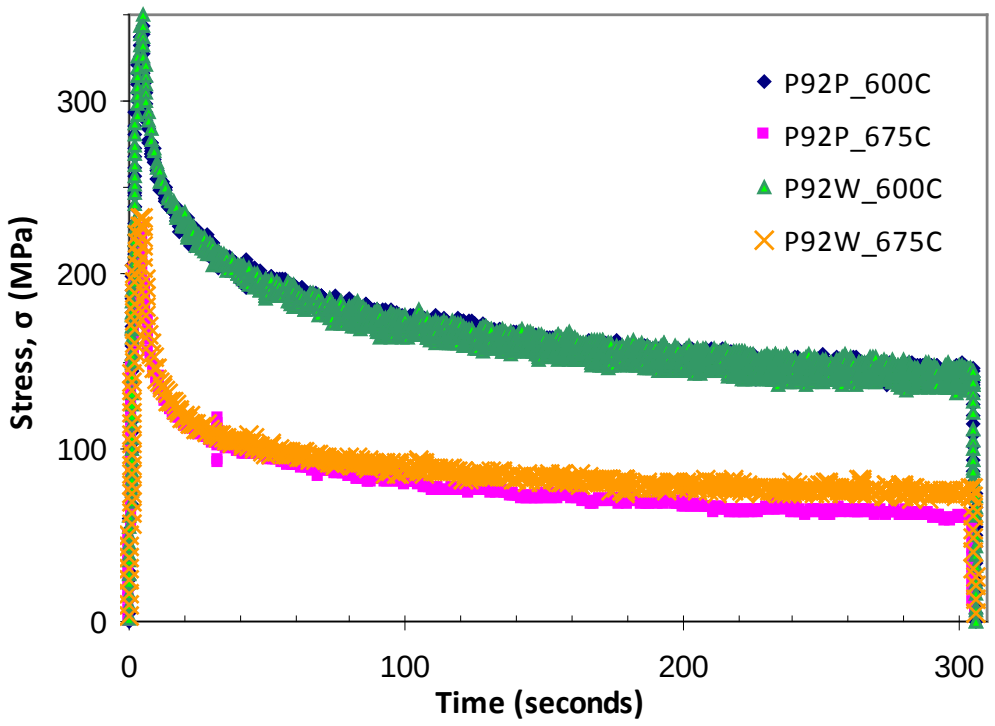

Figure 3.23: Stress relaxation data for the P92 parent material and the weld metal in the first cycle of isothermal tests with a 5 minute dwell period

3.6.3 TMF test results

Figure 3.24 shows the stress-strain behaviour of the P91 material in the thermomechanical fatigue test with in-phase and out-of-phase temperature cycles. It can be seen that the TMF tests, with in-phase temperature cycle produce higher total strains, than the out-of-phase tests, in which the controlled mechanical strain amplitude is ±0.5%,. The temperature cycle produces thermal strain which increases the total strain value in the TMF in-phase tests while the temperature cycle reduces the total strain value in the TMF out-of-phase test in order to maintain the mechanical strain value at specified amplitude.

Temperature phase loading also affects the value of maximum and minimum stress in the TMF tests and the loop shape. At the same test period, such as in the first tensile curve, the in-phase TMF test produced a lower maximum stress compared to

the out-of-phase TMF test. For example, the maximum stresses for the in-phase and the out-of-phase for a P92 specimen are 240 and 410 MPa, respectively. These values show the effect which temperature has on the resultant stress values. Furthermore, the maximum and the minimum stress values for the TMF tests seem to be similar to the stress values of the isothermal test data at the top and the bottom of the first cycles. For example, Figures 3.25 and 3.26 show the comparison of the first complete cycles of the in-phase and out-of-phase TMF test results, respectively, with the isothermal test results at 500 and 675°C for the temperature range of 500-675°C for P92 parent material. Also, the in-phase TMF tests showed a compressive mean stress while the out-of-phase TMF tests showed a tensile mean stress. All TMF tests show cyclic softening behaviour throughout the test, as plotted by the decrease of stress range in Figure 3.27.

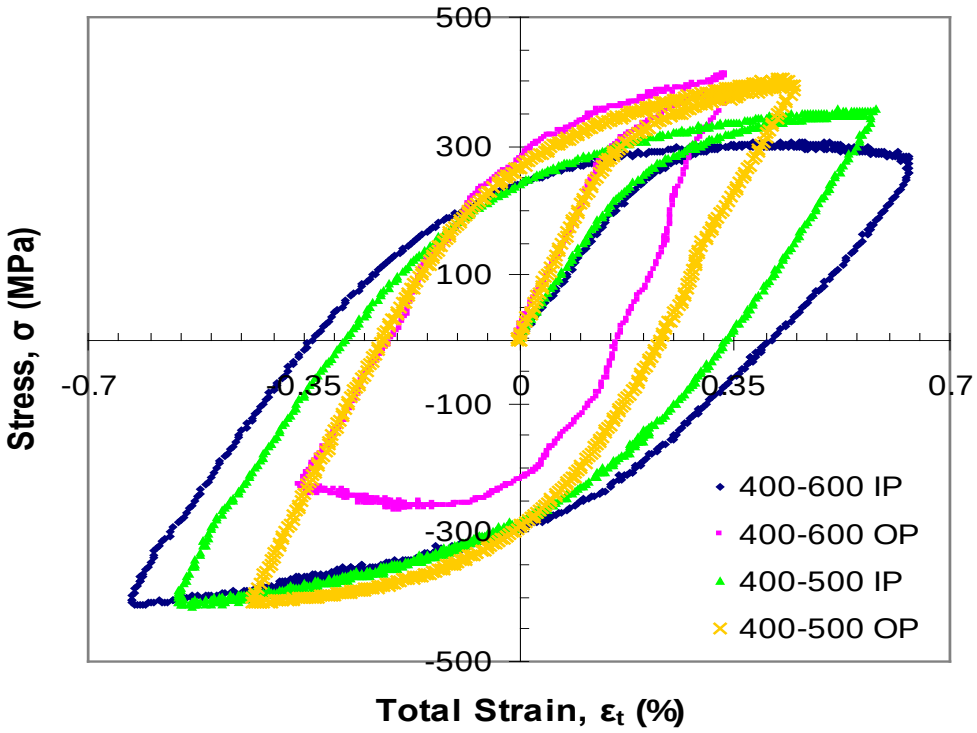

Figure 3.24: The stress-strain behaviour of the P91 parent material in the first complete cycle of a TMF test

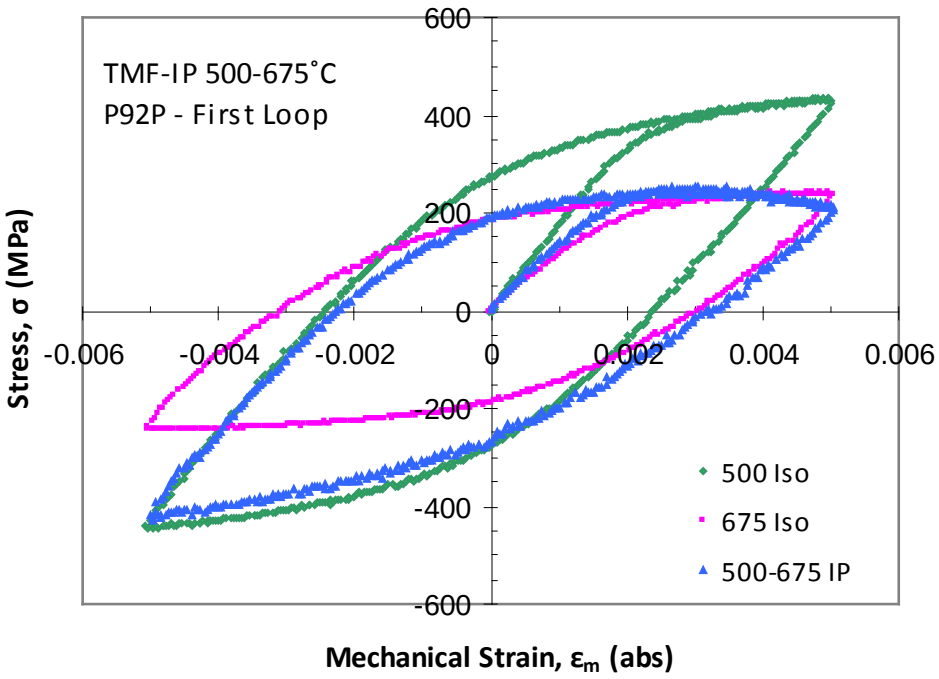

Figure 3.25: Comparison of the first complete cycles from the isothermal tests at 500 and 675°C and from the in-phase TMF test for a temperature range of 500-675°C, for the P92 parent material

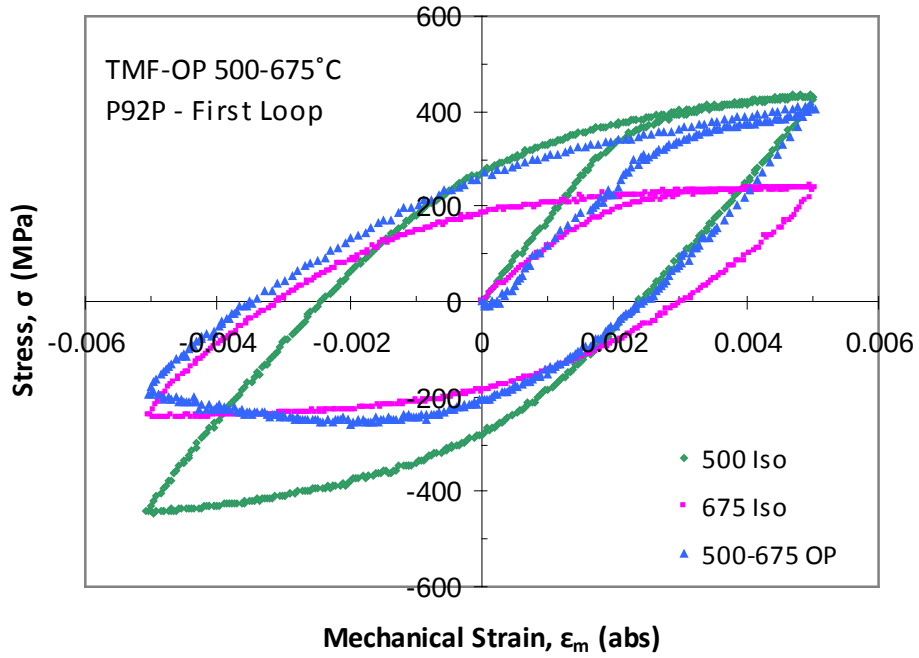

Figure 3.26: Comparison of the first complete cycles from the isothermal tests at 500 and 675°C and from the out-of-phase TMF tests for a temperature range of 500-675°C, for the P92 parent material

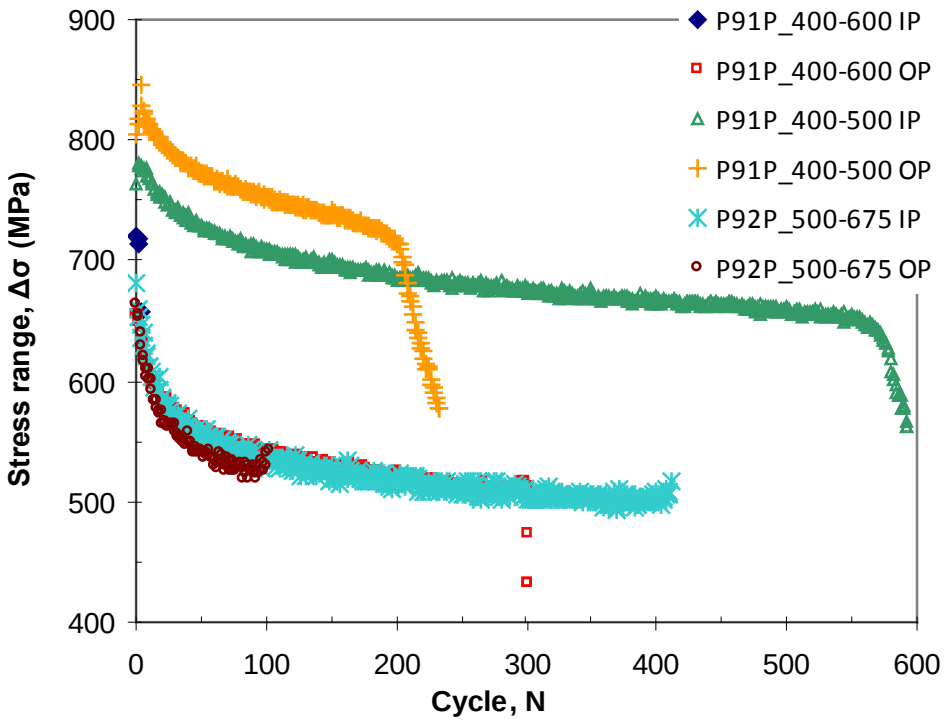

Figure 3.27: The evolution of the stress ranges obtained for in-phase and out-of-phase TMF tests for the P91 and P92 parent materials

3.6.4 Notched specimen test results

For isothermal notched specimen tests performed under a load-controlled mode, with 300MPa stress amplitude, the specimen displacement increases as the cycle increases, see Figures 3.28 and 3.29. The displacement of the notched bar test with a dwell period, shown in Figures 3.30 and 3.31, shows a ratchetting effect which produces a significant increase in displacement and a lower number of cycles to failure compared to the test with tension-compression loading. The shape of displacement range versus cycle number, for the notched bar test, is also similar to that of a typical creep test in which it can be divided into three stages with a longer secondary period and a sudden displacement range increase near the end of the test period up to the specimen fracture.

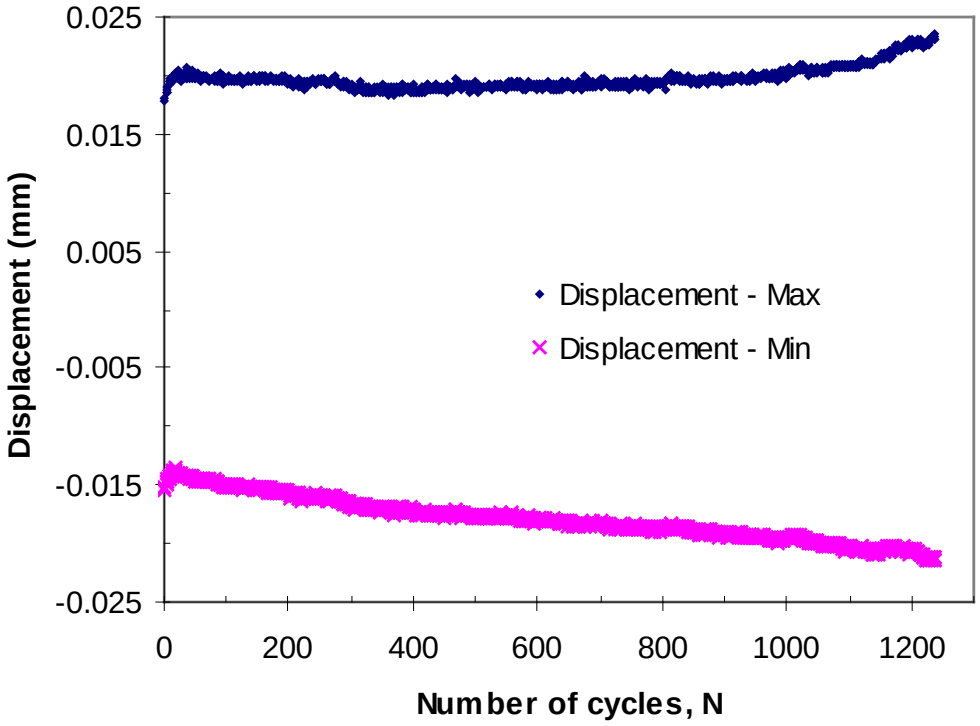

Figure 3.28: The maximum and minimum displacements obtained from the P91 notched specimen test in the load-controlled test at 600°C

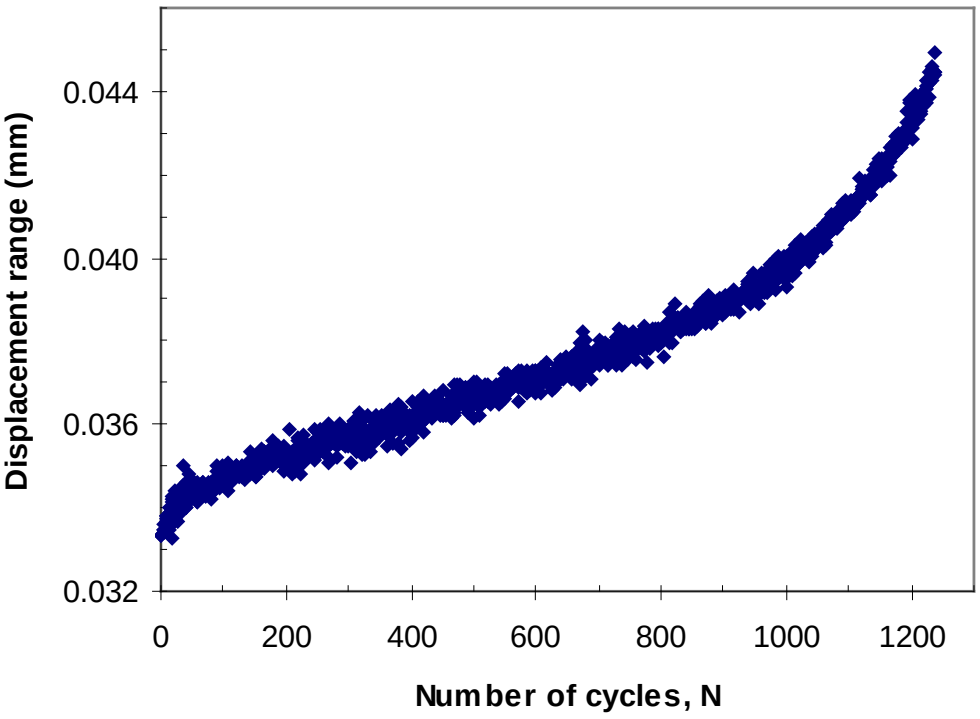

Figure 3.29: The displacement range obtained from the P91 notched specimen test in the load-controlled test at 600°C

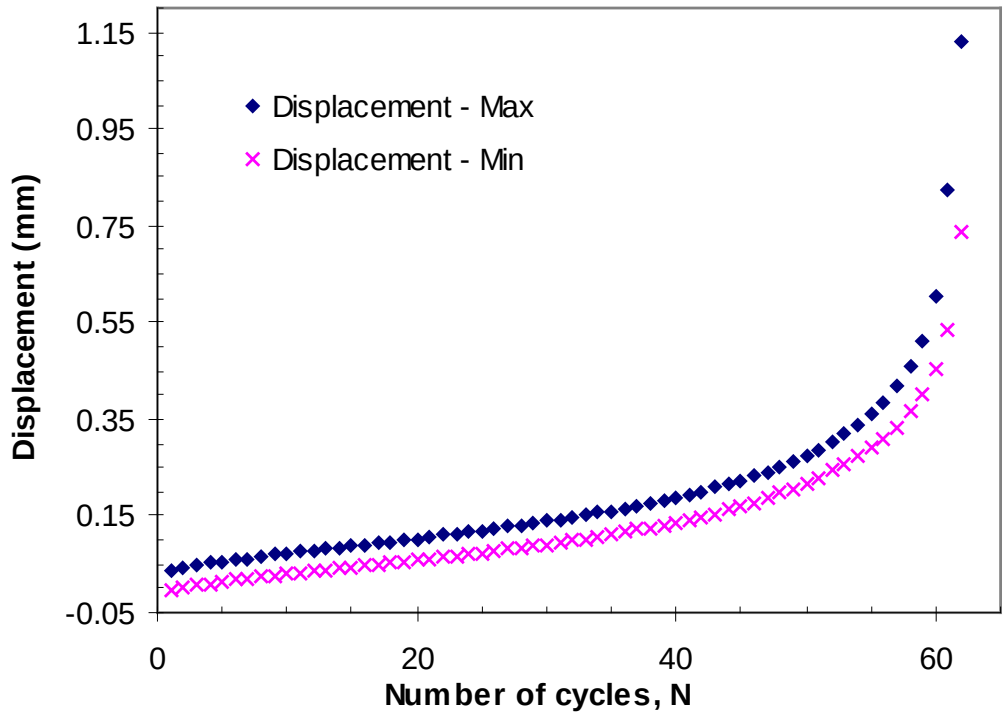

Figure 3.30: The maximum and minimum displacements obtained from the P91 notched specimen dwell test at 600°C

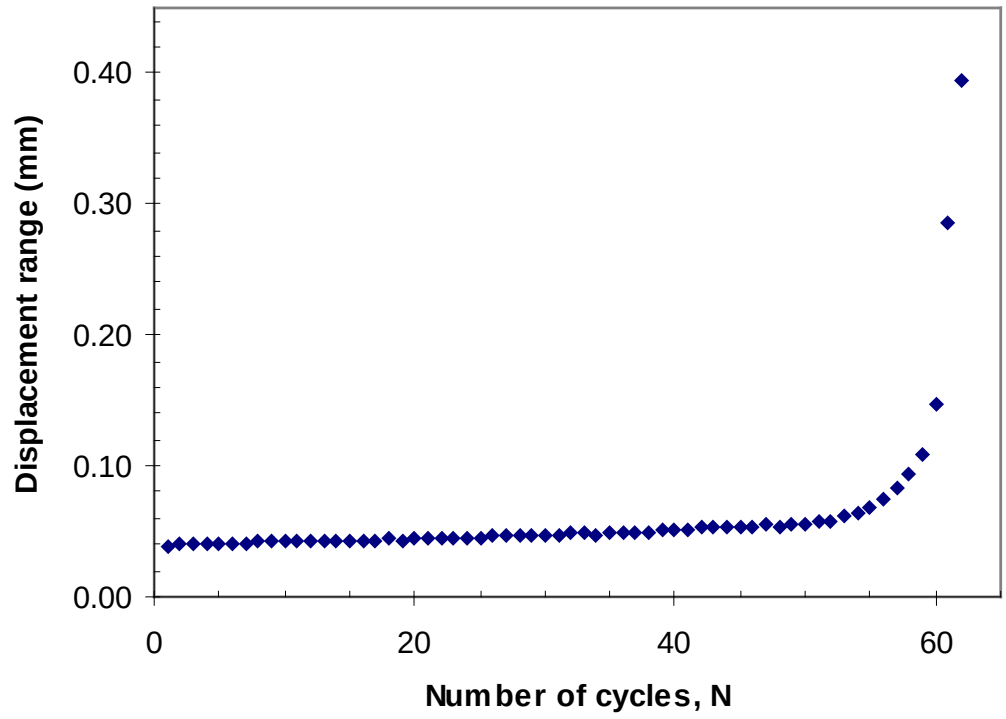

Figure 3.31: The displacement range obtained from the P91 notched specimen in the dwell test at 600°C

Chapter 4 –Stress-strain analysis and microstructure investigation of cyclic tests

4.1 Overview

This chapter contains an analysis of the stress-strain behaviour, and its related parameters, produced in strain-controlled tests of P91 steel, at 600°C. It also contains an investigation of the microstructural variations which occur in specimens during the cyclic tests. Based on the experimental stress-strain data, variations in the Young's modulus and the area enclosed in the hysteresis loops are determined, together with the variations in other parameters throughout the test. The strain and energy parameters obtained from strain-controlled tests with different strain amplitudes can be used to develop fatigue lifing methods. Also, the results of the microstructural investigations of the P91 steel, at different life fractions, using scanning and transmission electron microscopes, are presented. Finally, the relationships between the cyclic stress-strain data and the results obtained from the microstructural investigations are used to gain an understanding of the cyclic softening and failure mechanisms for the P91 steel.

4.2 Stress-strain analysis

Based on the results provided in Chapter 3, the P91 steel exhibited cyclic softening behaviour in all of the tests performed in this study. From the isothermal, strain-controlled tests, at 600°C, with different strain amplitudes, it can be seen that the material exhibits cyclic softening behaviour as can be seen in Figures 4.1 and 4.2, which present the evolutions of the maximum stress when various plastic strain ranges are applied throughout the tests. The same strain rate of 0.1%/s was used for all of the tests. Parameters such as Young's modulus, hysteresis loop area and

loop shape parameter were determined from the cyclic stress-strain loops; these are analysed in this section.

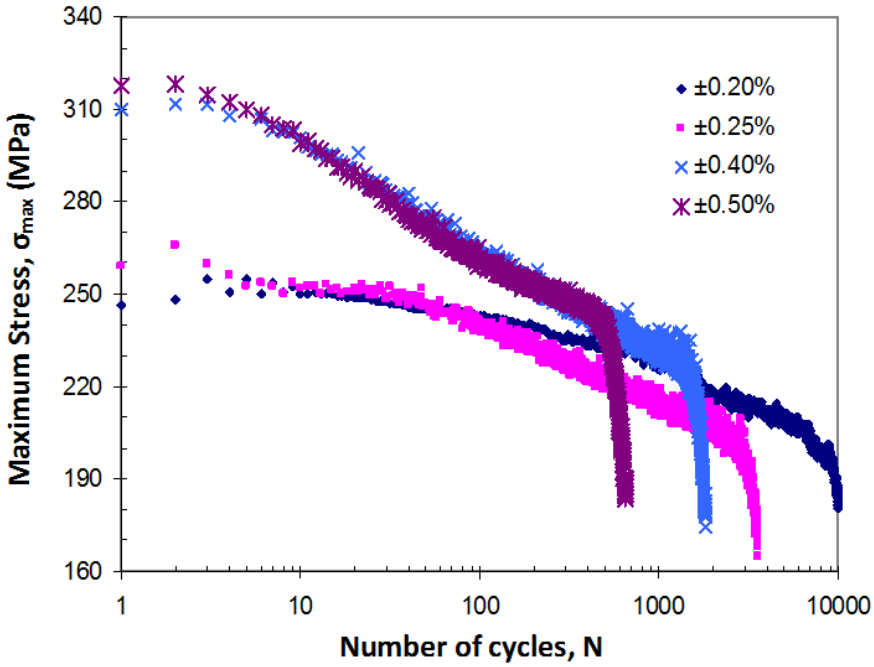

Figure 4.1: The evolution of maximum stress throughout the isothermal strain controlled tests performed at 600˚C on P91 steel, with various strain amplitudes

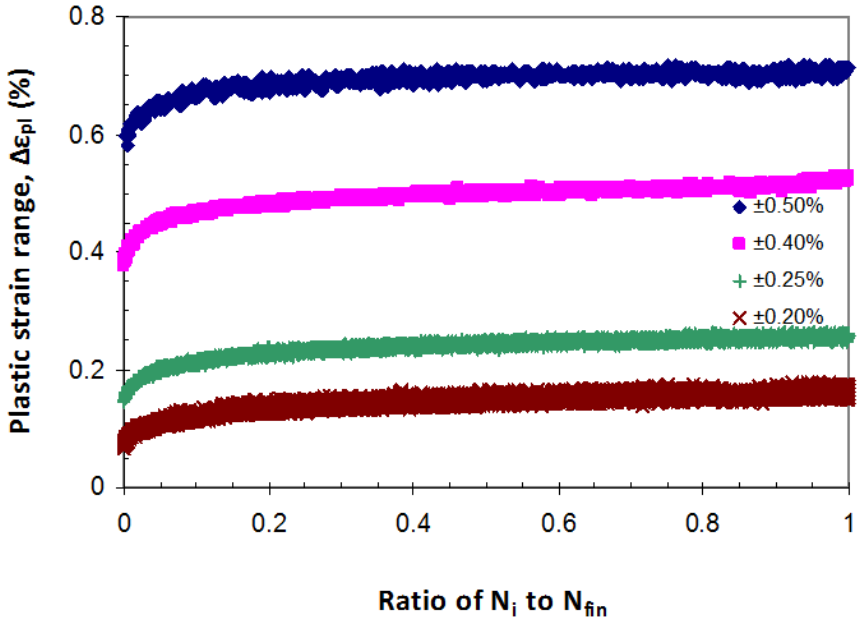

Figure 4.2: The evolution of plastic strain range throughout the isothermal strain controlled tests performed at 600˚C on P91 steel, with various strain amplitudes

4.2.1 Determination of N_{sta}, N_{tan} and N_f

All of the specimens tested in this study exhibited a cyclic softening behaviour, which consists of three stages; as can be seen from the evolution of the peak stress, as shown in Figure 4.3. In the initial stage, the peak stress level decreases rapidly with cycle number. The rate of decrease becomes slower before reaching a constant value during the second stage. The second stage occupies the largest proportion of the cycles. Finally, the rate of reduction of the stress level increases rapidly leading to failure. In this subsection, the number of cycles in each of the stages and the number of cycles to failure are described.

Figure 4.3 shows a definition of N_{sta}, N_{tan} and N_f. The N_{sta} and N_{tan} correspond to the beginning of the constant rate evolution of the peak stress level and the beginning of the stress drop in the third stage, respectively, as suggested by Constantinescu et al. (2004). The number of cycles to failure, N_f, is defined, according to the BS7270:2006 standard, as the cycle number at which the maximum stress has decreased by a prescribed percentage from that predicted by extrapolation of the second stage stabilisation curve. In the standard, a 10 percent drop (N_{f10}) is suggested, as a possible failure criterion. However, other percentages could be used. Finally, N_{fin} represents the final number of cycles applied in the cyclic test, as recorded by the TMF machine, before it stops as a result of the machine setting. This avoids the total fracture of the specimen, which could damage the machine. Table 4.1 shows the results obtained from the tests of the P91 specimens at 600°C.

Table 4.1: The values N_{sta}, N_{tan}, N_{f5} (5% failure criterion), N_{f10} (10% failure criterion) and N_{fin} for the P91 steel test at 600˚C

Strain amplitude	N_{sta}	N_{tan}	N_{f5}	N_{f10}	N_{fin}
±0.5%	220	425	556	590	656
±0.4%	400	1130	1348	1424	1462
±0.25%	990	2800	3308	3522	3590
±0.2%	1900	9242	10090	10512	10518

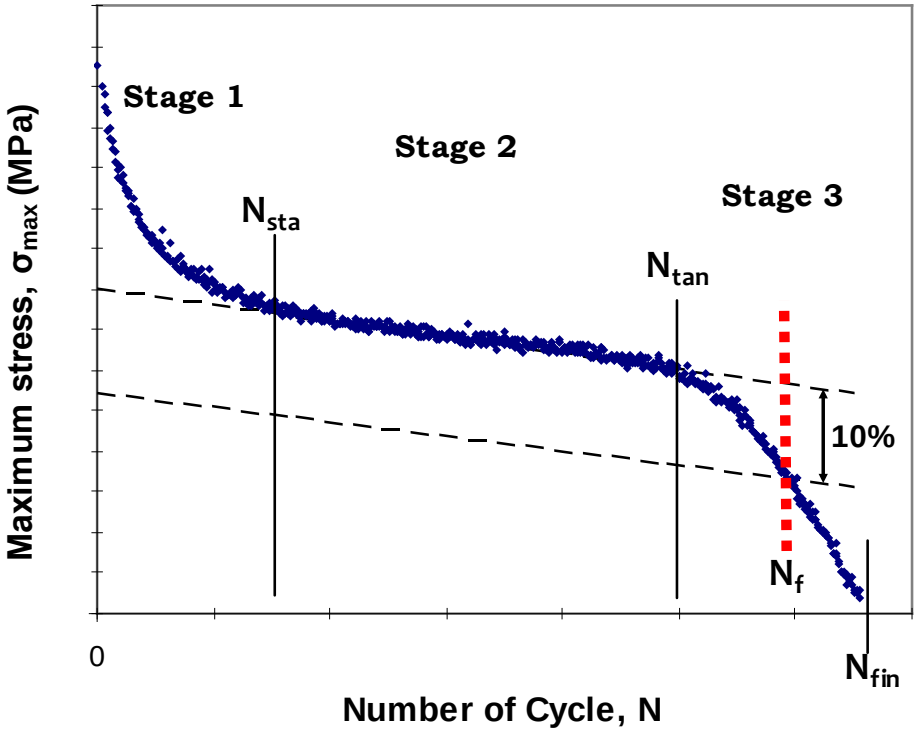

Figure 4.3: Definitions of N_{sta}, N_{tan} and N_f obtained from a cyclically softened material

4.2.2 Young's modulus analysis

The elastic modulus (or Young's modulus) is an important material parameter, representing the proportionality constant which describes the linear stress-strain response of a material. Also, the initial measurement of the modulus value, prior to starting the strain-controlled test, serves as an indication that the extensometer, on

the specimen's surface, has been correctly installed. In addition, according to Lemaitre and Chaboche (1994), the Young's modulus value can be taken as an indirect measurement of damage for a cyclically loaded specimen. One of the aims of this subsection is to investigate the evolution of the modulus throughout the life cycles for P91 steel, at 600°C.

The elastic modulus can be determined in several different ways. Generally, it is determined by measuring the slope of the linear region of the tensile stress-strain test curve. In a cyclic test, the modulus can be determined from each recorded hysteresis loop by calculating the average slope of the tension-going (E_{upload}) and compression-going ($E_{download}$) linear data, as suggested by Hales et al. (2002). Based on the results of P91 strain-controlled tests with different strain amplitudes, the values of E_{upload} and $E_{download}$ at each hysteresis loop are slightly different. However, the difference is small and much less than 10 percent.

Figure 4.4 shows the variation of elastic modulus with load cycles in the strain-controlled tests of P91 steel with different strain amplitudes. It can be seen that the modulus values are practically constant for about the first 70 percent of recorded hysteresis loops for each test. During the latter stages of life, the modulus values decrease significantly until the last recorded cycles. The modulus values for the test with ±0.5% strain amplitude exhibit the greatest decrease when compared with the other test data. This is because the data for the ±0.5% test were recorded up to the point where total separation of the specimen occurred, whereas, the other tests, with different strain amplitudes, were stopped before total fracture in order to avoid potential damage to the extensometers. However, major cracks can be clearly seen on the surfaces of these specimens.

The evolution of elastic modulus can be used as an indication of the strength degradation of the material. Lemaitre and Chaboche (1994) proposed that the damage, D, of a material may be given by the following equation:-

$$D = 1 - \frac{\tilde{E}}{E} \tag{4.1}$$

where E is the elastic modulus of the material free from damage, $\tilde{E}$ is the elastic modulus of the damaged material and $0 \le D \le 1$. The damage parameter is equal to zero for the undamaged material and totally damaged material is represented by $D = 1$. Figure 4.5 shows a plot of damage versus cycle for the test with ±0.5%. The damage values are negligible for the majority of cycles from the beginning and start to increase from the 500th cycle to the last recorded cycle, i.e. the 655th cycle, which gives the damage value of about 0.2, leading to sudden fracture of the specimen, with no clear sign of specimen necking, at the end of the test.

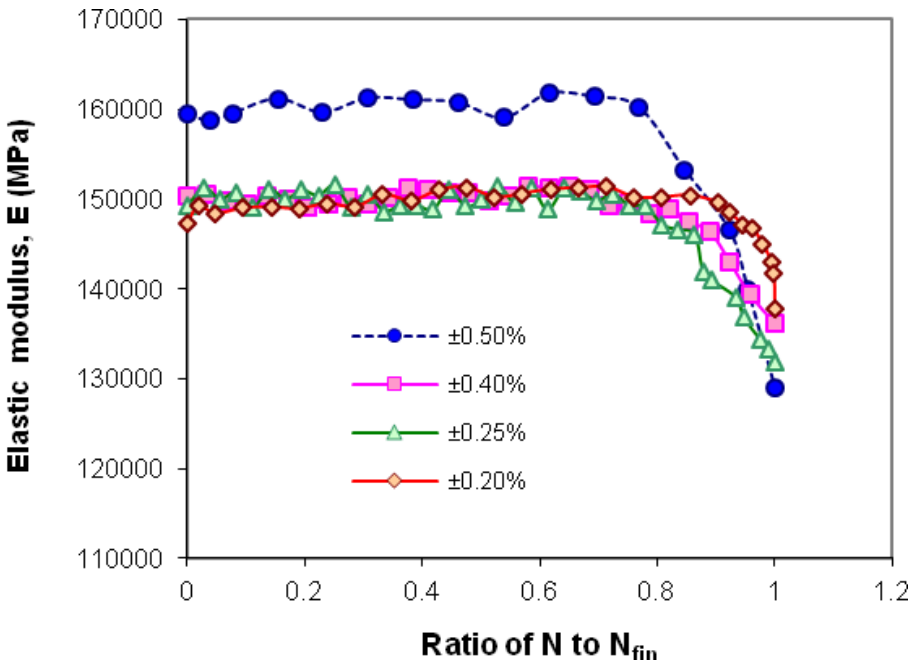

Figure 4.4: Plot of elastic modulus versus the ratio of the cycles number to the final recorded cycles for tests with various strain amplitudes for P91 steel, at 600°C

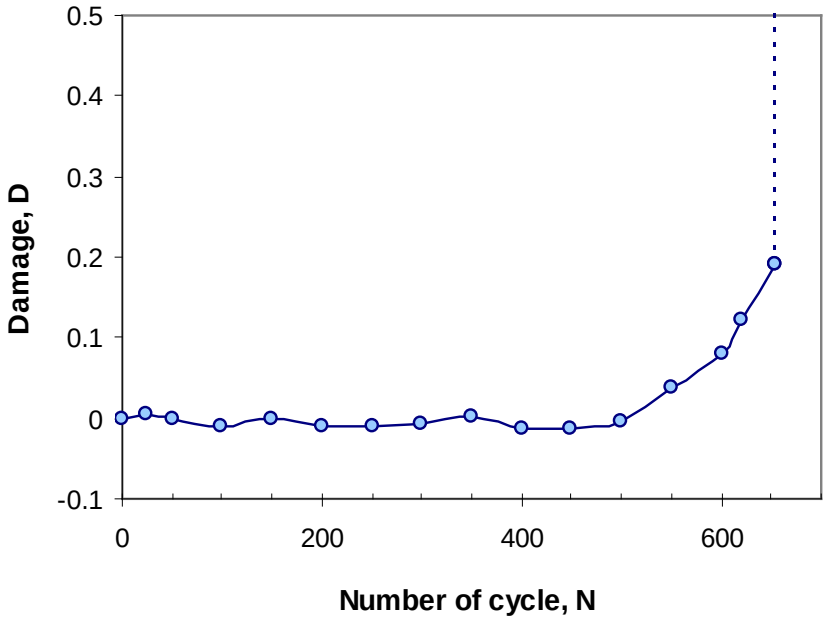

Figure 4.5: The evolution of damage throughout the ±0.5% strain-controlled test at 600°C, for the P91 steel

4.2.3 Hysteresis loop area analysis

The hysteresis loop area of a uniaxial, cyclic stress-strain test represents the plastic energy or plastic work per cycle for an elastic-plastic material. The parameter has been used to quantify low cycle fatigue damage (Charkaluk, 2009) so that accumulation of the plastic work can become a damage indicator (Skelton, 1991). The determination of hysteresis loop areas throughout the strain-controlled test of P91 specimen at 600°C is presented in this subsection.

The area of hysteresis loop can be determined through an integration process. For example, using the 350th loop from an isothermal strain-controlled test at 600°C, the test data can be divided into two curves representing the compressive going and the tensile going data, as shown in Figure 4.6. The two types of data can be represented by the following equations:-

$$y_i = a + bx + cx^2 + dx^3 + ex^4$$

A software called Diadem, which is data management software, produced by National Instruments, was used to produce a set of constants for the above equation to match the experimental data, as given in Table 4.2. The equation was integrated for the strain data range between -0.5 and 0.5 to obtain the area under the curve as follows:-

$$\text{Area of the hysteresis loop} = \int_{-0.5}^{0.5} (y_2 - y_1)dx \qquad (4.2)$$

which gives the value of 286.646 (ε in % and σ in MPa units)

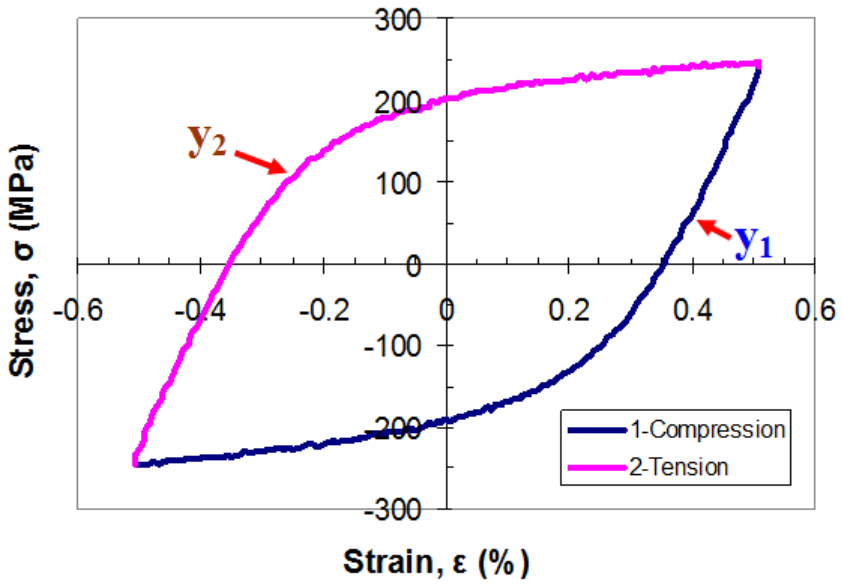

Figure 4.6: Hysteresis loop for the 350th cycle in an isothermal test of P91, at 600°C

Table 4.2: A set of constants approximated by Diadem for the hysteresis loop data

Constants	Compression, y_1	Tension, y_2
a	-194.20373	203.268464
b	180.209582	181.81991
c	467.443747	-553.44568
d	1172.61961	1202.39886
e	1102.36017	-957.8186

However, the calculation of the hysteresis loop area, using the integration method, requires many steps leading to it being a time-consuming process when used for many sets of hysteresis loop data are involved. A simple way is to use a statistical method (Billo, 2007) to calculate the area of the curve, as shown in Figure 4.7. For example, a trapezoid method can be used to approximate the area under the curve, by summing the individual trapezium areas calculated between two adjacent points, as given by the following equation:-

$$Area = \sum_{i=1}^{n-1} \frac{y_i + y_{i+1}}{2} (x_{i+1} - x_i) \qquad (4.3)$$

In the case of the experimental data, x and y represents the strain and the stress values for each cyclic test. For example, the hysteresis loop area for the 350th cycle, as shown in Figure 4.6, is predicted, using the trapezoid method, to be 286.774. This is very close to the value calculated by the integration process. Thus, the trapezoid method was used in this study to calculate the hysteresis loop areas of the cyclic stress-strain data.

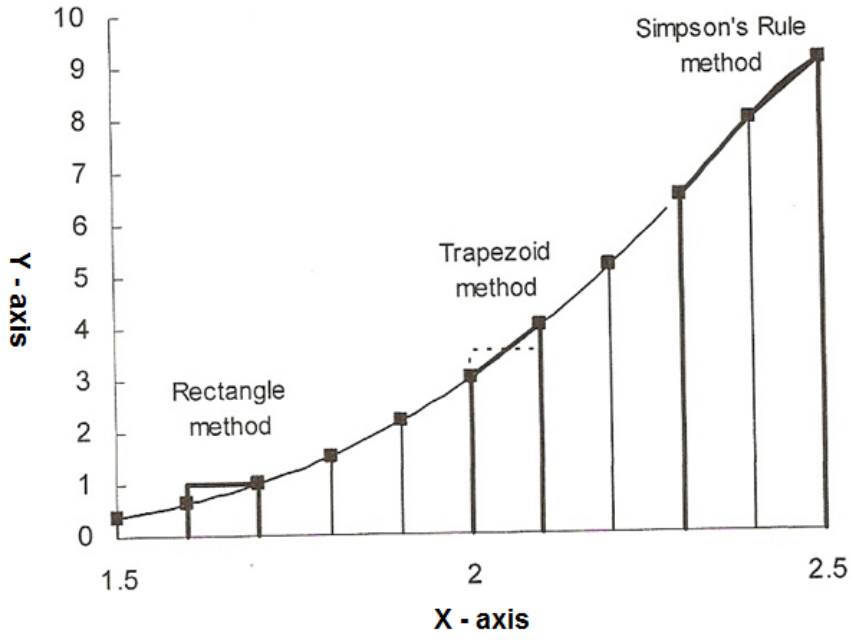

Figure 4.7: Example of the statistical methods for calculating area under curve (Billo, 2007)

Figure 4.8 shows the evolution of plastic strain energy per cycle determined using the trapezoid method, for the strain-controlled tests of P91 specimens, at 600°C. The results show that as the strain amplitude of a test increases, the resultant hysteresis loop area increases. The tests with lower strain amplitude (0.2% and 0.25%) show an increase of hysteresis loop area at the beginning of cyclic loading. However, a decrease of the hysteresis loop area occurs at the early stage observed in the tests with the ±0.4% and ±0.5% strain amplitudes. In Figure 4.8, it can be seen that the hysteresis loop areas are stable in the middle stage of the test at all strain amplitudes and also that the stabilised hysteresis loop areas are maintained for the majority of the cycles. Finally, the hysteresis loop areas, for all the tests, with various strain amplitudes, fall as the tests reach the third stage of cyclic softening.

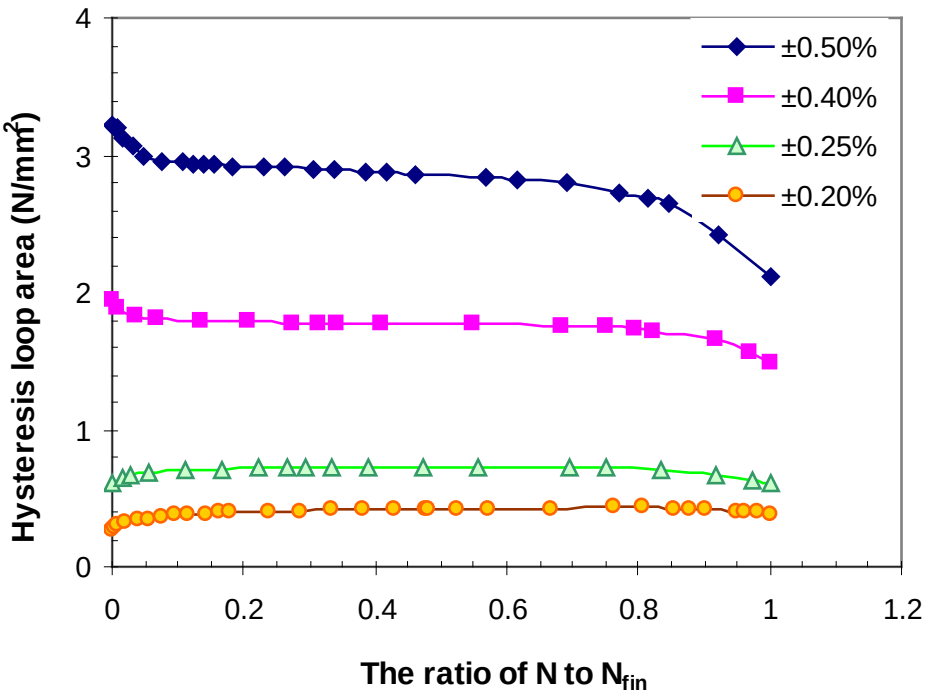

Figure 4.8: The evolution of the hysteresis loop area during the strain-controlled test of P91 steel, at 600°C

Table 4.3 gives the accumulated values of the hysteresis loop areas, also known as cumulative energy parameter (Skelton, 1991), at various stages of the tests. Generally, energy is represented by units of Joule (J) and thus the unit of hysteresis loop area, N/mm^2, is equal to MJ/m^3. The cumulative energy parameters were measured at 4 different points namely N_{sta}, $N_{f5/2}$, N_{tan} and N_{f5}, in which $N_{f5/2}$ is the number of the cycle at the midway point to failure with 5 percent failure criterion. The cumulative parameters are represented by ΣW_{sta}, $\Sigma W_{f5/2}$, ΣW_{tan} and ΣW_{f5}, respectively, in this study. At each stage of the tests, with various strain amplitudes, the cumulative energy parameters are different and the standard deviations (stdev) are as shown in Table 4.3.

The cumulative energy parameter at the beginning of the stabilized stage, ΣW_{sta}, has the lowest standard deviation, which only deviates from the average value by 4%, while the cumulative energy parameters, at the half life, $\Sigma W_{Nf5/2}$ and at the end of the stabilized stage, ΣW_{tan}, have the highest standard deviation values, which are 38 and 47 percent of the average values, respectively. This trend indicates that similar cumulative energy parameters are required in order to achieve stabilized conditions, at N_{sta} for P91 steel, with various strain amplitudes, at the same temperature. On the other hand, the differences of the cumulative energy parameters at the end of the stabilized stage may be influenced by crack initiation and propagation conditions. Thus, the test parameter at N_{sta} can be reasonably used as the stabilized point of the cyclic material behaviour; this was also observed by Charkaluk and Constantinescu (2000).

Table 4.3: The values of cumulative energy parameters of ΣW_{sta}, $\Sigma W_{f5/2}$, ΣW_{tan} and ΣW_{f5} for the P91 steel test at 600˚C

Strain amplitude	ΣW_{sta}	$\Sigma W_{f5/2}$	ΣW_{tan}	ΣW_{f5}
±0.5%	648.097	815.206	1233.975	1594.499
±0.4%	720.789	1206.572	2043.090	2311.203
±0.25%	687.036	1167.517	2001.819	2357.516
±0.2%	684.857	1987.211	3774.038	4124.601
Average ΣW	685.195	1294.127	2263.230	2596.955
Stdev	29.702	494.444	1073.732	1076.663

The hysteresis loop areas can be further analysed using a parameter called the loop shape parameter, V_H . The evolution of this parameter throughout the cyclic loading test indicates the occurrence of persistent slip bands at the surface of the specimen (Polak, 1991). The V_H parameter is given by the following equation:-

$$V_H = \frac{W}{4\varepsilon_{ap}\sigma_a} \tag{4.5}$$

where W is the hysteresis loop area, ε_{ap} is the plastic strain amplitude and σ_a is the stress amplitude. Figure 4.9 shows the evolution of loop shape parameter for the P91 steel specimen subjected to the ±0.5% strain-controlled test. At the beginning of the test, the V_H parameter decreases to a local minimum at about the 40th cycle. Then, the parameter increases to a local maximum which is located in the second stage of cyclic softening. Finally, the parameter decreases again in the final period of testing.

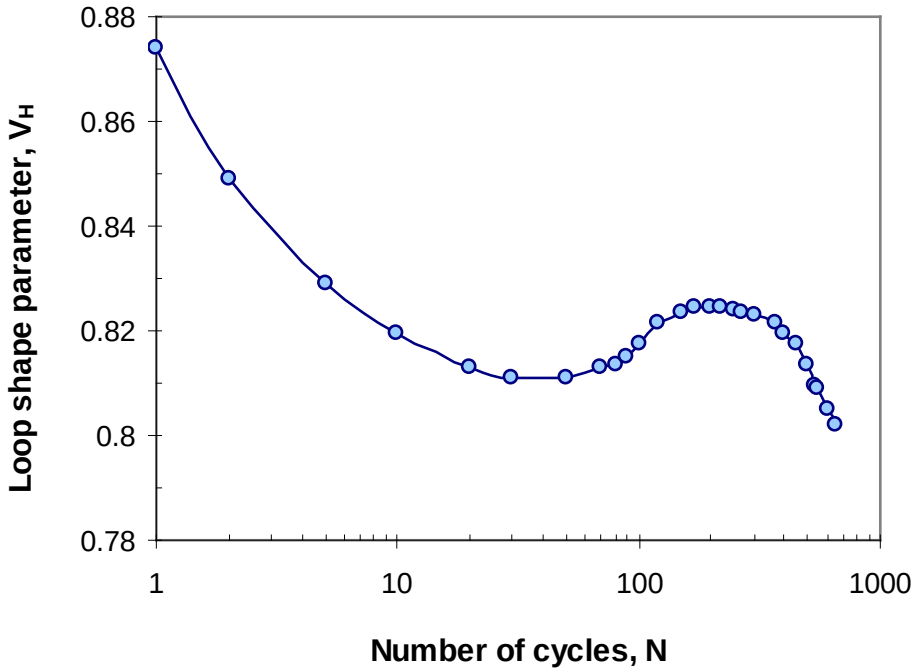

Figure 4.9: Evolution of the loop shape parameter, in the ±0.5% strain-controlled test, at 600°C, for P91 steel

4.3 Fatigue Model

Based on the number of the cycles to failure obtained in the fully-reversed isothermal strain-controlled tests, with 4 different strain amplitudes, a fatigue life model for the P91 steel, at 600°C, based on strain and energy parameters can be developed. In this study, the fatigue models constants were determined using the number of cycles to failure with a 5 percent stress drop failure criterion. The strain and energy parameters are normally taken from the stabilised, or saturated, condition of the cyclic loading tests, in which the peak stress level becomes constant, observed in a strain-controlled condition, for example. However, the plastic strain amplitude and energy parameters for P91 steel do not become constant, but they reach a low magnitude variation instead, in the stabilised period, as shown in Figures 4.2 and 4.8 respectively. Thus, the strain and energy parameters were taken at N_{sta} and $N_{f5/2}$ in order to determine the fatigue model

constants and for comparison purposes of the effect of the point selection in the P91 steel.

4.3.1 Strain-based model

The isothermal strain-controlled tests with 4 different strain amplitudes produced significant cyclic plastic strain and the number of cycles to failure for these tests are within the low cycle fatigue regime. Thus, the plastic strain based of the Coffin-Manson model is suitable for use in representing the failure of the test specimens. The Coffin-Manson equation is given below:-

$$\frac{\Delta\varepsilon_p}{2} = \varepsilon_f'(2N_f)^c \qquad (4.6)$$

where $\Delta\varepsilon_p/2$ is the plastic strain amplitude, $2N_f$ is the number of reversals to failure, ε_f' is the fatigue ductility coefficient and c is the fatigue ductility exponent. Equation 4.6 is based on Suresh (1998). The ε_f' and c constants can be determined by plotting the log (plastic strain amplitude) against log (number of reversals to failure), as shown in Figure 4.10. The ε_f' and c constants for the Coffin-Manson relationship, determined using parameters at N_{sta}, are 0.5241 and -0.6042, respectively, while the same constants, determined using parameters at $N_{f5/2}$, are 0.4896 and -0.5927, respectively. The figure shows that similar linear relationships are obtained for both types of data; the slope of the N_{sta} graph is slightly higher. The difference between the predicted number of cycles to failure up to 50000 cycles, using both sets of fits to the data, is less than 11 percent.

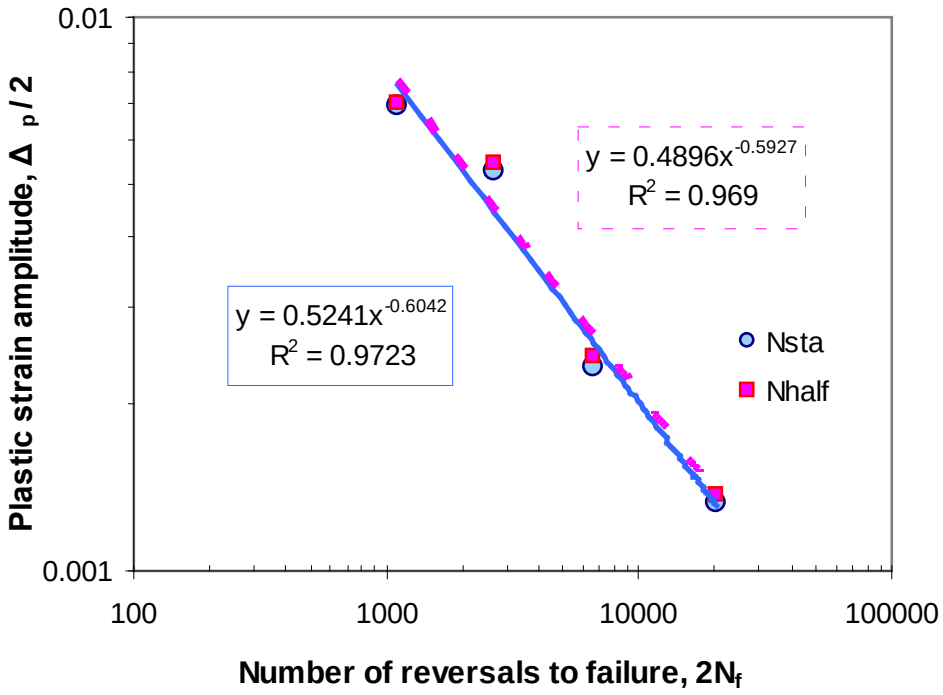

Figure 4.10: Determination of the Coffin-Manson fatigue model constants using the strain-controlled tests data for P91 steel, at 600°C

4.3.2 Energy-based model

The energy based, fatigue model, proposed by Ellyin and Kujawski (1984), is used to relate the plastic strain energy per cycle to the number of cycles to failure, using the following equation, i.e.:-

$$W = KN_f^{\alpha} \qquad (4.7)$$

where W is the plastic strain energy per cycle (or the hysteresis loop area), N_f is the number of cycles to failure and K and α are material constants. The constants can be determined by plotting log (plastic strain energy per cycle) against log (number of cycles to failure), as shown in Figure 4.11. The K and α constants, determined using parameters at N_{sta} are 271.36 and -0.714, respectively, while the corresponding constants, determined using parameters at $N_{f5/2}$, are 229.52 and -0.6907, respectively. Again, both set of data produce very similar graphs and a slightly

higher slope is produced when using the N_{sta} data. The difference between the predicted number of cycles to failure up to 50000 cycles, using both sets of fits to the data, is less than 13 percent.

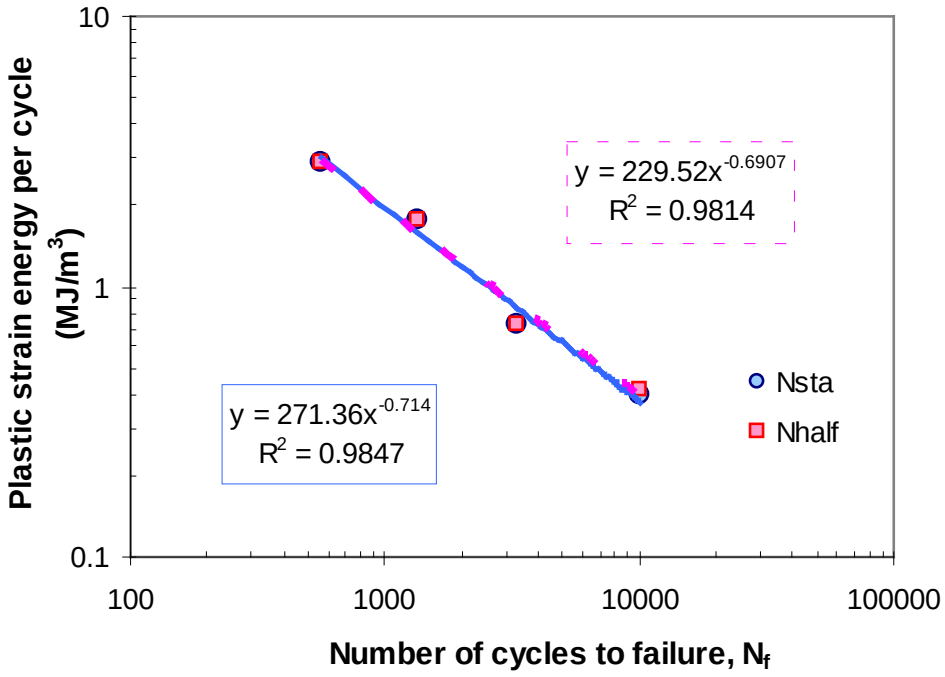

Figure 4.11: Plot of log (plastic strain energy per cycle) versus log (cycles to failure) for the strain-controlled tests of the P91 steel, at 600°C

4.4 Microstructure investigation

The experimental cyclic loading test results obtained from the P91 and P92 steels, at high temperatures, clearly indicate that both materials cyclically soften in three different stages, prior to complete fracture of the specimens. The cyclic softening behaviour is the focus of this section, in which an investigation of the microstructure of the fatigued specimens, at various life fractions, was performed in order to identify the evolution of microstructures and the failure mechanisms. The P91 specimens tested with strain amplitudes of ±0.5%, at 600°C, were used in this study. Four points throughout the lifetime were selected: firstly, the as-received material was analysed, to form the reference point for comparison; secondly, an

interrupted test specimen up to 200 cycles was analysed; thirdly, another specimen was interrupted at 400 cycles and finally a specimen tested to failure was analysed. The microstructures were observed, using a scanning electron microscope (SEM) and a transmission electron microscope (TEM).

4.4.1 Scanning electron microscopy

The Philips/FEI XL-30 scanning electron microscope (SEM) was used in this work. An accelerating voltage of 20kV and a working distance of 10mm were set to investigate the microstructure of the P91 specimen tested at ±0.5% strain amplitude. The SEM specimens were taken from the longitudinal direction of specimen's gauge section. The samples were then mounted with conductive phenolic mounting resin. The surfaces of the samples were ground and polished by using a rotary grinding machine, with silicon carbide paper, and diamond cloth, down to a 1μm finish. The samples were then further polished using colloidal silica, in order to remove the residual surface damage induced by the diamond cloth polishing. Finally, acidic ferric chloride was used as the chemical etchant to reveal the microstructural features of the material.

4.4.2 Transmission electron microscopy

An investigation, using a transmission electron microscope (TEM), was carried to observe the microstructural features at higher magnifications, looking in particular, for martensite lath structures, which cannot be clearly observed by SEM. The JEOL 2000FX transmission electron microscope at 200 kV was used in the examination of the steel. TEM investigations require an extremely thin specimen in order to allow the electrons to pass through it and to create the TEM images.

The thin foils specimen used in this work was taken from the P91 specimen, perpendicular to loading axis. A 2 mm thin slice was cut from the gauge section and it was ground down to approximately 100µm thick using silicon carbide paper. Then, the thin foil was punched into a 3 mm diameter disc using a mechanical puncher. The disc was further polished down to a thickness of approximately 50µm. Finally, the disc was thinned using dual jet electropolishing, at -10°C, in an electrolyte made up of 10% perchloric acid and 90% ethanol.

4.4.3 The microstructure investigation results

Figures 4.12 to 4.18 show the microstructure images of the SEM investigation on the P91 specimen. The as-received P91 steel has a lath martensite structure as shown in Figure 4.12 (a) and (b), in which the grain boundary size is approximately 15µm. There are smaller structures inside the grain boundary which can be related to packet, block and lath structure as represented schematically in Figure 4.12 (c). The microstructure of the steel, after 200th cycles, is shown in Figure 4.13, where a similar microstructure to that of the as-received specimen was observed. It is difficult to differentiate any microstructure changes using the SEM at this cycle range. As the cycle number increases further to the 400th cycle, microcracks of 10 to 30 µm length, which initiated at the specimen's surface, were observed at two locations as shown in Figure 4.14 (a) and (b). Transgranular cracks were observed at many locations near the final fracture surface specimen, as shown in Figure 4.15. Furthermore, branching of transgranular cracks was observed for the cracks with lengths longer than 100 µm, as shown in Figure 4.15 (b).

The microstructures at failure of a strain-controlled test specimen with a 2 minutes hold period cycles were also investigated and the results are shown in Figures 4.16 to 4.18. The cyclic loading dwell test was stopped before total fracture of the

specimen occurred, but one major crack can be clearly seen in Figure 4.16. Many cracks were initiated from the specimen's surface, and one major crack (the longest crack found in the specimen) can be observed in the centre of this figure. The major crack is about 1 mm in length. Interestingly, microcracks were observed in the middle of the specimen, as shown in Figure 4.17, but these were not found in the test specimen without the hold period. Figure 4.18 shows a close-up found in the major cracks of the P91 dwell specimen; there were cracks which were found to grow around the grain boundaries. This may indicate the interaction of the creep and fatigue effects in the crack propagation stage.

Figures 4.19 (a) to 4.19 (d) show the bright field TEM images at high magnification, after various life fractions produced in the interrupted cyclic loading test of P91 steel. The martensite lath, or the subgrain structures, can be clearly observed using the transmission electron microscope. For the as-received P91 specimen (zero cycle), the width of the subgrain are inconsistent, as shown in Figure 4.19 (a), and small subgrains were observed as highlighted by the dotted line. As the cycle number increases, the small subgrains become harder to observe in the TEM images, as can be seen in Figures 4.19 (b) to 4.19 (d). Also, the subgrains, or lath martensite structures, seem to have a longer structure than does the as-received subgrain structure. The average of the subgrain width or the subgrain size can be determined by the line intersection technique as the average of subgrain intercept lengths measured from the TEM images (Dubey et al., 2005). Based on the bright field TEM images, the subgrain sizes for Figures 4.19 (a) to 4.19 (d) are 0.383, 0.507, 0.551 and 0.604 µm, respectively. The subgrain size of 200th cycle specimen increases by about 32 percent from the size of the as-received specimen. Then, the subgrain sizes increase gradually up to fracture. From these results, there is a clear trend of subgrain coarsening as the number of cycles increase.

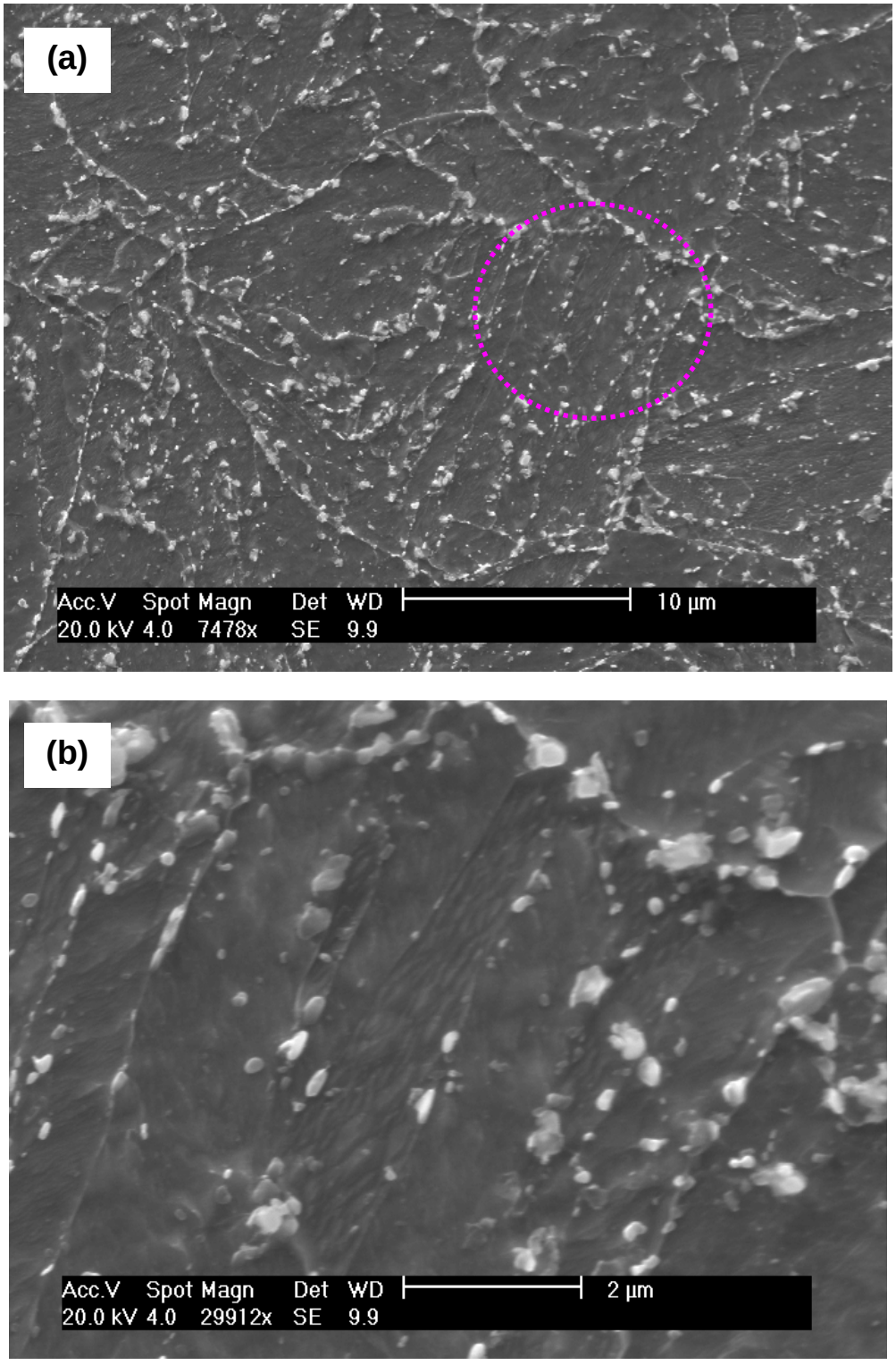

Figure 4.12: Microstructure of the as-received P91 steel showing (a) the lath martensite structure, (b) the microstructure at higher magnification for the dotted circle in (a), and (c) the schematic structure (Kitahara et al, 2006)

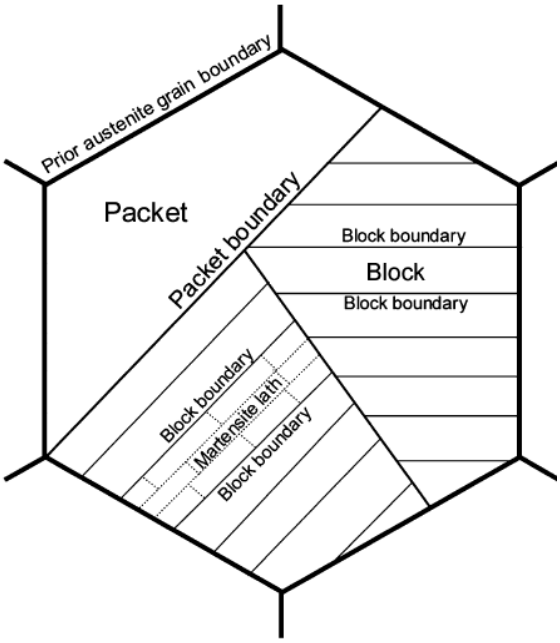

Figure 4.12: Microstructure of the as-received P91 steel showing (a) the lath martensite structure, (b) the microstructure at higher magnification for the dotted circle in (a), and (c) the schematic structure (Kitahara et al, 2006) (cont.)

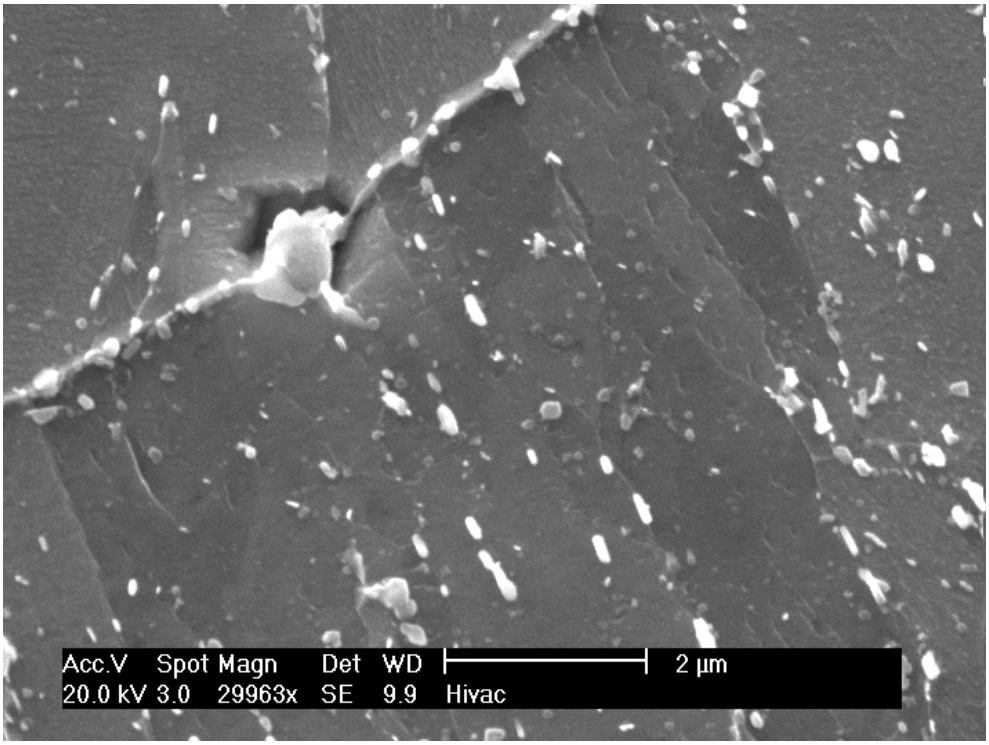

Figure 4.13: Microstructure of the P91 steel after a strain-controlled cyclic test for 200 cycles at 600°C

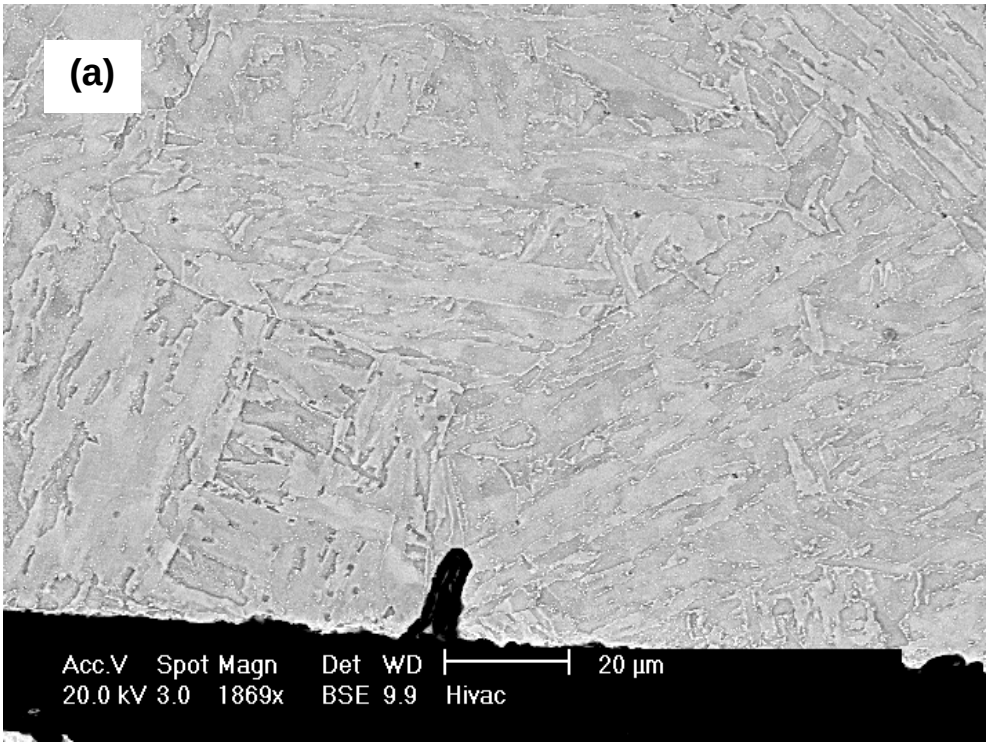

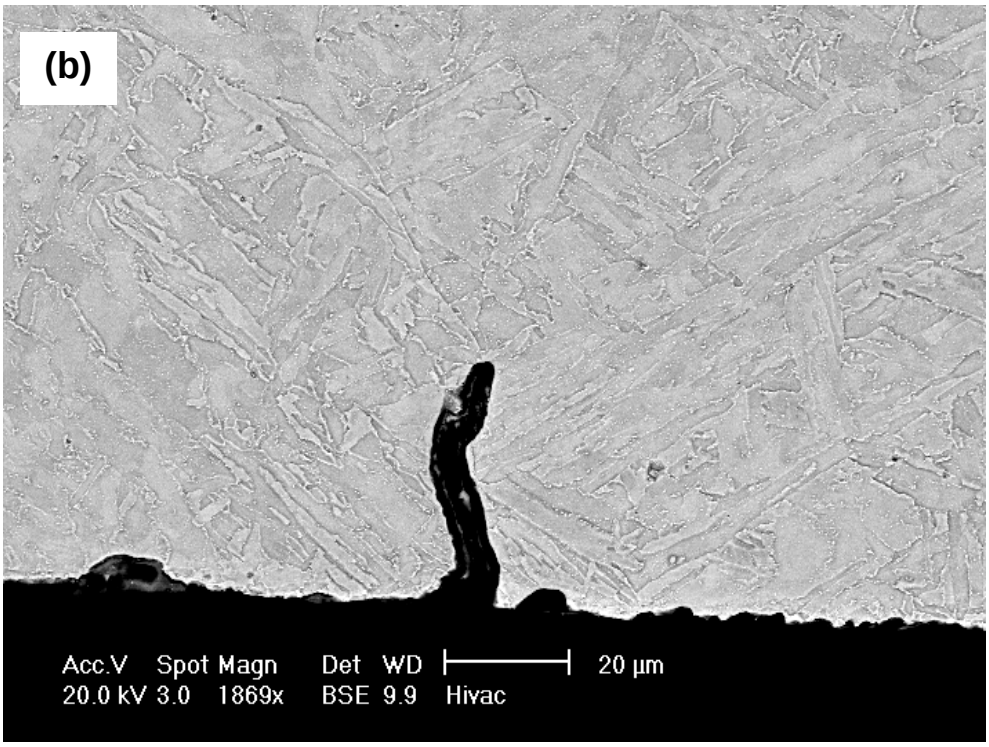

Figure 4.14: Microcracks observed in the surface of the P91 specimen after 400th cycles of cyclic loading, at 600°C, at two different locations, (a) and (b)

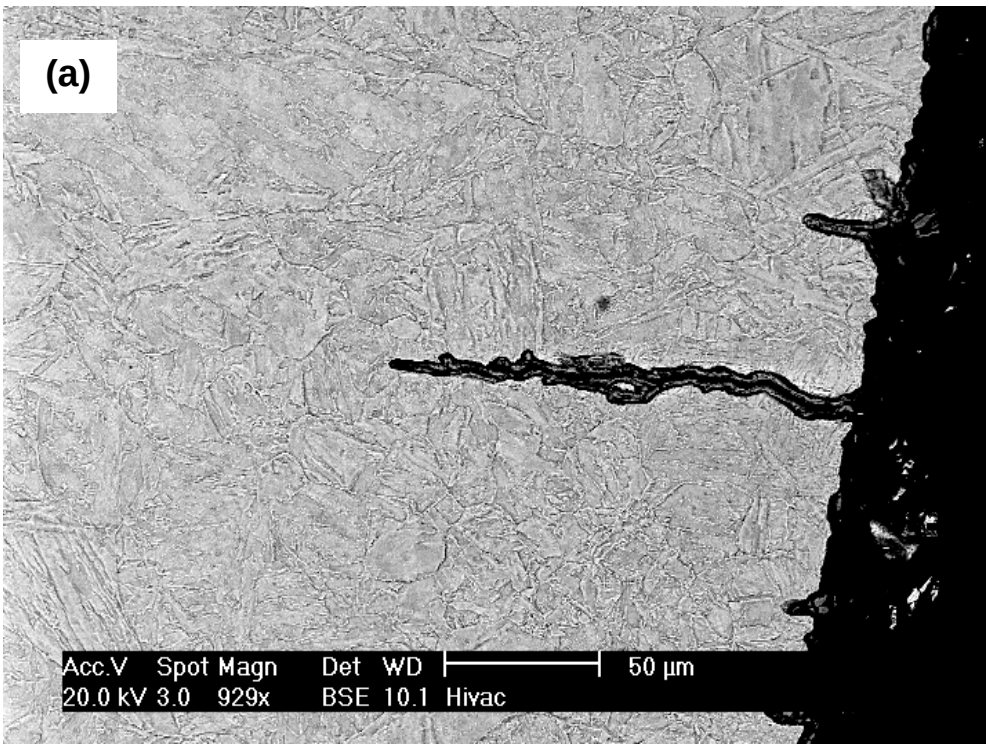

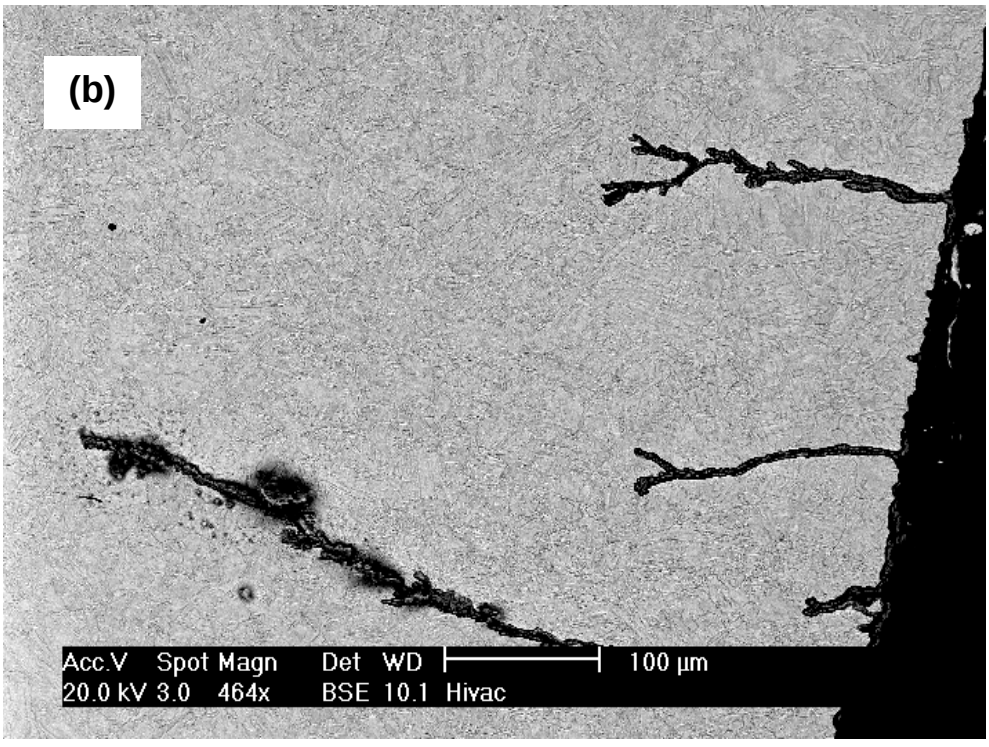

Figure 4.15: Cracks observed in the P91 fractured specimen showing (a) shorter cracks and (b) longer cracks with crack branching

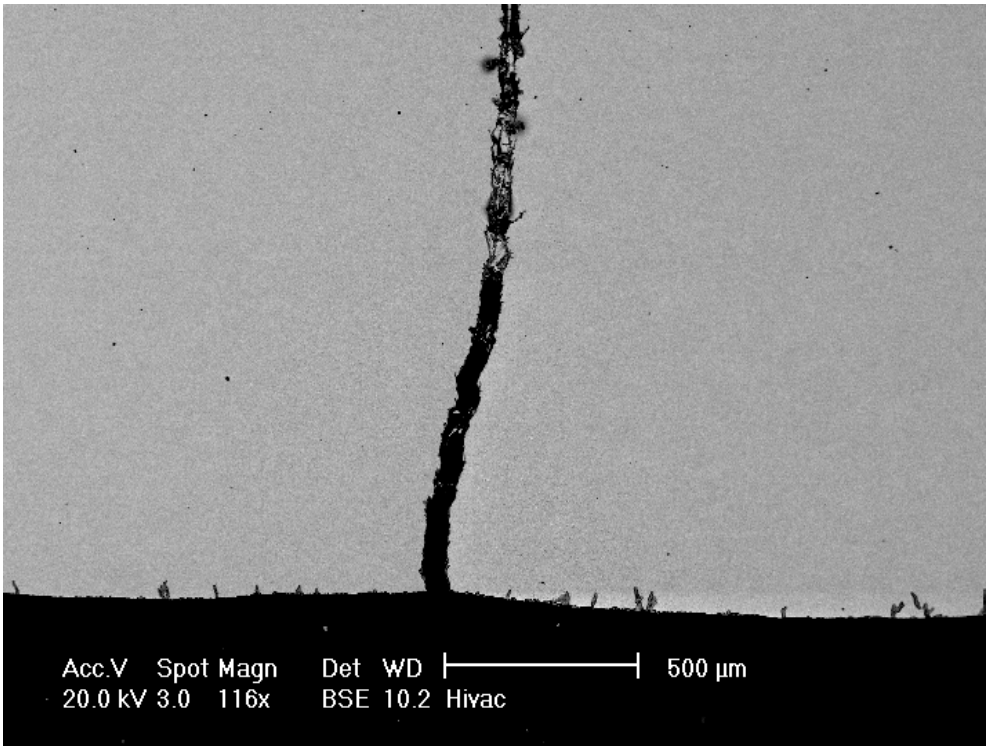

Figure 4.16: Cracks observed in the P91 steel after cyclic loading with 2 minutes dwell periods at the final recorded cycles

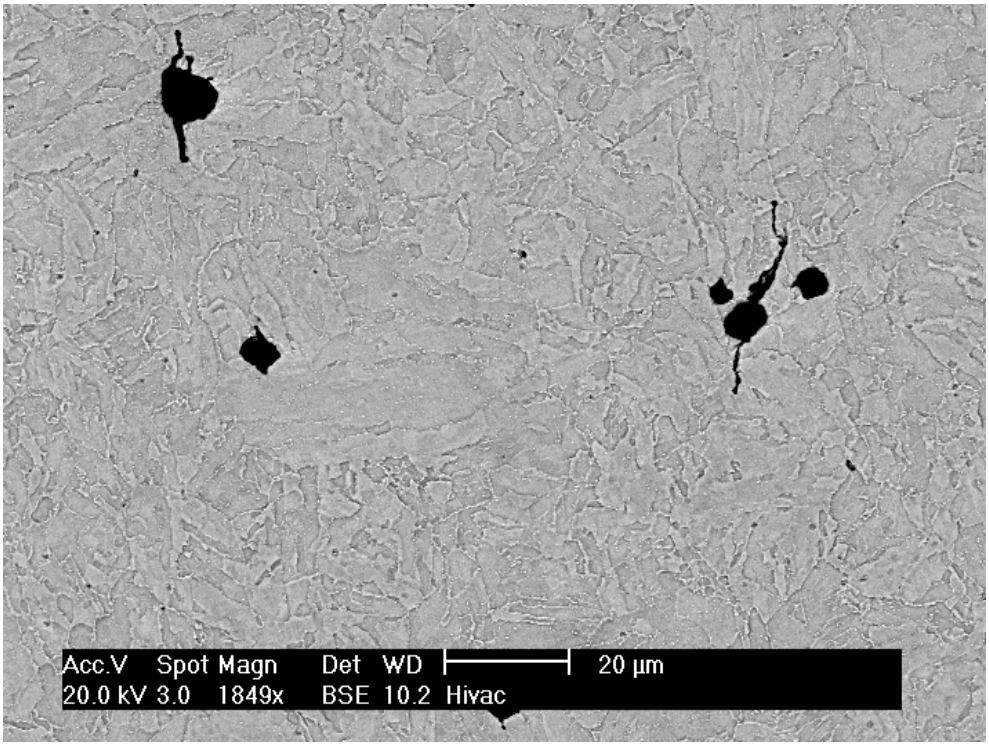

Figure 4.17: Microcracks observed in the middle of the P91 specimen with 2 minutes dwell periods at the final recorded cycles

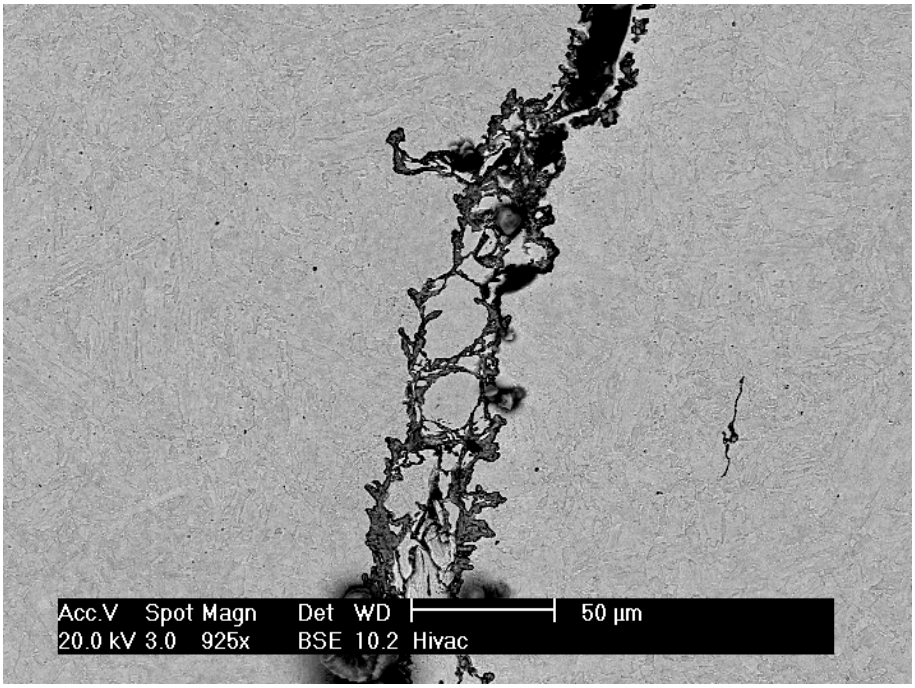

Figure 4.18: A mixture of transgranular and intergranular cracking observed on the major cracks of the P91 specimen with 2 minutes dwell periods

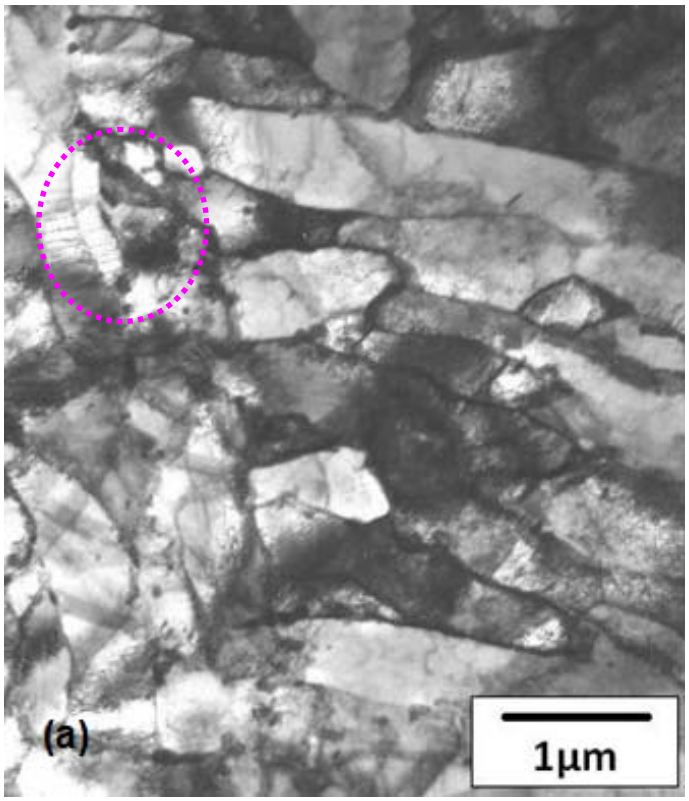

Figure 4.19: Bright field TEM images for (a) the as-received material, and the subgrain evolution which occurs in ±0.5% strain-controlled test after (b) the 200th cycle, (c) the 400th cycle and (d) the 656th cycle

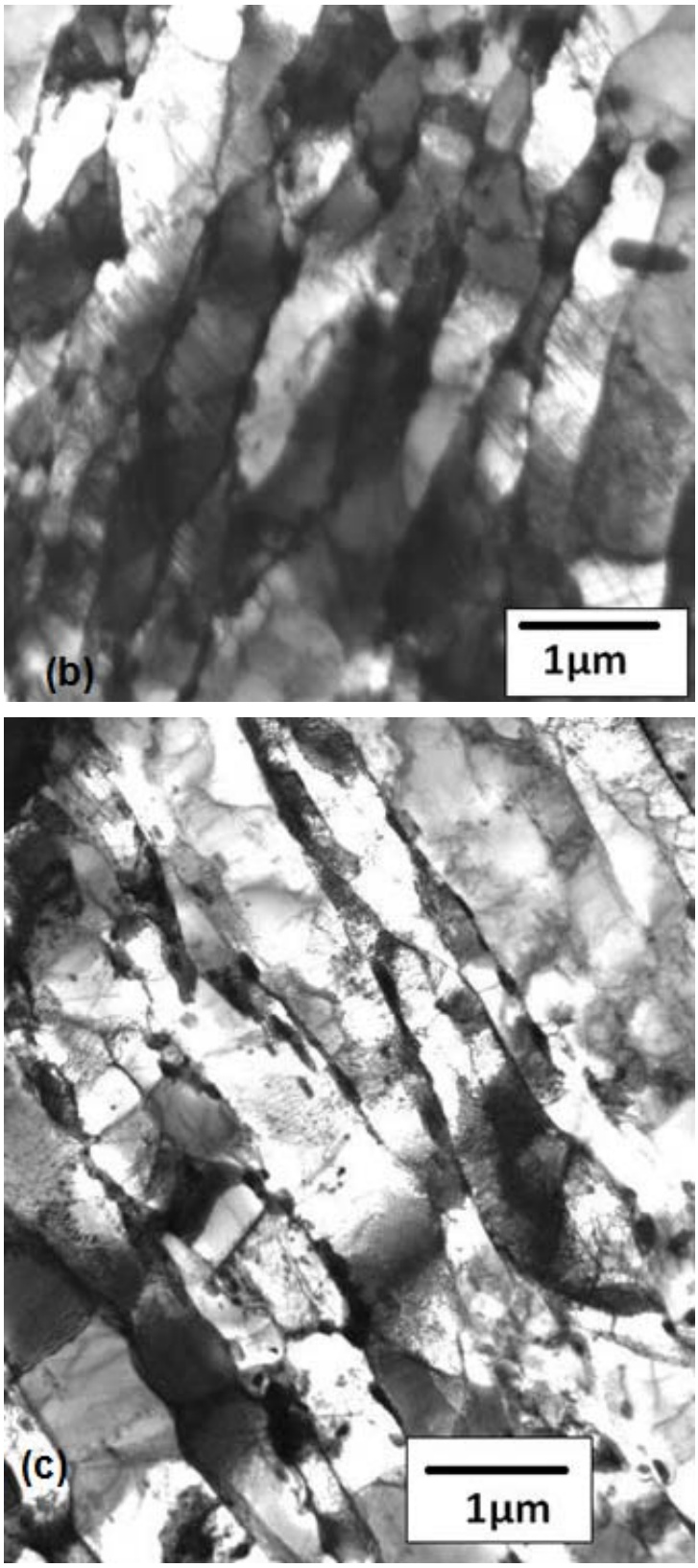

Figure 4.19: Bright field TEM images for (a) the as-received material, and the subgrain evolution which occurs in ±0.5% strain-controlled test after (b) the 200th cycle, (c) the 400th cycle and (d) 656th cycle

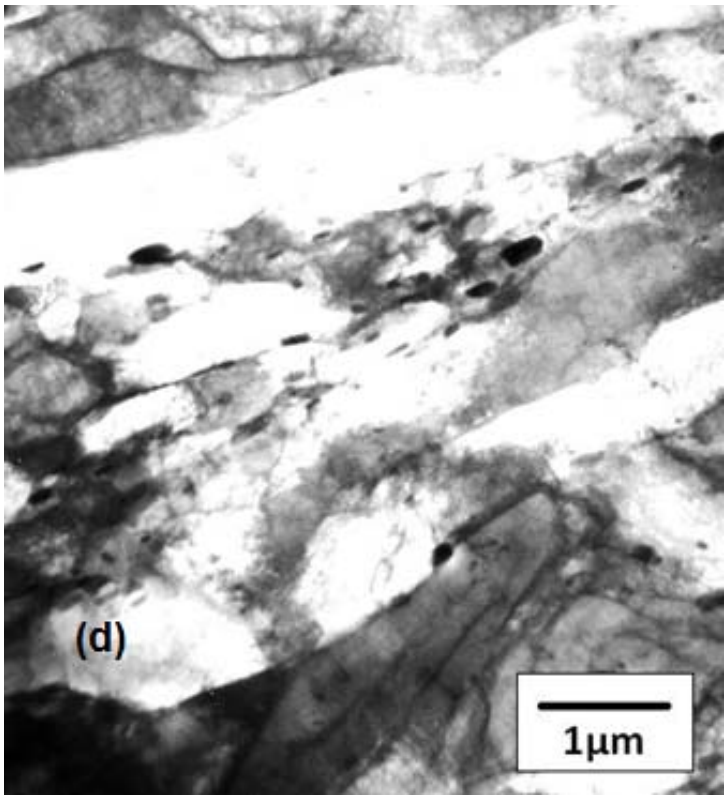

Figure 4.19: Bright field TEM images for (a) the as-received material, and the subgrain evolution which occurs in ±0.5% strain-controlled test after (b) the 200th cycle, (c) the 400th cycle and (d) 656th cycle

4.5 Discussions on the cyclic softening mechanisms

The P91 steel exhibits cyclic softening throughout the test, with three distinct stages. Mechanical parameters such as the peak stress level and the plastic strain range continued to evolve throughout the strain-controlled test and these parameters can be related to microstructure evolution. In this section, the relationship between the results of the microstructure investigation of interrupted tests and the analysis of the experimental stress-strain data with ±0.5% strain amplitude, at 600°C, are discussed.

The microstructure of the P91 steel consists of small subgrain sizes and high dislocation densities prior to the starting of the cyclic loading test. The steel has

been manufactured with these features included as parts of the strengthening mechanisms of the steel; these act as obstacles to plastic deformation (Abe, 2008). During the first stage of the cyclic softening of the steel, the peak stress level and the plastic strain range vary significantly. Also, in this stage, the microstructure evolution has occurred, particularly in the martensite lath, or subgrain, structure, without affecting the strength of the specimen, as indicated by the Young's modulus values. The results of the TEM investigation show rapid subgrain coarsening during this stage. At the same time, the dislocation density also decreases due to cyclic deformation, as reported by Fournier et al. (2009b) for a similar material, at high temperature. The subgrain coarsening is attributed to the annihilation of low angle boundaries, as explained by Sauzay et al. (2005). The author reports that the misorientation angles between laths (or subgrains) are low (smaller than 5°) and that they can be modelled as dislocation arrays. During plastic deformation, mobile dislocations move towards low angle boundaries of opposite signs and the interactions between the opposite signs of dislocations cause the dislocations to be annihilated. As the cycle number continues to increase the dislocations inside the subgrains decrease and finally contribute to the disappearance of the low angle boundaries. Consequently, the subgrain size coarsens and the density of the dislocations decreases, which means that there is a reduction of the number of obstacles to plastic deformation. Thus, lower stresses are required to achieve a certain deformation, as shown by the rapid decrease of the peak stress levels.

In the second stage of cyclic softening, the peak stresses and the plastic strain ranges slowly and steadily change with an almost constant rate of peak stress reduction. The subgrain structures, between the 200^{th} and the 400^{th} cycles, also show a slight increase in the subgrain size, which may indicate a slow rate for the annihilation process. The stabilisation of the cyclic stress-strain response may

indicate the formation of persistence slip bands (PSBs) (Kruml and Polak, 2001). Based on Figure 4.9, the loop shape parameter reaches global maximum at some point between the 200th and the 300th cycle, which corresponds to the formation of a microstructure with PSBs (Petrenec et al., 2011). In this stage, microcracks initiate without affecting the strength of the specimen, as the size of cracks are small, as shown by the SEM results at the 400th cycle.

During the third and final stage of cyclic softening there is a nonlinear decrease of the peak stress level. In this period, the plastic strain range and the subgrain size have slightly increased. However, it is clear that during this stage the microcracks, which were observed at the end of the second stage, continue to propagate. The SEM images of failed specimens show transgranular cracking with crack branching. Similar crack observations have been found by Nagesha et al. (2002) for the modified 9Cr-1Mo steel, at the same temperature. The authors relate the branching of the transgranular cracks to the high strain amplitudes of testing. As the size of cracks becomes larger, they affect the Young's modulus value of the material, leading to a reduction of modulus value. This can be attributed to a degradation of strength of the material, as shown by the evolution of damage, D, in Figure 4.5. As the material becomes weaker, lower stresses are required to achieve the targeted strains in the cyclic testing specimens.

4.6 Conclusions

The following conclusions can be drawn from the analysis of the stress-strain data and the microstructure investigation:-

- Three distinct stages of cyclic softening have been identified from the full cycle data of the P91 cyclic tests.

- The cumulative energy parameters obtained for the cyclic tests with different strain amplitudes were found to be similar at the beginning of the stabilisation stage of cyclic softening.
- The coarsening of the subgrains occurs rapidly in the first stage of cyclic softening but slows down in the second and third stages.
- The nonlinear decrease of the peak stress level in the first stage is due to a reduction of the number of obstacles to plastic deformation, as a result of subgrain coarsening.
- The cyclic mechanical parameters become stabilised in the second stage of cyclic softening. Also, the initiation of cracks begins in this stage. The changes of structure, on a micro-scale, do not significantly affect the strength of the specimen, as the Young's modulus values of the specimen remain approximately constant up to the end of the stage 2 cyclic softening.
- The nonlinear decrease of the peak stress level, which occurs in the third stage, is due to crack propagation. The cracks cause the material to become weaker, as indicated by the decrease of Young's modulus value.
- Transgranular cracks were found in the fractured specimen of the strain-controlled test of ±0.5% strain amplitude, with a 0.1%/s strain rate. This indicates that the strain rate used in this test can produce purely fatigue condition.
- The introduction of a 2 minutes hold period, in the tension-compression test, produces a mixture of transgranular and intergranular type of cracks, indicating a creep-fatigue interaction effect.

Chapter 5 - Viscoplasticity model development

5.1 Overview

This chapter presents the development of the material constitutive models for P91 and P92 steels, under cyclic loading conditions, at high temperature. The results of the isothermal, strain-controlled, tests are presented in Chapter 3; these show the cyclic softening and stress relaxation behaviour which occurs in the steels. The results in Chapter 3 are used extensively in this chapter in order to develop the material models. A viscoplasticity model has been selected to represent the cyclic plasticity and the time dependent behaviour of the materials. The material constants were initially determined by using a step by step procedure and then the constants were improved by using an optimisation program developed in Matlab in order to obtain better stress-strain predictions. In the end, the model was further improved by modifying it to include linear cyclic softening predictions resulting in better stress evolution predictions up to the end of the secondary stage of cyclic softening.

5.2 The viscoplasticity model

The Chaboche, unified, viscoplasticity model was chosen to model the cyclic behaviour of the P91 and P92 steels. The model is a time-dependent plasticity model which includes the effects of isotropic and kinematic hardening as well as the rate dependency effects associated with creep. The model is called a unified viscoplasticity model for two reasons: there is no partitioning of the inelastic strain into plastic and creep strain components; and the hardening rules, which are isotropic and kinematic hardening, are chosen to be similar to the time-independent case (Chaboche, 1989). The inelastic strain is also called a viscoplastic strain; however the former term is used in this study.

The inelastic strain rate, $\dot{\varepsilon}_p$, of the model are given by the following equations:-

$$\dot{\varepsilon}_p = \left\langle \frac{f}{Z} \right\rangle^n \operatorname{sgn}(\sigma - \chi) \tag{5.1}$$

$$\operatorname{sgn}(x) = \begin{cases} 1, & x > 0 \\ 0, & x = 0 \\ -1, & x < 0 \end{cases} \text{ and } \langle x \rangle = \begin{cases} x, & x > 0 \\ 0, & x \le 0 \end{cases} \tag{5.2}$$

$$f = |\sigma - \chi| - R - k \tag{5.3}$$

where Z and n are material constants; σ is the applied stress; f is the yield function; k is the initial cyclic yield stress, also known as the initial elastic limit, representing the initial size of the yield surface in a deviatoric plane; χ is the kinematic hardening parameter, also known as the back stress; and R is the isotropic hardening parameter, also known as the drag stress (Chaboche and Rousselier, 1983).

The kinematic hardening model is used to express the behaviour of non-proportional monotonic or cyclic loadings (Chaboche, 2008). In a deviatoric stress plane, the kinematic hardening represents a translation of yield surface. Its behaviour is described by the following equation:-

$$\dot{\chi}_i = C_i(a_i \dot{\varepsilon}_p - \chi_i \dot{p}) \tag{5.4}$$

$$\chi = \sum_{i=1}^{M} \chi_i \tag{5.5}$$

where i=1,2,…,M ; p is the accumulated inelastic strain; a_i and C_i represent the stationary values of χ_i and the speed to reach the stationary values, respectively. The use of more than one back stress (Equation 5.4) allows a better description of a the nonlinear behaviour of a material. In this study, it has been chosen that M = 2 which gives the total back stress as follows:-

$$\chi = \chi_1 + \chi_2 \tag{5.6}$$

As the number of cycles increase in a cyclic loading condition, a material may harden or soften with respect to the plastic flow, often as a function of accumulated inelastic strain. This behaviour is represented by an expansion or contraction of the yield surface in the deviatoric stress plane. It is referred to as isotropic hardening due to the fact that it changes uniformly in all directions, in the stress space (Dunne and Petrinic, 2005) and is described by the following equation:-

$$\dot{R} = b(Q - R)\dot{p} \tag{5.7}$$

where Q is the asymptotic value of the isotropic variable, R, at the stabilized cyclic condition and b governs the stabilization speed.

In the combined isotropic and kinematic hardening of a plasticity model, the applied stress consists of yield stress, drag stress and back stress. Plastic flow occurs when the yield function is equal to zero. For the viscoplasticity model, the plastic yield limit is no longer applied and the load point may lie outside the yield surface. This specific behaviour for the model is represented by a viscous stress, σ_v, as follows:-

$$\sigma_v = Z\dot{p}^{1/n} \tag{5. 8}$$

Thus, the applied stress can be decomposed as:-

$$\sigma = \chi + (R + k + \sigma_v)\mathrm{sgn}(\sigma - \chi) = E(\varepsilon - \varepsilon_p) \tag{5.9}$$

The equations described above are in the uniaxial form of the viscoplasticity model which consists of ten temperature dependent material properties, namely E, k, Q, b, a_1, C_1, a_2, C_2, Z and n. A description of how the constants are determined is given in the next section, using a step by step procedure and an optimisation approach. Also, the viscoplasticity model, in the uniaxial form, has been implemented in a

Microsoft Excel spreadsheet in order to calculate the stress-strain relationship for the steels in tension-compression loading.

5.3 The initial constants of the viscoplasticity model

A step by step procedure (Zhan, 2004) was implemented in estimating the initial values of the constants for the viscoplasticity model. From the isothermal test data, the test results such as stress-strain data from the first cycle, the evolution of the maximum stress against the number of cycles in a tension-compression test and the stress relaxation data from a dwell test were used in determining these constants. Several assumptions were made during the calculations in order to simplify the equations involved.

5.3.1 Identification of initial yield stress and Young's modulus

Young's modulus, E, was identified from the slope of linear region in the first quarter cycle of the experiment, as shown in Figure 5.1. Generally, the first point to deviate from the linear region is considered to be the yield stress. For instance, the stress at that point for P91 steel at 600, as shown in Figure 5.1, is around 200MPa. However, the typical yield stress definition cannot be used in the viscoplasticity model because the yield stress value is higher than an applied stress in a creep test which produces creep strain. As mentioned earlier, the model represents plastic and creep strain in one parameter namely the inelastic strain.

Several creep tests were initially performed using uniform ridged specimens of the same P91 parent material at 600°C, with constant applied loads, between 140 and 180 MPa. The test with the lowest applied stress (140MPa) produced creep straining and failed at 1454 hours. From Figure 5.1, the stress level of 140MPa was located on the linear line of the first tensile data from the beginning. Thus, a lower

yield stress value than the conventional yield stress definition will be used in this study. The initial cyclic yield stress, k, value was estimated as suggested by Zhan (2004) and as shown in Figure 5.1.

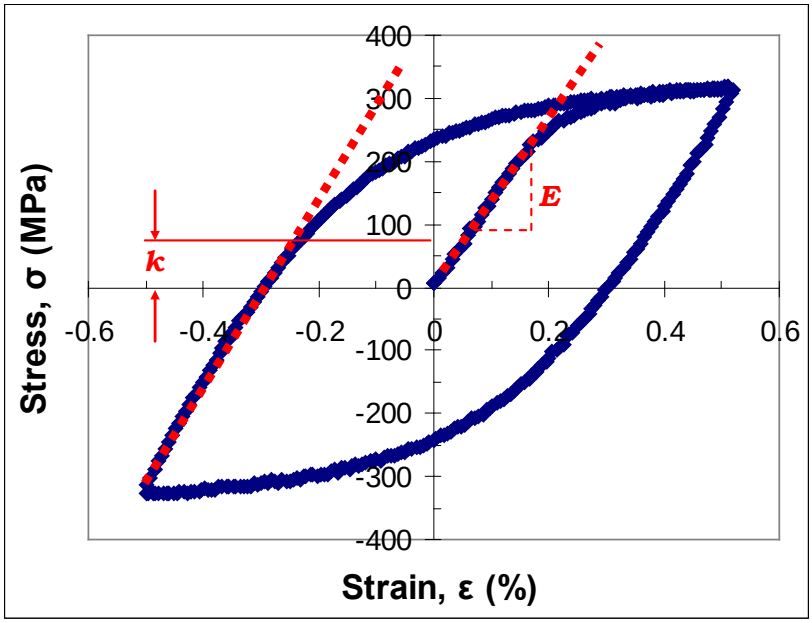

Figure 5.1: Example plot for obtaining Young's modulus, E, and estimation of initial cyclic yield stress, k, for the P91 parent material at 600˚C

5.3.2 Identification of isotropic hardening parameters

The evolution of the stress range against number of cycles data obtained from a tension-compression test was used in the determination of the isotropic hardening parameters. All of the test results showed cyclic softening behaviour, in which the stress range decreases as the number of cycles increase, with three different stages. Normally, parameters Q and b are determined by using stress values at a stabilized period in a test where the stress range values become constant. However, before achieving the constant stress values in the P91 and P92 tests, the material continued to cyclically soften which may be due to material damage, as shown by the test data in Figure 5.2. Thus, the stabilized period was assumed to be that at the point at which half of the failure life cycles was produced.

Equation (5.7) can be integrated to give the evolution of isotropic hardening as:-

$$R = Q(1 - e^{-bp}) \tag{5.10}$$

The value of R at a certain number of cycles was taken to be the difference between the maximum stress at that cycle and the maximum stress at the first cycle. Also, the constant Q was taken to be the maximum stress difference between the first and stabilized cycles, which gives a negative value for Q. The parameter p is approximately two times the plastic strain range data for each cycle and its value accumulates as cycles increase. Then, constant b was determined by fitting equation (5.10) to the test data as shown in Figure 5.2.

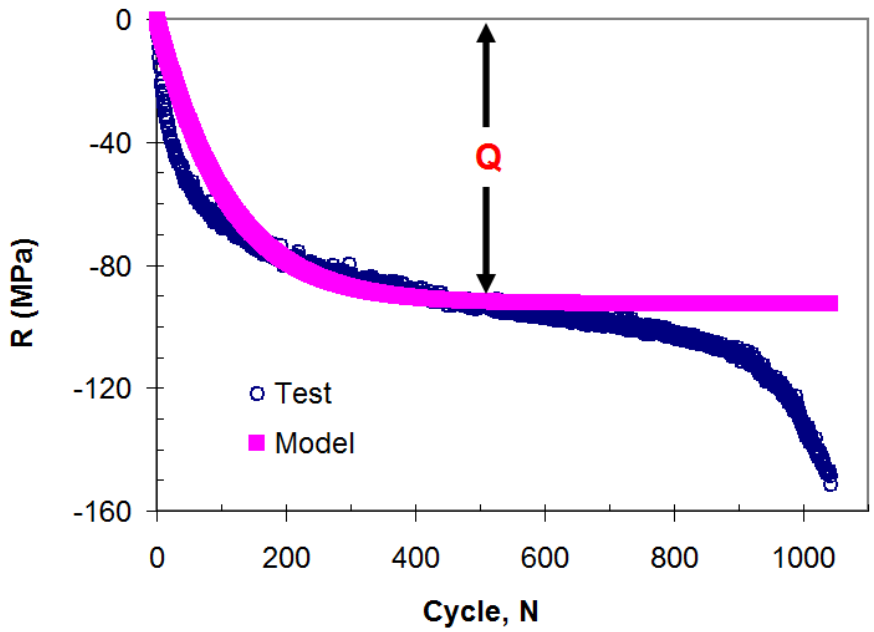

Figure 5.2: Determination of isotropic hardening parameters Q and b for the P92 parent material at 600˚C

5.3.3 Identification of kinematic hardening parameters

Kinematic hardening constants a_1, C_1, a_2 and C_2 were determined using the first-quarter of the first cycle from the tension-compression strain-controlled tests. The non-proportional hardening data of the tensile curve were generally divided into two

regions, as shown in Figure 5.3, to represent firstly the transient region of the inelastic deformation, where χ_1 becomes the dominant inelasticity contribution, and secondly the region with greater inelastic strain in which χ_2 is the dominant parameter.

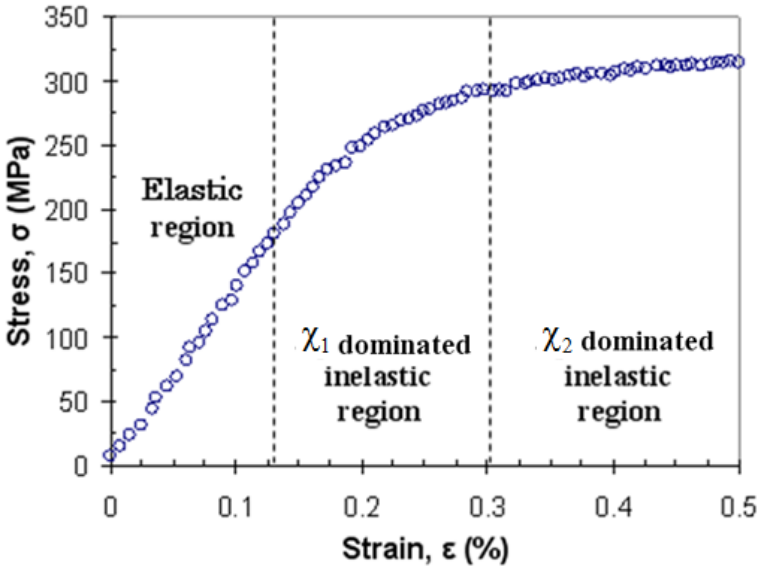

Figure 5.3: Partition of the first quarter of the first cyclic loop for the strain-controlled test data into an elastic region followed by an inelastic region with χ_1 and χ_2 dominated region

Equation (5.4) can be integrated with respect to time to give the following equations:-

$$\chi_1 = a_1(1 - e^{-C_1 p}) \tag{5.11}$$

$$\chi_2 = a_2(1 - e^{-C_2 p}) \tag{5.12}$$

in which $p = \varepsilon_p$ in the first tensile curve data. Equations (5.11) and (5.12) can be substituted into equation (5.9) to give:-

$$\sigma = a_1(1 - e^{-C_1 \varepsilon_p}) + a_2(1 - e^{-C_2 \varepsilon_p}) + R + k + \sigma_v \tag{5.13}$$

Differentiating equation (5.13), with respect to ε_p, by assuming that χ_1 has a negligible effect on the hardening of χ_2 and that k and σ_v are not dependent on ε_p, gives:-

$$\frac{\partial \sigma}{\partial \varepsilon_p} - \frac{\partial R}{\partial \varepsilon_p} = a_2 C_2 e^{-C_2 \varepsilon_p} \tag{5.14}$$

Thus, plotting $\ln[(\partial\sigma/\partial\varepsilon_p) - (\partial R/\partial\varepsilon_p)]$ versus ε_p using data from χ_2 dominated inelastic region, as shown in Figure 5.4, allows the identification of C_2 from the gradient and a_2 from the y-axis intercept. In order to plot Figure 5.4, $\partial\sigma/\partial\varepsilon_p$ and $\partial R/\partial\varepsilon_p$ must be determined first as explained by Hyde (2010).

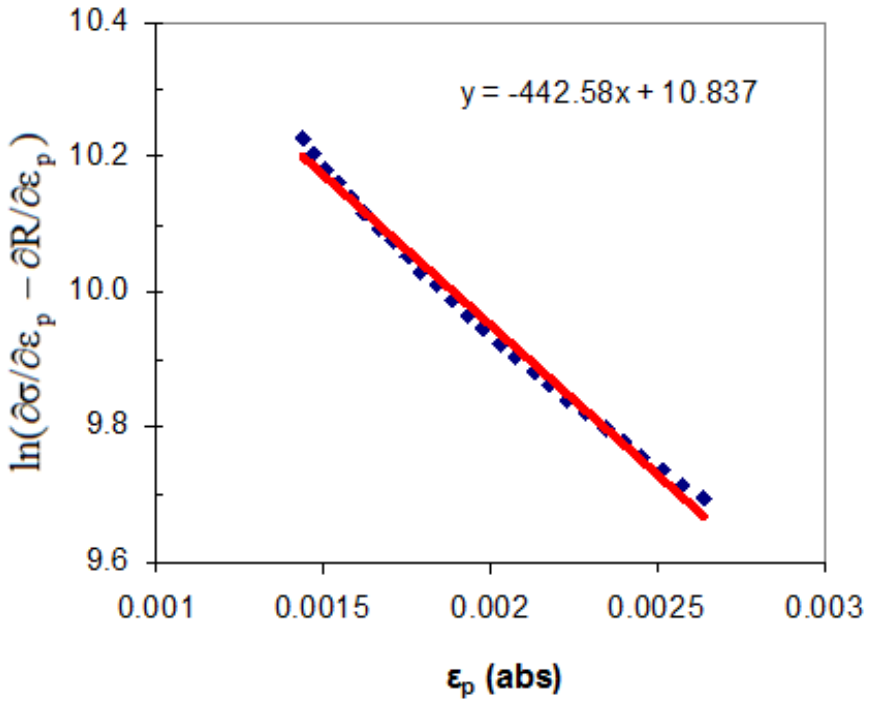

Figure 5.4: Determination of kinematic hardening constants a_2 and C_2 for P92 parent material at 600˚C

$\partial R/\partial \varepsilon_p$ can be calculated based on Equation 5.10. The accumulated inelastic strain, p, parameter in the equation can be substituted with ε_p ($p = \varepsilon_p$ in the first quarter cycle) and the equation can be differentiated with respect to ε_p to give:-

$$\frac{\partial R}{\partial \varepsilon_p} = bQ.e^{-b\varepsilon_p} \tag{5.15}$$

Rearranging $\frac{d\sigma}{d\varepsilon_p}$ by multiplying with $\frac{dt}{dt}$ and $\frac{d\varepsilon}{d\varepsilon}$ gives the following equation:-

$$\frac{d\sigma}{d\varepsilon_p} = \frac{d\sigma}{d\varepsilon}.\frac{1}{\dot{\varepsilon}_p}.\dot{\varepsilon} \tag{5.16}$$

Based on equation (5.16), $\frac{d\sigma}{d\varepsilon}$ and $\dot{\varepsilon}_p$ need to be calculated while the $\dot{\varepsilon}$ value is the controlled parameter in the tension-compression test.

In the current model with isothermal application, total strain, ε, is represented by the following equation:-

$$\varepsilon = \varepsilon_e + \varepsilon_p \tag{5.17}$$

in which the elastic strain, ε_e, is equal to $\frac{\sigma}{E}$. The inelastic strain rate, $\dot{\varepsilon}_p$, can thus be calculated based on equation (5.17) as following:-

$$\dot{\varepsilon}_p = \dot{\varepsilon}\left(1 - \frac{1}{E}\frac{d\sigma}{d\varepsilon}\right) \tag{5.18}$$

The value of $\frac{d\sigma}{d\varepsilon}$ in equation (5.16) and (5.18) can be calculated using experimental data; however, the scatter in the data causes a very poor accuracy for the derivative curve (Zhan, 2004).

In order to avoid the problem mentioned above, the Ramberg-Osgood equation was used as a smoothening function as given below:-

$$\frac{\varepsilon}{\varepsilon_0} = \frac{\sigma}{\sigma_0} + \left(\frac{\sigma}{\sigma_0}\right)^{n_0} \tag{5.19}$$

where $\varepsilon_0 = \sigma_0/E$, σ_0 and ε_0 are reference stress and strain, respectively, and n_0 is the hardening exponent. Equation (5.19) can be rearranged, in order to determine the Ramberg-Osgood constants, as given by the following equation:-

$$\log(E\varepsilon - \sigma) = n_0 \log\sigma + (1 - n_0)\log\sigma_0 \tag{5.20}$$

Thus, plotting $\log(E\varepsilon - \sigma)$ versus $\log(\sigma)$ using experimental data, as shown in Figure 5.5, allows the identification of n_0 from the gradient and σ_0 from the y-axis intercept. For example, the ε_0, σ_0 and n_0 constants to represent the tensile curve of the P92 parent material at 600°C are 0.24 %, 350MPa and 8.3, respectively. Equation (5.19) can again, be differentiated with respect to ε to give the following equations:-

$$\frac{d\sigma}{d\varepsilon} = \frac{\sigma_0}{\varepsilon_0\left(1 + n_0\left(\frac{\sigma}{\sigma_0}\right)^{n_0 - 1}\right)} \tag{5.21}$$

By using equation (5.21) and the Ramberg-Osgood equation constants, $\frac{d\sigma}{d\varepsilon_p}$ can be determined.

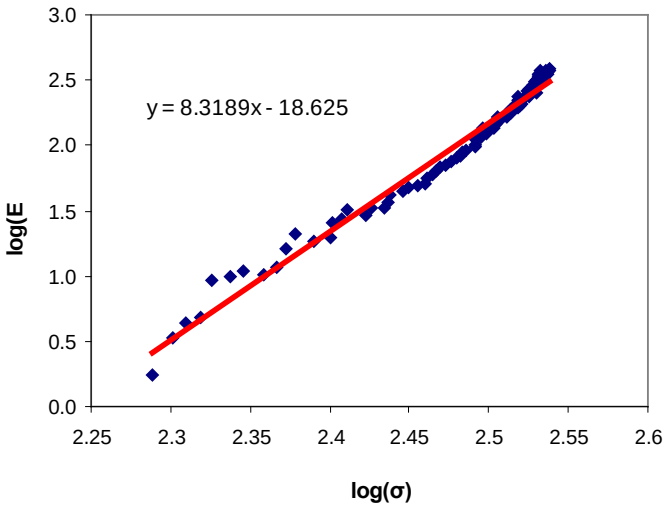

Figure 5.5: Determination of the Ramberg-Osgood equation constants for P92 parent material at 600°C

On the other hand, as the constants a_2 and C_2 were obtained previously, equation (5.13) can be differentiated with respect to ε_p to give the following equation:-

$$\frac{\partial\sigma}{\partial\varepsilon_p} - \frac{\partial R}{\partial\varepsilon_p} - \frac{\partial\chi_2}{\partial\varepsilon_p} = a_1 C_1 e^{-C_1\varepsilon_p} \qquad (5.22)$$

The constants a_1 and C_1, from the χ_1 dominated inelastic region, can be determined by plotting $\ln[(\partial\sigma/\partial\varepsilon_p) - (\partial R/\partial\varepsilon_p) - (\partial\chi_2/\partial\varepsilon_p)]$ versus ε_p as shown in Figure 5.6. Similar procedures to those described earlier, were used to calculate $\partial\sigma/\partial\varepsilon_p$ and $\partial R/\partial\varepsilon_p$ for the χ_1 dominated inelastic region data.

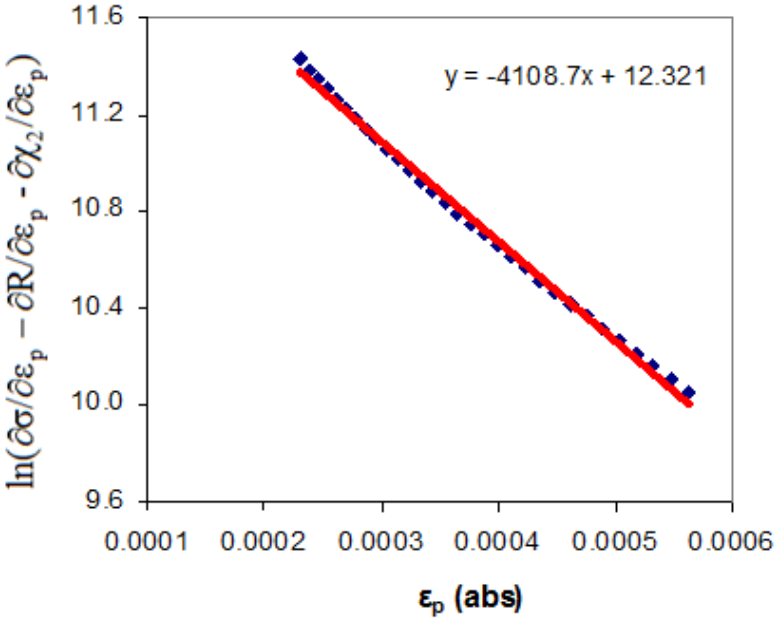

Figure 5.6: Determination of kinematic hardening constants a_1 and C_1 for P92 parent material at 600˚C

5.3.4 Identification of Z and n constants

The viscous constants of Z and n were estimated using the stress relaxation data in the first cycle from the dwell test based on the assumption that the cyclic hardening will not significantly affect the Z and n values. The viscous stress equation can be rearranged to give the following equation:-

$$\log(\sigma_v) = \frac{1}{n}\log(\dot{p}) + \log(Z) \tag{5.23}$$

In the stress relaxation period, the total strain was held constant and thus the total strain rate equals zero, in which the inelastic strain rate can be determined using the dwell test data by the following equation:-

$$\dot{p} = \dot{\varepsilon}_p = -\frac{\dot{\sigma}}{E} \tag{5.24}$$

On the other hand, viscous stress can be calculated by simplifying equation (5.9), asssuming $\sigma > \chi$ in the first dwell period, and rearranged to give:-

$$\sigma_v = \sigma - \chi - R - k \qquad (5.25)$$

By plotting $\log(\sigma_v)$ versus $\log(\dot{p})$ from equation (5.8), as shown in Figure 5.7, the n and Z constants can be identified from the slope of the graph and the y-axis intercept, respectively.

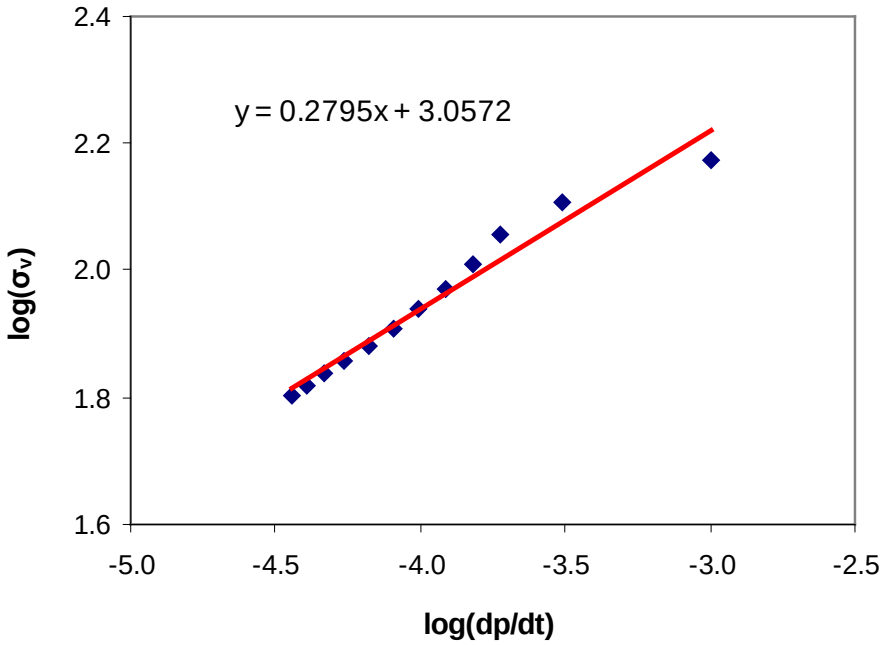

Figure 5.7: Determination of viscous constants Z and n for P92 parent material at 600˚C

The initial viscoplasticity constants at three different temperatures, for the P91 and P92 parent materials, are shown in Table 5.1 and 5.2, respectively. These constants were used as the starting parameters in the optimisation process. For the P92 weld metal, the same initial constants as those for the initial constants of P92 parent material were used in the optimisation process due to a very similar stress-strain loop, at the first cycle, for both parent and weld materials, at each temperature.

Table 5.1: The initial constants of the viscoplasticity model for P91 parent material at 400, 500 and 600°C

T (˚C)	E (MPa)	k (MPa)	Q (MPa)	b	a_1 (MPa)	C_1	a_2 (MPa)	C_2	Z (MPa.$s^{1/n}$)	n
400	197537	96	-55.0	0.45	150.0	2350.0	120.0	405.0	2000	2.25
500	181322	90	-60.0	0.6	98.5	2191.6	104.7	460.7	1875	2.55
600	139395	85	-75.4	1.0	52.0	2055.0	67.3	463.0	1750	2.70

Table 5.2: The initial constants of the viscoplasticity model for P92 parent material at 500, 600 and 675°C

T (˚C)	E (MPa)	k (MPa)	Q (MPa)	b	a_1 (MPa)	C_1	a_2 (MPa)	C_2	Z (MPa.$s^{1/n}$)	n
500	173870	150	-74.5	0.65	102	5471	98	479	1200	2.8
600	145780	90	-92.7	0.75	55	4109	115	443	1141	3.6
675	111810	70	-68.8	0.63	54	4955	49	555	500	3.7

5.4 Constants optimisation

The initially determined viscoplasticity constants obtained by using the step-by-step procedure, described above, can be used to reasonably accurately predict the stress-strain behaviour of the steel. However, the way in which the initial material constants have been determined does not take into account the interactions which take place between the various hardening (kinematic, isotropic) parameters and the creep relaxation behaviour of the material. Thus, a simultaneous procedure was further used in this study to obtain optimized constants in order to improve the stress-strain predictions of the model.

An optimisation program, developed by Gong et al. (2010), was used for the simultaneous determination of the material constants. In this program, a least squares algorithm was applied in which the aim is to search for the global minimum of the differences between predicted and measured stresses in the cyclic loops. The 10 material constants are the optimisation variables. The program was implemented

in Matlab using the nonlinear least squares optimisation function lsqnonlin provided within the Matlab optimisation toolbox. Two different optimisation programs were developed previously in which the programs were based on different objective functions. The applications of these programs in determining the viscoplasticity constants of the P91 and P92 steels are presented below.

5.4.1 Two objective function optimisation

Firstly, the two objective function optimisation program was used in order to obtain more accurate stress-strain prediction of tension-compression test data. In this program, two types of data obtained from the isothermal tension-compression test were used as the objective functions; the first is the stress-strain response and the other is the evolution of stress range in cyclic softening material which occurs throughout the test. The optimisation process using the two objective function program is described in detailed by Hyde (2010) as shown in Figure 5.8.

Several types of inputs were defined in the program prior to starting the optimisation process. First, the stress-strain data from the isothermal tension-compression tests, up to the secondary stage of cyclic softening were supplied into the program and the detail of the test parameters such as the strain rate, $\dot{\varepsilon}$, the minimum strain, $\varepsilon_{\min}$ and the maximum strain, $\varepsilon_{\min}$, were also defined. The lower bound, LB, and the upper bound, UB, for each of the material constants were set as the searching boundaries for the viscoplasticity model constants in the optimisation process. The initial viscoplasticity constants were set as the starting point for the determination of an optimised constant set.

Some guidelines were used in defining the lower and upper bound of material constants so that the optimised constants can be a reasonable representation of the

test data based on the constants definition. For example, the minimum and the maximum values of linear data slope measured in each cycle through out the test were defined as the LB and UB constants for Young's modulus, E. For kinematic hardening constants, a higher value of C_1 constants (compared to C_2 constants) were set as the boundaries so that the stress in the nonlinear hardening data particularly in the χ_1 dominated inelastic region, as shown in Figure 5.3, were mostly contributed by the a_1 constant. The minimum and maximum boundaries for the asymptotic value of isotropic hardening were set based on the value of peak stresses along the secondary stage of cyclic softening. For viscous constant Z and n, a bigger range of boundaries as compared to the initial constants range determined in the section 5.3.4 were used.

During the optimisation process, as shown in the dashed box in Figure 5.8, the global minimum of the differences between numerical and experimental stresses were searched by the program starting from the initially estimated sets of constants. The objective function, $F(x)$, is described mathematically as follows (Hyde, 2010):-

$$F(x) = \sum_{j=1}^{N} w_j F_j(x) = \frac{1}{2} \sum_{j=1}^{N} w_j \sum_{i=1}^{M_j} (A(x)_{ij}^{pre} - A_{ij}^{\exp})^2 \tag{5.26}$$

$$F_1(x) = \sum_{i}^{M_1} w_1 (\sigma(x)_{i1}^{pre} - \sigma_{i1}^{\exp})^2 \tag{5.27}$$

$$F_2(x) = \sum_{i}^{M_2} w_2 (\Delta\sigma(x)_{i2}^{pre} - \Delta\sigma_{i2}^{\exp})^2 \tag{5.28}$$

$$w_j = \frac{\sum_{j}^{N} M_j}{M_j \max\left|A_{ij}^{\exp}\right|} \tag{5.29}$$

where $A(x)_{ij}^{pre}$ and $A_{ij}^{\exp}$ represent the predicted and the corresponding measured stresses, respectively. x is the optimisation variable set consisting of the full set of

material model constants. N is the number of experimental data types, which is 2 for this program. $\sigma(x)_{i1}^{pre}$ and $\sigma(x)_{i1}^{\exp}$ represent the stress at a specific time, i, when $j=1$ while $\Delta\sigma(x)_{i2}^{\exp}$ and $\Delta\sigma(x)_{i2}^{pre}$ represent the stress range when $j=2$. M_j is the total number of data points in each j^{th} type of experiment data. A weight factor, w_j, is used to control the contributions of each objective function.

In the program, the predicted stresses, $A(x)_{ij}^{pre}$, were determined by using a numerical method. Gong et al. (2010) used the ODE45 function, which is Matlab's standard solver for ordinary differential equations, within the Matlab Mathematics Toolbox, to solve a set of differential equations of the viscoplasticity model. The optimisation process was repeated until the same set of parameter was returned from a series of restart positions.

The optimisation process was implemented using data points within 300 cycles for each set of isothermal tension-compression data. At 300 cycles, all materials were in the secondary stage of cyclic softening behaviour in which the maximum stress decreases at an approximately constant rate. The optimisation process took more than 12 hours of computer calculation using Matlab in order to obtain the optimised constants which gives good prediction for the overall selected stress-strain cycles. The process may take longer if the lower and upper bound were set to wider ranges. The optimized isothermal constants obtained for three temperatures, using the two objective function program, are given in Table 5.3, 5.4 and 5.5 for the P91 parent, P92 parent and P92 weld metal, respectively.

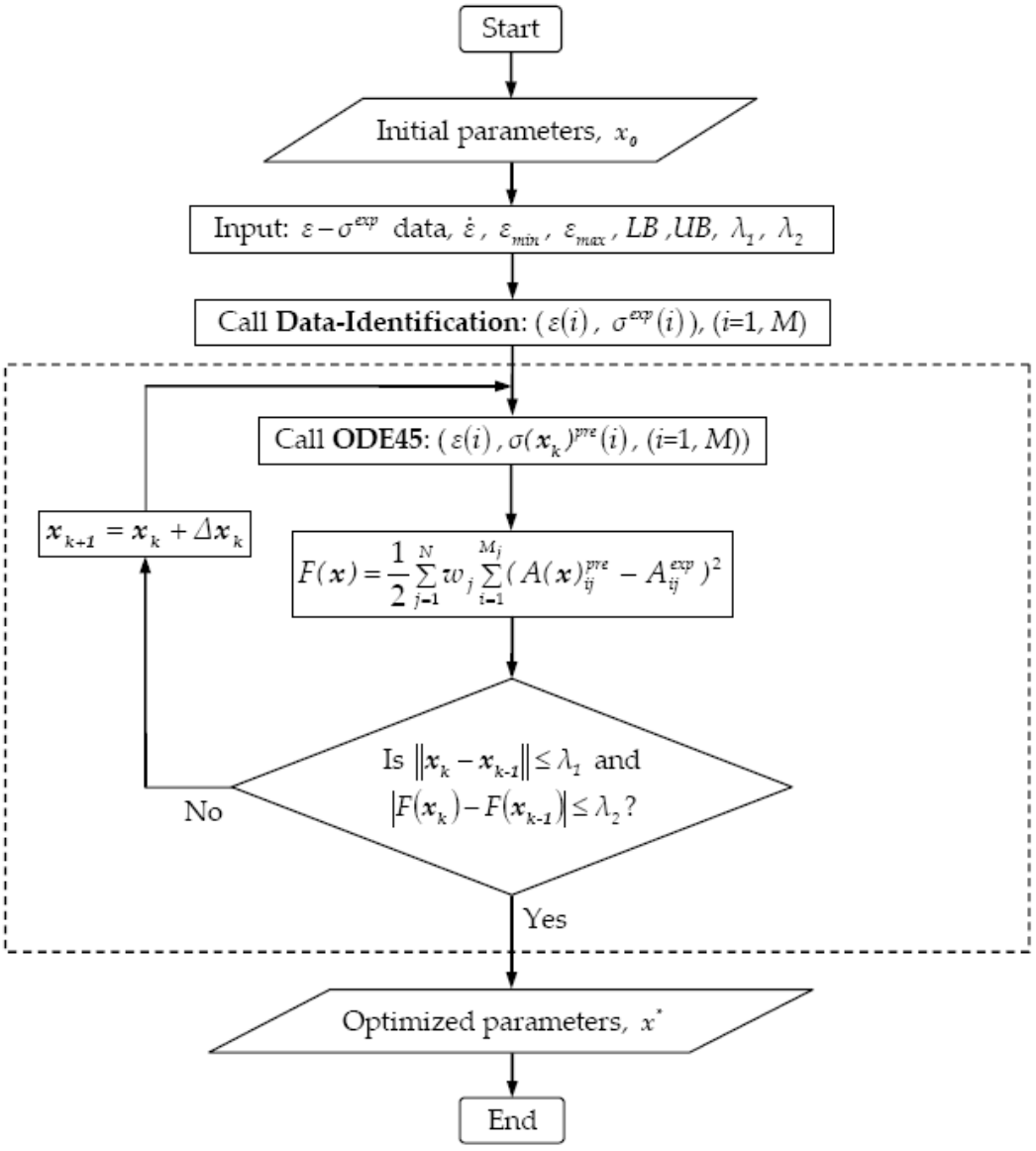

Figure 5.8: The process flowchart in determining the optimised constants using the nonlinear least squares algorithm in Matlab (Hyde, 2010)

Table 5.3: The optimised constants of viscoplasticity model, using the 2 objective function optimisation, for P91 parent material at 400, 500 and 600°C

T (˚C)	E (MPa)	k (MPa)	Q (MPa)	b	a_1 (MPa)	C_1	a_2 (MPa)	C_2	Z (MPa.s$^{1/n}$)	n
400	188000	200	-51	1	68	3763	165	460	1355	2
500	182500	175	-59	0.9	58	3024	121	400	2428	2
600	172771	104	-62	1.7	80	3680	87	418	203	5.1

Table 5.4: The optimised constants of viscoplasticity model, using the 2 objective function optimisation, for P92 parent material at 500, 600 and 675°C

T (˚C)	E (MPa)	k (MPa)	Q (MPa)	b	a_1 (MPa)	C_1	a_2 (MPa)	C_2	Z (MPa.s$^{1/n}$)	n
500	175000	150	-66	0.8	80	2000	128	300	2257	2.35
600	150000	100	-90	0.78	40	5000	105	400	500	4.51
675	120000	80	-60	0.7	50	5000	50	164	500	3.59

Table 5.5: The optimised constants of viscoplasticity model, using the 2 objective function optimisation, for P92 weld metal at 500, 600 and 675°C

T (˚C)	E (MPa)	k (MPa)	Q (MPa)	b	a_1 (MPa)	C_1	a_2 (MPa)	C_2	Z (MPa.s$^{1/n}$)	n
500	175000	150	-75	0.8	96	2000	126	300	2997	2.07
600	150000	100	-80	1	40	3997	84	400	500	4.9
675	120000	80	-64	0.7	50	1559	70	50	500	3.76

The stress-strain prediction using the optimised constants

Typical stress-strain responses predicted using the optimised constants, compared with the predictions using the initial constants, are presented in Figure 5.9, for the P92 parent material at 600°C. It can be seen that using the optimised constants gives better stress-strain predictions than does the initial constants. The differences are due to the assumptions made during the determination of initial constants. For instance, kinematic constants a_1 and C_1 are assumed to have negligible effect on the hardening behaviour at high strain values when used to obtain constants a_2 and C_2. The nonlinear hardening behaviour is sensitive to the changes of the constants a_1, C_1, a_2, C_2, Z and n. Furthermore, in the determination of initial constants, the viscous parameters Z and n were only determined after the other 8 constants had been finalised. In the real situation, the viscous effects described by Z and n constants will have their role as the deformation becomes inelastic. This indicates that Z and n constants may affect the kinematic and isotropic hardening behaviour.

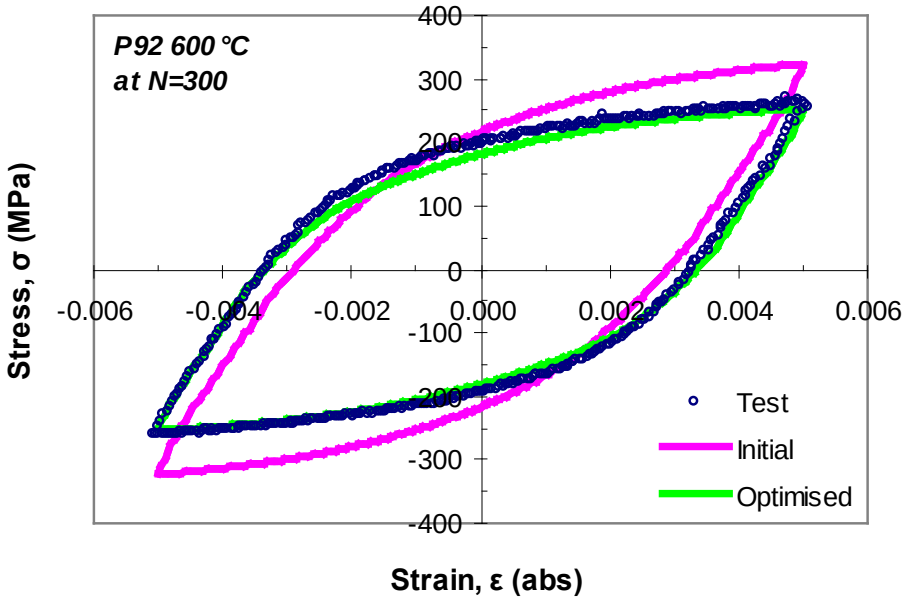

Figure 5.9: Results comparison between the prediction of the initial constants and the optimised constants for P92 parent material at 600°C and 300th cycle

Figures 5.10 to 5.18 show predictions, using the optimised viscoplasticity constants, compared with experimental data for each of the materials tested in this study. In each set of figures, the first figure shows the results for the first cycle, followed by the results for the 300th cycle and finally the results for the corresponding maximum and minimum stress evolution. In general, the optimised constants produce a very good set of stress-strain relationships as compared to the test data. For some cases, for the first cycle, in for example, the P92 parent at 675°C, the prediction results for the nonlinear hardening curve is less accurate, when compared to the test data, than is generally the case, as shown in Figure 5.13(a). However, the model prediction, for the nonlinear curve becomes better as cycles progress, and also the evolution of maximum and minimum stresses up to the 300th cycle are in very good agreement as shown in Figure 5.13(c).

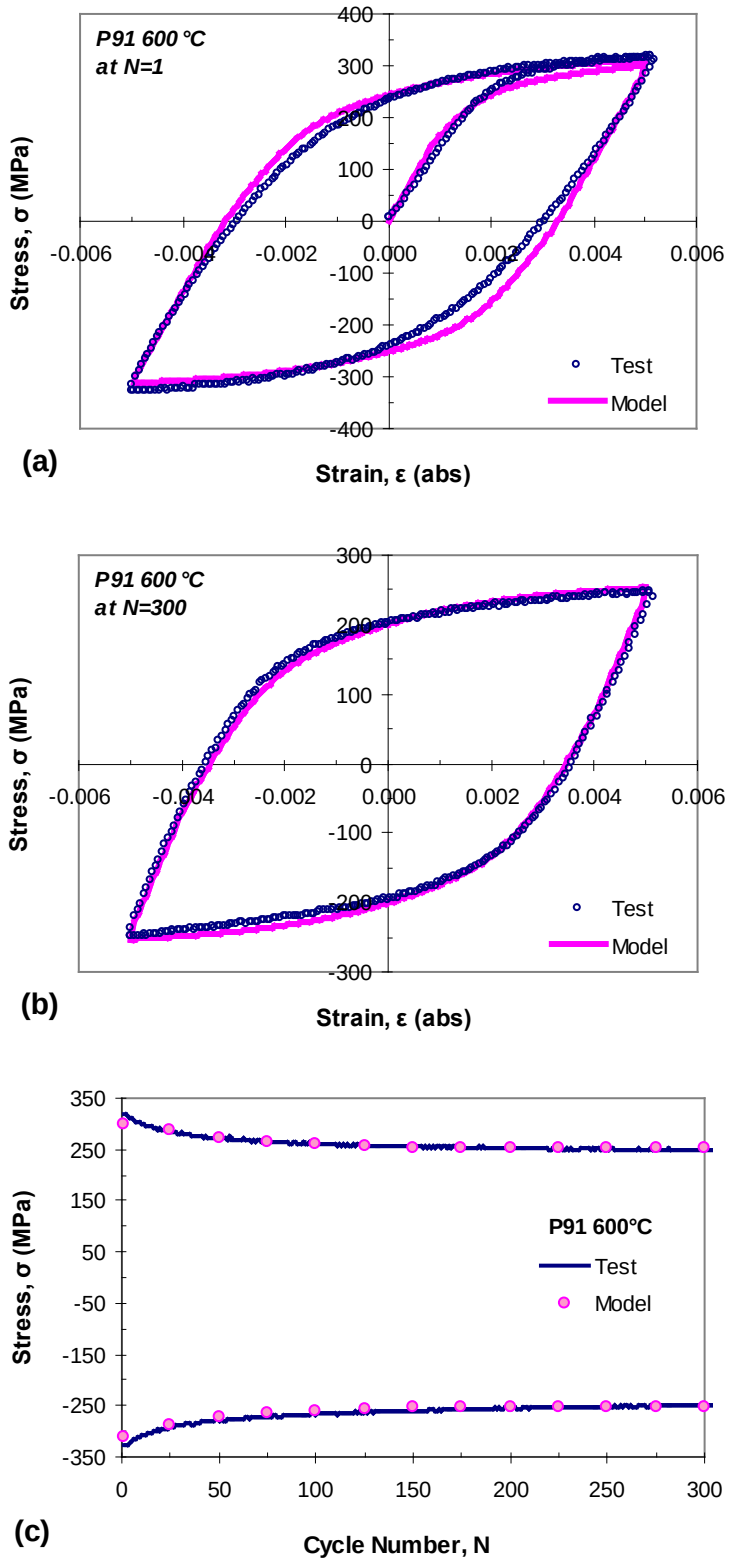

Figure 5.10: Comparison of the test and the optimised model results for the isothermal tension compression loading of P91 parent material at 600°C for (a) the first cycle, (b) the 300th cycle and (c) the evolution of maximum and minimum stresses during the optimisation process

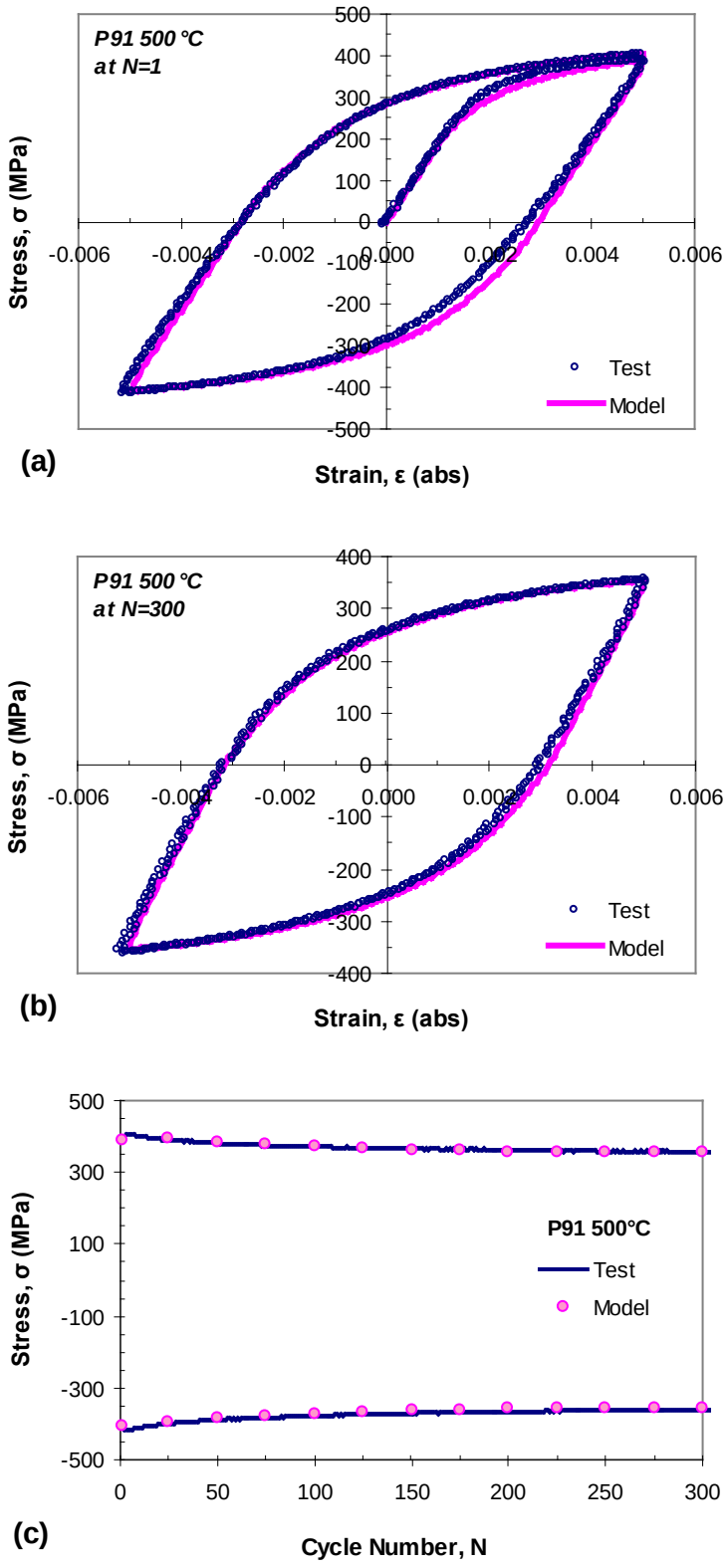

Figure 5.11: Comparison of the test and the optimised model results for the isothermal tension compression loading of P91 parent material at 500°C for (a) the first cycle, (b) the 300th cycle and (c) the evolution of maximum and minimum stresses during the optimisation process

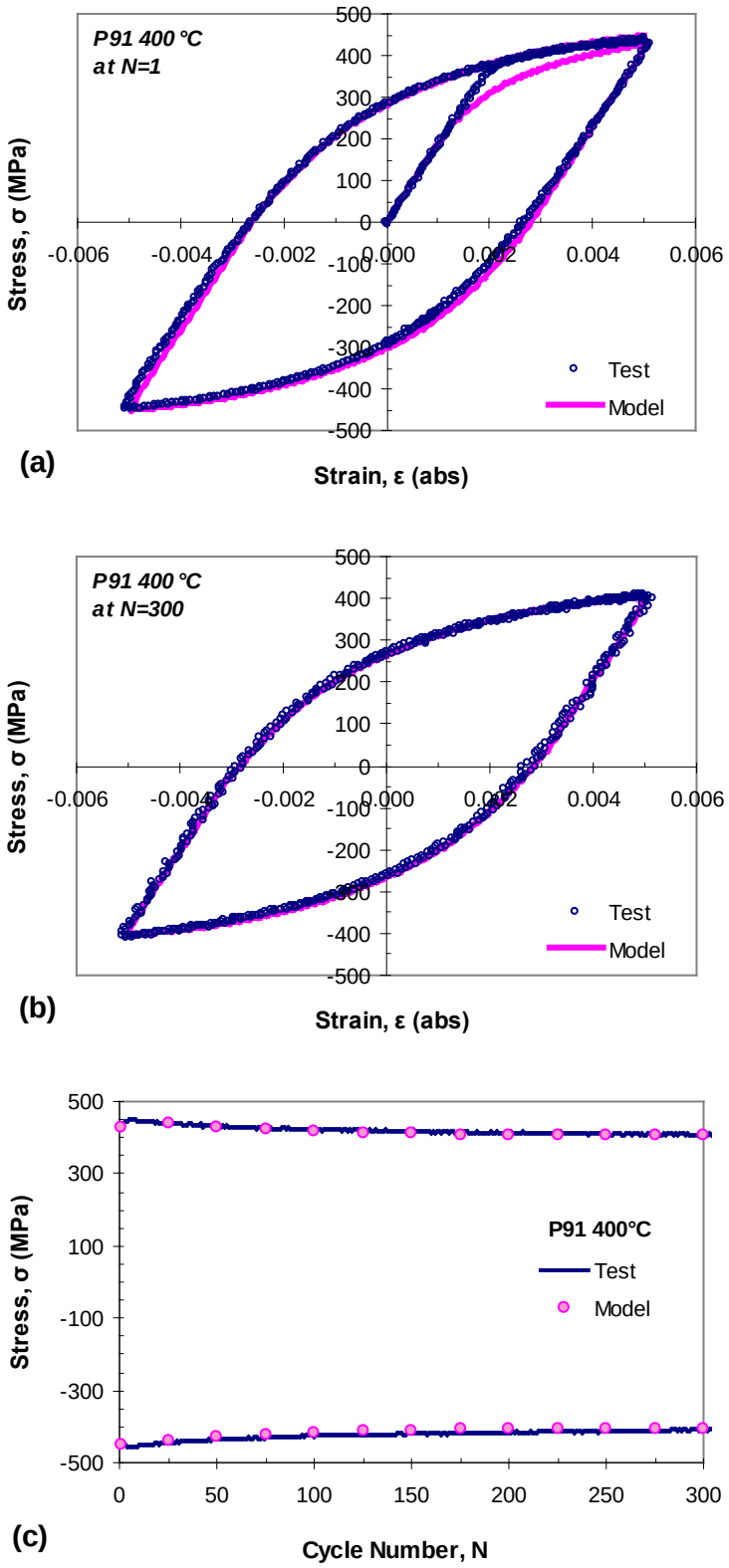

Figure 5.12: Comparison of the test and the optimised model results for the isothermal tension compression loading of P91 parent material at 400°C for (a) the first cycle, (b) the 300th cycle and (c) the evolution of maximum and minimum stresses during the optimisation process

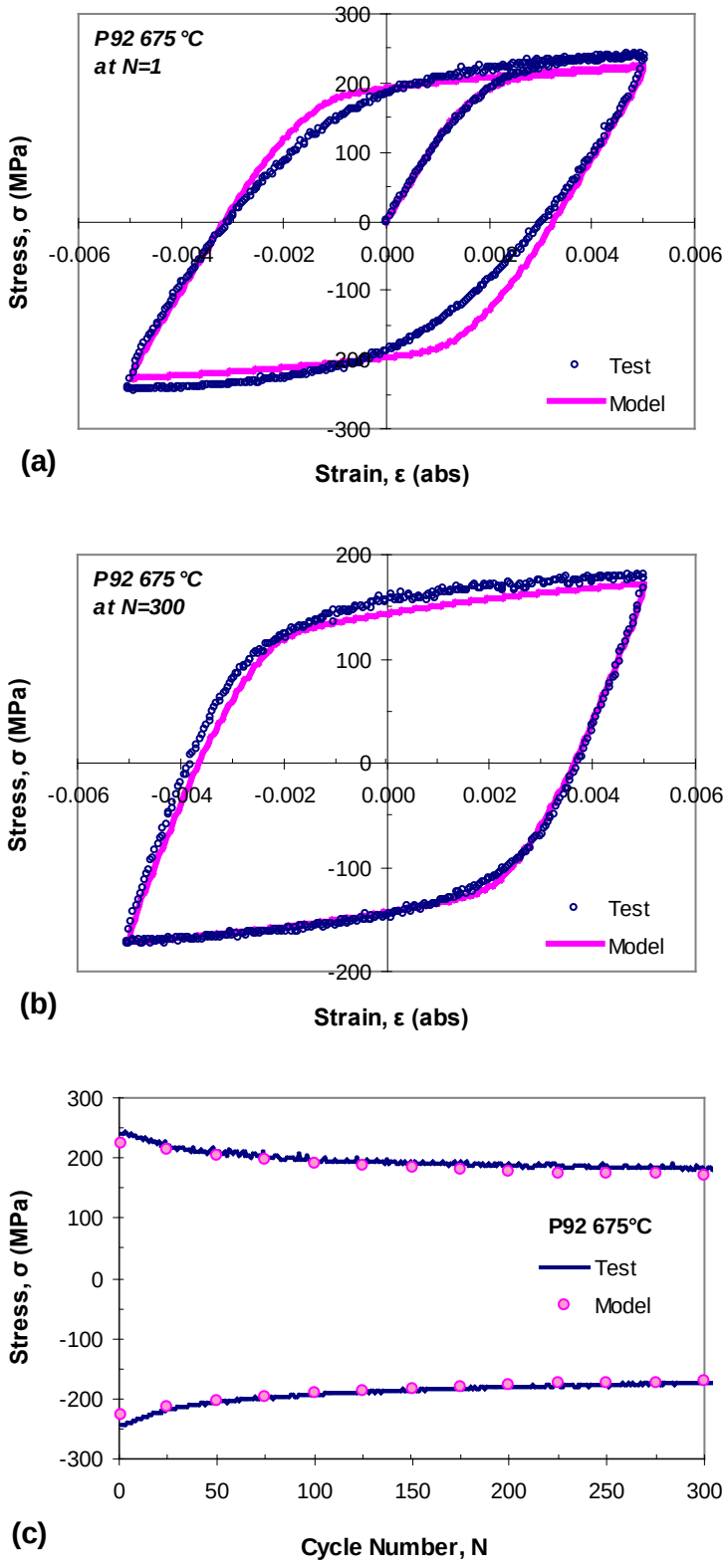

Figure 5.13: Comparison of the test and the optimised model results for the isothermal tension compression loading of P92 parent material at 675°C for (a) the first cycle, (b) the 300th cycle and (c) the evolution of maximum and minimum stresses during the optimisation process

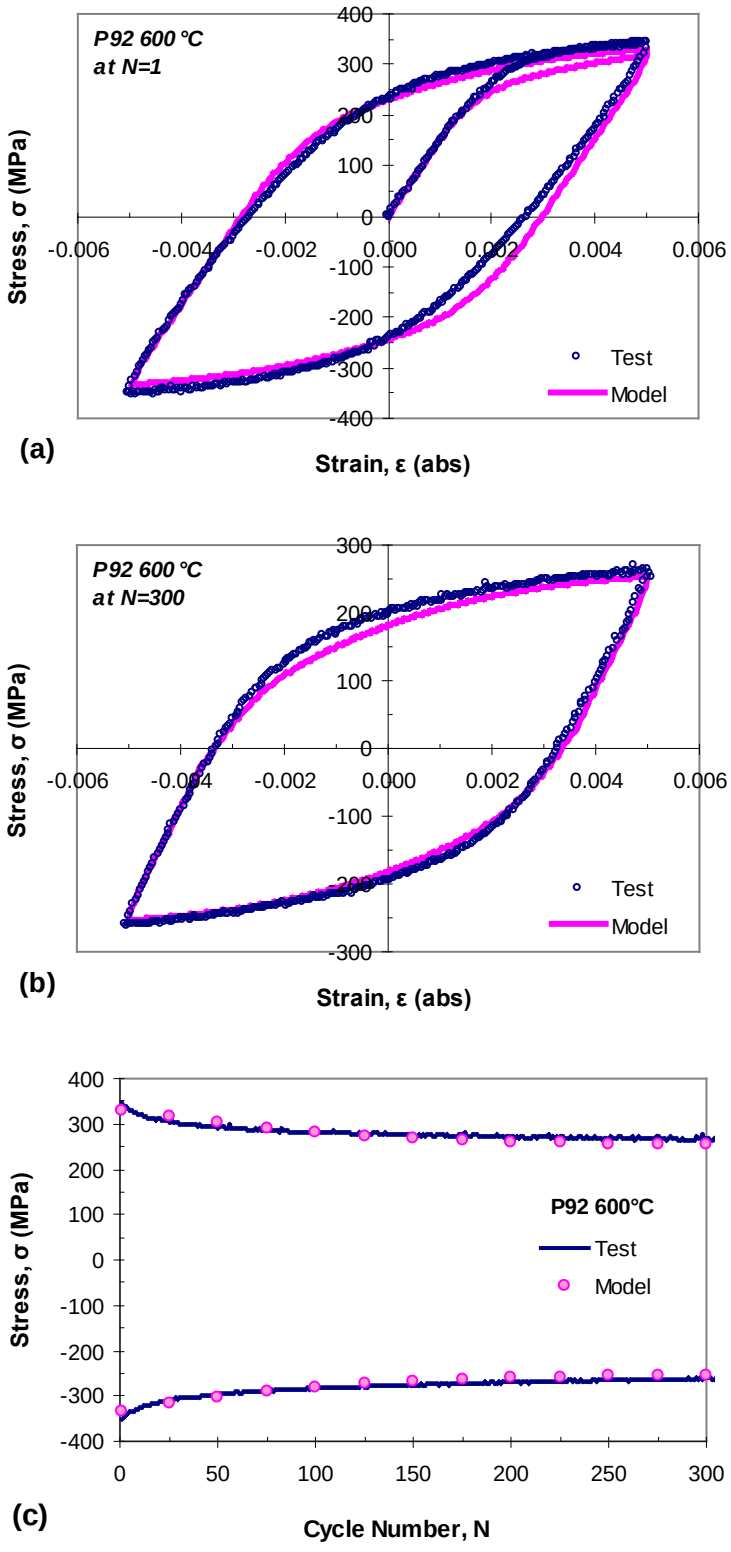

Figure 5.14: Comparison of the test and the optimised model results for the isothermal tension compression loading of P92 parent material at 600°C for (a) the first cycle, (b) the 300th cycle and (c) the evolution of maximum and minimum stresses during the optimisation process

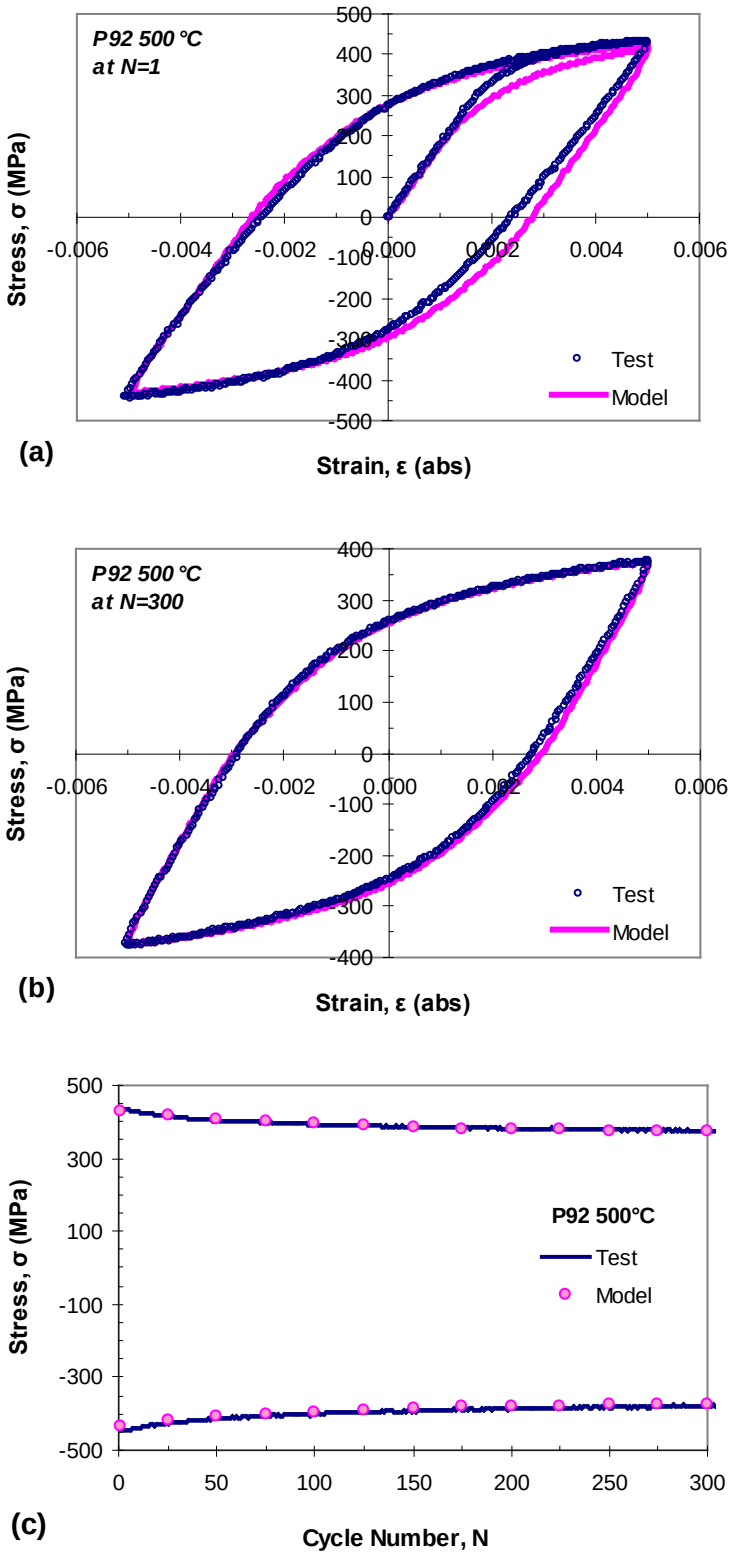

Figure 5.15: Comparison of the test and the optimised model results for the isothermal tension compression loading of P92 parent material at 500°C for (a) the first cycle, (b) the 300th cycle and (c) the evolution of maximum and minimum stresses during the optimisation process

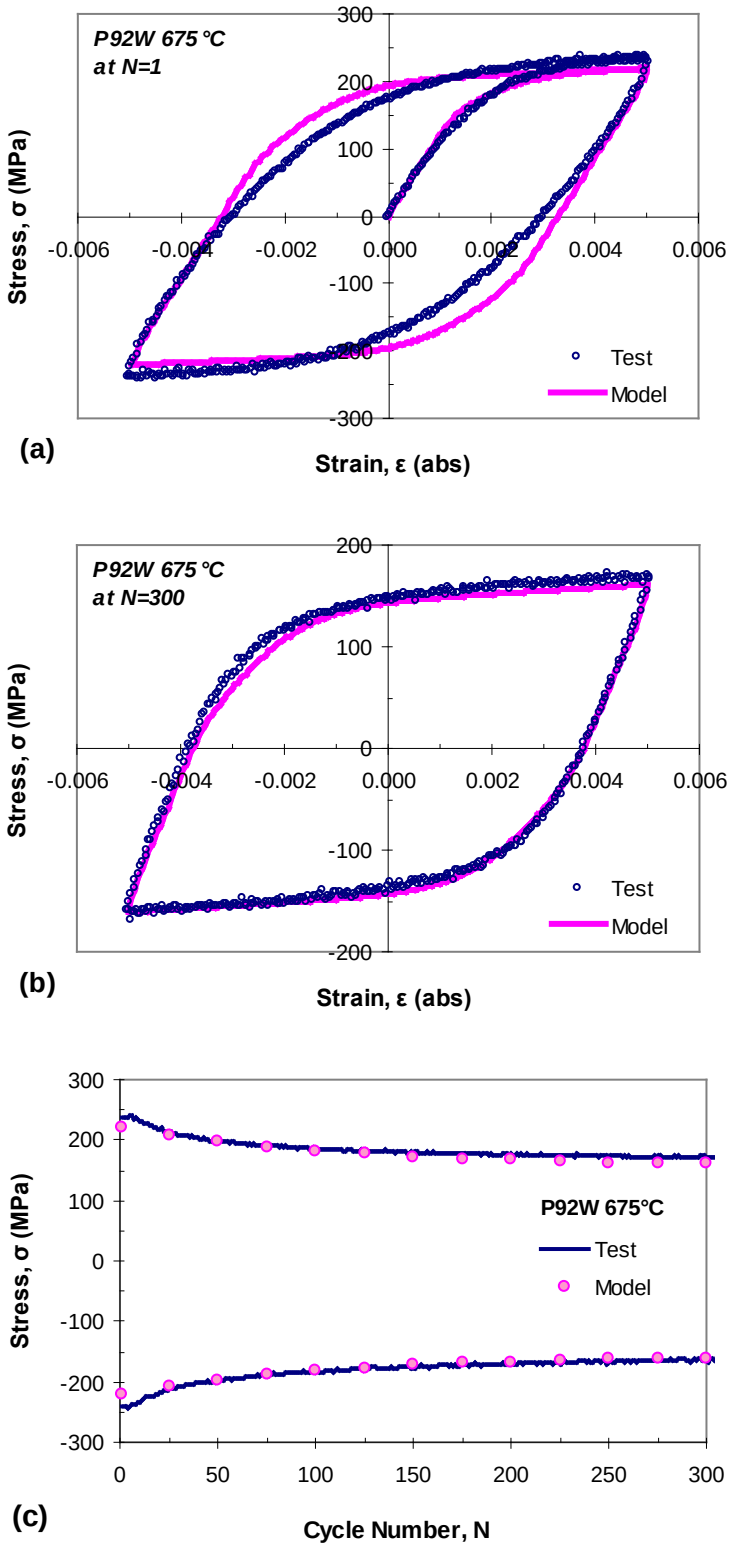

Figure 5.16: Comparison of the test and the optimised model results for the isothermal tension compression loading of P92 weld metal at 675°C for (a) the first cycle, (b) the 300th cycle and (c) the evolution of maximum and minimum stresses during the optimisation process

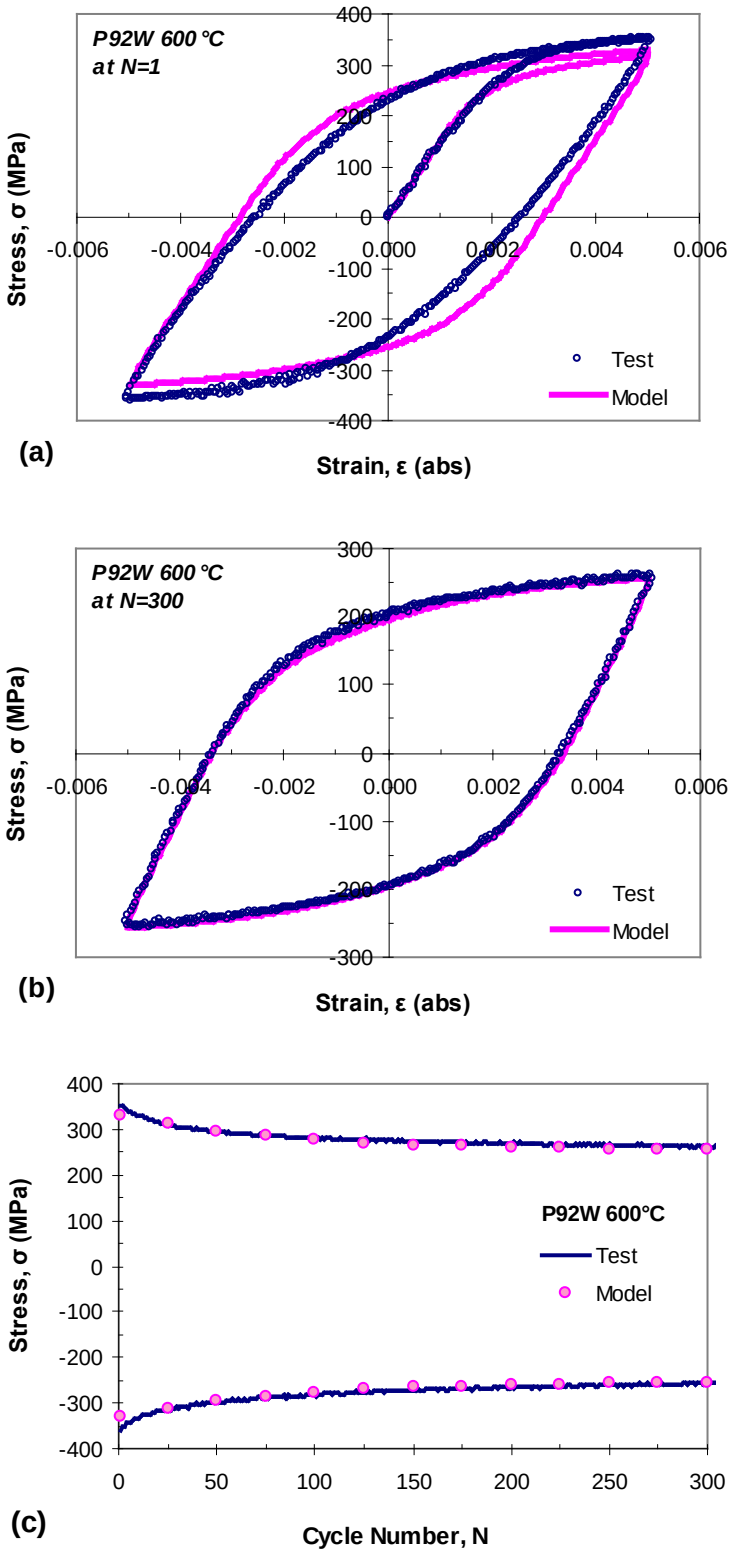

Figure 5.17: Comparison of the test and the optimised model results for the isothermal tension compression loading of P92 weld metal at 600°C for (a) the first cycle, (b) the 300th cycle and (c) the evolution of maximum and minimum stresses during the optimisation process

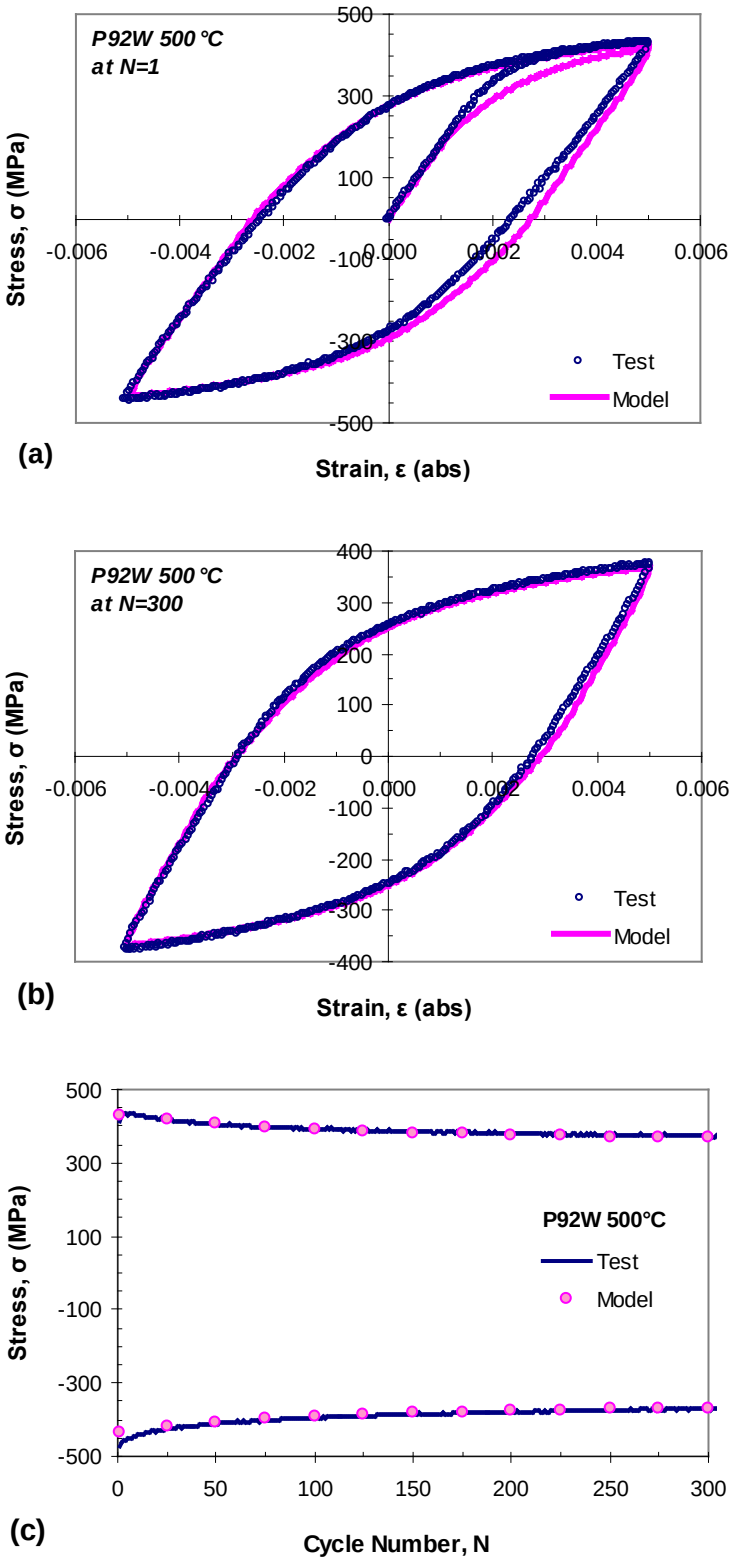

Figure 5.18: Comparison of the test and the optimised model results for the isothermal tension compression loading of P92 weld metal at 500°C for (a) the first cycle, (b) the 300th cycle and (c) the evolution of maximum and minimum stresses during the optimisation process

5.4.2 Three objective function optimisation

The optimisation program in the previous section, which produced a set of viscoplasticity constants with good predictions capability for the stress-strain relationships, only focused on the tension-compression test data. However, the effect of a constant dwell period was ignored in the program. From the results in the section 3.6.2, it has been shown that the holding period for tensile strain at high temperature in the isothermal strain-controlled tests produced a stress relaxation behaviour in which the stress level drop in a constant strain controlled test. In this section, a three objective function optimisation program has been used to improve the performance of the viscoplasticity model. A similar optimisation program to that program developed by Gong et al. (2010) was used for this purpose.

The three objective functions optimisation program considers three types of data in the optimisation process. These are the stress-strain response, the evolution of stress range which shows the cyclic softening behaviour and the stress relaxation data during the holding period. An additional objective function equation was defined as incorporated into equation (5.26) as follows:-

$$F_3(x) = \sum_{i}^{M_3} w_3(\sigma(x)_{i3}^{pre} - \sigma_{i3}^{\exp})^2 \tag{5.30}$$

There are two limitations of the current 3 objective functions program. Firstly, the program performs the optimisation process by considering only one supplied test data, which is the test with a dwell period. The prediction of the resultant optimised constants may give good prediction results if compared to the dwell test data only. However, the set of determined constants may give less accurate prediction of the tension-compression data, particularly at higher number of cycles. This kind of situation was observed in the initial stage of using the three objective functions

program. Secondly, the optimisation can only be done using a limited number of cycles, for example only experimental data within 20 cycles were used in this study. The current 3 objective functions program is still being improved in order to include more data during the optimisation process.

In order to produce a set of constants which satisfy both sets of test data, several procedures were implemented. At the end of the optimisation process using the three-objective function program, the optimised constants performance compared to the tension-compression data were performed manually. If the results were not in a good agreement, the optimisation process using the three objective functions was repeated by changing the boundaries of the lower and upper constants in the program. The optimisation process may need to be repeated several times, with the help of spreadsheet calculation to select the constant boundaries, in order to obtain a set of constants which gives reasonably good predictions for both types of test data. The optimised constants obtained using the 3 objective function program are given in Table 5.6, 5.7 and 5.8 for the P91 parent material, P92 parent material and P92 weld metal, respectively. Due to limitation of P92 material, only two isothermal tensile peak strain dwell tests were performed which are at 600 and 675°C. So, the optimisation using the 3 objective function program at 500°C cannot be implemented.

Some of the predictions of the optimised constants in this section are shown in Figures 5.19 to 5.22. Figure 5.19(a) shows the effect of the three-objective functions program on the prediction of stress relaxation behaviour in which a better shape and better stress values are achieved. Although the optimisation was implemented using data from 20 cycles, the determined set of constants give reasonable predictions at higher cycles than 20, as shown in Figure 5.19(b). As mentioned earlier, a repeated

optimisation process was done in order to get improved predictions for the stress-strain behaviour, for both tension-compression and dwell test data. In all of Figures 5.20, 5.21 and 5.22, the figure (a) and (b) show the stress-strain behaviour for a test with and without the dwell period, respectively, at the 300th cycle. The figures show good comparison between the predictions and the test data. These comparisons indicate the suitability of determined constants to produce good stress-strain behaviour predictions for cyclic loading and a time-dependent behaviour such as stress relaxation.

Table 5.6: The optimised constants of viscoplasticity model using 3 objective functions program for P91 parent material at 400, 500 and 600°C

T (˚C)	E (MPa)	k (MPa)	Q (MPa)	b	a_1 (MPa)	C_1	a_2 (MPa)	C_2	Z (MPa.s$^{1/n}$)	n
400	185000	151	-45	0.4	183	1000	200	40	1250	2.48
500	174228	120	-65	0.7	130	1000	120	45	1200	3.01
600	140000	90	-70	1.1	70	900	100	50	1000	3.48

Table 5.7: The optimised constants of viscoplasticity model using 3 objective functions program for P92 parent material at 600 and 675°C

T (˚C)	E (MPa)	k (MPa)	Q (MPa)	b	a_1 (MPa)	C_1	a_2 (MPa)	C_2	Z (MPa.s$^{1/n}$)	n
600	149987	94	-80	0.99	81.2	800	100	50	1051.3	3.5
675	115000	40	-50	0.70	30	300	10	500	1000	3.7

Table 5.8: The optimised constants of viscoplasticity model using 3 objective functions program for P92 weld metal at 600 and 675°C

T (˚C)	E (MPa)	k (MPa)	Q (MPa)	b	a_1 (MPa)	C_1	a_2 (MPa)	C_2	Z (MPa.s$^{1/n}$)	n
600	150000	100	-80	1	75	700	100	50	1000	3.55
675	125000	40	-60	0.7	30	300	10	500	900	3.88

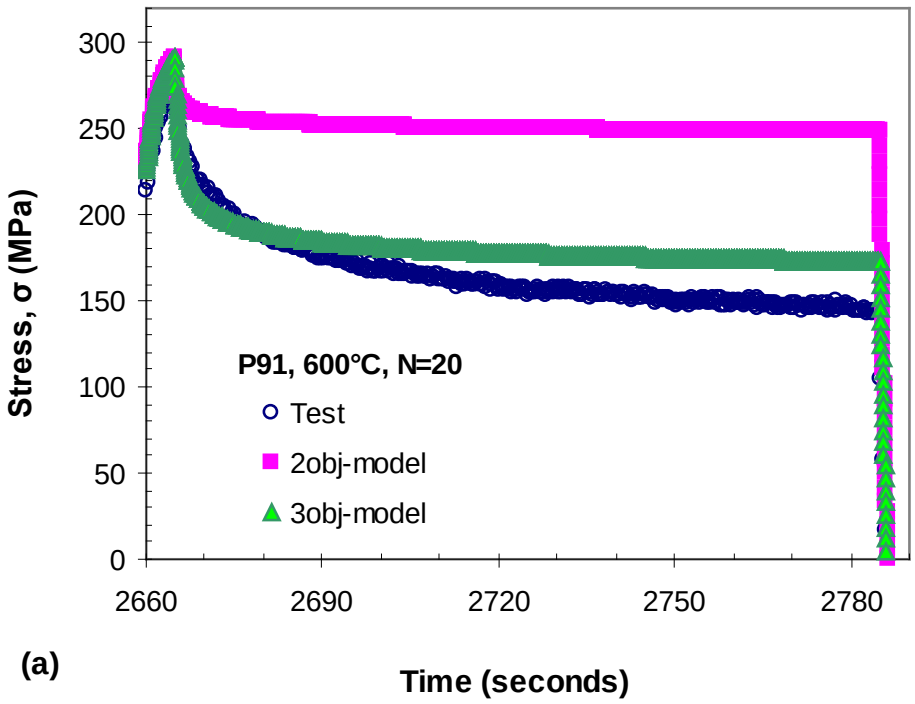

(a)

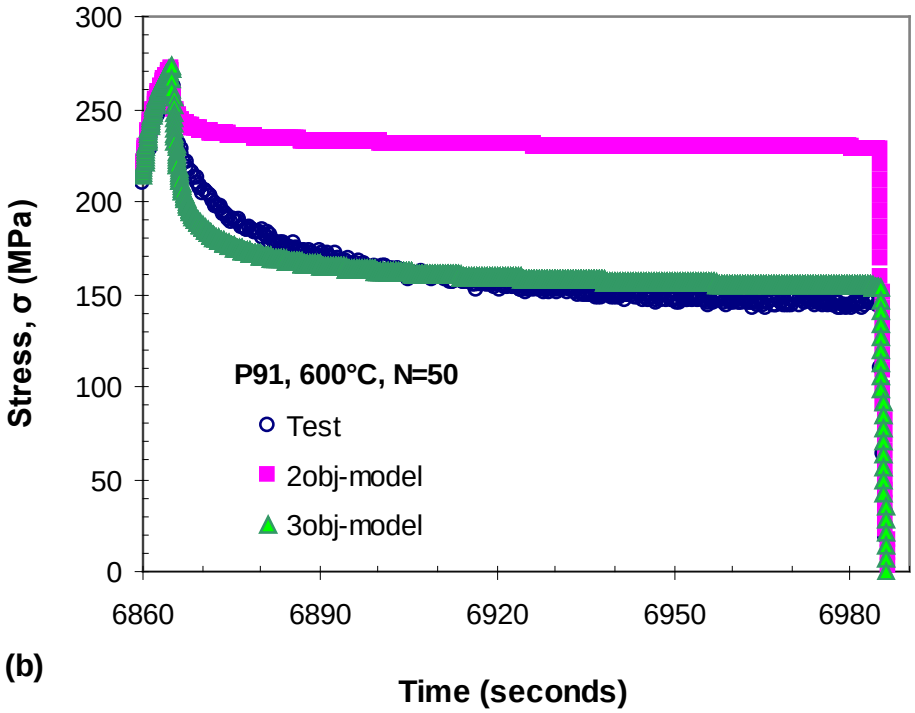

(b)

Figure 5.19: Example of plots for the P91 test at 600°C with a 2 minutes holding period compared with the results of model prediction using the set of constants from two and three objective functions program. (a) The results at 20th cycle and (b) the results at higher number of cycles (50th cycle)

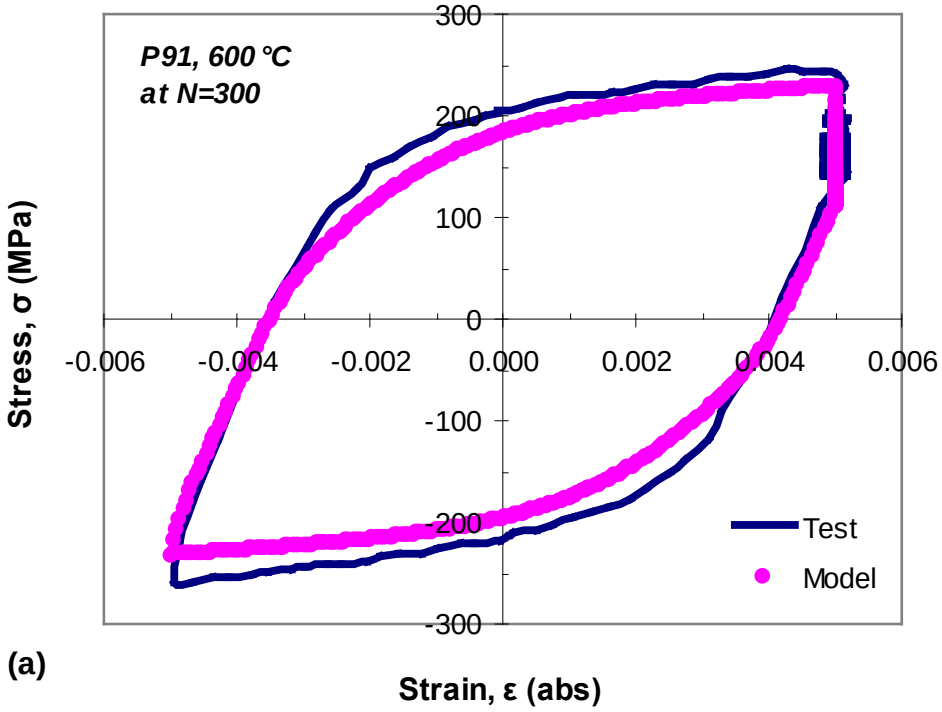

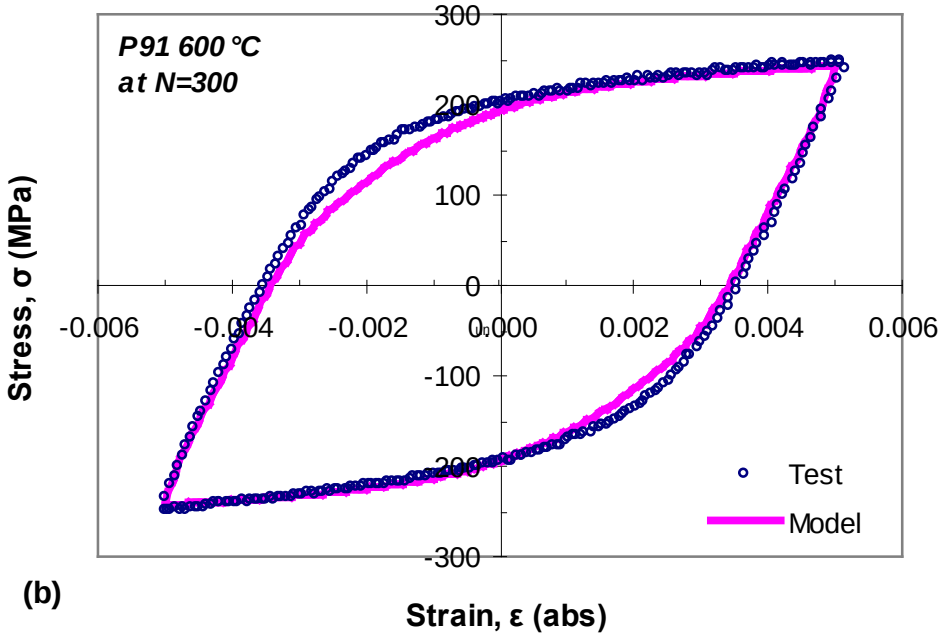

Figure 5.20: The comparison of stress-strain relationship of P91 parent material at 600°C during 300th cycle between experimental data and prediction of the optimised constants using 3 objective function program for (a) the test with holding period of 2 minutes and (b) the tension-compression test

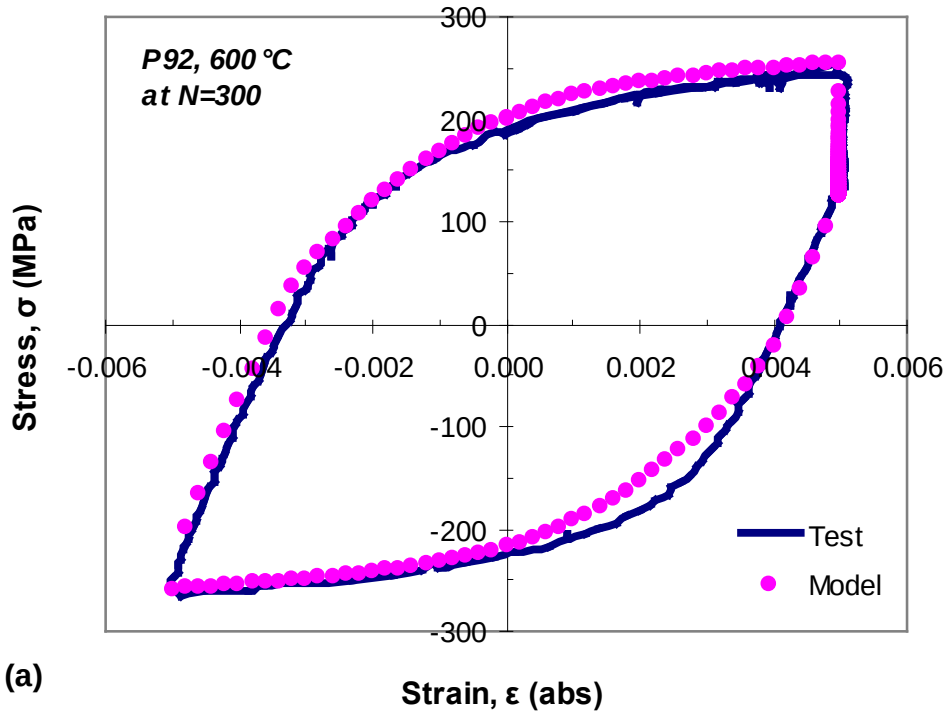

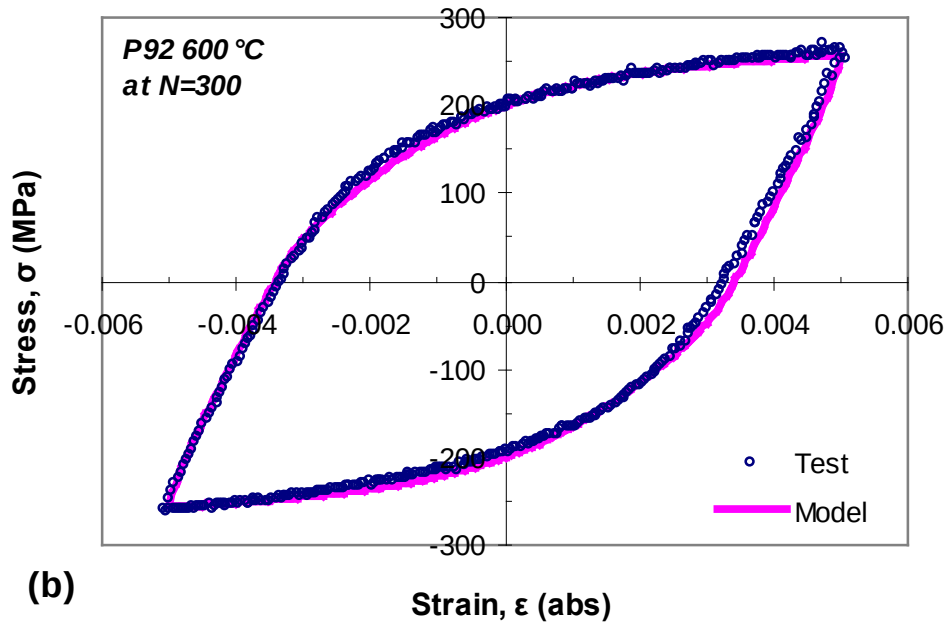

Figure 5.21: The comparison of stress-strain relationship of P92 parent material at 600°C during 300th cycle between experimental data and prediction of the optimised constants using 3 objective function program for (a) the test with holding period of 5 minutes and (b) the tension-compression test

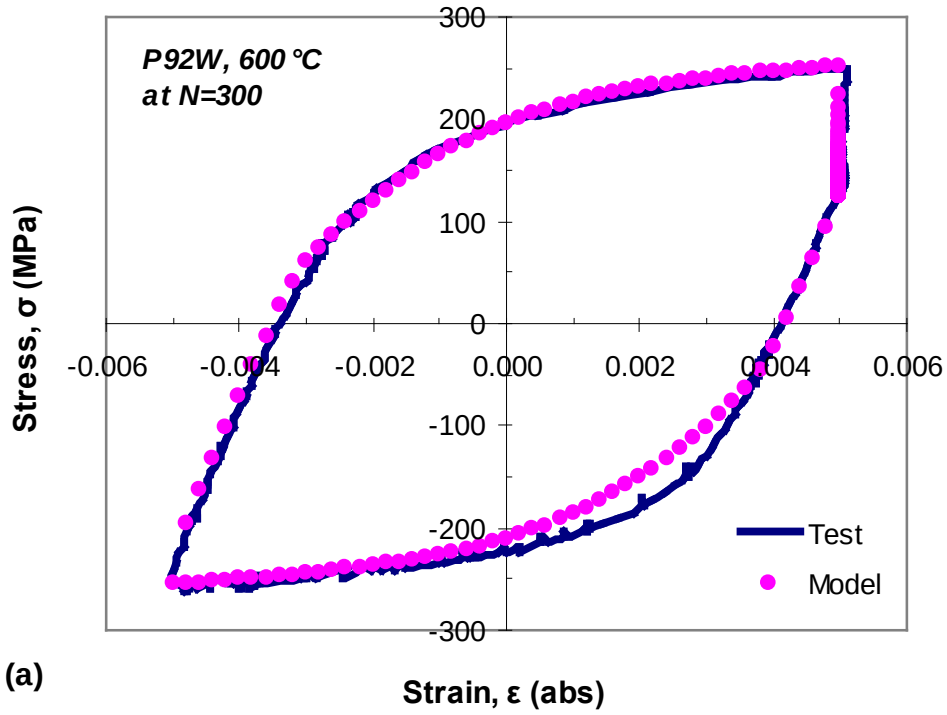

(a)

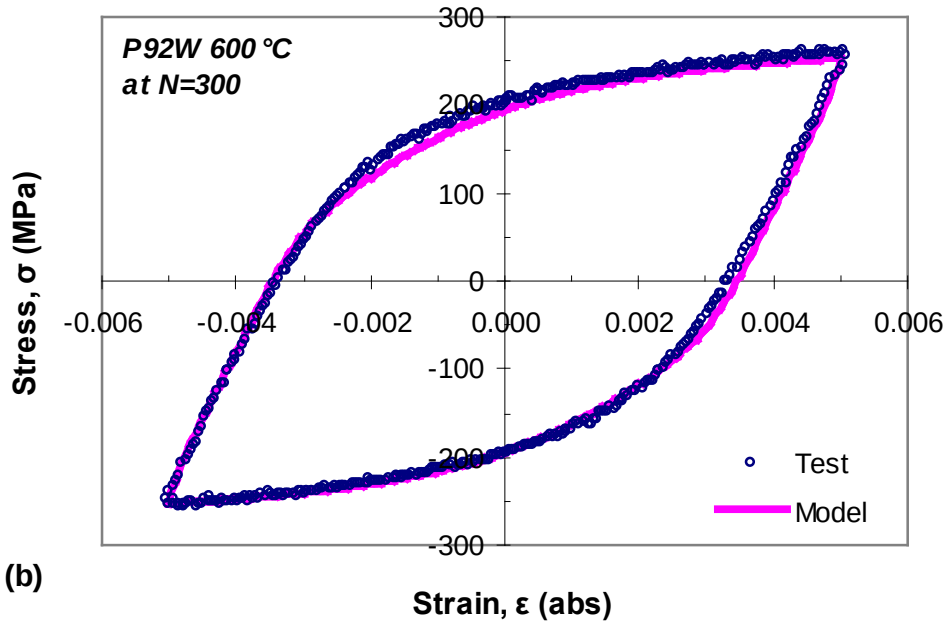

(b)

Figure 5.22: The comparison of stress-strain relationship of P92 weld metal at 600°C during 300th cycle between experimental data and prediction of the optimised constants using 3 objective function program for (a) the test with holding period of 5 minutes and (b) the tension-compression test

5.5 Two stages of isotropic hardening

Use of the optimised set of constants, which include the nonlinear isotropic hardening equation, enables good stress-strain predictions to be obtained for the P91 and the P92 steels. However, the shape of the peak stress evolution prediction, up to the end of the second stage of cyclic softening, is unrealistic as compared to the experimental data in which the rate of peak stress evolution becomes zero when the specimen reaches a certain number of cycles. From the experimental data, the rate of peak stress evolution is almost constant in the second stage, before cracks begin to propagate near the end of the test. Thus, it is the aim of this section to further improve the prediction of cyclic softening behaviour of the P91 and the P92 steels in order to obtain more realistic shapes for the cyclic softening curves.

A combined linear and nonlinear isotropic hardening model, as given by Lemaitre and Chaboche (1994), is used to improve the cyclic softening predictions. In this combined model, the previous nonlinear equation of isotropic variable, as shown in equation (5.10), is modified by adding a linear term, given by the following equation:-

$$R = Hp + Q(1 - e^{-bp}) \qquad (5.31)$$

where Hp is the linear term. H is a constant and the linear term corresponds to the slope for the second stage of cyclic softening (Bernhart et al., 1999). The constants previously determined by the optimisation programme are assumed to remain the same except for constants Q and b which represent the stage 1 of the cyclic softening in this model. Q can be estimated as the difference between point X and maximum stress at first cycle in Figure 5.23, while b is the speed to reach the maximum stress at the end of stage 1. The accumulated plastic strain, p, can be taken to be $2\Delta\varepsilon_p N$ and thus the constant H can be estimated as the slope of the second stage of softening and is equal to $2\Delta\varepsilon_p H$.

The initial constants of Q, b and H for the combined linear and nonlinear isotropic hardening model, estimated as mentioned in the above procedures, are further improved to get better prediction of the peak stress evolution as the number of cycle increases. The Q, b and H constants, with the 3-objective function optimised viscoplasticity constants, were implemented in the tension-compression calculation of the strain-controlled condition to observe the prediction of the constants as compared to the experimental data. For the P92 parent and weld materials at 500°C, the 2 objective function optimised constants were used due to unavailability of experimental data for these conditions. A slight adjustment to the value of initial constants of Q, b and H was made in order to get better peak stress evolution. The final constants of the combined linear and nonlinear isotropic hardening model are given in Table 5.9. In the future, equation 5.31 will be included in the optimisation program in order to determine the constants of the combined linear and nonlinear isotropic hardening model.

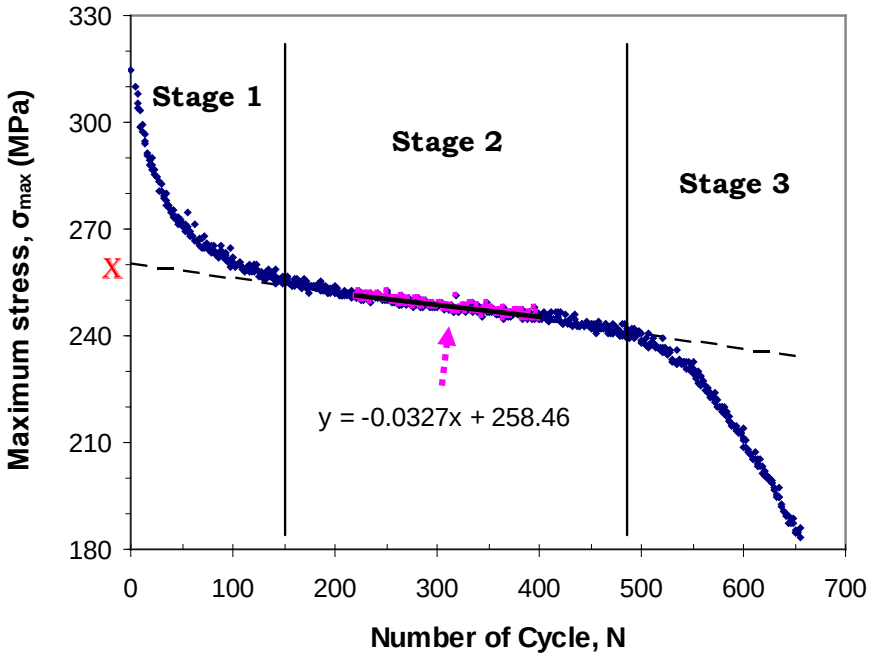

Figure 5.23: Example of the determination of material constants for the combined linear and nonlinear isotropic hardening model for P91 parent material at 600°C

Table 5.9: The material constants of the combined linear and nonlinear isotropic hardening model for P91 parent, P92 parent and P92 weld metal at different temperatures

Constants	P91 parent			P92 parent			P92 weld		
	400°C	500°C	600°C	500°C	600°C	675°C	500°C	600°C	675°C
Q	-30	-42	-52	-52	-58	-40	-55	-60	-45
b	0.8	1.3	1.9	1.1	1.6	1.2	1.2	1.3	1.2
H	-1.8	-2.1	-2.9	-2.7	-2.7	-1.6	-3.5	-2.7	-1.9

Figure 5.24 shows the predictions obtained using the viscoplasticity model for P91 parent material at 600°C using the nonlinear equation and the combined linear-nonlinear equation for isotropic hardening model. It can be seen in the figure that the peak stress level prediction using the nonlinear isotropic hardening model becomes constant around 300th cycles onwards. Also, a clear gap exists between the test data and the model predictions, using the nonlinear model, located at around 200th cycles, even though the maximum stress difference at the 200th cycle is only around 6 MPa. It is clear that the isotropic hardening model with the combined linear-nonlinear model has improved the prediction of the peak stresses evolution shape, as shown in Figure 5.24, which is more realistic to represent the linear curve of the cyclic softening in the secondary stage. The prediction of the cyclic softening shape is good up to the end of secondary stage before the final stage of rapid softening occurs due to crack propagation in the material. The current model is unable to predict the final stage of cyclic softening unless a damage mechanics concept is introduced into the model, which is the subject of another research program. The predictions of the stress evolution for each specimen at different temperatures, using the linear nonlinear isotropic hardening model constants in Table 5.9, are shown in Figures 5.25, 5.26 and 5.27 for the P91 parent, P92 parent and P92 weld metal respectively. All of the predictions are in good agreement with the experimental data.

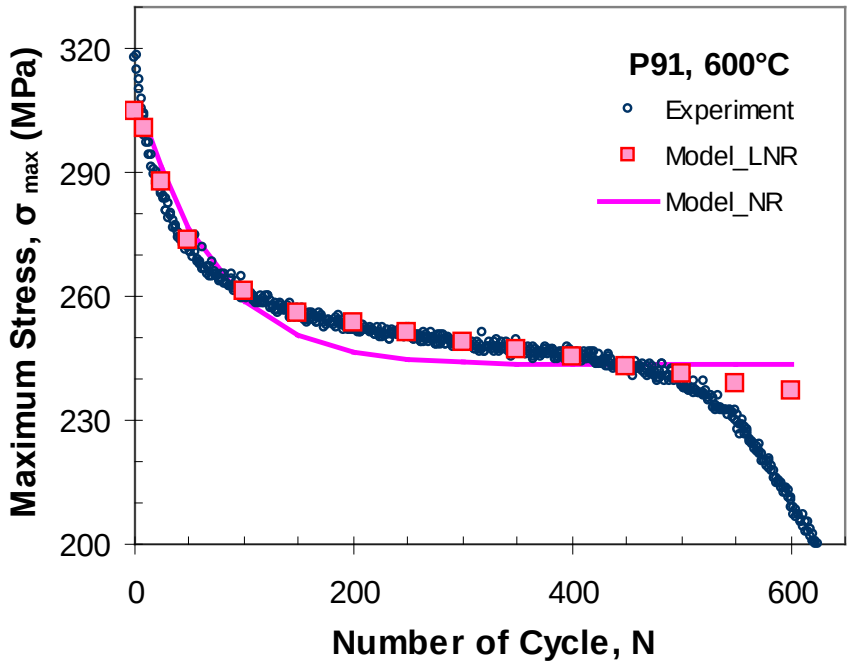

Figure 5.24: Example of plots for the comparison of the maximum stress evolution prediction between the nonlinear (NR) and the linear nonlinear (LNR) models of P91 parent material at 600°C

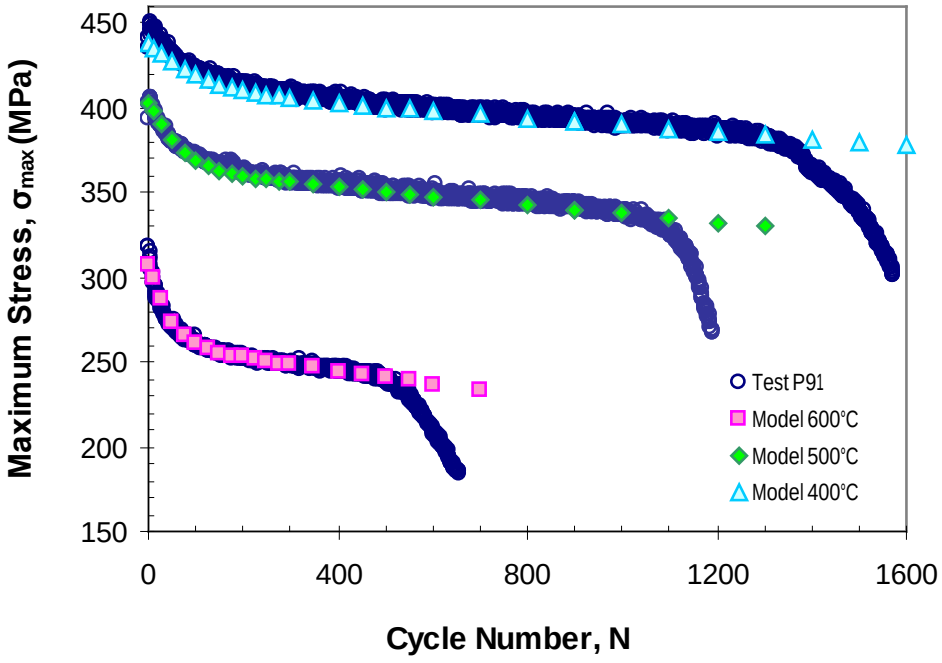

Figure 5.25: The prediction results of the viscoplasticity model with linear nonlinear isotropic hardening for P91 parent material at different temperatures

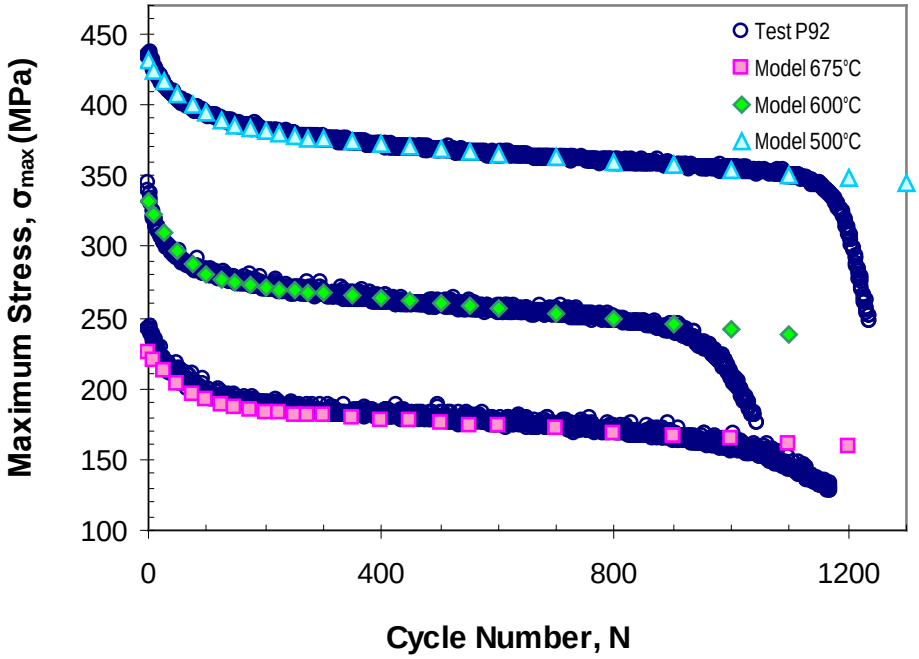

Figure 5.26: The prediction results of the viscoplasticity model with linear nonlinear isotropic hardening for P92 parent material at different temperatures

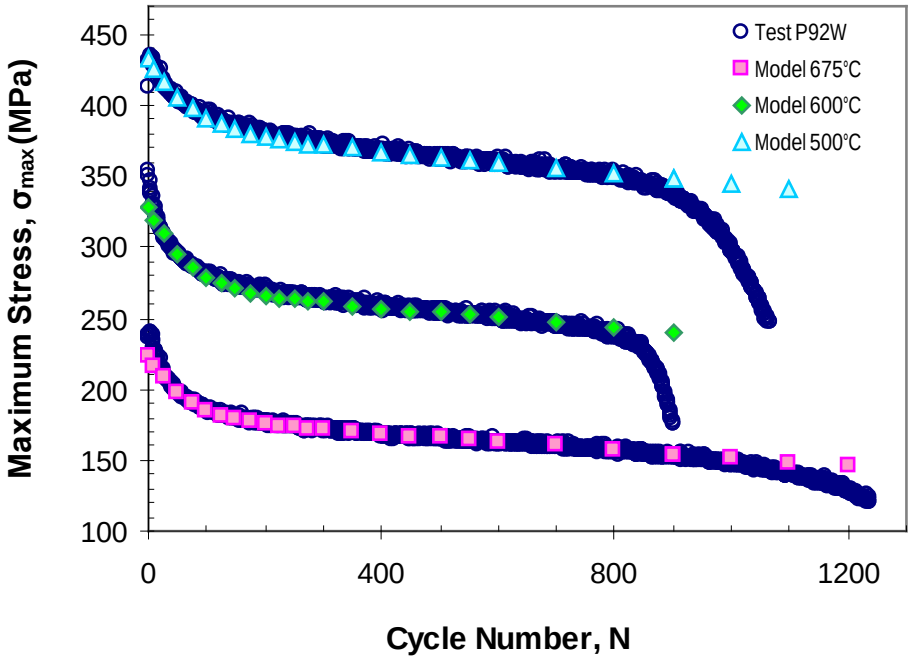

Figure 5.27: The prediction results of the viscoplasticity model with linear nonlinear isotropic hardening for P92 weld metal at different temperatures

5.6 Conclusions

A viscoplasticity model has been developed and is presented in this section for the P91 and P92 steels under cyclic loading and high temperatures. Several conclusions can be drawn from this section, as follows:

- The unified viscoplasticity model is able to model the cyclic plasticity behaviour and time-dependent effects such as stress relaxation. The model used in this study has 10 temperature dependent material constants.
- Initial constants can be estimated from tension-compression test data, in which 8 of the constants can be estimated from the first monotonic tensile curve of the first cycle, and two of the constants can be estimated using the stress relaxation data of the first cycle.
- The accuracy of the initial constants can be improved by using an optimisation procedure. The 2 objective functions program has successfully produced a set of material constants which give very good predictions of the stress-strain behaviour, as compared to the experimental data.
- The three objective functions program was also implemented to improve the accuracy of the predictions of the model, particularly the stress relaxation behaviour. The optimisation of the constants results in good predictions for both the tension-compression tests and the constant strain dwell test data.
- The stress evolution behaviour can be improved by using the combined linear and nonlinear isotropic hardening model. The model has been used to successfully represent the linear evolution in the second stage of cyclic softening. Thus the current set of models is capable of accurately predicting the stress-strain behaviour of the P91 and the P92 steels for the majority of the specimen's lifetime, excluding the third stage of cyclic softening which corresponds to the crack propagation stage.

Chapter 6 – Finite element simulation using the viscoplasticity model

6.1 Overview

In this study, the ABAQUS finite element (FE) simulation software was used to simulate the behaviour of the P91 and the P92 steels. The constitutive model of the steels was defined using an external software called Zmat which is compatible with ABAQUS. This chapter focuses on validating the performance of the developed viscoplasticity model by comparing the finite element simulation results with experimental data such as those obtained from the isothermal tests at different strain ranges, the thermo-mechanical fatigue tests and the notched specimen tests.

6.2 Implementation of the viscoplasticity model in ABAQUS

The unified Chaboche viscoplasticity model was implemented in the commercial finite element software ABAQUS through the use of an external software called Zmat. The Zmat software is a material library software which provides facilities for defining advanced material constitutive equations. The components of the viscoplasticity model equations such as the inelastic strain rate, the kinematic hardening and the isotropic hardening equations can be defined in a material definition file which is linked to the ABAQUS input file.

The multiaxial form of the unified viscoplasticity model is as follows:-

$$\dot{\boldsymbol{\varepsilon}}_p = \dot{\lambda}\frac{\partial f}{\partial \boldsymbol{\sigma}} \tag{6.1}$$

$$f = J(\boldsymbol{\sigma} - \boldsymbol{\chi}) - R \tag{6.2}$$

$$J(\boldsymbol{\sigma} - \boldsymbol{\chi}) = \left(\frac{3}{2}(\boldsymbol{\sigma}' - \boldsymbol{\chi}) : (\boldsymbol{\sigma}' - \boldsymbol{\chi})\right)^{1/2} \tag{6.3}$$

$$\frac{\partial f}{\partial \boldsymbol{\sigma}} = \frac{3}{2}\frac{(\boldsymbol{\sigma}' - \boldsymbol{\chi})}{J(\boldsymbol{\sigma} - \boldsymbol{\chi})} \tag{6.4}$$

where f is the yield function, $\boldsymbol{\sigma}'$ is the deviatoric stress tensor, $\boldsymbol{\chi}$ is the back stress tensor and R is the isotropic measure of the yield size, λ is the plastic multiplier which corresponds to magnitude of plastic increment and $\frac{\partial f}{\partial \boldsymbol{\sigma}}$ determines the direction of the plastic flow. In Zmat, the plastic multiplier is defined by selecting a flow type named as *Norton* flow law (which is similar to the classical Norton creep power law) corresponding to the time dependent behaviour as given by the following equation:-

$$\dot{\lambda} = \left\langle \frac{f}{K} \right\rangle^{n} \tag{6.5}$$

where K and n are material constants. The constant K is the same constant as the constant Z in Equation 5.1. For the von Mises yield criterion behaviour, the plastic multiplier is equal to the accumulated plastic strain ($\lambda = p$).

The kinematic hardening evolution equation, in multiaxial form as given by Zmat software, is as follows:-

$$\dot{\boldsymbol{\chi}}_i = \frac{2}{3} c \dot{\boldsymbol{\varepsilon}}_p - D \boldsymbol{\chi}_i \dot{p} \tag{6.6}$$

where i=1,2,…,M and c and D are material constants. Equation 6.6 is defined by selecting the nonlinear option for the kinematic properties in the software. The value of c/D is the saturation of the stress value in the plastic region and this value is represented by the constant a in Equation 5.4. The constant D is equal to the constant C in Equation 5.4 which represents the speed to reach the saturation values. The decomposition of the total backstress into a number of additive parts can also be implemented in Zmat by defining several nonlinear kinematic hardening

properties in the material definition file. In this study, it has been chosen that M=2 in order to decompose the kinematic hardening equations into two components.

The isotropic hardening equation, as given in Equation 5.10, is defined in Zmat by selecting the nonlinear option for the isotropic properties and the nonlinear isotropic hardening in Zmat is given by the following equation:-

$$R = R_0 + Q(1 - e^{-bp}) \tag{6.7}$$

where constant Q is the asymptotic value of the isotropic variable, constant b is related to the speed towards saturation and the saturation yield surface radius will be $R_0 + Q$ for large accumulated plastic strain. The value of R_0 for initial yield surface radius is noted here to be the onset of plasticity, and not the engineering yield stress, and the method of determining this constant is explained in section 5.3.1. As the P91 and the P92 steels exhibit a gradual linear decrease in the middle of the test period, after a nonlinear decrease of stress amplitudes, the isotropic hardening behaviour is better described by the two-stage isotropic hardening model, as described in Chapter 5 as the combined linear and nonlinear isotropic hardening. In Zmat, the "linear_nonlinear" option can be selected for this purpose and its equation is given as follows:-

$$R = R_0 + Hp + Q(1 - e^{-bp}) \tag{6.8}$$

where H is a material constant representing the slope of the linear period during cyclic softening of the steels. The examples of the Zmat's material definition file for the unified viscoplasticity model are given in the appendix section.

6.3 FE simulation of the isothermal cyclic loading

The optimized viscoplasticity constants for the P91 and P92 steels in this study were determined using the isothermal strain-controlled test data with a ±0.5% strain amplitude at different temperatures. In this section, the optimised viscoplasticity

model with linear nonlinear isotropic hardening at 600°C was used in finite element simulation in order to simulate the isothermal stress-strain behaviour at different strain ranges, namely ±0.2%, ±0.25% and 0.4% strain amplitudes and to compare the simulation results with the experimental data. The cyclic period for each simulation was identical to its testing period with a 0.1%/s strain rate.

An axisymmetric model with a 3.25mm radius, R_1, and a 7.5mm height, H, as shown in Figure 6.1(a), was used in the simulation to represent the gauge section of the solid specimen, where the extensometer arms were placed during the strain-controlled tests. Figure 6.1(b) shows the axisymmetric model of the tubular specimen, with a 2mm inner radius, R_2, used for the thermomechanical fatigue tests. Displacement control was applied in order to obtain the same strain range as that for the experimental data. The boundary conditions on the axisymmetric models are shown in Figures 6.1(a) and 6.1(b). The 8-node biquadratic, reduced integration, element, called CAX8R in the Abaqus finite element software, were used for all the geometries presented in this chapter.

Figures 6.2 to 6.4 show the comparison between the simulation and the testing results of the P91 steels performed at 600°C with ±0.4%, ±0.25% and ±0.2% strain amplitudes, respectively. The simulation and the testing results show good comparison at each test particularly at the first complete cycle. The stress amplitude recorded in each cycle decreases as the number of cycle increases and a larger number of cycles is required to achieve the saturation period of the cyclic softening for the tests with lower strain amplitudes. The comparison of these results with experimental data shows promising results up to the secondary stage of cyclic softening for each test with different strain amplitudes. The results in this section indicate the suitability of selecting the strain-controlled test data with higher strain

amplitude to be used in the determination of the material model constants. The accuracy of the stress-strain behaviour of the viscoplasticity model may be inmproved by considering a different set of data with different strain amplitudes in the optimisation procedure in determining the material constants in the model.

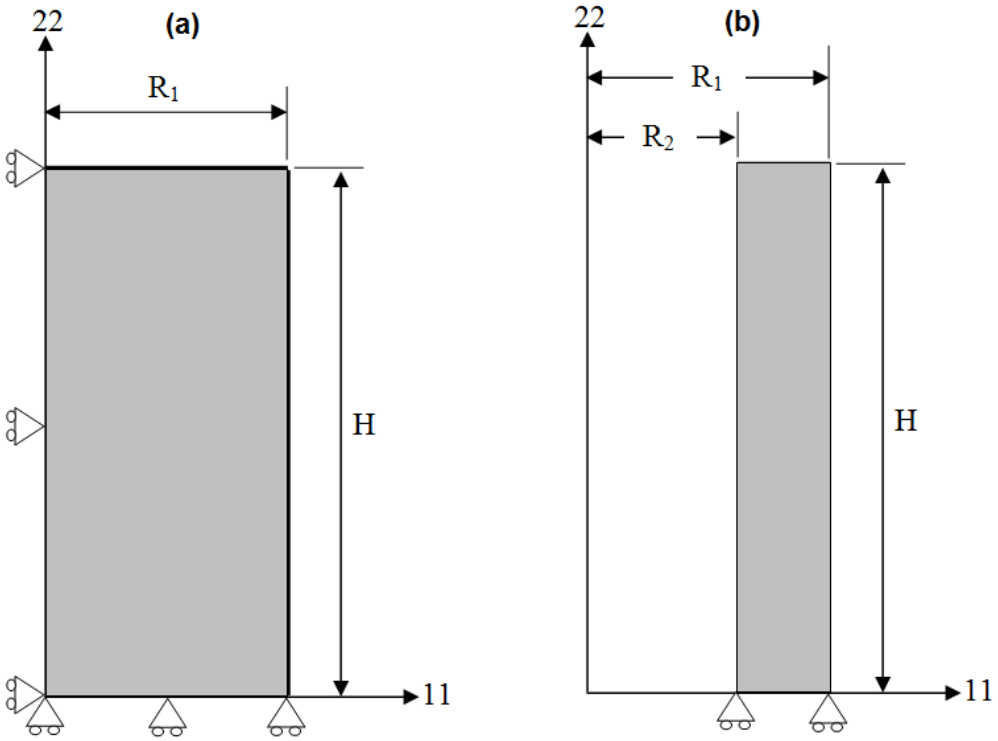

Figure 6.1: The axisymmetric model geometries of (a) the solid specimen and (b) the tubular specimen used in the uniaxial finite element simulation

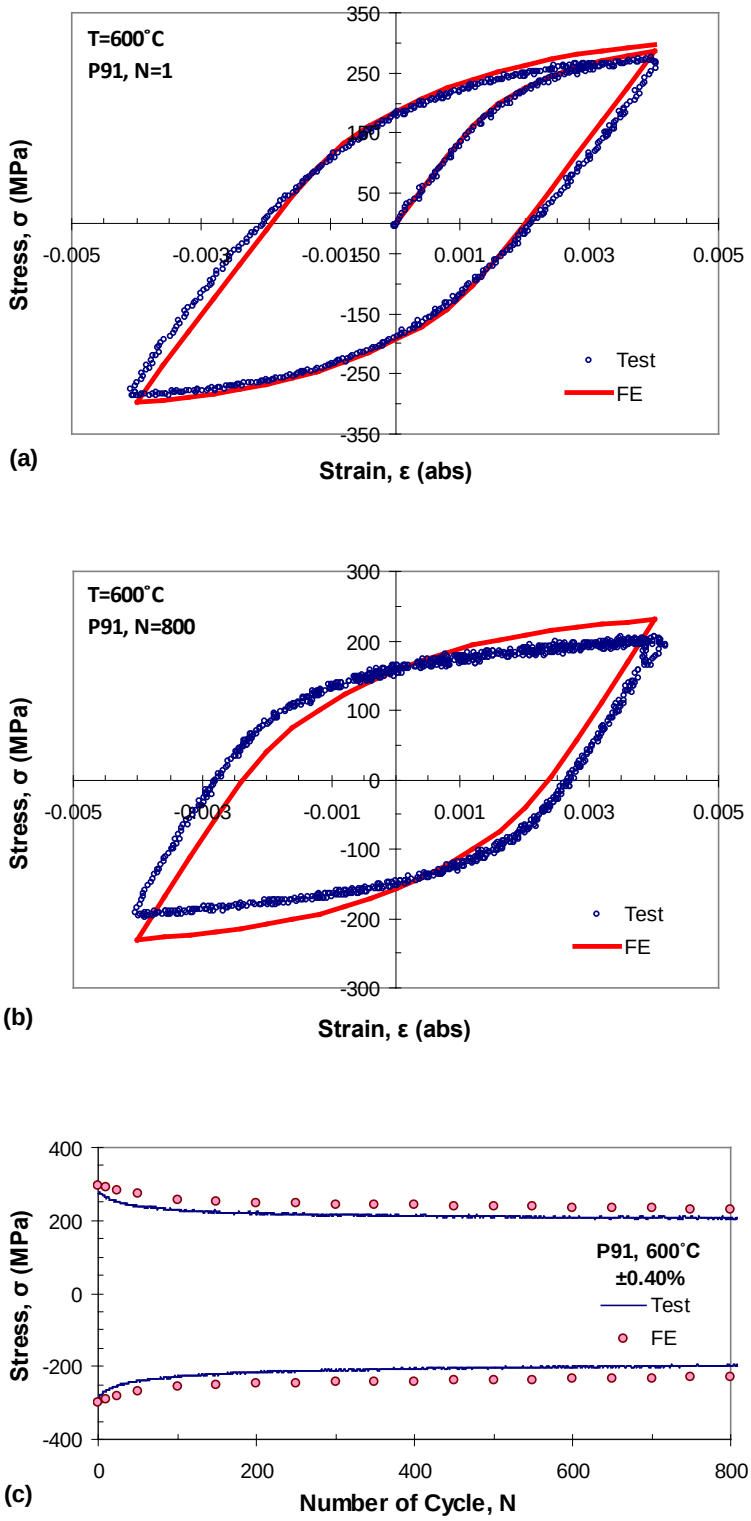

Figure 6.2: Comparison of the test and the FE simulation results for the P91 parent material, isothermal strain-controlled test of ±0.40% amplitude at 600°C, for (a) the first cycle, (b) the 800th cycle and (c) the evolution of maximum and minimum stresses up to 800th cycle

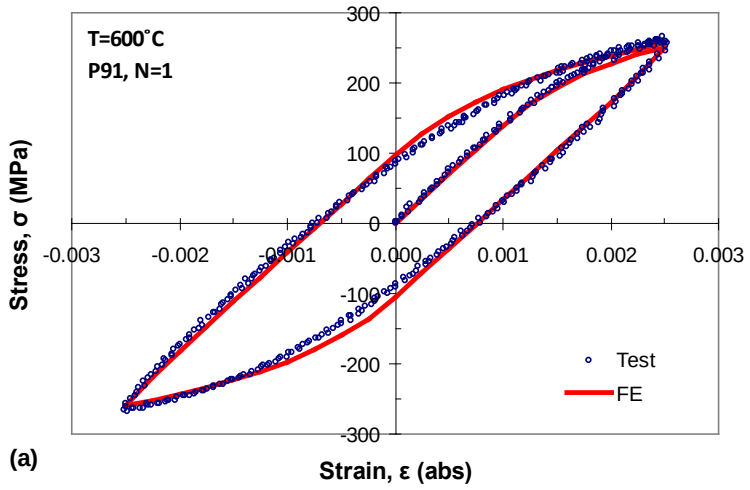

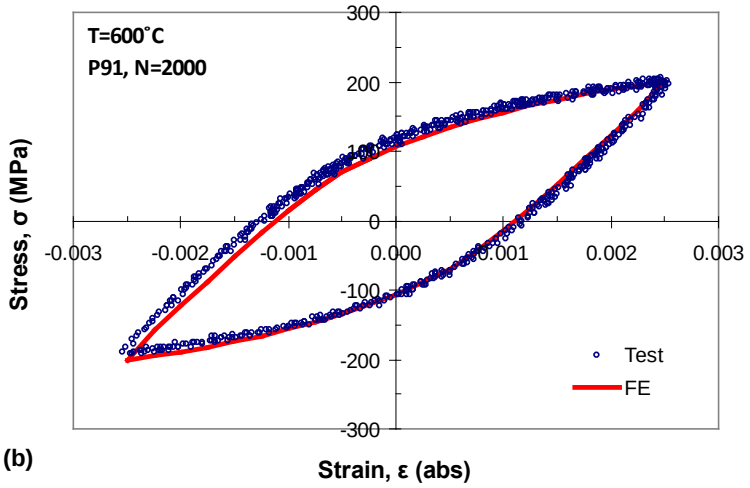

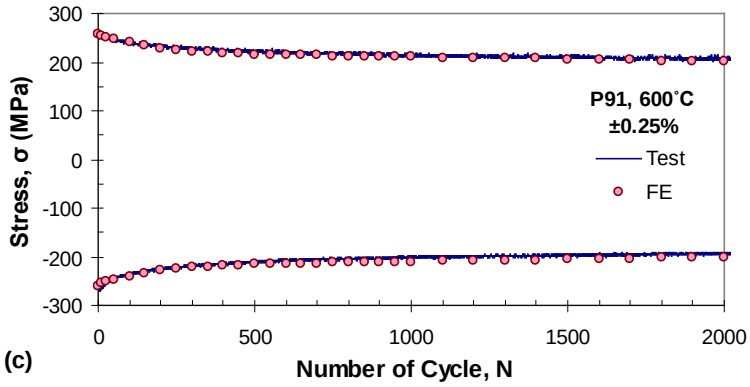

Figure 6.3: Comparison of the test and the FE simulation results for the P91 parent material, isothermal strain-controlled test of ±0.25% amplitude at 600°C, for (a) the first cycle, (b) the 2000th cycle and (c) the evolution of maximum and minimum stresses up to 2000th cycle

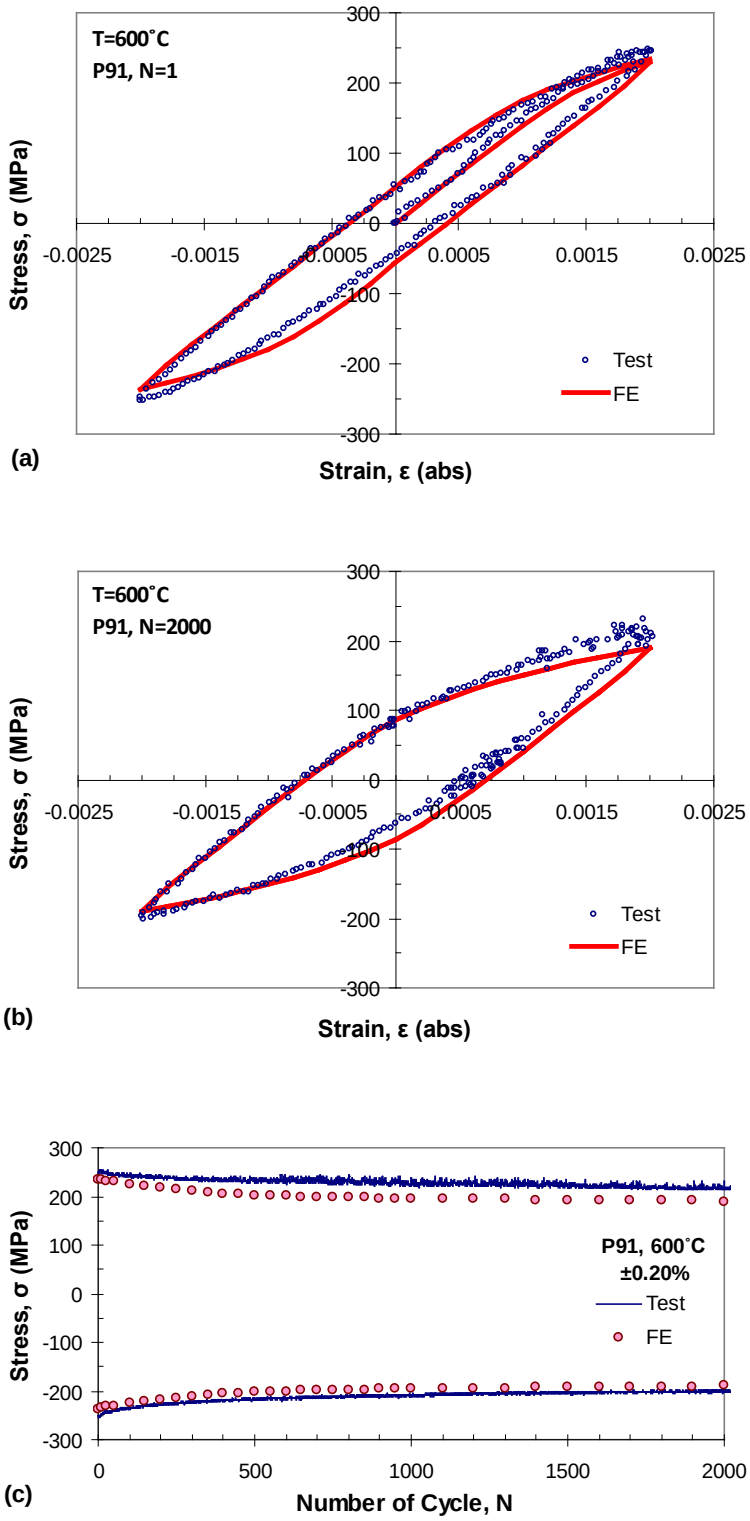

Figure 6.4: Comparison of the test and the FE simulation results for the P91 parent material, isothermal strain-controlled test of ±0.20% amplitude at 600°C, for (a) the first cycle, (b) the 2000th cycle and (c) the evolution of maximum and minimum stresses up to 2000th cycle

6.4 FE simulation of the isothermal notched specimen

The aim of the finite element simulation of the notched specimen is to validate the multiaxial behaviour of the developed viscoplasticity model. Again, the optimised constants for the viscoplasticity model with two-stage cyclic softening for the P91 steel at 600°C were used in the simulation. The notched specimen, as given in Figure 3.4, was represented by an axisymmetic model, from a quarter of the actual specimen, in the simulation as shown in Figure 6.5. The boundary conditions on the notched bar model are complete displacement constraint in the 22-direction for all nodes located on the 11-axis. The simulations were carried out with two-types of load-controlled condition. Firstly, the model was subjected to a fully reversed triangular waveform of load-controlled condition with maximum load of ±42.188MPa at the top of specimen, as indicated by the red arrow, resulting an approximately ±300MPa mean axial stress on the minimum notch cross-section, in the model which is the same as the test loading for a 20 seconds of cyclic period. The second simulation applied similar loading as the first simulation with an additional 2 minutes holding period at tensile peak load resulting in a cyclic period of 140 seconds.

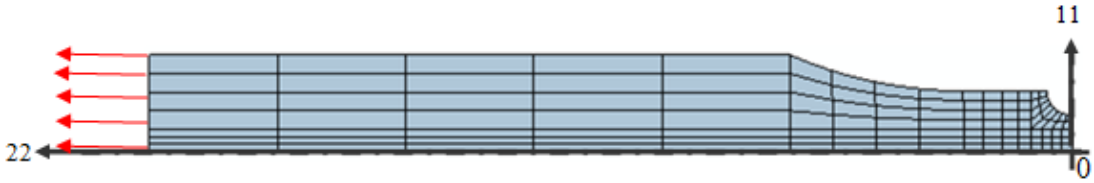

Figure 6.5: The axisymmetric model geometry of the notched specimen used in the finite element simulation

Figure 6.6 shows the simulation results of the notched specimen at the first complete loop (time equal to 25 seconds). The maximum von-Mises stress (red-contour) is located at the notch root of the specimen. The notch root area is the critical area of the specimen as the fracture of the specimen occurs in this area. The stress-strain simulation results in different directions at the location of the notch root,

indicated by point A, are shown in Figure 6.7. From the figure, it is clear that the stress-strain response in the 22-direction, which is the loading direction, is the most significant direction in the simulation and the loop indicates clearly the effect of plasticity at the notch root position. On the contrary, the nodal stress-strain results at the tip of the extensometer arm reveal linear stress-strain behaviour in all directions as shown in Figure 6.8. The extensometer arms is illustrated by the grey pin and located at 6.25mm from the centre line, as shown in Figure 6.6.

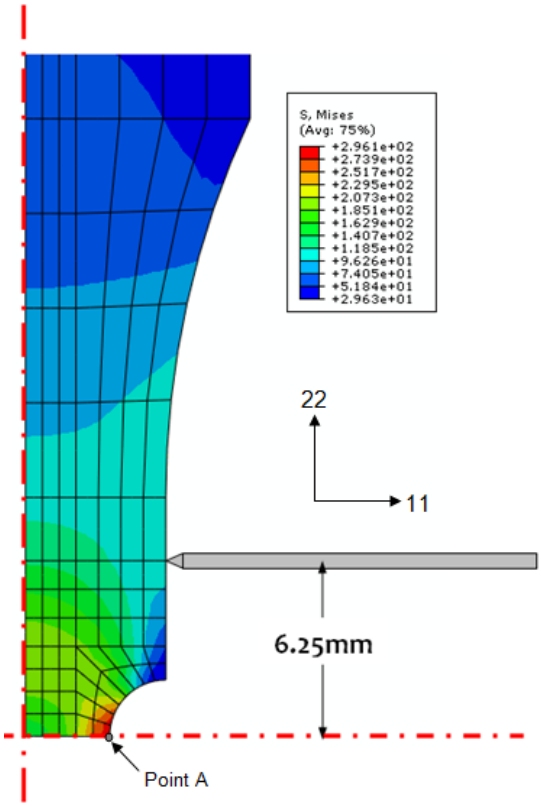

Figure 6.6: The von Mises stress results of the notched bar fully reversed simulation at 25 seconds and the schematic representation of the extensometer location on the specimen

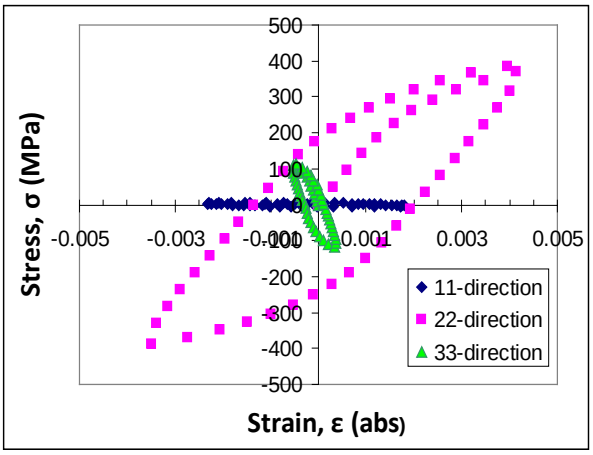

Figure 6.7: The nodal stress-strain simulation results of the fully reversed load-controlled condition at the notch root location

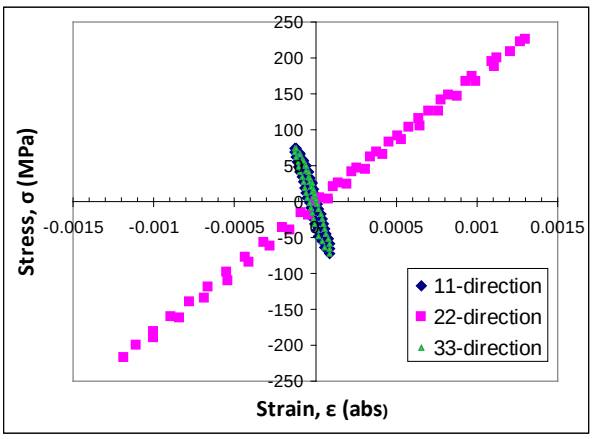

Figure 6.8: The nodal stress-strain simulation results of the fully reversed load-controlled condition at the extensometer arm location

Figures 6.9 (a) to (c) show the simulation results of the notched bar specimen with tension-compression loading for 3 specimen's models with different mesh densities around the notch root. The reason for conducting the simulation on these models is to observe the mesh sensitivity effect around the notch root area. The results for the figures were taken at 985 seconds, which is the 50th cycle of the test. The nodal von-Mises stress results at the notch root for Figures 6.9 (a) to (c) are 307.304, 304.868 and 301.158 MPa, respectively. The increase of mesh density contributes to the decrease of the stress results. However, it has been shown that the difference between the predictions of the model is small (less than 1.2% difference in the

stress results). Thus, the model in Figure 6.9(c) was chosen to be used in further analyses.

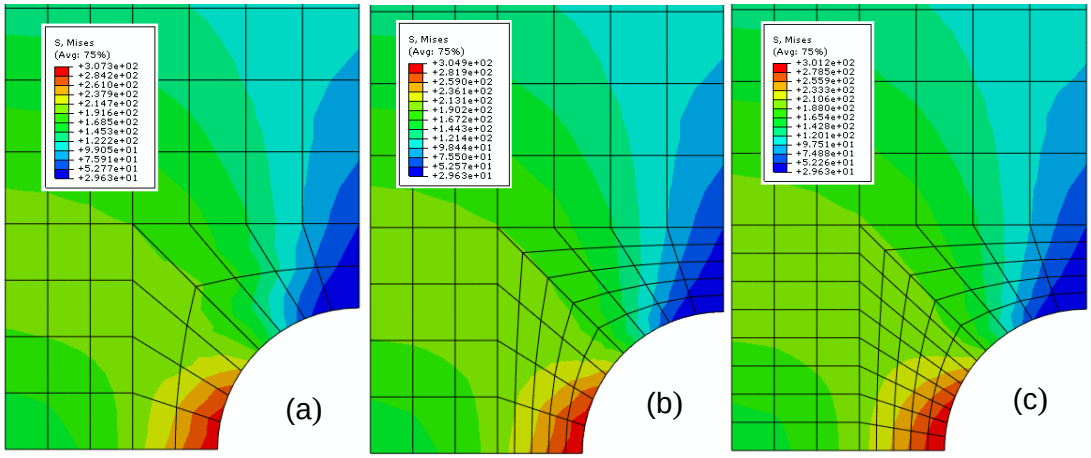

Figure 6.9: The von-Mises stress distribution in the notched specimen model for 3 different mesh densities around the notch root

The displacement of the extensometer in actual testing is the only parameter that can be used as comparison to the finite element calculations. Figure 6.10 shows the peak displacement values of the simulation results of the extensometer point in a cycle up to 1000 cycles and the corresponding test results of the fully reversed stress-controlled test. The simulation and the test results are in good agreement. After the 1000th cycle, the displacement of the actual test increases relatively more rapidly due to propagation of cracks for which the material model is not capable to model. For the notched specimen test with 2 minutes dwell periods, both the simulation and the test results show the ratchetting effect in the test in which the peak displacement value in a cycle keeps increasing as the number of cycles increases, as shown in Figure 6.11. The test and the simulation results with dwell periods show good comparison for the first 4 cycles. However, the simulation results deviate from the test results as the number of cycle increase which may be due to the effect of ratchetting. Since the comparison for the fully reversed stress-

controlled case has shown a promising result, the simulation results may be further used to predict the failure life of the notched specimen.

The fatigue life of the notched specimen in the fully reversed stress-controlled test can be predicted using the energy based fatigue model. In Chapter 4, the fatigue model is developed using the solid specimen subjected to uniaxial loading as given in Equation 4.7. The number of cycles to failure, N_f, in the equation is based on a 5 percent stress drop failure criterion in the strain-controlled test. By using this 5 percent criterion in the stress-controlled test of the notch specimen, during which the displacement values increase through out the test as the P91 steel shows cyclic softening behaviour, the number of cycles to failure is 1150 cycle as shown in Figure 6.12.

In multiaxial cases such as the notched specimen, the plastic strain energy per cycle can be determined from the sum of the hysteresis loop areas associated with all components (Charkaluk, 2009). The hysteresis loop areas were determined from the stress-strain results at the start of the stabilized period where the displacement range increases steadily as the number of cycles increases as suggested by Constantinescu et al. (2004). Based on the simulation results, the stabilized stage started at the 50^{th} cycle. The stress-strain values during the 50^{th} cycle at the notch root area (point A), which is the critical area for the crack initiation and growth in the notched specimen, were used to estimate the number of cycles to failure. The results of the nodal stress-strain at point A can be reasonably used where the difference of the von-Mises stress results at the 985^{th} seconds between the nodal point and the integration point is small (less than 5 MPa). The hysteresis loop areas were determined using the trapezoid method as described in Chapter 4. The sum of the hysteresis loop areas, based on the nodal stress-strain results of point A, is 2.51

MJ/m^3. By using the values of 271.36 and -0.714 for K and α constants, respectively, for Equation 4.7, the predicted number of cycles to failure is 631 cycle, which is 45 percent lower than the experimental N_f.

According to several researches on the evaluation of fatigue life of notched components (Leidermark et al., 2011; Susmel, 2008; Susmel and Taylor, 2007), the stress-strain results at the notch root point predict less accurate number of cycles to failure. The authors implement the "theory of critical distances" in predicting the fatigue life of notched component in order to find a satisfying fatigue life. In the case of the simulation of notched specimen in this study, considering the node at notch root as reference point, the simulation results at different node locations predicted different number of cycles to failure as shown in Table 6.1. From the table, the point inside the specimen which is 0.24mm to the left of notch root in Figure 6.9(c), the predicted number of cycles to failure is 1038 cycle, which is very close to the test results. The result indicates that the critical distance seems to give more accurate results and a better method to predict the failure life of notched specimen and it should be studied further on the P91 and the P92 steels in future work.

Table 6.1: Prediction of failure life based on the simulation results at different node locations located to the left of notch root

Node location (mm)	**$\Sigma Area_{loop}$ (MJ/m^3)**	**N_f**
0	2.719	631
0.12	2.296	799
0.24	1.905	1038
0.36	1.575	1355
0.48	1.275	1821

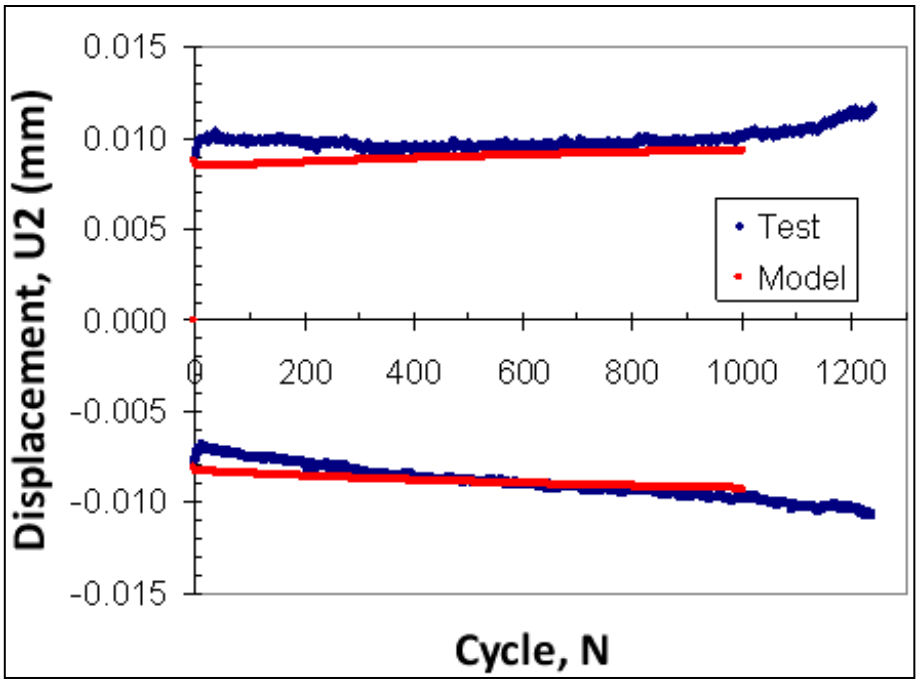

Figure 6.10: The comparison of extensometer displacement in the test and the nodal displacement of the same location in the FE simulation for the fully reversed load-controlled condition

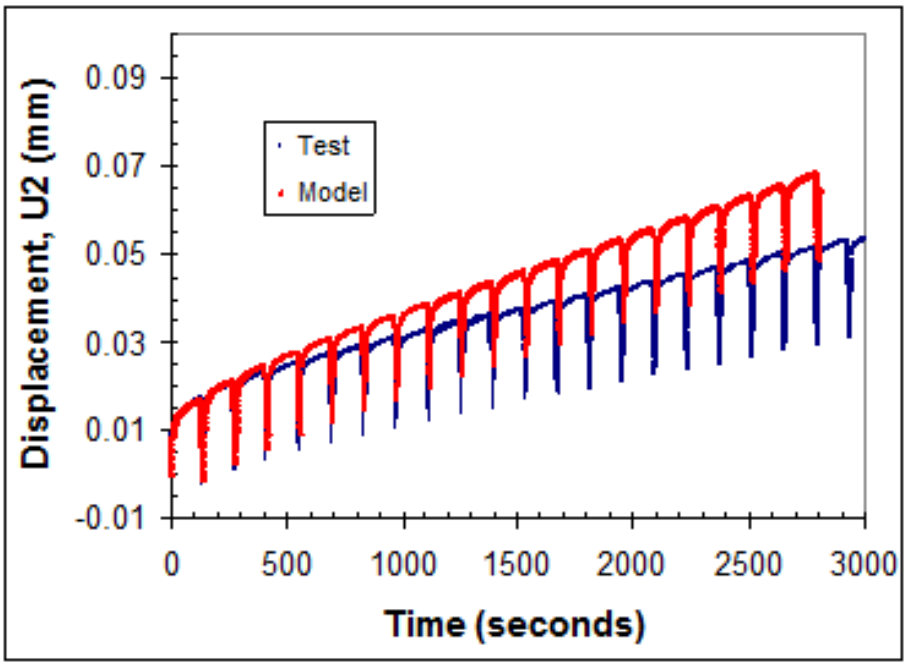

Figure 6.11: The comparison of extensometer displacement in the test and the nodal displacement of the same location in the FE simulation for the notched specimen test with 2 minutes dwell periods

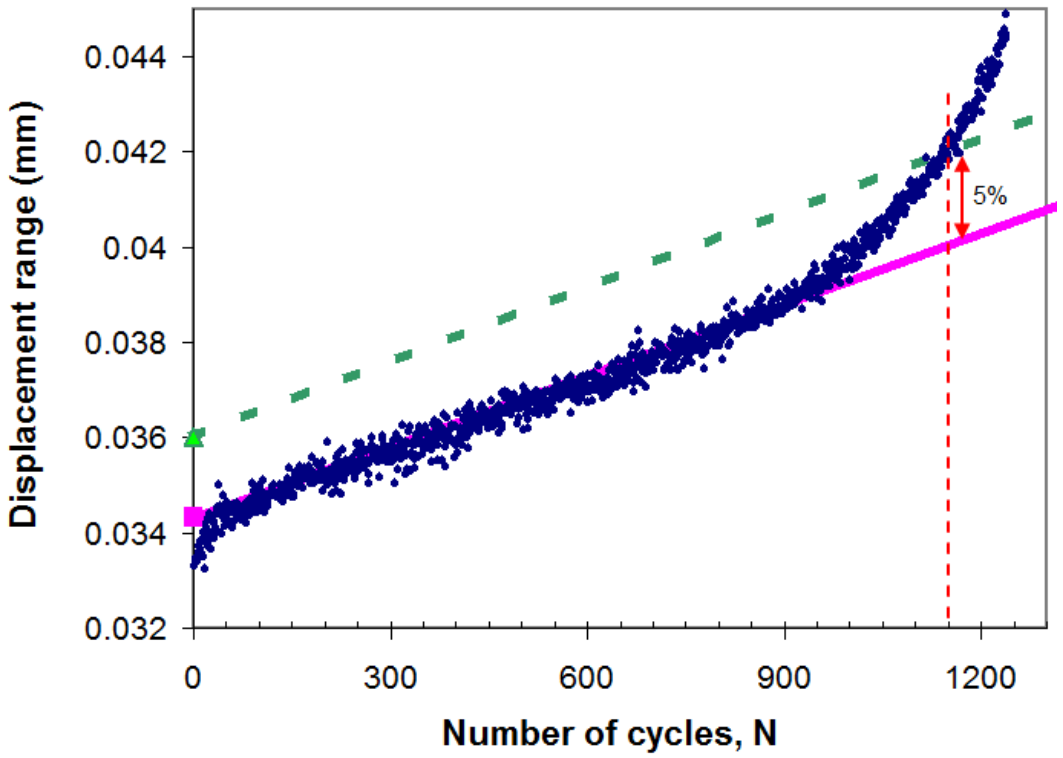

Figure 6.12: Determination of the number of cycles to failure for the fully reversed stress-controlled test of the P91 steel

6.5 FE simulation of anisothermal fatigue loading

The optimised constants for the viscoplasticity model for the P91 and the P92 steels, determined using the isothermal tests data, were further used to simulate the stress-strain behaviour of the steels under cyclic thermal and mechanical conditions. In the thermo-mechanical fatigue tests, as described in Chapter 3, the tubular specimens were used and the experimental results are compared to the simulation results in this chapter. The specimen was modelled as an axisymmetric model in the finite element simulation as shown in Figure 6.1(b). In the simulation of the anisothermal condition, temperature was applied for the whole geometry and a coefficient of thermal expansion (CTE), determined from TMF test results, was applied to include the effect of thermal strain to the total strain value. The CTE

constants for the P91 and the P92 steels used in the simulations are 14.5×10^{-6}/˚C and 14.9×10^{-6}/°C, respectively.

The comparison of thermo-mechanical simulations and experimental results of the P91 steels is shown in Figures 6.13 to 6.16. The simulation results are generally in good agreement with experimental data. These figures also show that the P91 steel softens cyclically under TMF conditions as indicated by the stress range reduction with cycle number. The stress amplitude evolution stabilises around the 100th cycle. Figure 6.14, which presents the results at 400-600˚C under an out-of-phase condition, gives 100MPa peak stress difference in compression. However, the cyclic trends of this figure are similar where the stress levels become stable, between 500 and 600˚C in compressive strain, before achieving the maximum total strain which is controlled in this study. This observation may correspond to the creep phenomenon which is important at high temperature. Similarly, Figure 6.13 also shows a similar trend for steady stress levels at temperatures between 500 and 600˚C. Even though the specimen corresponding to this figure (Figure 6.13) failed after a very small number of cycles (less than 10 cycles), the stress-strain data are still important in order to show the significance of the creep between 500 and 600˚C for the P91 steel. Figures 6.15 and 6.16 show a very good comparison between the simulation and the experimental data for the in-phase and the out-of-phase conditions in temperature range of 400-500°C for the P91 steel. For this temperature range, the stabilization of stress level in a cyclic loop is not observed which may indicate less significant creep effect for the temperature below 500°C.

Figures 6.17 and 6.18 show the comparison between the experimental data and the simulation results of the P92 parent material in the in-phase and the out-of-phase TMF conditions, respectively, for the temperature range of 500 to 675°C. The

stress-strain loops for these figures also indicate the stability of the stress level at high temperature particularly at temperature approximately above 580°C. In general, the comparison of the stress-strain loops and the evolution of stress amplitudes are in good agreement up to the stabilization stage of cyclic softening behaviour.

For this TMF experimental data presented, it can be seen that there is some instability (i.e. data is not as smooth) when compared to the isothermal equivalents. This is due to the instability of the air cooling through the centre of the specimen due to the waveform being used (i.e. small time period per cycle and therefore sudden, rapid heating/cooling which results heating/cooling 'blasts'). Subsequently, it has been found that this effect can be reduced by constantly applying a small amount of cooling air through the centre of the specimen (~5%) during all regions of the waveform, including the heating of the specimen. This means that when an increase in air cooling is required, it can ramp up in a much more controlled manner.

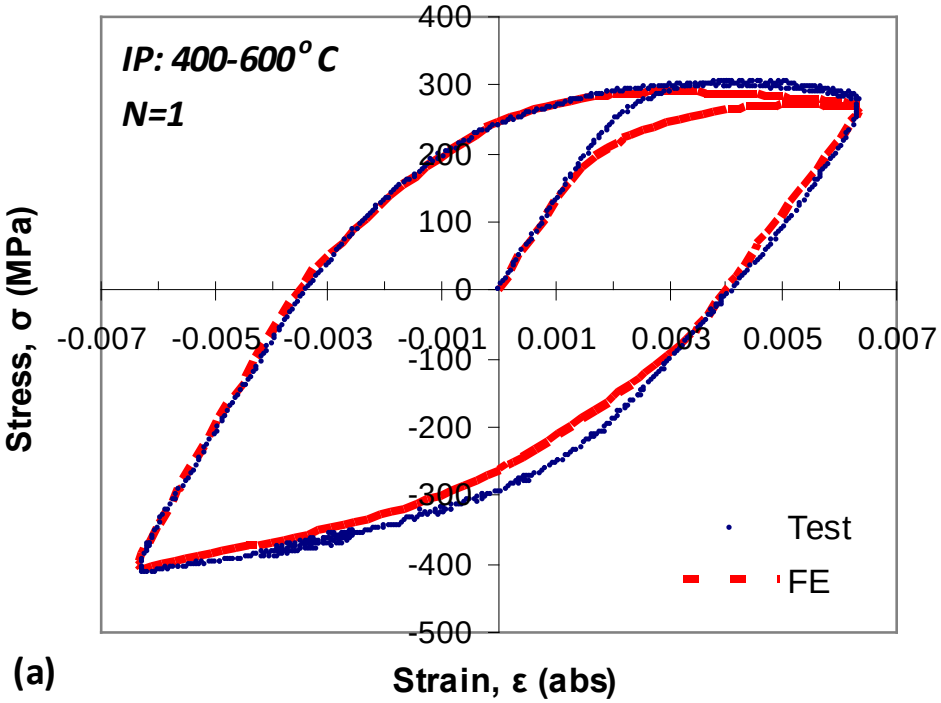

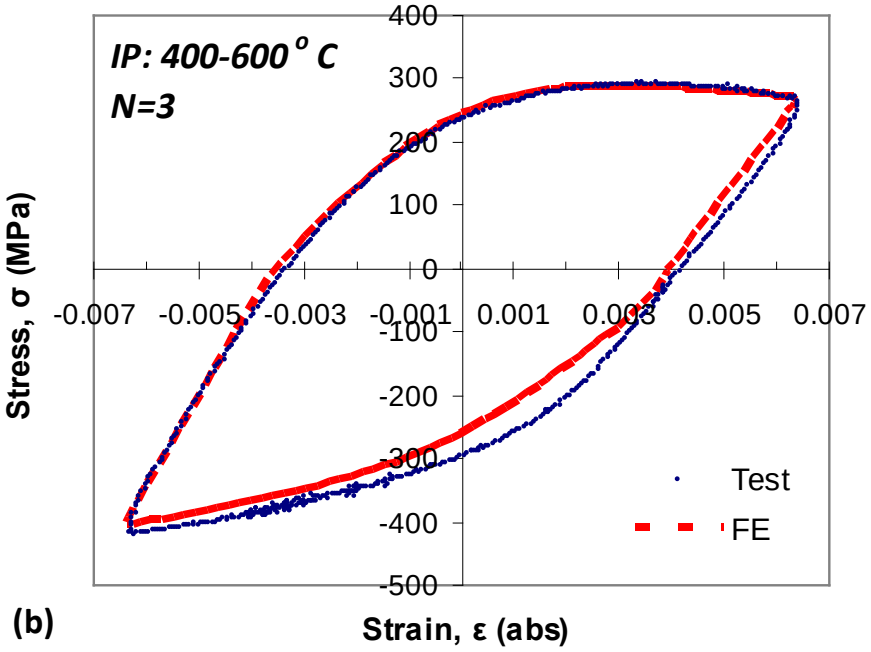

Figure 6.13: Comparison of the test and the FE simulation results for the P91 parent material with TMF in-phase, 400-600°C, for (a) the first cycle and (b) the third cycle

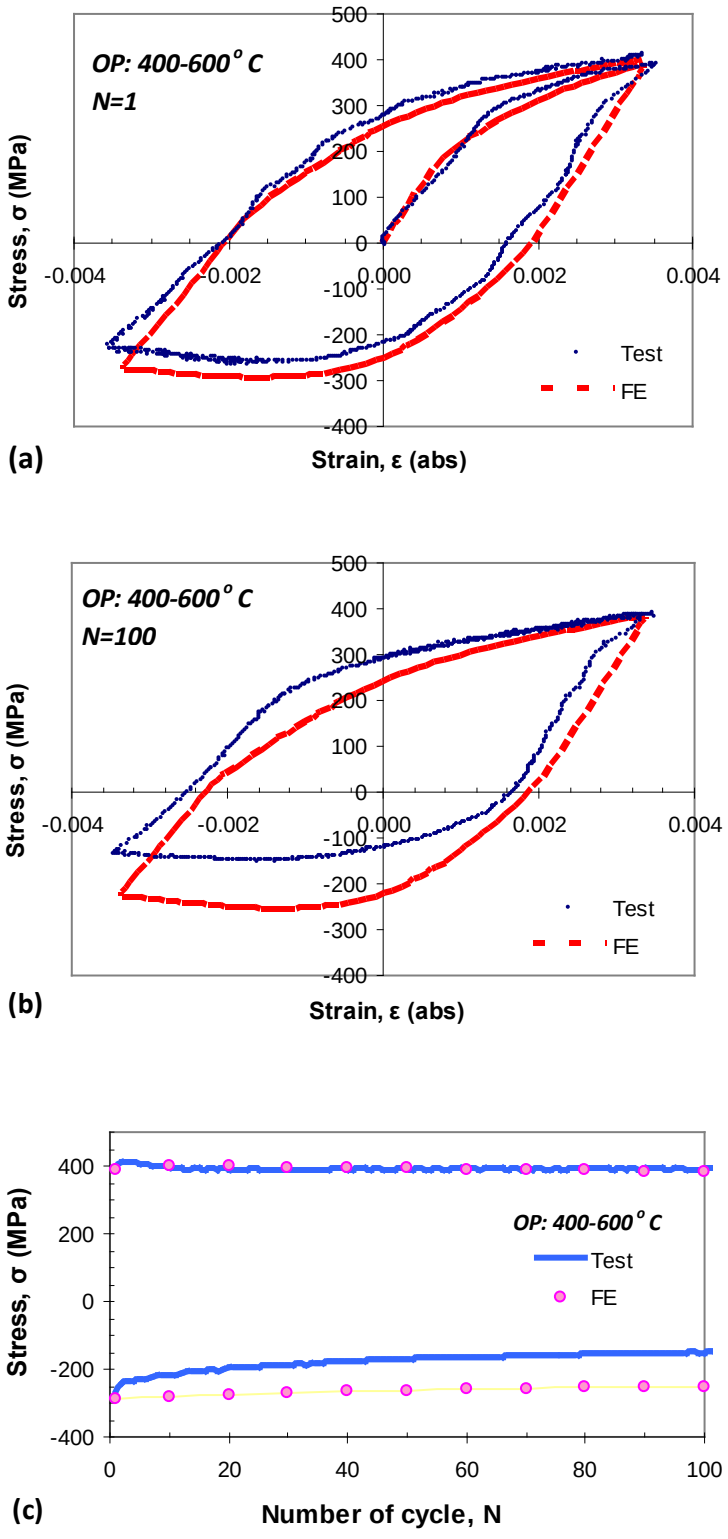

Figure 6.14: Comparison of the test and the FE simulation results for the P91 parent material with TMF out-of-phase, 400-600°C, for (a) the first cycle, (b) the 100th cycle and (c) the evolution of maximum and minimum stresses up to 100th cycle

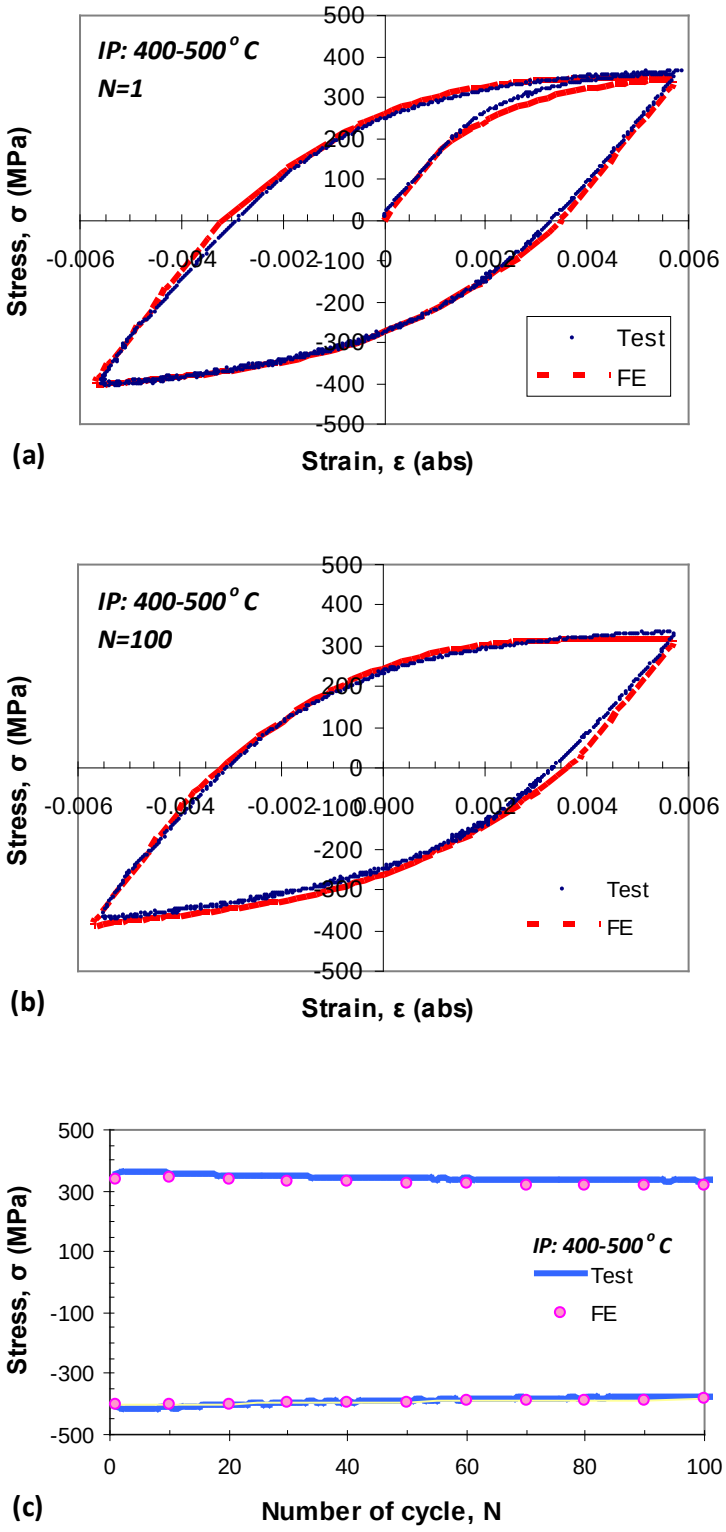

Figure 6.15: Comparison of the test and the FE simulation results for the P91 parent material with TMF in-phase, 400-500°C, for (a) the first cycle, (b) the 100th cycle and (c) the evolution of maximum and minimum stresses up to 100th cycle

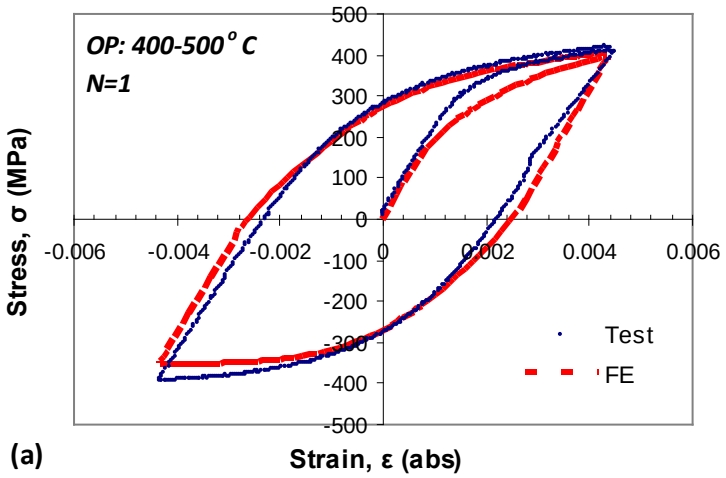

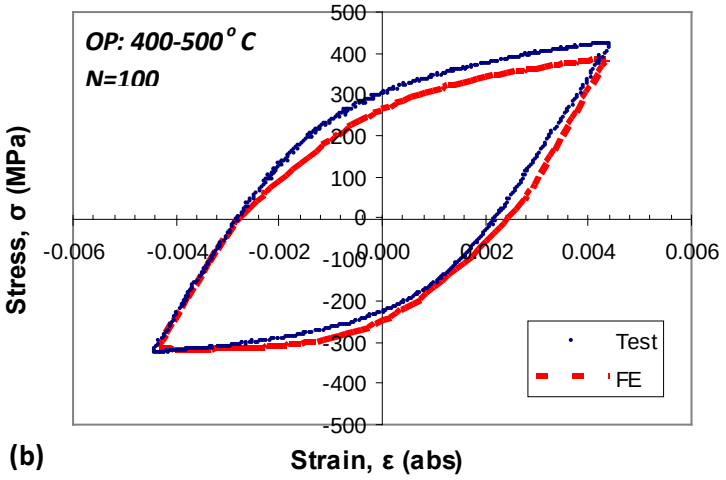

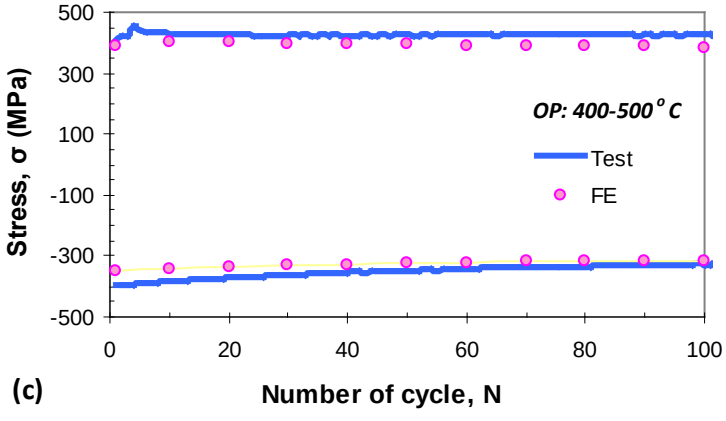

Figure 6.16: Comparison of the test and the FE simulation results for the P91 parent material with TMF out-of-phase, 400-500°C, for (a) the first cycle, (b) the 100th cycle and (c) the evolution of maximum and minimum stresses up to 100th cycle

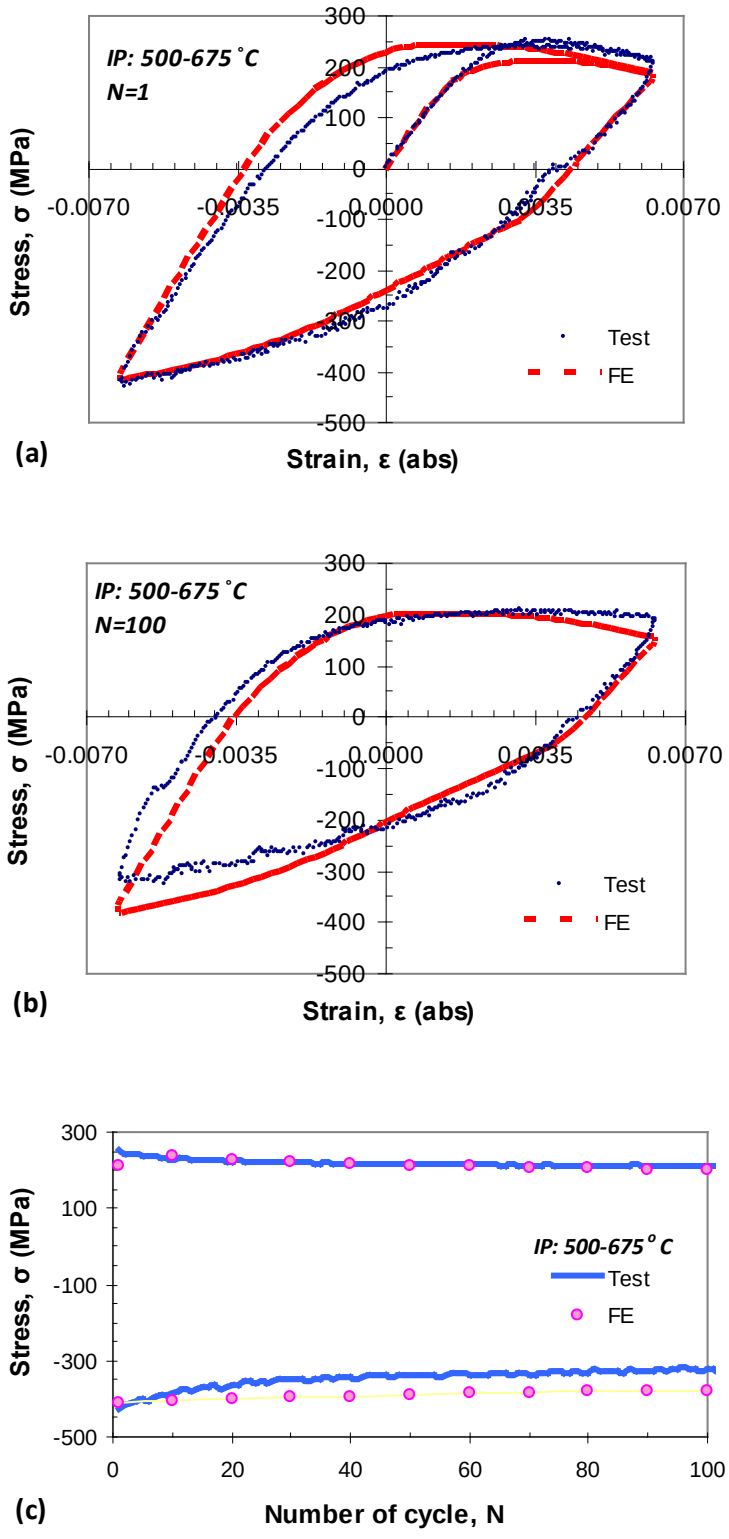

Figure 6.17: Comparison of the test and the FE simulation results for the P92 parent material with TMF in-phase, 500-675°C, for (a) the first cycle, (b) the 100th cycle and (c) the evolution of maximum and minimum stresses up to 100th cycle

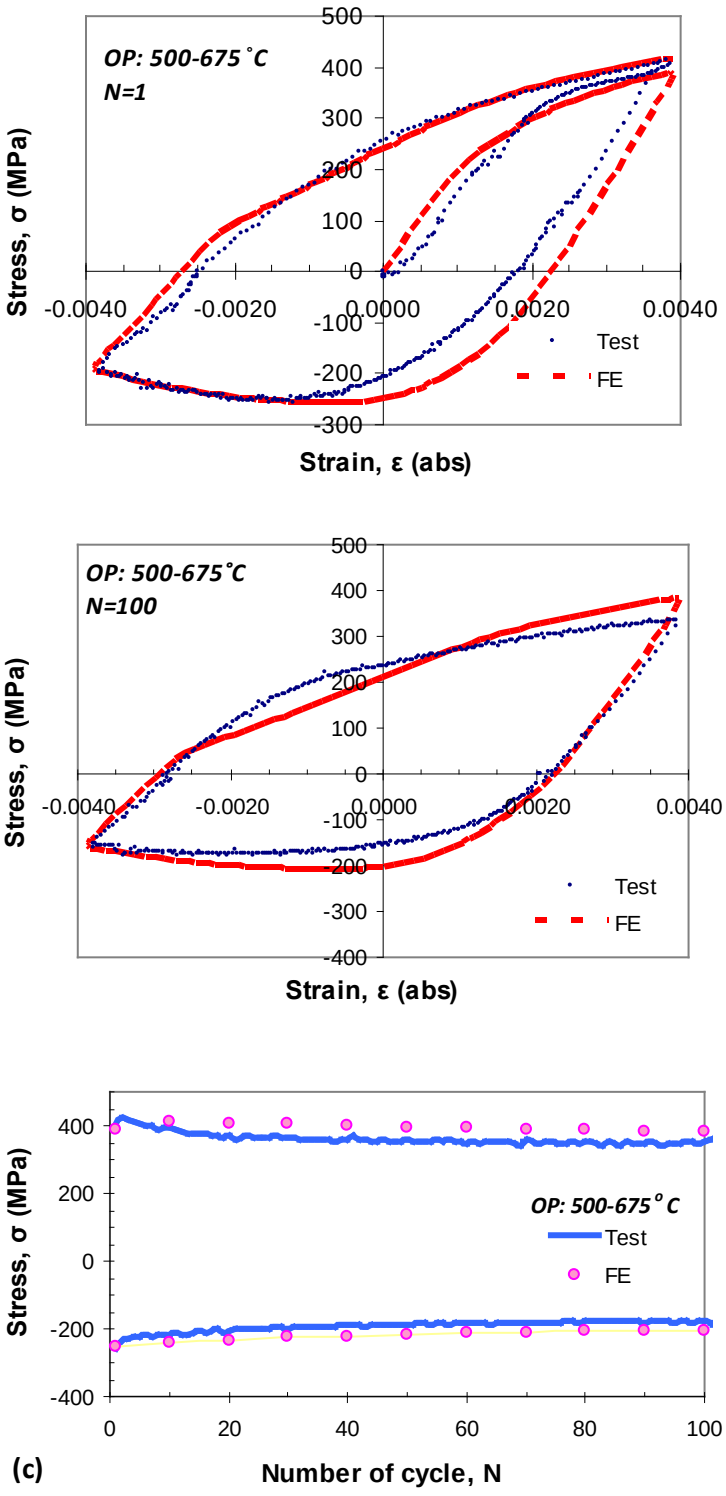

Figure 6.18: Comparison of the test and the FE simulation results for the P92 parent material with TMF out-of-phase, 500-675°C, for (a) the first cycle, (b) the 100th cycle and (c) the evolution of maximum and minimum stresses up to 100th cycle

6.6 Conclusions

This chapter has presented the simulation results of the P91 and the P92 steel behaviour using the viscoplasticity model. The following conclusions can be drawn from this chapter:

- The simulation of the viscoplasticity model, developed by using data from high strain amplitude tests, gives good stress-strain comparison to the lower strain amplitudes.
- The simulation results of the notched specimen indicate the capability of the model to predict the stress-strain behaviour in multiaxial conditions. The prediction of the notched specimen's failure life can be further improved by implementing the critical distance theory.
- Identification of viscoplasticity constants using data from the isothermal tests gives good comparison to the thermo-mechanical behaviour.
- All the simulation results show cyclic softening behaviour where the stress amplitude decreases in a strain-controlled test while the strain amplitude increases in the stress-controlled test. The nonlinear evolution of cyclic parameters (i.e. stress or strain amplitude) in the initial cyclic period and then the stabilisation of the parameters have been modelled satisfactorily by the developed viscoplasticity model.

Chapter 7 – Conclusions and future work

The research has focussed on the testing and the development of a material constitutive model of the P91 and the P92 steels under thermo-mechanical fatigue condition at high temperature. Based on the stress-strain data obtained in the test, the sets of material constants for the viscoplasticity models of the steels have been determined and the constants can be used in a commercial finite element software for further analysis.

7.1 Conclusions

The cyclic loading tests on the P91 and the P92 steels have been performed on three types of specimens in isothermal and anisothermal conditions using the Instron 8862 TMF testing system. The temperature gradient along the gauge section of the specimens was controlled to within ±10°C of the target temperature. The main thermocouple, which controls the temperature of the test specimen, was instrumented on the shoulder of specimen initially in order to avoid crack initiation at the welding point of thermocouple wires. It has been found that in most cases the instrumentation of the main thermocouple in the middle of gauge section with a low possible current during spot welding will not initiate cracks at the welding point of thermocouple wires.

The results of the cyclic loading tests of the steels at high temperature exhibit cyclic softening behaviour with three distinct stages. The stages of one to three represent rapid cyclic softening followed by a stabilisation period and finally a crack growth stage. The mechanical parameters, such as the plastic strain range, the stress range and the hysteresis loop area, show a stabilised condition in the second stage of cyclic softening. The softening behaviour is associated with the coarsening of the

subgrains and it has been observed in the microstructural investigations of the cyclic loading specimens at different life fractions. The coarsening of the subgrains occurs rapidly in the first stage of cyclic softening and it slowly continues in the second and the third stage. The microstructural evolutions during the first two stages of cyclic softening do not significantly cause damage to the steels as indicated by the plot of Young's modulus. The initiation of cracks at the end of the stabilisation stage indicates the starting point of the significant material's damage and the load bearing capacity of the steel decreases as a consequence of macro crack development in the third stage of softening.

The viscoplasticity models for the P91 and the P92 steels have been developed and the stress-strain predictions have shown good comparison to experimental data, particularly in temperature range of 400 to 600°C and 500 to 675°C respectively. The material constants were initially estimated from the tension-compression test data. The implementation of the optimisation programme significantly improves the accuracy of stress-strain predictions of the viscoplasticity model. The constants give very good predictions of the stress-strain behaviour in cyclic stress-strain conditions up to about half the number of cycles to failure. The model also gives reasonably good predictions of stress relaxation behaviour. The stress-strain behaviour predictions of the stabilisation stage has been further improved by using the combined linear and nonlinear isotropic hardening model and consequently the viscoplasticity model is capable of predicting stress-strain softening behaviour up to the end of stabilisation stage.

The finite element simulation using the viscoplasticity model has been implemented in ABAQUS software with an external material library software called Zmat. The simulation results of the behaviour of the steels with various strain ranges, cyclic

thermo-mechanical conditions and notched geometry show good comparison to the experimental data. The promising predictive capability indicates that the model can be used in cyclic thermo-mechanical conditions and under multiaxial stress states at high temperature. The simulation of notched specimen indicates the requirement to select the stress-strain data at a point near the notch root in order to predict better failure lives.

7.2 Future work

Based on the research work presented in this study, some potential work can be further implemented in order to improve and extend the current work in the future as follows:

- Repetition of test should be implemented, which depends on the availability of specimens, in order to check the scatter of the experimental data. The repetition of test can also increase the level of confidence for the determination of the number of cycles to failure, particularly for the thermo-mechanical fatigue tests in which the trend of stress amplitude evolution of the third stages of cyclic softening seems inconsistent between the TMF tests.
- The understanding of the steels behaviour and the capability of the viscoplasticity model can be further improved by conducting the strain rate effect and ratchetting behaviour in the future research. However, the consideration of this kind of behaviour will require more specimens in the testing programme.
- The microstructural investigation of the interrupted cyclic tests specimens using the transmission electron microscope should be further studied by focussing on the dislocation density evolution. The statistically representative data, such as the misorientation angles, should be also

studied by using the electron microscope with electron backscattered diffraction (EBSD) capability in order to support the research finding quantitatively. However, this work is more relevant to specific research on the metallurgy of the steels.

- The optimisation programme can be further improved by considering more than one set of test data as the objective functions so that the programme can produce the optimised constants which give good prediction for different set of loading types. The current optimisation programme only considers one set of experimental data in each optimisation process.
- The two-stage isotropic hardening equation can be included in the current optimisation programme in order to obtain optimised material constants which can predict good stress-strain behaviour up to the end of stabilised stage of the cyclic softening of the steels.
- The finite element prediction of welded pipes, which consist of parent material and weld metal, subjected to realistic thermo-mechanical fatigue loading can be implemented to observe the stress-strain behaviour in real components of power plant.
- The experimental works on the determination of critical distance in a notched specimen should be implemented in order to improve the understanding of the stress-strain behaviour in the notched specimen and predict better number of cycles to failure.

REFERENCES

ABE, F., KERN, T.-U. & VISWANATHAN, R. (2008) *Creep resistant steels,* Cambridge, Woodhead Publishing.

ARMAS, A. F., PETERSEN, C., SCHMITT, R., AVALOS, M. & ALVAREZ, I. (2004) Cyclic instability of martensite laths in reduced activation ferritic/martensitic steels. *Journal of Nuclear Materials,* 329-333**,** 252-256.

AVANZINI, A. (2008) Mechanical characterization and finite element modelling of cyclic stress-strain behaviour of ultra high molecular weight polyethylene. *Materials & Design,* 29**,** 330-343.

BARI, S. & HASSAN, T. (2000) Anatomy of coupled constitutive models for ratcheting simulation. *International Journal of Plasticity,* 16**,** 381-409.

BECK, T. & RAU, K. (2008) Temperature measurement and control methods in TMF testing â€“ a comparison and evaluation. *International Journal of Fatigue,* 30**,** 226-233.

BENDICK, W., CIPOLLA, L., GABREL, J. & HALD, J. (2010) New ECCC assessment of creep rupture strength for steel grade X10CrMoVNb9-1 (Grade 91). *International Journal of Pressure Vessels and Piping,* 87**,** 304-309.

BERNHART, G., MOULINIER, G., BRUCELLE, O. & DELAGNES, D. (1999) High temperature low cycle fatigue behaviour of a martensitic forging tool steel. *International Journal of Fatigue,* 21**,** 179-186.

BHADESHIA, H. K. D. H. (2003) Mechanisms and Models for Creep Deformation and Rupture. IN MILNE, I., RITCHIE, R. O. & KARIHALOO, B. (Eds.) *Comprehensive Structural Integrity.* Oxford, Pergamon.

BILLO, E. J. (2007) *Excel for scienctists and engineers: numerical methods,* New Jersey, John Wiley & Sons.

BRETT, S. J. (2003) Service experience of weld cracking in CrMoV steam pipework systems. *2nd International Conference on Integrity of High Temperature Welds.* London.

BRETT, S. J. (2007) UK experience with modified 9Cr (grade 91) steel. *VTT Symposium (Valtion Teknillinen Tutkimuskeskus),* 1**,** 48-60.

CALLISTER, W. D. (2000) *Materials science and engineering: an introduction,* New York, John Wiley & Sons.

CHABOCHE, J. L. (1986) Time-independent constitutive theories for cyclic plasticity. *International Journal of Plasticity,* 2**,** 149-188.

CHABOCHE, J. L. (1989) Constitutive equations for cyclic plasticity and cyclic viscoplasticity. *International Journal of Plasticity,* 5**,** 247-302.

CHABOCHE, J. L. (2001) Unified Model of Cyclic Viscoplasticity Based on the Nonlinear Kinematic Hardening Rule. IN LEMAITRE, J. (Ed.) *Handbook of Materials Behavior Models.* Burlington, Academic Press.

CHABOCHE, J. L. (2008) A review of some plasticity and viscoplasticity constitutive theories. *International Journal of Plasticity,* 24**,** 1642-1693.

CHABOCHE, J. L. & ROUSSELIER, G. (1983) On the Plastic and Viscoplastic Constitutive Equations - Part 1: Rules Developed With Internal Variable Concept. *Journal of Pressure Vessel Technology,* 105**,** 153-159.

CHABOCHE, J. L. & GALLERNEAU, F. (2001) An overview of the damage approach of durability modelling at elevated temperature. *Fatigue and Fracture of Engineering Materials and Structures,* 24, 405-418.

CHARKALUK, E., BIGNONNET, A., CONSTANTINESCU, A. & DANG VAN, K. (2002) Fatigue design of structures under thermomechanical loadings. *Fatigue and Fracture of Engineering Materials and Structures,* 25**,** 1199-1206.

CHARKALUK, E. (2009) Energy as a damage factor in fatigue: Plenary lecture at the international conference low cycle fatigue 6. *Materialpruefung/Materials Testing,* 51**,** 269-275.

CHARKALUK, E. & CONSTANTINESCU, A. (2000) Energetic approach in thermomechanical fatigue for silicon molybdenum cast iron. *Materials at High Temperatures,* 17**,** 373-380.

CHUN, B. K., JINN, J. T. & LEE, J. K. (2002) Modeling the Bauschinger effect for sheet metals, part I: theory. *International Journal of Plasticity,* 18**,** 571-595.

CONSTANTINESCU, A., CHARKALUK, E., LEDERER, G. & VERGER, L. (2004) A computational approach to thermomechanical fatigue. *International Journal of Fatigue,* 26**,** 805-818.

DESHPANDE, A. A., LEEN, S. B. & HYDE, T. H. (2010a) Finite element prediction of creep-plastic ratchetting and low cycle creep-fatigue for a large SPF tool. *Journal of Materials Engineering and Performance,* 19**,** 452-466.

DESHPANDE, A. A., LEEN, S. B., SUN, W. & HYDE, T. H. (2010) Thermo-mechanical analysis and lifing of Ni-Cr SPF tool. *International Journal of Material Forming,* 3**,** 1151-1154.

DESHPANDE, A. A., LEEN, S. B. & HYDE, T. H. (2008) Finite element based predictions of life limiting behaviour for a large SPF tool. *Materialwissenschaft und Werkstofftechnik,* 39**,** 309-316.

DUBEY, J. S., CHILUKURU, H., CHAKRAVARTTY, J. K., SCHWIENHEER, M., SCHOLZ, A. & BLUM, W. (2005) Effects of cyclic deformation on subgrain evolution and creep in 9-12% Cr-steels. *Materials Science and Engineering: A,* 406**,** 152-159.

DUNNE, F. & PETRINIC, N. (2005) *Introduction to computational plasticity,* Oxford, Oxford University Press.

DUNNE, F. P. E. & HAYHURST, D. R. (1992a) Continuum damage based constitutive equations for copper under high temperature creep and cyclic plasticity. *Proceedings of the Royal Society: Mathematical and Physical Sciences,* 437**,** 545-566.

DUNNE, F. P. E. & HAYHURST, D. R. (1992b) Modelling of combined high-temperature creep and cyclic plasticity in components using continuum damage mechanics. *Proceedings of the Royal Society: Mathematical and Physical Sciences,* 437**,** 567-589.

DUNNE, F. P. E., MAKIN, J. & HAYHURST, D. R. (1992) Automated procedures for the determination of high temperature viscoplastic damage constitutive equations. *Proceedings of the Royal Society: Mathematical and Physical Sciences,* 437**,** 527-544.

EL GHARAD, A., ZEDIRA, H., AZARI, Z. & PLUVINAGE, G. (2006) A synergistic creep fatigue failure model damage (case of the alloy Z5NCTA at 550 °C). *Engineering Fracture Mechanics,* 73**,** 750-770.

ELLYIN, F. & KUJAWSKI, D. (1984) Plastic strain energy in fatigue failure. *Journal of Pressure Vessel Technology, Transactions of the ASME,* 106**,** 342-347.

ENNIS, P. J. & CZYRSKA-FILEMONOWICZ, A. (2003) Recent advances in creep-resistant steels for power plant applications. Sadhana - Academy Proceedings in Engineering Sciences, 28, 709-730.

ESSMANN, U. & MUGHRABI, H. (1979) ANNIHILATION OF DISLOCATIONS DURING TENSILE AND CYCLIC DEFORMATION AND LIMITS OF DISLOCATION DENSITIES. *Philosophical Magazine A: Physics of Condensed Matter, Structure, Defects and Mechanical Properties,* 40**,** 731-756.

EVANS, R. W. & WILSHERE, B. (1985) *Creep of metals and alloys,* London, Institute of Metals.

FAULKNER, R. G. (2008) Grain boundaries in creep-resistant steels. IN ABE, F., KERN, T.-U. & VISWANATHAN, R. (Eds.) *Creep-resistant steels.* Cambridge, Woodhead Publishing, CRC Press.

FIGIEL, L. & GÜNTHER, B. (2008) Modelling the high-temperature longitudinal fatigue behaviour of metal matrix composites (SiC/Ti-6242): Nonlinear time-dependent matrix behaviour. *International Journal of Fatigue,* 30**,** 268-276.

FOURNIER, B., SAUZAY, M., CAËS, C., NOBLECOURT, M. & MOTTOT, M. (2006) Analysis of the hysteresis loops of a martensitic steel: Part I: Study of the influence of strain amplitude and temperature under pure fatigue loadings using an enhanced stress partitioning method. *Materials Science and Engineering: A,* 437**,** 183-196.

FOURNIER, B., SAUZAY, M., CAËS, C., NOBLECOURT, M., MOTTOT, M., ALLAIS, L., TOURNIE, I. & PINEAU, A. (2009a) Creep-Fatigue Interactions in a 9 Pct Cr-1 Pct Mo Martensitic Steel: Part I. Mechanical Test Results. *Metallurgical and Materials Transactions A,* 40**,** 321-329.

FOURNIER, B., SAUZAY, M., BARCELO, F., RAUCH, E., RENAULT, A., COZZIKA, T., DUPUY, L. & PINEAU, A. (2009b) Creep-Fatigue Interactions in a 9 Pct Cr-1 Pct Mo Martensitic Steel: Part II. Microstructural Evolutions. *Metallurgical and Materials Transactions A,* 40**,** 330-341.

FOURNIER, B., DALLE, F., SAUZAY, M., LONGOUR, J., SALVI, M., CAES, C., TOURNIE, I., GIROUX, P. F. & KIM, S. H. (2011a) Comparison of various 9-12%Cr steels under fatigue and creep-fatigue loadings at high temperature. *Materials Science and Engineering A,* 528, 6934-6945.

FOURNIER, B., SAUZAY, M. & PINEAU, A. (2011b) Micromechanical model of the high temperature cyclic behaviour of 9-12%Cr martensitic steels. *International Journal of Plasticity,* 27, 1803-1816.

FREDERICK, C. O. & ARMSTRONG, P. J. (2007) A mathematical representation of the multiaxial Bauschinger effect. *Materials at High Temperatures,* 24**,** 1-26.

GONG, Y. P., HYDE, C. J., SUN, W. & HYDE, T. H. (2010) Determination of material properties in the Chaboche unified viscoplasticity model *Proceedings of the Institution of Mechanical Engineers, Part L: Journal of Materials: Design and Applications,* 224**,** 19-29.

HAARMANN, K., VAILLANT, J. C., VANDENBERGHE, B., BENDICK, W. & ARBAB, A. (2002) *The T91/P91 book*, Vallourec & Mannesmann Tubes.

HÄHNER, P., RINALDI, C., BICEGO, V., AFFELDT, E., BRENDEL, T., ANDERSSON, H., BECK, T., KLINGELHÖFFER, H., KÜHN, H.-J., KÖSTER, A., LOVEDAY, M., MARCHIONNI, M. & RAE, C. (2008) Research and development into a European code-of-practice for strain-controlled thermo-mechanical fatigue testing. *International Journal of Fatigue,* 30**,** 372-381.

HALD, J. (2008) Microstructure and long-term creep properties of 9-12% Cr steels. *International Journal of Pressure Vessels and Piping,* 85**,** 30-37.

HALES, R., HOLDSWORTH, S. R., O'DONNELL, M. P., PERRIN, I. J. & SKELTON, R. P. (2002) A code of practice for the determination of cyclic stress-strain data. *Materials at High Temperatures,* 19**,** 165-185.

HARTROTT, P. V., HOLMSTROM, S., CAMINADA, S. & PILLOT, S. (2009) Life-time prediction for advanced low alloy steel P23. *Materials Science and Engineering A,* 510-511, 175-179.

HAYHURST, R. J., MUSTATA, R. & HAYHURST, D. R. (2005) Creep constitutive equations for parent, Type IV, R-HAZ, CG-HAZ and weld material in the range 565-640 °C for Cr-Mo-V weldments. *International Journal of Pressure Vessels and Piping,* 82**,** 137-144.

HAYHURST, D. R., LIN, J. & HAYHURST, R. J. (2008) Failure in notched tension bars due to high-temperature creep: Interaction between nucleation controlled cavity growth and continuum cavity growth. *International Journal of Solids and Structures,* 45**,** 2233-2250.

HERTZBERG, R. W. (1996) *Deformation and fracture mechanics of engineering materials,* New York, John Wiley & Sons.

HOLDSWORTH, S. (2010) Creep-fatigue interaction in power plant steels. HIDA-5 International Conference, 23-25 June 2010, Guildford, UK.

HYDE, C. J., SUN, W. & LEEN, S. B. (2010) Cyclic thermo-mechanical material modelling and testing of 316 stainless steel. *International Journal of Pressure Vessels and Piping,* 87**,** 365-372.

HYDE, C. J. (2010) Thermo-mechanical fatigue and creep of high temperature materials. University of Nottingham.

HYDE, T. H., SUN, W. & WILLIAMS, J. A. (2003) Creep analysis of pressurized circumferential pipe weldments - A review. *Journal of Strain Analysis for Engineering Design,* 38**,** 1-30.

HYDE, T. H., BECKER, A. A., SUN, W. & WILLIAMS, J. A. (2006) Finite-element creep damage analyses of P91 pipes. *International Journal of Pressure Vessels and Piping,* 83**,** 853-863.

IGARASHI, M. (2008) Alloy design philosophy of creep-resistant steel. IN ABE, F., KERN, T.-U. & VISWANATHAN, R. (Eds.) *Creep-resistant steels.* Cambridge, Woodhead Publishing, CRC Press.

JIANG, Y. & KURATH, P. (1996) Characteristics of the Armstrong-Frederick type plasticity models. *International Journal of Plasticity,* 12**,** 387-415.

JIANG, Y. & ZHANG, J. (2008) Benchmark experiments and characteristic cyclic plasticity deformation. *International Journal of Plasticity,* 24**,** 1481-1515.

KICHENIN, J., VAN, K. D. & BOYTARD, K. (1996) Finite-element simulation of a new two-dissipative mechanisms model for bulk medium-density polyethylene. *Journal of Material Science,* 31**,** 1653-1661.

KIM, T.-W., KANG, D.-H., YEOM, J.-T. & PARK, N.-K. (2007) Continuum damage mechanics-based creep-fatigue-interacted life prediction of nickel-based superalloy at high temperature. *Scripta Materialia,* 57**,** 1149-1152.

KIM, J.-B., LEE, H.-Y., PARK, C.-G. & LEE, J.-H. (2008) Creep-fatigue test of a SA 316SS structure and comparative damage evaluations based upon elastic and inelastic approaches. *International Journal of Pressure Vessels and Piping,* 85**,** 550-556.

KIMURA, M., YAMAGUCHI, K., HAYAKAWA, M., KOBAYASHI, K. & KANAZAWA, K. (2006) Microstructures of creep-fatigued 9-12% Cr ferritic heat-resisting steels. *International Journal of Fatigue,* 28**,** 300-308.

KITAHARA, H., UEJI, R., TSUJI, N. & MINAMINO, Y. (2006) Crystallographic features of lath martensite in low-carbon steel. *Acta Materialia,* 54**,** 1279-1288.

KOO, G. and LEE, J. (2007) Investigation of ratcheting characteristics of modified 9Cr-1Mo steel by using the Chaboche constitutive model. *International Journal of Pressure Vessel*, 84, 284-292.

KOSTKA, A., TAK, K. G., HELLMIG, R. J., ESTRIN, Y. & EGGELER, G. (2007) On the contribution of carbides and micrograin boundaries to the creep strength of tempered martensite ferritic steels. *Acta Materialia,* 55**,** 539-550.

KRAUSS, G. (1999) Martensite in steel: strength and structure. *Materials Science and Engineering A,* 273-275**,** 40-57.

KREMPL, E. (2000) Viscoplastic models for high temperature applications. *International Journal of Solids and Structures,* 37**,** 279-291.

KRUML, T. & POLÁK, J. (2001) Fatigue softening of X10CrAl24 ferritic steel. *Materials Science and Engineering A,* 319-321**,** 564-568.

LEEN, S. B., DESHPANDE, A. & HYDE, T. H. (2010) Experimental and numerical characterization of the cyclic thermomechanical behavior of a high temperature forming tool alloy. *Journal of Manufacturing Science and Engineering, Transactions of the ASME,* 132.

LEIDERMARK, D., MOVERARE, J., SEGERSALL, M., SIMONSSON, K., SJOSTROM, S. & JOHANSSON, S. (2011) Evaluation of fatigue crack initiation in a notched single-crystal superalloy component. *Procedia Engineering,* 10**,** 619-624.

LEMAITRE, J. (2001) *Handbook of Materials Behavior Models,* Burlington, Academic Press.

LEMAITRE, J. & CHABOCHE, J. L. (1994) *Mechanics of solid materials,* Cambridge, Cambridge University Press.

MANNAN, S. L. & VALSAN, M. (2006) High-temperature low cycle fatigue, creep-fatigue and thermomechanical fatigue of steels and their welds. *International Journal of Mechanical Sciences,* 48**,** 160-175.

MARUYAMA, K., SAWADA, K. & KOIKE, J. I. (2001) Strengthening mechanisms of creep resistant tempered martensitic steel. *ISIJ International,* 41**,** 641-653.

MINICHMAYR, R., RIEDLER, M., WINTER, G., LEITNER, H. & EICHLSEDER, W. (2008) Thermo-mechanical fatigue life assessment of aluminium components using the damage rate model of Sehitoglu. *International Journal of Fatigue,* 30**,** 298-304.

MORITO, S., TANAKA, H., KONISHI, R., FURUHARA, T. & MAKI, T. (2003) The morphology and crystallography of lath martensite in Fe-C alloys. *Acta Materialia,* 51**,** 1789-1799.

MRÓZ, Z. (1967) On the description of anisotropic workhardening. *Journal of the Mechanics and Physics of Solids,* 15**,** 163-175.

MURAKAMI, S., KAWAI, M., AOKI, K. & OHMI, Y. (1989) Temperature-dependence of multiaxial non-proportional cyclic behavior of type 316 stainless steel. *Journal of Engineering Materials and Technology,* 111**,** 32-39.

NAGESHA, A., VALSAN, M., KANNAN, R., BHANU SANKARA RAO, K. & MANNAN, S. L. (2002) Influence of temperature on the low cycle fatigue behaviour of a modified 9Cr-1Mo ferritic steel. *International Journal of Fatigue,* 24**,** 1285-1293.

OKRAJNI, J., JUNAK, G. & MAREK, A. (2008) Modelling of the deformation process under thermo-mechanical fatigue conditions. *International Journal of Fatigue,* 30, 324-329.

OLLER, S., SALOMÓN, O. & OÑATE, E. (2005) A continuum mechanics model for mechanical fatigue analysis. *Computational Materials Science,* 32**,** 175-195.

PETRENEC, M., POLÁK, J. & BUCEK, P. (2011) Cyclic plasticity and strain localization in cast [gamma]-TiAl based alloy. *Procedia Engineering,* 10**,** 1391-1396.

POLAK, J. (1991) *Cyclic plasticity and low cycle fatigue life of metals*, Elsevier.

PRAGER, W. (1949) Recent developments in the mathematical theory of plasticity. *Journal of Applied Physics,* 20**,** 235-241.

RICHARDOT, D., VAILLANT, J. C., ARBAB, A. & BENDICK, W. (2000) *The T92/P92 book*, Vallourec & Mannesmann Tubes.

SAUZAY, M., BRILLET, H., MONNET, I., MOTTOT, M., BARCELO, F., FOURNIER, B. & PINEAU, A. (2005) Cyclically induced softening due to low-angle boundary annihilation in a martensitic steel. *Materials Science and Engineering A,* 400-401**,** 241-244.

SAUZAY, M., FOURNIER, B., MOTTOT, M., PINEAU, A. & MONNET, I. (2008) Cyclic softening of martensitic steels at high temperature--Experiments and physically based modelling. *Materials Science and Engineering: A,* 483-484**,** 410-414.

SHANG, J., LEEN, S. B. & HYDE, T. H. (2006) Finite-element-based methodology for predicting the thermo-mechanical behaviour of superplastic forming tools. *Proceedings of the Institution of Mechanical Engineers, Part L: Journal of Materials: Design and Applications,* 220**,** 113-123.

SHANG, D.-G. & YAO, W.-X. (1999) A nonlinear damage cumulative model for uniaxial fatigue. *International Journal of Fatigue,* 21**,** 187-194.

SHANKAR, V., VALSAN, M., RAO, K. B. S., KANNAN, R., MANNAN, S. L. & PATHAK, S. D. (2006) Low cycle fatigue behavior and microstructural evolution of modified 9Cr-1Mo ferritic steel. *Materials Science and Engineering: A,* 437**,** 413-422.

SHIBLI, A. & STARR, F. (2007) Some aspects of plant and research experience in the use of new high strength martensitic steel P91. *International Journal of Pressure Vessels and Piping,* 84**,** 114-122.

SHIBLI, A. (2008) Performance of modern high strength steels (P91, P92) in high temperature plant. *2007 Proceedings of the ASME Pressure Vessels and Piping Conference - 8th International Conference on Creep and Fatigue at Elevated Temperatures - CREEP8.*

SKELTON, R. P. (1991) Energy criterion for high temperature low cycle fatigue failure. *Materials Science and Technology,* 7**,** 427-439.

SOLASI, R., ZOU, Y., HUANG, X. & REIFSNIDER, K. (2008) A time and hydration dependent viscoplastic model for polyelectrolyte membranes in fuel cells. *Mechanics of Time-Dependent Materials,* 12**,** 15-30.

SURESH, S. (1998) *Fatigue of materials,* Cambridge, Cambridge University Press.

SUSMEL, L. (2008) The theory of critical distances: a review of its applications in fatigue. *Engineering Fracture Mechanics,* 75**,** 1706-1724.

SUSMEL, L. & TAYLOR, D. (2007) The Theory of Critical Distances to estimate lifetime of notched components subjected to variable amplitude uniaxial fatigue loading. *International Journal of Fatigue,* 33**,** 900-911.

SWINDEMAN, R. W., SANTELLA, M. L., MAZIASZ, P. J., ROBERTS, B. W. & COLEMAN, K. (2004) Issues in replacing Cr-Mo steels and stainless steels with 9Cr-1Mo-V steel. International Journal of Pressure Vessels and Piping, 81, 507-512.

TIMOSHENKO, S. (1953) *History of strength of materials,* New York, McGraw-Hill.

TONG, J. & VERMEULEN, B. (2003) The description of cyclic plasticity and viscoplasticity of waspaloy using unified constitutive equations. *International Journal of Fatigue,* 25**,** 413-420.

TONG, J., ZHAN, Z. L. & VERMEULEN, B. (2004) Modelling of cyclic plasticity and viscoplasticity of a nickel-based alloy using Chaboche constitutive equations. *International Journal of Fatigue,* 26**,** 829-837.

VAILLANT, J. C., VANDENBERGHE, B., HAHN, B., HEUSER, H. & JOCHUM, C. (2008) T/P23, 24, 911 and 92: New grades for advanced coal-fired power plants--Properties and experience. *International Journal of Pressure Vessels and Piping,* 85**,** 38-46.

YAGHI, A. H., HYDE, T. H., BECKER, A. A. & SUN, W. (2008) Finite element simulation of welding and residual stresses in a P91 steel pipe incorporating solid-state phase transformation and post-weld heat treatment *The Journal of Strain Analysis for Engineering Design,* Volume 43**,** 275-293.

YAGUCHI, M. & TAKAHASHI, Y. (2000) A viscoplastic constitutive model incorporating dynamic strain aging effect during cyclic deformation conditions. *International Journal of Plasticity,* 16**,** 241-262.

YAGUCHI, M. & TAKAHASHI, Y. (2005) Ratchetting of viscoplastic material with cyclic softening, part 2: application of constitutive models. *International Journal of Plasticity,* 21**,** 835-860.

YAGUCHI, M., YAMAMOTO, M. & OGATA, T. (2002) A viscoplastic constitutive model for nickel-base superalloy, part 2: modeling under anisothermal conditions. *International Journal of Plasticity,* 18**,** 1111-1131.

YEOM, J. T., LEE, C. S., KIM, J. H., LEE, D. G. & PARK, N. K. (2007) Continuum damage model of creep-fatigue interaction in Ni-base superalloy. *Key Engineering Materials.*

ZHAN, Z. (2004) A study of creep-fatigue interaction in a new nickel-based superalloy. University of Portsmouth.

ZHAN, Z., FERNANDO, U. S. & TONG, J. (2008) Constitutive modelling of viscoplasticity in a nickel-based superalloy at high temperature. *International Journal of Fatigue,* 30**,** 1314-1323.

ZHAN, Z. L. & TONG, J. (2007) A study of cyclic plasticity and viscoplasticity in a new nickel-based superalloy using unified constitutive equations. Part I:

Evaluation and determination of material parameters. *Mechanics of Materials,* 39**,** 64-72.

ZHANG, J. & JIANG, Y. (2008) Constitutive modeling of cyclic plasticity deformation of a pure polycrystalline copper. *International Journal of Plasticity,* 24**,** 1890-1915.

ZHAO, L. G., TONG, J., VERMEULEN, B. & BYRNE, J. (2001) On the uniaxial mechanical behaviour of an advanced nickel base superalloy at high temperature. *Mechanics of Materials,* 33**,** 593-600.

British Standard BS7270:2006 *Metallic materials – Constant amplitude strain controlled axial fatigue – Method of test.*

Appendices

Appendix 1. The Zmat's material definition file for the unified viscoplasticity model for P91 steel at 400˚C.

```
***behavior gen_evp
  **elasticity isotropic
            young 185000.0
            poisson 0.3
  **potential gen_evp ev
          *store_all
        *criterion mises
        *flow norton
            n 2.48
            K 1250.0
         *kinematic nonlinear
            C 183000.0
            D 1000.0
         *kinematic nonlinear
            C 8000.0
            D 40.0
         *isotropic nonlinear
            R0 151.0
            Q -45.0
            b 0.4
***return
```

Appendix 2. The Zmat's material definition file for the unified viscoplasticity model (with two stage isotropic hardening) for P91 steel at 600˚C.

```
***behavior gen_evp
  **elasticity isotropic
            young 140000.0
            poisson 0.3
  **potential gen_evp ev
          *store_all
        *criterion mises
        *flow norton
            n 3.482
            K 1000.0
         *kinematic nonlinear
            C 63000.0
            D 900.0
         *kinematic nonlinear
            C 5000.0
            D 50.0
         *isotropic linear_nonlinear
            R0 90.0
            H -2.9
            Q -52.0
            b 1.9
***return
```

Appendix 3. The Zmat's material definition file for the unified viscoplasticity model for P91 steel used in the TMF simulation between 400 and 600˚C.

```
***behavior gen_evp
  **elasticity isotropic
          young temperature
          185000.0 400.0
          174228.0 500.0
          155000.0 600.0
          poisson 0.3
  **thermal_strain isotropic
          alpha 14.5e-6
  **potential gen_evp ev
       *criterion mises
       *flow norton
                  n temperature
                  2.48 400.0
                  3.01 500.0
                  3.482  600.0
                  K temperature
                  1250.0 400.0
                  1200.0 500.0
                  1000.0 600.0
        *kinematic nonlinear
                  C temperature
                  183000.0 400.0
                  130000.0 500.0
                  63000.0  600.0
                  D temperature
                  1000.0 400.0
                  1000.0 500.0
                  900.0 600.0
        *kinematic nonlinear
                  C temperature
                  8000.0 400.0
                  5400.0 500.0
                  5000.0 600.0
                  D temperature
                  40.0 400.0
                  45.0 500.0
                  50.0 600.0
        *isotropic nonlinear
                  R0 temperature
                  151.0  400.0
                  120.0  500.0
                  90.0  600.0
                  Q temperature
                  -45.0 400.0
                  -65.0 500.0
                  -70.0 600.0
                  b temperature
                  0.4 400.0
                  0.7 500.0
                  1.1 600.0
***return
```